Development of Novel Photocatalytic Materials and Surfaces for Environmental Clean-up

Thesis submitted to the Bhavnagar University, Bhavnagar

for the degree of

Doctor of Philosophy

in

Chemistry

By

Praveen Kumar Surolia

Under the Guidance of

Dr. R. V. Jasra

Discipline of Inorganic Materials and Catalysis

Central Salt and Marine Chemicals Research Institute (CSMCRI)

Council of Scientific and Industrial Research (CSIR)

Bhavnagar - 364021. Gujarat (India)

September 2009

This thesis is dedicated to: My mom, dad, brother, sisters and my fiancée. Thank you for your love, support and sacrifice throughout my life.

CANDIDATE'S STATEMENT

I hereby declare that the work incorporated in the present thesis is original and has not been submitted to any University / Institution for the award of a Diploma or a Degree. I further declare that the results presented in the thesis and the considerations made therein, contribute in general to the advancement of knowledge in Chemistry and in particular to entitled **"Development of Novel Photocatalytic Materials and Surfaces for Environmental Clean-Up"**

Place: Bhavnagar

Date:

PRAVEEN KUMAR SUROLIA

Senior Research Fellow

CSMCRI, Bhavnagar

CERTIFICATE BY THE Ph. D. GUIDE

This is to certify that the contents of this thesis entitled "**Development of Novel Photocatalytic Materials and Surfaces for Environmental Clean-Up**" is the original research work of **Mr**. **Praveen Kumar Surolia** carried out under my supervision at Discipline of Inorganic Materials & Catalysis, Central Salt and Marine Chemicals Research Institute (Council of Scientific and Industrial Research - CSIR), Bhavnagar, Gujarat.

I further certify that the work has not been submitted either partly or fully to any other University or Institution for the award of any degree.

Place: Bhavnagar **(R. V. JASRA)**

Date:

Acknowledgment

If one has to consider the significant milestones in his own life, it would become necessary to also consider those who have made these milestones possible. Here, I will do my best to acknowledge the people who have made this thesis a reality.

Above all, all glory to God, creator in which all things are possible. I would like to begin by thanking my advisor and mentor, ***Dr. Raksh Vir Jasra*** *for his persistence, guidance and advice. His scientific input and mentoring support provides an example of someone who has truly found their calling in life. My gratitude and appreciation goes to him for his guidance and constructive appreciations during my research work which was invaluable and highly appreciated.*

I am particularly grateful to ***Dr. H. C. Bajaj****, Head, Discipline of Inorganic Materials and Catalysis, for his friendliness, encouragement, support and fruitful discussion during my research work.*

I am indebted to ***Dr. P. K. Ghosh****, Director, CSMCRI, who have always been encouraging to all the students, for allowing me to carry out research work at CSMCRI, Bhavnagar.*

My sincere thanks to ***Dr. R. J. Tayade*** *who introduced me to the photocatalysis research for his valuable suggestions during my research work.*

My special thanks go to Dr. R. S. Shukla, Dr. S. H. R. Abdi, Dr. R. I. Kureshy, Dr. N. H. Khan, Dr. R S. Somani, , Dr. S. Kannan, Dr. B. Tyagi, Dr. S. D. Bhatt, Dr. H. M. Modi, Dr. Jugnu Bhatt, Dr. A. B. Panda and Dr. A. B. Boricha from whom I received encouraging and supportive words and also for useful discussion.

I am thankful to Mr. P. G. M. Pillai, Mr. J. M. Parmar, Mr. B. B. Parmar, and Mr. A. H. Lakhani for all the support they provided in due course of my research.

To my co-workers past and present, especially to Manoj A. Lazar and Nilofer Lakhani, I say thank you for the useful discussions and friendliness.

Cordially thank to my laboratory co-workers and friends Sunil, Govind, G. P. Dangi, Kannan, Prashanth, Renjith, Phani, Dinesh, Munusami, Subba Reddy, Manoj C. Raj and Thillai for their continuous support throughout my work.

I express my sincere thanks and regards to Munir, Krishnamohan, Mallikarjun, Vishal, Santosh and Bharat for the valuable discussions, support and friendship throughout my CSMCRI-life.

I extend my thankfulness to all my wonderful seniors and colleagues at CSMCRI for their assistance and friendship. I deeply appreciate the help I obtained from my seniors Dr. J. Sebastian, Dr. V. K. Srivastava, Dr. D. U. Parmar, Dr. Mukesh Yadav, Dr. Surendra Singh, Dr. Irshad Ahmed, Dr. M. K. Mishra, Dr. Achyut, Dr. Kalpesh, Dr. Hasmukh, Dr. Sumeet and Dr. Kavita Pathak at the initial stage, and difficult times when I began this work.

My time in institute has been blessed with many great friends. I wish to thank Asif, Kunal, Churchil, Manu, Ulka, Shaik Basha, Manish Dixit, Ghanshyam, JayaPratap, Sudheesh, Jinesh, Murugan, Amit, Arpan, Bhavesh, Sumit Jadhav, Koilraj, Nirali, Shaji, Radheshyam, Pravein, Manish, Sandesh, Narottam, Arghya, Vikram, Jaideep, Apurba, Nabin, Praful, Adarsh, Sivashunmugam and Amit Chathurvedi for their prompt help and support. I also thank to my other friends in and out of the institute.

I have no words to express my heartfelt thanks to my wonderful friends Gayatri, Dhayal, Shubu, Rajkumar, Arvind, Ajeet, Kiran, Afsar, Prabhash, Gaurav, Sanjay, Mihir, Manoj Aggrawal, Giridhar, Rajendra, BPT, Shuklaji, Sanjiv, Teji, Yogesh, Tushar, Manoj, Nirali, Mithilesh, Vishal, Manoj Kesharwani, Subrato, Prasenjit, Dipti and Prakash Chaudhary for giving me a constructive outlet to release my research aggressions. Friends, I could enjoy my research life only because of you all.

I would like to extend my gratitude to technical assistance of Dr. (Mrs.) P. Bhatt, for P-XRD analysis, Dr. D. N. Srivastava for TEM analysis Mr. Vinod Agrawal for FT-IR analysis, Mr. Chandrakanth C. K. for SEM analysis, Mr A. K. Das for LC-MS analysis, Mr. Shobhit Singh for instrumentation, Prasanth, Renjith and Govind for surface characterization, Harish and Mitul for ICP analysis, Dr. Jagan Mohan for TGA analysis, H. Bhatt and Satyaveer for TOC analysis.

I like to extend my special thanks to Mr. Atul Shah, Mr. Kashyap, Mr. Yagnesh Trivedi, Mr. S. Upadhyay, Dr. R. Meena, Dr. D. R. Chaudhary, Dr. Babulal, Mr. Rajesh Patidar, Mr.

Kumar Rahul, Mr. Rambabu, Mr. Avnish Kumar, Mr. Merut, Mr. Harikrishnan, Mr. Arvind Sharma and Mr. Srikant Sharma for their kind support and invaluable assistance.

I convey my word of appreciation to IT Cell especially Mr. Pramod Makwana, for his significant contributions related to PC and software during this period.

To my other co-workers in the CSMCRI who are too numerous to name here, I thank all of you for your help, time and input. I am lucky to have had the opportunity to meet all of you.

I wish to thank my family and friends for their support and encouragement. To my parents, I thank you for the values that you have instilled in me. From you, I have learned what it means to set goals and to work hard to achieve them. Thank you for your encouragement and confidence. I would like to thank my brother and sisters without them I would not have made it this far in life. They have been there for me every step of the way, have always loved me unconditionally, and have aided me through all of my tough decisions.

Many thanks go to my caring fiancée, Namrta for her understanding, patience, unconditional love and emotional support.

I highly acknowledge The Council of Scientific and Industrial Research (CSIR), New Delhi to provide me financial assistance to carried out my research work.

Finally I place my regards to all those who helped me knowingly or unknowingly.

Place: Bhavnagar

Date:

PRAVEEN KUMAR SUROLIA

Senior Research Fellow

CSMCRI, Bhavnagar

TABLE OF CONTENTS

Chapter 1

Introduction

1.1. INTRODUCTION

During the past several decades, the growth of population and the activities in industries and agriculture have significantly altered the environment and reduced the availability of natural resources. Moreover, some of the activities results in persistent and toxic organic substrates and hazardous wastes as pollutants in wastewater effluent, underground storage tanks and dump sites of industrial manufacture. Typical wastes of concern include volatile organics, chlorinated volatile organics, dioxins, dibenzofurans, pesticides, nitro-aromatic compounds, PCB's, chlorophenols, asbestos, heavy metals, arsenic compounds, aviation fuel, solvents, and degreasing agents. Due to disposal of these chemicals, the surrounding soil and underlying groundwater aquifers have become contaminated resulting into lot of stress on the availability of fresh water. Therefore, the control of chemical pollutants has received much attention. The removal of the pollutants by complete mineralization of a wide range of chemical compounds has become relevant and important. Innovative water and wastewater technologies are needed to meet the challenges of deterioration of water quality. The methods widely used currently for cleaning water streams involve stoichiometric chemical treatment with oxidizing reagents, usually either chlorine or ozone to oxidatively degrade the chemical contaminants **[1]**. Conventional techniques such as activated carbon or air stripping are becoming unacceptable because they do not destroy the pollutants but only transfer the contaminants from one phase to another. The chemical treatments employed in these methods are limited in effectiveness in attaining only incomplete purification and by the need for large quantities of the oxidizing reagent consumed in the operation.

Advanced physicochemical processes such as semiconductor photocatalysis is emerging as alternative to conventionally used processes such as high temperature incineration, amended activated sludge digestion, and anaerobic digestion for the destruction of hazardous chemical wastes. Heterogeneous photocatalysis, one of the Advanced Oxidation Processes (AOPs), has been utilized to remove a wide range of pollutants in liquid and gas phase over the past several decades **[2-8]**. This technology is based on the formation of nonselective and highly reactive hydroxyl radicals ($^{\bullet}OH$) and superoxide radical anions ($O_2^{\bullet-}$), as initiators of the oxidative degradation. Photocatalysis uses light

energy to react with a molecule leading to the formation of radicals in the solution. These radicals can be formed from the molecule itself and are capable of oxidizing or reducing and thereby destroying the target contaminants.

1.2. WATER POLLUTION

1.2.1. Factors Responsible for Water Pollution

Many causes of pollution include sewage and fertilizers containing nutrients such as nitrates and phosphates. In excess levels, these nutrients over stimulate the growth of aquatic plants and algae. Excessive growth of these types of organisms consequently clogs our waterways, use up dissolved oxygen as they decompose, and block light to deeper waters. Under natural conditions, lakes, rivers, and other water bodies undergo Eutrophication, an aging process that slowly fills in the water body with sediment and organic matter. When these sediments enter various bodies of water, fish respiration becomes impaired, plant productivity and water depth become reduced, and aquatic organisms and their environments become suffocated.

Pollution is also caused when silt and other suspended solids, such as soil, wash-off ploughed fields, construction and logging sites, urban areas, and eroded river banks when it rains. Pollution in the form of organic material enters waterways in many different forms as sewage, as leaves and grass clippings, or as runoff from livestock feedlots and pastures. Pollutants also enter in water as effluents of industrial manufacturer and normal households. These organic materials start to use the dissolved oxygen in water after the break down by bacteria and protozoan. The decreased quantity of dissolved oxygen starts to kill aquatic organism which leads to disruption in the food chain.

1.2.2. Additional Forms of Water Pollution

The petroleum, radioactive substances, and heat are the other three forms of water pollution. Petroleum from oil spills, large scale accidental discharges and off-shore drilling operations are mainly responsible factors for pollution of water bodies. The number of organic compounds has been synthesized since many decades and many of

these are now found in the waste water from industries **[9]**. The waste from nuclear power plants, uranium and thorium mining and refining, industries, medical and scientific fields are responsible for radioactive water pollution. The heat is another form of water pollution and the increased temperature result in the death of many aquatic organisms.

1.2.3. Contaminants of concern found in wastewater

The important contaminants of concern in wastewater treatment are listed in **Table-1.1 [9]**. The treatment standards for wastewater are concerned with the removal of biodegradable organic, suspended solids, and pathogens.

Table-1.1. Contaminants of concern in wastewater treatment

Contaminants	Reasons for importance
Suspended solids	Suspended solids can lead to the development of sludge deposits and anaerobic conditions when untreated wastewater is discharge in the aquatic environment
Biodegradable organic	Composed principally of proteins, carbohydrates, and fats, biodegradable organic are measured most commonly in terms of BOD (Biological oxygen demand) and COD (chemical oxygen demand) if discharged untreated to the environment, their biological stabilization can lead to the depletion of natural oxygen resources and to the development of septic conditions
Pathogens	Communicable diseases can be transmitted by the pathogenic organisms in wastewater
Nutrients	Both nitrogen and phosphorous, along with carbon, are essential nutrients for growth. When discharge to the aquatic environment, these nutrients can lead to the growth of undesirable aquatic life. When discharge in excessive amounts on land, they can also lead to the pollution of groundwater
Priority pollutants	Organic and inorganic compounds selected on the basis of their known or suspected carcinogenicity, mutagenicity, teratogenicity, or high acute toxicity. Many of these are found in wastewater
Refractory organics	These organics tend to resist congenital methods of wastewater treatment. Typical examples include surfactant, phenols, and agricultural pesticides
Heavy metals	Heavy metals are usually added to wastewater from commercial and industrial activities and may have to be removed if the wastewater is to be used
Dissolved inorganics	Inorganic constituents such as calcium. Sodium, and sulphate are added to the original domestic water supply as a result of water use and may be have to be removed if the wastewater is to be reused
Hydrocarbons	Large-scale accidental discharges of petroleum are an important cause of pollution along shore lines. Besides the super tankers, off-shore drilling operations contribute a large share of pollution

1.3. FUNDAMENTALS OF SEMICONDUCTOR PHOTOCATALYSIS

1.3.1. Photocatalysis

The term photocatalysis has been defined as "*a catalytic reaction involving light absorption by a catalyst or a substrate*" **[10]** and "*catalytic reaction involving production of a catalyst by absorption of light*" **[11]**. In a general view, "*photocatalysis is a reaction which uses light to activate a substance which modifies the rate of a chemical reaction without being involved itself"*. In 1972, Fujishima and Honda discovered the photocatalytic splitting of water on a TiO_2 single-crystal electrode which marked the beginning of a new era in heterogeneous photocatalysis. It soon became apparent that the novel redox reactions of organic and other inorganic substrates could also be induced by band-gap irradiation of a variety of semiconductor particles (e.g. TiO_2, ZnO, CdS, and ZnS etc.), of sizes ranging from clusters and colloids to powders and large single crystals. These redox reactions are developed for the degradation of organic compounds to give CO_2, water and other associated inorganic components in water treatment process **[12-14]**. Consequently, heterogeneous photocatalysis has been utilized to remove a wide range of pollutants in both liquid and gas phases over the past two decades **[2-7]**.

Heterogeneous photocatalysis has been proven to be able to achieve the following **[15-17]**:

(1) A wide variety of organic pollutants in aqueous and gaseous media can be completely degraded or mineralized.

(2) Heterogeneous photocatalysis can be used to inactivate pathogenic organisms including bacteria, viruses, fungi, protozoa, and algae.

(3) Dissolved metal ions can be removed in their metallic form through photocatalytic reduction.

(4) Photocatalytic reactions take place under ambient conditions, and no other chemical is required.

(5) It can provide a potentially inexpensive and convenient way of treating organic contaminants.

1.3.2. Semiconductor

Materials are characterized as metals, semiconductors and insulators based on their electronic structure. The electronic structure can be described by the band theory of materials **[18]**. According to band theory, the valence band exists as filled energy levels, while the conduction band consists of available electronic states that are vacant, until the material is thermally or electronically excited. The energy gap that exists between the valence band and conduction band is known as band gap and the materials are classified on the basis of this band gap. **Figure-1.1 [19]** schematically illustrates the differences in the electronic structure of an insulator (very large band gap), a semiconductor (some band gap) and a metal (no band gap, but rather a continuum of electronic states throughout the material).

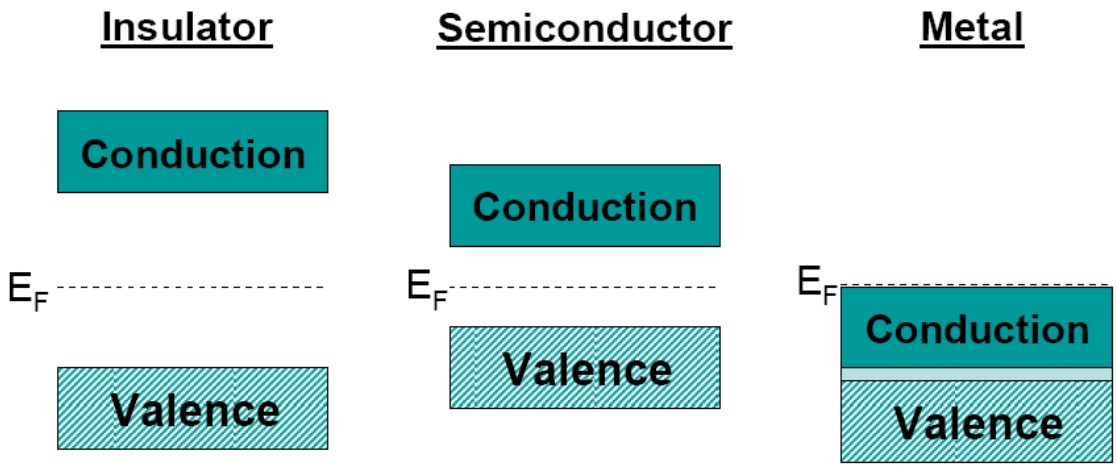

Figure-1.1. Electronic band structure of an insulator, semiconductor and a metal

The Fermi level, E_F, is defined as the energy level in the middle of the band gap for the intrinsic (pure) semiconductor as shown in **Figure-1.1** as a dotted line. For the extrinsic or doped semiconductor, the Fermi level varies based on the concentration and type of the dopant. For an *n*-type semiconductor like TiO_2, the Fermi level is can be derived according to:

$$E_F = E_i + k_B T ln\left(\frac{N_D}{n_i}\right) \quad (1.1)$$

The E_F is the Fermi energy, E_i is the initial energy (or the position of E_F for an intrinsic semiconductor), k_B is the Boltzmann constant, T is the temperature (K), N_D is the concentration of donors, and n_i is the intrinsic carrier density. As such, for *n*-type semiconductors, the Fermi level is slightly elevated towards the conduction band.

1.4. SEMICONDUCTOR PHOTOCATALYSTS

An efficient photocatalyst is a solid, harmoniously combines good chemisorptive and photoelectronic properties to have attributes (i) to absorb efficient photons; (ii) to generate electron-hole pairs and (iii) to separate them with a minimum of recombination. The solid semiconductors mostly used as photocatalysts are chalcogenides like sulfides or oxides of the transition metals. In past few years, many catalysts have been tried for photocatalytic oxidation of water environmental contaminants. The most common semiconductors employed photocatalysis are summarized in Table 1.2 with their band gap energies (E_{bg}) and respective wavelength sensitivity.

Table-1.2. Band gap energy and wavelength sensitivity of semiconductors [20]

Semiconductor	**E_{bg} (eV)**	**λ (nm)**
CdS	2.4	517
Fe_2O_3	2.3	539
$SrTiO_3$	3.2	388
TiO_2(rutile)	3.0	413
TiO_2(anatase)	3.2	388
WO_3	2.8	443
ZnO	3.2	388
ZnS	3.6	344

The potential energy of the photoinduced electron-hole (e^--h^+) pairs and consequently their strength to produce oxidative or reductive pathways can be explained using an energy-level diagram as shown below in **Figure-1.2 [20]**. This figure reports the energy levels for some of these semiconductors with respect to the normal hydrogen electrode (NHE) at pH=0. The energy level at the bottom of conduction band is actually the reduction potential of photoinduced electrons. The energy level at the top of valence band determines the oxidizing ability of photoinduced holes, each value reflecting the ability of the system to promote reductions and oxidations **[21-22]**. Different semiconductors have varying oxidation and reduction potentials for their conductance and valence bands (**Table-1.2**). The redox potentials for these semiconductors range between 4.1 and -2.3 volts versus Normal Hydrogen Electrode (NHE).

Various *n*-type semiconductor metal oxides, such as TiO_2, ZnO, CdS, SnO_2 and WO_3 etc. have been tested for photocatalytic oxidation of organic pollutants in water and air. The drawbacks to using these metal oxides are their (a) large band gap, often necessitating near-UV light ($\lambda < 400$ nm) to induce electron photoexcitation, (b) instability in aqueous medium, leading to photocatalyst decomposition, and (c) high electron-hole recombination rates. Zinc oxide self-deactivates by forming Zn^{2+} ions when react with photogenerated holes in water which can dissolve into solution **[23-24]**. CdS also show the same photocorrosion effect in solution by releasing toxic Cd^{2+} ions in aqueous media **[23, 25]**. Tin oxide has wider band gap of 3.5-4.2 eV (350-300 nm), which utilizes a lesser fraction of UV light and thus has lower relative photoactivity **[26]**.

Among the semiconductors reported in **Table-1.2**, TiO_2 has generally exhibited the highest photocatalytic activity in a wider range of environmental applications. Moreover, the preferential use of TiO_2 for the photocatalytic degradation of organic substrates is based on its low-cost, non-toxic, photochemical stability and also, its appropriate energetic separation between the VB and CB (+3.1 and -0.1 eV) which can be surpassed by the photonic solar energy, leading to the use of sun light for semiconductor photocatalytic application **[27]**. The properties of TiO_2 have lead to its wide use in mediating photocatalytic reactions. The band gap of titanium dioxide is 3.2 V (**Table-**

1.2), allowing photooxidation to occur with adsorption of light in the near ultra violet region (~ 380 nm).

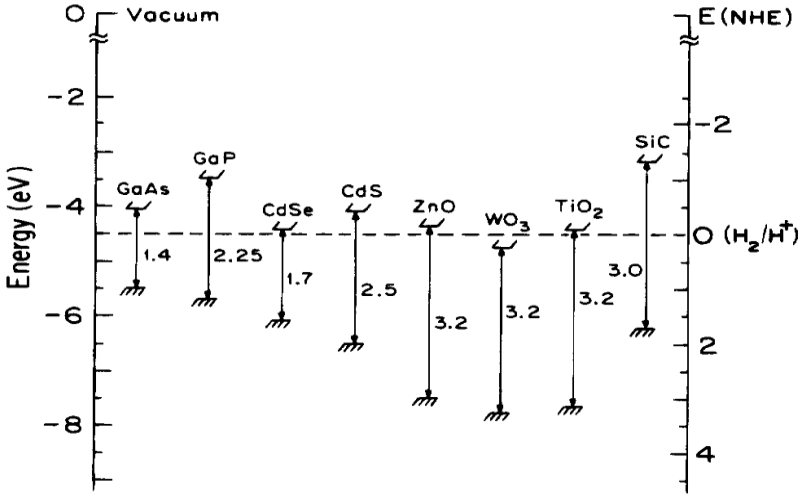

Figure-1.2. The potential energy diagram of the different semiconductor photocatalysts in aqueous media at pH=0 [20]

1.4.1. Basic Principle

Semiconductors possess electronic structure characterized by a filled valence band and an empty conduction band. The energy difference between the conduction band and the valence band is called band gap energy. The basic principle of photocatalysis process is a semiconductor photo excitation as result of radiation absorption, normally near ultraviolet spectrum (**Figure-1.3**). Under near UV irradiation, a suitable semiconductor material can be excited by photons possessing energies of sufficient magnitude to produce conduction band electrons and valence band holes **[2, 28-29]**. Both the electron and hole pair are then active to do chemistry at the surface of the semiconductor material. The components of this activated pair are capable of reducing and oxidizing a surface-adsorbed substrate respectively, and react with both water and organic compounds. The holes are powerful oxidants and should thus be able to oxidize almost all chemicals, as well as water, resulting in the formation of hydroxyl radicals **[30]**. It is generally assumed that both photocatalytic oxidative and reductive reactions occur simultaneously. The surface containing electrons and holes generate $^{\bullet}OH$ radicals and other radicals formed by the oxidation of oxygen, water, or hydroxide ions.

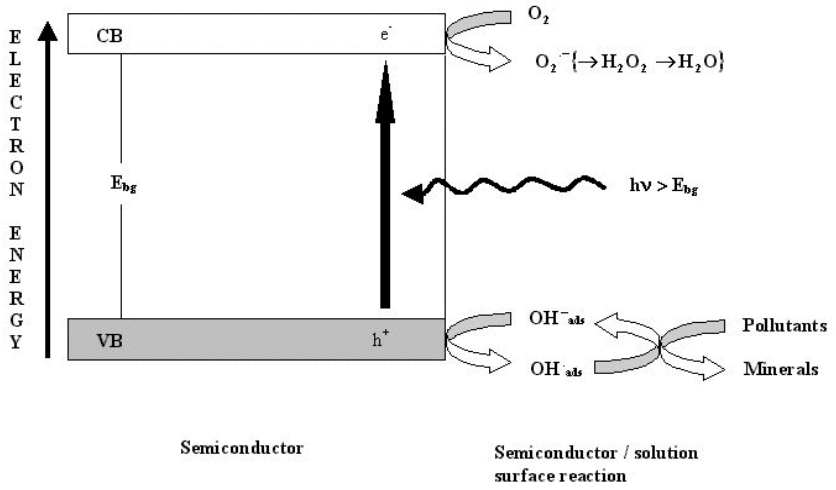

Figure-1.3. e^{-}-h^{+} pair generation phenomena in semiconductor

Irradiation of aqueous semiconductor suspension affects oxidation of pollutants resulting into pollutant abatement and mineralization of organics into CO_2, H_2O, and other associated inorganic components **[12-14]**. The principle of photocatalytic process has been extensively discussed. The degradation of organic substrates seems to be mediated by a series of reactions initiated by these primary oxidizing species, predominantly $^{\bullet}OH$ radicals **[31-34]**. The photocatalytic efficiency of the process is dependent on many factors, such as photoreactor design, light intensity, organic substrate, solution composition, and photocatalyst surface composition **[35-36]**. Moreover, the adsorption of organic substrates onto the surface of TiO_2 plays an important role in the photocatalytic degradation **[37-38]**.

1.4.2. Basic Properties of TiO_2

The photocatalytic splitting of water on TiO_2 electrodes by Fujishima and Honda in 1972 was the starting point of a new era in heterogeneous photocatalysis **[39]**. Since then heterogeneous photocatalytic oxidation, using TiO_2 has been studied extensively in areas such as photovoltaic conversion and energy storage but more attention has been given in the remediation of water and air. The toxic contaminants and organic pollutant are found to be destructed efficiently by TiO_2 at ambient temperature and pressure, using oxygen as the oxidant to produce CO_2, H_2O, NO_3^- and NO_2^- in case of nitrogenous organic

compounds and HCl in case of chlorinated organic compounds. TiO_2 occurs mainly in two different photocatalytic active crystal forms known as anatase and rutile, under the near-UV irradiation. However, anatase is pronounced more photoactive than rutile. The level of conduction band (CB) for anatase is 0.2 eV higher than rutile as illustrated in **Figure-1.4 [40]**.

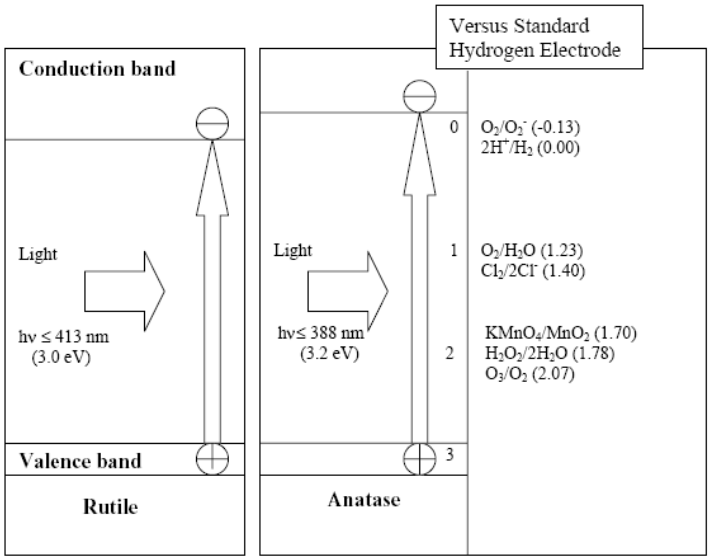

Figure-1.4. Energy diagram for anatase and rutile phase of TiO_2 and relevant redox potentials

The higher conduction band energy of anatase than rutile shows the high reducing power which can effectively drive the very important phenomenon of electrolytic reduction of molecular oxygen (O_2) to superoxide (O_2^-). This makes the anatase phase more effective for the photocatalytic activity towards organic material degradation. TiO_2 is able to absorb about 5% of the solar light, which consist mainly of UV light but modification by doping with transition metals and carbon, photocatalysis is able to proceed under visible light (solar light). The refractive index is 2.9 and 2.5 for rutile and anatase respectively **[41]**. The rutile form is extensively utilized for pigments due to its high refractive index while the later is more commonly use in the photooxidation with its high photoreactivity characteristics. The rutile has the higher recombination rate for the excess charged carriers compared to anatase form. The recombination inhibits the charge transfer from

catalyst to reactants at catalyst surface. Thus, the rutile is used in paint formulation instead of the slow recombining and highly efficient charged transfer anatase form **[42]**.

1.4.3. Lattice Structure of TiO_2

The bulk structure of TiO_2 exists in three forms: rutile, anatase and brookite. Among these crystal structures, rutile and anatase are commonly used in photocatalysis, whereas brookite is not photoactive. The rutile phase is the thermodynamically stable form and the anatase phase transfer to rutile phase when the temperature above 600 ^{o}C **[43]**. The basic structural characteristics of often used anatase and rutile forms have been reviewed by Diebold **[44]**. The crystal structures of both anatase and rutile are in the distorted octahedron class of TiO_6 **[45]**. Each Ti^{4+} ion is surrounded by an octahedron of six O^{2-} ions. The two crystal structures differ by the distortion of each octahedron and by the assembly pattern of the octahedral chains. In the rutile, the distortion is slightly orthorhombic where the unit cell is stretched beyond a cubic shape. In the anatase, the resulting symmetry is less orthorhombic because the distortion of cubic lattice is more significant compared to rutile **[22, 44]**. The structural diagram of the bulk rutile and anatase material is shown in **Figure-1.5 [46]**. The bond lengths and bond angles between atoms are described and showing the stretched cubic shape.

The different lattice structure of anatase and rutile cause different electronic band structure leading to different band gap. Therefore, the absorption thresholds correspond to 388 and 413 nm wavelength for the anatase and rutile phases, respectively and both the form exhibit different photocatalytic activity. The anatase form exhibit higher activity than rutile due to its wider band gap by about 0.2 eV and higher degree of surface hydroxylation **[2, 47]**.

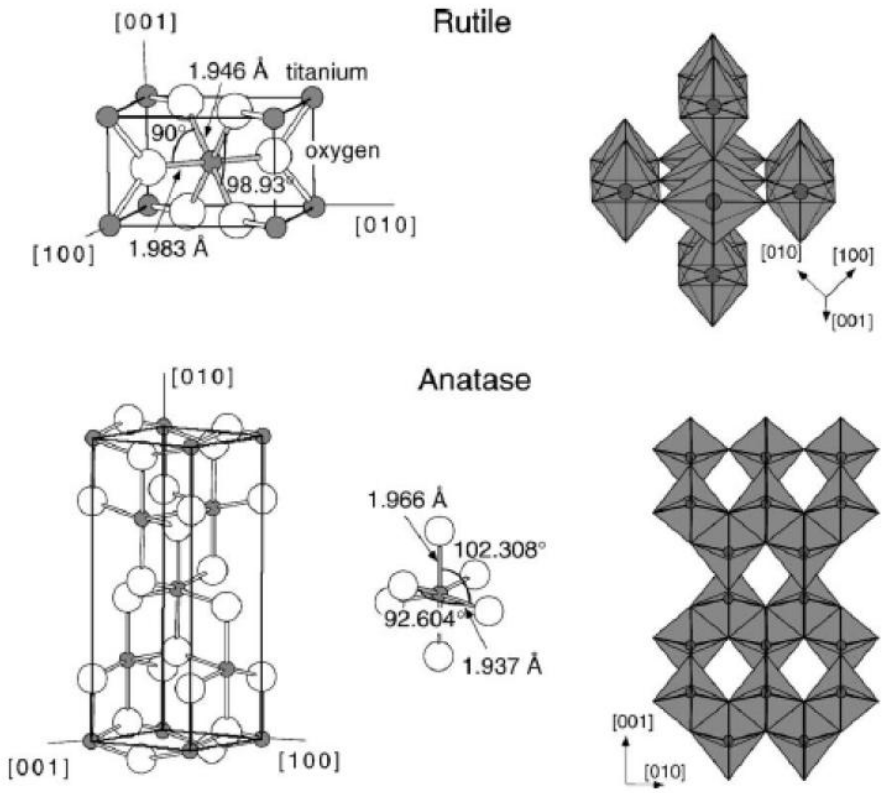

Figure-1.5. Bulk structure of rutile and anatase titanium dioxide showing the bond lengths and angles between atoms [48]

TiO_2 is an *n*-type semiconductor due to the oxygen vacancies. An *n*-type semiconductor has higher potential near the surface than in the bulk. This forces the photoinduced electrons to move into the bulk and the photoinduced holes to remain on the surface, calling the phenomenon charge separation. The charge separation increase the life time of the generated e^--h^+ pairs, providing enough time for charge transfer to adsorbed species on the semiconductor surface and photocatalytic reaction proceed more effectively. Thus if in this process the semiconductor remains intact and the charge transfer to the adsorbed species is continuous and exothermic, the process is termed heterogeneous photocatalysis.

1.4.4. Mechanism of UV/TiO_2 Photocatalysis

The overall process of a classical heterogeneous catalysis in aqueous media can be described as five independent steps.

1. Diffusion of the reactants to the catalyst surface in the reaction solution

2. Adsorption of the reactant at the catalyst surface

3. Reaction in the adsorbed phase to convert reactant to product

4. Desorption of the products from the active sites of the catalyst

5. Removal of the products from the interface region

The steps 2, 3 and 4 depend on the chemical compatibility of reactant and product molecules with the active sites and one of these step control the overall rate of reaction. The photocatalytic reaction occurs in the step (3). For light-induced redox processes semiconductors can act as sensitizers due to their electronic structure. This electronic structure is characterized by their band structure. The absorption of a photon by semiconductor (TiO_2) photocatalyst produces reactive radicals (mainly $^{\bullet}OH$ radicals) which can oxidize organic compounds and totally mineralize them. When a photon with an energy equal or higher than the band gap energy (Eg) of the semiconductor, an electron, e^-, from valence band (VB) is promoted into the conduction band (CB) leaving a hole behind (Equation 1.2) **[2, 28-29]**. The widely accepted **[2, 28]** three major processes can occur following electronic excitation: The photogenerated electrons can reduce as electron acceptor (Equation 1.3) while photogenerated holes can oxidize an electron donor (Equation 1.4). In competition with charge transfer to adsorbed species, there is the possibility that both e^--h^+ pair recombination and trapped carrier recombination take place within a short time period of picoseconds to nanoseconds (Equation 1.5) **[2]**. Photocatalytic efficiency is often controlled by the suppression of e^--h^+ pair recombination, carrier trapping, and interfacial charge transfer **[2]**. The generated single e^--h^+ pairs that may recombine; follow the pseudo-first order kinetics **[49]** with release of heat. These processes are illustrated in **Figure-1.6 [50-51]**.

$$A + D \xrightarrow[light \geq E_{bg}]{semiconductor} A^- + D^+ \qquad (1.2)$$

$$A + e^-_{surface} \rightarrow A^{\cdot -} \qquad (1.3)$$

$$D + h^{+}_{surface} \rightarrow D^{\cdot+} \quad (1.4)$$

$$e^{-} + h^{+} \rightarrow heat \quad (1.5)$$

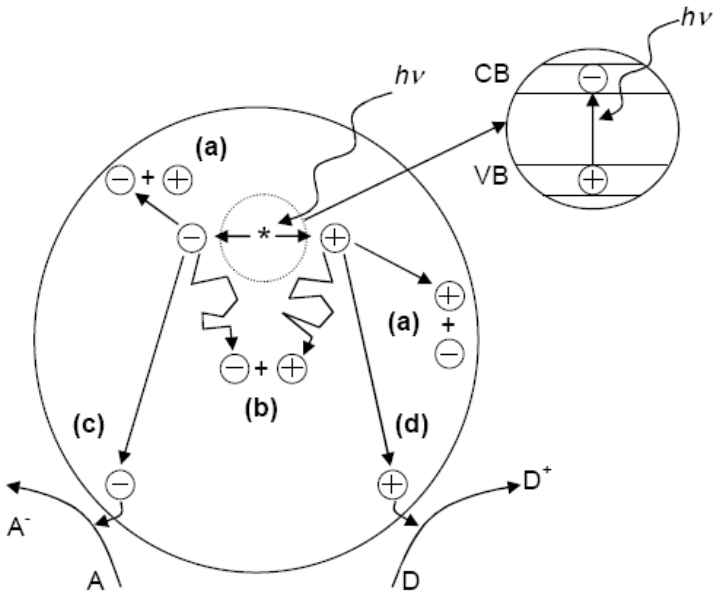

Figure-1.6. Major processes occurring on a semiconductor particle following electron excitation, electron hole recombination can occur at the surface (a) or in the bulk (b) of the semiconductor. At the surface, photogenerated electrons can reduce an electron acceptor 'A' (c) and photogenerated holes can oxidize an electron donor 'D' (d)

The reduction and oxidation processes involving electrons and holes, reactions c and d **(Figure-1.6)**, must compete effectively with the major deactivation processes involving e^{-}-h^{+} recombination, reactions 'a' and 'b' (**Figure-1.6**). Photoinduced holes can directly oxidize adsorbed molecules or react with surface hydroxyl groups to produce $^{\bullet}$OH radicals to act as primary oxidizing species **[52].** The formation and involvement of $^{\bullet}$OH radicals are confirmed by various studies **[53-54]**. The oxidizing potential of $^{\bullet}$OH radical is 2.80 V and can act as strong oxidizing species for almost any organic compound **[55-56].** It can react with organic compounds by hydrogen abstraction, electrophilic addition and electron transfer **[57-58]**. In the case of aromatic compounds, reaction can proceed

via either addition to the aromatic ring or by hydrogen abstraction mainly from substituted alkyl side chain.

The semiconductor is activated by absorption of UV photons of energy greater than the band gap energy (E_{BG}). This phenomenon leads to formation of (e^-_{CB}) - hole (h^-_{VB}) pairs (Equation 1.6). The band gap energy (E_{BG}) of anatase phase of TiO_2 is 3.2 eV (λ = 385 nm), while for rutile phase, it is 3.0 eV(λ = 410 nm). The redox potential for h^-_{VB} and e^-_{CB} is +2.53 V and -0.52V respectively with respect to standard hydrogen electrode (SHE). The redox potential of h^-_{VB} is sufficiently oxidizing to overcome the +2.27 V SHE binding energy of e^- in OH^+ to form a hydroxyl radical $OH^{\cdot}$ ($E_{B,VB}$) from water **[59]**, shown in Equation 1.7. Similarly, e^-_{CB} is sufficiently reductive to react with O_2 to form O_2^- ($E_{B,CB}$ = -0.28 V SHE) **[59]**, shown in Equation 1.8. The O_2^- may also react with H^+ to form the perhydroxyl / hydroperoxyl radical $HO_2^{\cdot}$ as shown in Equation 1.9. These values are reported at pH=7. The $HO_2^{\cdot}$ is also reactive, but weaker than $OH^{\cdot}$. The $HO_2^{\cdot}$ also can combine with another H^+ to form yet less reactive H_2O_2.

$$TiO_2 \xrightarrow{h\vartheta \geq E_{BG}} e^-_{CB} + h^-_{VB} \qquad (E_{BG} = 3.0 - 3.2\ eV) \qquad (1.6)$$

$$h^+_{VB} + H_2O \rightarrow OH^{\cdot} + H^+ \qquad (E_{B,VB} = +2.27V\ SHE) \qquad (1.7)$$

$$e^-_{CB} + O_2 \rightarrow O_2^- \qquad (E_{B,CB} = -0.28V\ SHE) \qquad (1.8)$$

$$O_2^- + H^+ \rightarrow HO_2^{\cdot} \qquad (1.9)$$

1.5. FACTORS INFLUENCING HETEROGENEOUS PHOTOCATALYSIS

The photocatalytic efficiency of the UV/TiO_2 process depends on many factors such as photoreactor design, light intensity, organic substrate, solution composition and photocatalyst surface composition **[35-36]**. Moreover, the adsorption of organic substrates onto the surface of TiO_2 plays an important role in the photocatalytic

degradation **[37, 60-61]**. The key feature of UV/TiO_2 process is that TiO_2 produces strong oxidants.

1.5.1. Factors influencing the TiO_2 photocatalytic activity

The TiO_2 crystals commonly used for the photocatalytic purpose are anatase and rutile. The physicochemical property of the TiO_2 varies with preparation and treatment methods. The variation in the preparation and treatment processes changes to crystal structure, specific surface area, particle size distribution, surface defects of the synthesized TiO_2 which influence the catalytic activity of irradiated TiO_2. The presence of dopants and impurities also affect the TiO_2 catalytic activity. The following parameters are mainly found to affect the photocatalytic activity of TiO_2.

1.5.1.1. *TiO_2 phase, crystallinity and composition*

The photocatalytic application of TiO_2 in water and air purification, hazardous waste control and water disinfection is found to be influenced by its crystallinity **[22, 62-64]** and anatase phase appeared most photoactive among all **[65-70]**. The higher recombination rate of electron and hole in rutile phase **[71]** and main product from molecular oxygen on rutile and anatse particles are also responsible for the different photocatalytic activity. The difference observed in photocatalytic activity of both the phases is due to various parameters mainly higher rate of electron-hole recombination on rutile because of its low capacity to adsorb O_2 **[28**]. Molecular oxygen gives super oxide on rutile while hydrogen peroxide on anatase **[72]** which generate more active $^{\bullet}OH$ radicals responsible for higher photocatalytic activity. However, in some cases the destruction rate was found to be almost same **[73-74]**. The addition of strong electron acceptors which can replace the molecular oxygen such as Fe^{3+} ion can increase the photocatalytic activity of rutile phase also **[87]**. The Degussa P-25 is the most studied photocatalyst in UV/TiO_2 process and many of them reported that the photocatalytic activity of Degussa P-25 is higher than pure anatase TiO_2 **[75-77]**. The other mixed phase TiO_2 photocatalysts also demonstrated the superior photocatalytic activity than pure anatase or rutile phase **[78-80]**. The reason behind it is the smaller band gap of rutile which acts as defect site to extend the photoactivity into visible wavelength generating e^-

-h^+ pairs. The electron generated in rutile phase conduction band would transfer to be trapped in anatase phase, inhibiting the recombination. This allows the separation of charged species and photoinduced holes can migrate to the surface of the particle to participate in photocatalytic degradation **[81-82]**.

1.5.1.2. *Preparation methods and surface physical properties*

The large surface area of photocatalyst can increase the degradation rate as more adsorbed organic molecule involve in degradation process **[83]**. The decreasing diameter of particles increases the specific surface area and the corresponding increase the available active sites **[84]**. However, an optimum particle size is required for the maximum photocatalytic activity due to quantum size effect. The optimum value contributes to a promotion of surface reaction versus e^--h^+ pair recombination due to the increase in the semiconductor band gap. The nanocluster semiconductor particles are more efficient for surface electron and hole trapping by having shorter distance to reach the surface for redox reaction. The surface hydroxyl groups play an important role in the photocatalytic degradation **[62-68]**. Surface hydroxyl groups can trap the holes and produce very reactive surface $^{\bullet}OH$ radicals. Moreover, these groups can increase the adsorption of the reactant molecule by acting as active sites **[3]**. This is another reason of high photocatalytic activity of P-25.

1.5.1.3. *Photocatalyst modification*

The modifications to semiconductor surfaces by addition of metals, dopants, or combinations with other semiconductors can be beneficial in decreasing the e^--h^+ pair recombination rate and thereby increasing the quantum yield of the photocatalytic process. These modification techniques include (1) surface chelation and covalent attachment **[85-86]**. (2) co-deposition and doping of metals **[87-88]**, **Figure-1.7** and (3) photocatalysts mixtures, i.e., coupled semiconductor **[22], Figure-1.8**. Chelating agents such as sulfur-containing compounds, EDTA, and OH^- anions may shift the conduction band of some semiconductors to a more negative potential and improve its photocatalytic activity. Doping of semiconductor with a certain kind of metal and metal ion has been frequently attempted not only to retard the fast e^--h^+ pair recombination but also to enable

visible light absorption by providing defect states in the band gap **[86, 89]**. Impregnation, co-precipitation, and sol-gel methods are used to introduce dopants. Moreover, coupled semiconductors provide an interest to promote the efficiency of photocatalytic degradation by increasing the charge-carrier separation and extending the energy range of photoexcitation for the photocatalytic system.

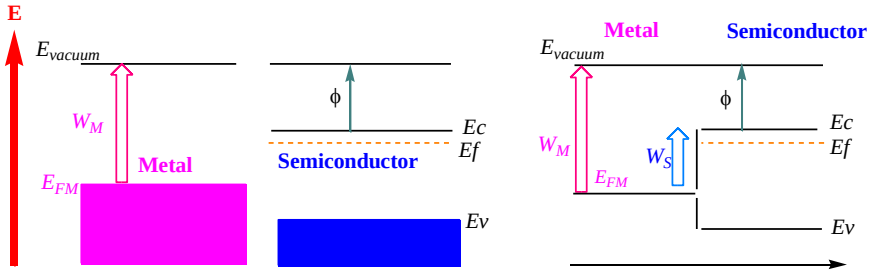

Figure-1.7. Metal doping in semiconductor

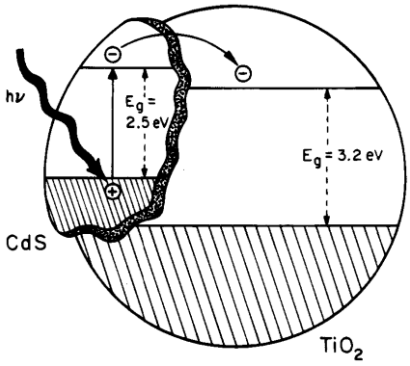

Figure-1.8. Coupled semiconductor system

1.5.1.4. *Deactivation by anions*

The anions impregnated in the catalyst or present in polluted water can be responsible for deactivation which is an important issue for practical applications of photocatalysts. Anions (Cl^- , ClO_4^- , NO_3^- , CO_3^{2-} , HCO_3^- ,SO_4^{2-} , PO_4^{3-}) commonly found in neutral or polluted waters compete for radicals or by blocking the active sites of the semiconductor photocatalyst such as TiO_2 photocatalyst **[90-92]** having a retarding effect on oxidation rate of organic compounds. Studies indicated that inorganic anions affect the

photocatalytic degradation of organic compounds by competitive adsorption occurs mainly on the photocatalyst. During the photocatalytic reaction, due to the degradation of organic compound, the formation of intermediates and byproducts take place, which may have higher adsorption ability to the TiO_2 surface than the corresponding reactant. Moreover, there may be formation of "heavy products" that are difficult to decompose **[93-94]**. Cl^- anions are known to reduce the rate of adsorption and compete for UV photons. It is also prone to reacting with available $^{\bullet}OH$ ions (Equation 1.10) **[95]**. Carbonate and bicarbonate also generate the same kind of effect on the overall rate of photodegradation (Equation 1.11 and 1.12). Sulfate, however was reported to have a minimal effect on the adsorption rate and rate of degradation.

$$OH^{\cdot} + Cl^- \rightarrow Cl^{\cdot} + OH^- \quad (1.10)$$

$$CO_3^{2-} + OH^{\cdot} \rightarrow CO_3^{\cdot -} + OH^{\cdot -} \quad (1.11)$$

$$HCO_3^{2-} + OH^{\cdot} \rightarrow CO_3^{\cdot -} + H_2O \quad (1.12)$$

This deactivates TiO_2 towards the degradation of reactant. This adverse effect could have a great impact in the application of photocatalysis as a cleaning method because anions such as chlorides, nitrates and bicarbonates are ever-present in natural waters and a removal of these ions will be necessary.

1.5.1.5. *Cation effect*

As for the effect of the cations, experimental results have shown that with low concentration of metal ion, degradation rate tends to increase slightly **[96]**. But as the concentration increases past the optimum point, the degradation rate starts to decrease. Transitional metal ion doping and rare earth metal ion doping have been extensively investigated for enhancing the TiO_2 photocatalytic activities. The doping of metal ion could at times expand the photo-response of TiO_2 into visible spectrum **[97]**. As metal ions are incorporated into the TiO_2 lattice, impurity energy levels in the band gap of TiO_2 are formed, as indicated below:

$$M^{n+} + h\vartheta \rightarrow M^{(n+1)+} + e_{cb}^{-} \quad (1.13)$$

$$M^{n+} + h\vartheta \rightarrow M^{(n-1)+} + h_{vb}^{+} \quad (1.14)$$

Where, *M* and M^{n+} represent metal and the metal ion dopant, respectively. Furthermore, electron-hole recombination can also be altered by electron (hole) transfer between metal ions and TiO_2:

$$Electron\ trap: M^{n+} + e_{cb}^{-} \rightarrow M^{(n-1)+} \quad (1.15)$$

$$Hole\ trap: M^{n+} + h_{vb}^{+} \rightarrow M^{(n+1)+} \quad (1.16)$$

The energy level of $M^{n+}/M^{(n-1)+}$ should be less negative than that of the CB edge of TiO_2, while the energy level of $M^{n+}/M^{(n+1)+}$ should be less positive than that of the VB edge of TiO_2 for electron and hole trapping. The metal ion requires the doping near the surface of TiO_2 particles for better carrier transferring which is very important. The deep doping has somewhat lack of efficiency as in this case metal ion act as recombination centers. Thus, there exists an optimum concentration of doped metal ion, above which the photocatalytic activity decreases due to the increase in recombination. The different effects of metal ions result from their abilities to trap and transfer electrons/holes. For example, Cu and Fe ions can trap not only electrons but also holes, and the impurity energy levels introduced are near to CB as well as VB edges of TiO_2. Therefore, doping of either Cu or Fe ions could be recommended for enhancement of photocatalytic activity **[98]**.

1.5.1.6. *Effect of dye*

Dyes have the visible light sensitivity and redox property which can be used for photocatalytic systems **[99-100]**. When the dyes are illuminated by visible light, these can eject electrons to CB of semiconductors to initiate the catalytic reactions as illustrated in **Figure-1.9**.

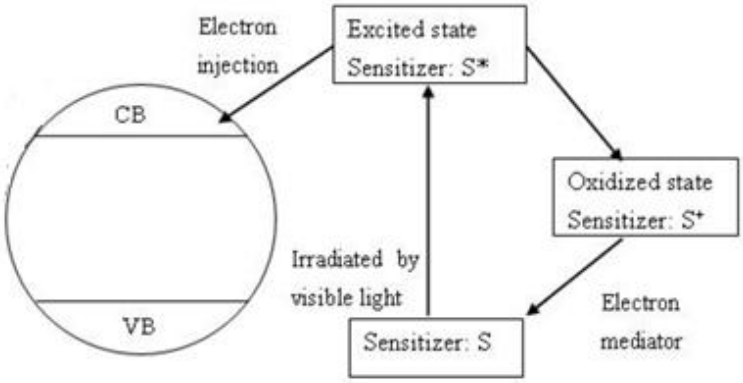

Figure-1.9. Dye sensitization of the photocatalyst under the visible light irradiation

$$dye \xrightarrow{h\vartheta} dye^* \quad (1.17)$$

$$dye^* \xrightarrow{TiO_2} dye^+ + e^- \quad (1.18)$$

$$dye^* + e^- \rightarrow dye \quad (1.19)$$

Thus as for principles of the improved photocatalyst activity of TiO_2 by dye sensitization, the benefits are as follows: Inhibiting recombination by increasing the charge separation and therefore efficiency of the photocatalytic process increased and increasing the spectrum response range (i.e. excitation of wide band gap semiconductors by visible light).

1.5.2. Optimized condition of the reaction parameter

It was stated that the photocatalytic efficiency of the process is affected by many factors, such as light intensity, organic substrate, and solution composition **[101-102]**. The dependence of the operating parameters on the photocatalytic reaction of various organic substrates is different.

1.5.2.1. *Reactant concentration*

The increasing concentration of model pollutant increases the degradation rate but decrease the degradation and mineralization efficiency until a certain level **[103]**. As the concentration of model pollutant increases, more and more molecules get adsorbed at

photocatalyst surface. The substrate concentration is an important parameter for optimization between high degradation rate and efficiency **[71, 104]**. The degradation rate was found increased with the increase in substrate concentration for dye.

1.5.2.2. *Light intensity of the source*

The light irradiance determines the number of created e^{-}-h^{+} pairs. The increasing light intensity which corresponds to increasing incident photon rate leads to increase the number of e^{-}-h^{+} pairs generated. This would result in an increase in photocatalytic reaction rate. The high photon flux increases the collision probability between photons and activated sites on the catalyst surface and enhances the rate of photocatalytic reaction. At the low light intensity and correspondingly low carrier concentration, the rate of particular compound is proportional to light intensity whereas at higher incident light intensity, the degradation rate is proportional to the square root of the light intensity **[105]**. The square root relationship can be explained by bulk recombination of e^{-}-h^{+} pairs within the catalyst particles. Furthermore, at sufficient high light intensity levels, the collision between photons and activated sites approaches its limit, and further increase in the light intensity will have no effect on the reaction rate.

1.5.2.3. *Photocatalyst concentration*

The photocatalytic reaction rate and efficiency would increase with the photocatalyst concentration in the reaction mixture due to the increase in the total surface area or the active sites available for the photocatalyst reaction **[61, 106-107]**. After an optimum value, however, when TiO_2 is overdosed, the number of active sites on the TiO_2 surface may become almost constant because of the decreased light penetration, the increased light scattering and the loss in surface area occasioned by agglomeration (particle-particle interactions) at high solid concentration **[108-109]**.

1.5.2.4. *pH of reaction solution*

The pH of an aqueous solution directly affects the surface charge on the semiconductor particles, the aggregation size and the energy of the conduction and valence bands according to Nerst's law which states that, varying the solution pH would shift the energy

of the valence and conduction band edges, by 0.059 per pH unit at ambient temperature **[2, 110]**. This makes the valence band electron more effective and the conduction band holes less effective at higher pH. Thus, the change in the pH affect semiconductor particles in the aqueous media specially oxides. TiO_2 particles suspended in water are known to be amphoteric and principal amphoteric surface functionality is the "titanol" surface group, ≡ TiOH. For the suspended metal oxides, two equilibria must be considered (Equation 1.20 and 1.21). The optimum pH of the reaction mixture also depends upon other various operating conditions. However, for neutral compounds over moderate pH range, the effect of pH was not major **[3]**.

$$M - OH + H^+ \leftrightarrow M - OH_2^+ \quad K_1 \tag{1.20}$$

$$M - OH \leftrightarrow M - O^- + H^+ \quad K_2 \tag{1.21}$$

1.5.2.5. *Reaction temperature*

One of the important aspects in the photocatalysis is adsorption and desorption of the reactant molecule at the photocatalyst surface. However, these potentially temperature dependent steps are not rate determining steps and accordingly, the effect of temperature become insignificant in some temperature range **[111]**. A slight benefit to using higher temperature for photocatalytic reactions has also been demonstrated **[92, 112]**. However, higher temperatures may have a negative effect on the concentration of dissolved oxygen (DO) in the solution. DO concentration below a certain point may allow for e^--h^+ recombination at the surface of the TiO_2. In this respect, photocatalytic treatment is appropriate for treating liquid water at temperature close to the ambient conditions.

1.5.2.6. *Electron scavenger*

The e^--h^+ pair recombination decrease the rate of degradation and the photocatalytic efficiency requiring the removal of photoinduced electrons. Owing to the electrophilic property, oxygen plays a decisive role in the mechanism of the photocatalytic degradation **[113- 114]** and can be reduced to the superoxide, $O_2^{\cdot -}$, which may also participate in the degradation reaction of the organic molecules or be further reduced to hydrogen peroxide (H_2O_2). The inorganic oxidants also suppress the e^--h^+ recombination by electron

scavenging. The optimum concentrations of inorganic peroxides are required to enhance the degradation rate of several organic pollutants **[115]**. The $S_2O_8^{2-}$ and HSO_5^- are also found to enhance the photocatalytic mineralization **[116]**.

1.6. IMMOBILIZATION OF TiO_2 AND NEW PHOTOCATALYSTS

The recovery of photocatalyst after the reaction from the suspension is a very important aspect to make the catalyst reusable and the photocatalytic process cost effective. Another very important thing that needs to be considered is fine TiO_2 particles of high surface area to achieve the maximum output in the practical application. These can be acquired by fixing or immobilization of TiO_2 particles on supporting material such as MCM-41, MCM-48, SBA-15, clays **[117-118]**, silica gel **[119-120]**, activated carbon **[121]** and zeolites **[122-123]**. Such a fixation occurs through the Ti-O-Si or Ti-O-Al linkage. The fixation of TiO_2 has been studied on glass matrix **[124]**, optical fibers **[125]** and stainless steel plate **[119]**. Though, the photocatalytic activity become lower than that of suspended TiO_2 because supported catalysts have low surface area per reaction volume mixture and suffers from mass transfer limitation. Finding supports which improve adsorption without reducing photoactivity may be most promising path to practical systems. Recently the photocatalytic materials are trying to be synthesized of high surface area having in built TiO_2 photoactive units such as ETS-4 and ETS-10 **[126]**. These are easy to recover and provide high surface area to adsorb the organic molecule.

1.7. KINETICS OF TiO_2 PHOTOCATALYTIC DEGRDADATION

Reaction kinetics gives information about the reaction rates and the mechanisms by which the reactants are converted to the products. The rate law is used to predict the reaction rate of the photocatalytic oxidation. The kinetics of heterogeneous catalysis would follow the Langmuir-Hinshelwood (L-H) model, in which the reaction rate (r) of a unimolecular surface reaction varies proportionally with the surface coverage as:

$$r = k\theta = \frac{kKC}{1+KC} \quad (1.22)$$

$$\frac{1}{r} = \left(\frac{1}{kKC} + \frac{1}{k}\right) \quad (1.23)$$

where, *k* and *K* are the reaction rate constant and the adsorption equilibrium constant, and *C* is the concentration of organic compound to be degraded. A linear plot of the reciprocal value of the initial rate (1/*r*) against the reciprocal values of the organic compound initial concentration (1/*Co*) gives *k* as the L-H rate constant and *K* as the Langmuir adsorption constant of the organic compound in the photocatalytic degradation reaction. The surface hydroxyl groups at the TiO_2 surface also contribute to increase the adsorption of organic substrate at the TiO_2 surface. When the term KC_0 is much less than 1 ($KC << 1$), the L-H rate equation results in pseudo-first-order reaction. At the initial stage the equation 1.24 is valid and L-H rate constant *k* and the adsorption constant *K* can be evaluated. However, during the photocatalytic process, intermediates are formed and their *KC* terms must be included in the L-H rate equation even when their adsorption on the TiO_2 surface may be rather weak. For simplicity, it is better to employ only the initial degradation rate for the application of the equation. Theoretically, the reaction rate can be simply expressed as the decreasing rate of any of the reactants or the increasing rate of any of the products against time. A common way to express the reaction rate is to use the rate law:

$$rate\ (r) = -\frac{d[A]}{dt} = k[A]_n \quad (1.24)$$

where *k* is the rate constant, *n* is the order of the reaction and [*A*] is the concentration of reactant *A*. The reaction rate of photocatalytic oxidation is a parameter of the efficiency of photooxidation reaction and can be influenced by such factors as humidity, light intensity, contaminant concentration and oxygen concentration. A necessary step of a photocatalytic reaction is that the reactant molecules are adsorbed on the catalyst surface and only adsorbed species can be oxidized makes the adsorption process very important in the photocatalytic oxidation process.

1.8. APPLICATIONS OF SEMICONDUCTOR PHOTOCATALYSIS

There are numerous niche possibilities of semiconductor photocatalysis for application purposes. The commercial potential of different applications of photocatalysis appears to be as follows:

1.8.1. Self cleaning surfaces

Self-cleaning surfaces are attracting significant industrial interest and are already well on their way toward widespread commercialization **[127]**. The irradiated TiO_2 films acts both hydrophilic as well as ampiphilic. The hydrophilicity depends upon the surface OH group density. The surface contains both hydrophilic and hydrophobic microdomains, which attract drops of polar or nonpolar liquids respectively. This allows a water rinse to flush away an oily coating **[128]**. The organic compounds can also be degraded on photocatalyst coatings **[129-133]** and these are tested for fatty acids (e.g., octadecanoic (stearic) acid **[130]**, hexadecanoic (palmitic) acid **[131, 133]**.

1.8.2. Air purification and deodorization

The photocatalysis appears well suited to the purification and deodorization of ambient air for indoor and outdoor environment. All the organic pollutants can be oxidized and transformed into NO, NO_2 and SO_2 using this technology. The rate of degradation can be improved by addition of dioxygen, ozone or air **[134, 135]**. However, several characteristics of photocatalytic reactions and indoor air composition and conditioning need to be considered to achieve proper purification.

1.8.3. Water purification

The quality and quantity of the water to be treated are the deciding factor for the use of photocatalysis for water purification. The solar photocatalysis is found to treat the water of agriculture effluent containing pesticides **[136-138]**, textile industries **[139]** and for inactivate to harmful microorganism such as bacteria. NASA is interested in photocatalysis to provide drinkable water in space shuttles **[140]**.

1.8.4. Water splitting

The photocatalysis was started with the phenomenon of water splitting **[39]**. The challenges for this process are significant. The semiconductor must be able to oxidize water to O_2 and to reduce H^+ to H_2, without being itself decomposed. The various materials have been used as a photocatalyst **[141-145]** to achieve the target but still a great area to concern this study.

1.8.5. Cooling buildings

It has been proposed to cover buildings with TiO_2-coated hydrophilic materials and to pour water from the building top along the facades in order to cool them and thereby to decrease the average temperature in city centers with a high density of elevated buildings. The studies have shown a 1.5 K indoor temperature drop using this technique **[146]**. An alternate means of cooling with TiO_2 is the use of ‘‘smart windows’’, which can be darkened by sunlight or an applied voltage, thereby reducing the solar flux into a building **[147-149]**.

1.8.6. Corrosion protection

TiO_2 coatings have been used to provide reductive protection against corrosion. The TiO_2 coating on stainless steel can reduce the corrosion under the UV irradiation **[150]**. A composite TiO_2–WO_3 film stores photogenerated electrons in the WO_3 particles, resulting in corrosion protection that persists for a few hours after irradiation is ceased **[151]**.

1.8.7. Potential medical applications

The TiO_2 photocatalysis has been tried to treat cancer **[152]**. The human human bladder cancer cells deposited on TiO_2-coated glass have been shown to be killed under UV irradiation and TiO_2 was found to reduce the formation of pyrimidine dimmers (believed to cause skin cancer) upon UV irradiation of human cells in vitro and mouse skin in vivo **[153]**. As a different application, photocatalysis has been used for manufacturing a silicone catheter internally and externally coated with TiO_2 and sufficient light penetrates to render the catheter self-sterilizing and self-cleaning throughout **[154]**. After use, the catheter is sterilized in a small box containing a UV lamp.

1.9. CHEMICAL ANALYSIS

1.9.1. Chemical oxygen demand (COD)

The COD test can be used to measure the content of organic matter of both wastewater and natural waters. COD value depends on the amount of oxygen present to oxidize the contained oxygen matter in the solution. The oxygen equivalent of the organic matter that can be oxidized is measured by using a strong chemical oxidizing agent in an acidic medium. Potassium dichromate has been found to be excellent for these purposes. The test must be performed at an elevated temperature. A catalyst (silver sulphite) is required to aid the oxidation of certain classes of organic compounds. Since some inorganic compounds interface with the test, care must be taken to eliminate them. The COD test used to measure the organic matter in the wastes that contain compound which are toxic to biological life. As the photocatalytic oxidation advances, the organic matter starts to break down and finally convert to CO_2. The process decreases the organic content in the reaction mixture and also corresponding COD values.

1.9.2. Total organic carbon (TOC)

Another means for measuring the organic matters present in the water is the TOC test, which is especially applicable to small concentrations of organic matter. This test is performed by injecting a known quantity of sample into a high-temperature furnace or chemically-oxidizing environment. The organic carbon is oxidized to carbon dioxide in the presence of a catalyst. The carbon dioxide that is produced is quantitatively measured by means of an infrared analyzer. Acidification and aeration of the sample prior to analysis eliminate errors due to the presence of inorganic carbon.

Samples are introduced into the combustion chamber by means of an automatic sampler, the water is vaporized and the organic matter is completely oxidized to CO_2 and water by catalytic oxidation. The gas stream carries away the CO_2 produced through a condenser and into a gas/liquid separator to remove most of the water formed. Remaining water can be removed by a dehumificator. The dry gas containing the CO_2 passes finally reaches a nondispersive infrared analizer (NDIR) to determine the amount of total carbon (TC). In the present case, TC is equivalent to TOC as the amount of inorganic carbon (IC) is

negligible. The fraction of organic carbon that passes through a 0.45 μm-pore-diameter filter is called dissolved organic carbon (DOC). The test can be performed rapidly and is becoming more popular. Certain resistant organic compound may not be oxidized, and the measured TOC value will be slightly less than the actual amount present in the sample.

1.9.3. UV-Visible spectrophotometric analysis

The UV-Visible spectrophotometry can be used to calculate the chemical concentration of any compound. In the presence of light, the absorbance (A) of any liquid containing a chemical at concentration (c) can be expressed by Lambert's law:

$$A = \varepsilon \cdot l \cdot c \tag{1.25}$$

Where (l) is the path length of the incident light in the liquid and (ε) is the absorption constant which depend on the nature of the chemical. When a curve is plotted between concentrations (c) versus absorbance (A), this would be linear. Hence, in the range of concentration where A=f(c) is linear (f= $\varepsilon \cdot l$), the absorbance of a chemical polluted solution at a specific wavelength can be used to determine the concentration of the chemical in the reaction media.

1.9.4. High performance liquid chromatography-mass spectroscopy (HPLC-MS)

The substrate conversion and product formed during the reaction course can be identified by the use of HPLC-MS spectra. The oxidation products can be identified by spiking using standards and by retention times in HPLC traces. The components are identified based on the retention time of each component recorded on the chromatogram. Each component has a specific retention time. The nature of some of the products can be further confirmed by mass to charge ratios of molecular ion peaks and fragmentation patterns as obtained from a liquid chromatograph connected to a mass spectrometer (LC/MS). The combined technique of HPLC and Mass is a useful tool to identify the intermediate products in the aqueous media form during the photocatalytic process.

1.9.5. Gas chromatography (GC)

Gas chromatography is one of the widely utilized techniques for the analysis of volatile compounds. This technique can be used to separate a mixture of compounds into individual components. The components are identified based on the retention time of each component recorded on the chromatogram. Each component has a specific retention time which creates a "*fingerprint*" of that component. The amount or concentration of the component can be obtained from the values of the peak area. Gas chromatography involves a sample being vaporized and injected onto the head of the chromatographic column. The sample is transported through the column by the flow of inert, gaseous mobile phase. The column itself contains a liquid stationary phase, which is adsorbed onto the surface of an inert solid. The concentration of the test compound was measured by integrating the area under the peak and compared with a calibration curve. The calibration curve can be obtained by the preparing samples of varying amount of test organic compound with the constant amount of the solvent and plotting the curve of the peak area ratio of test organic compound with the solvent versus volume of organic compound.

1.10. OBJECTIVES OF THE PRESENT WORK

1.10.1. Effect of anions on the photocatalytic degradation

The work focuses on the photocatalytic activity of Fe (III) salts impregnated TiO_2 catalysts for studying the effect of anions on the photocatalytic activity of the salt impregnated catalysts. The anions compete for radicals or block the active sites of the semiconductor photocatalyst such as TiO_2 photocatalyst **[90-92]** having a retarding effect on oxidation rate of organic compounds. Fe metal ions impregnation has been studied for photocatalytic efficiency enhancement of the TiO_2 catalysts and varied results are reported. **[12, 97, 155-156]**. The present work was carried out to specifically study the effect of anion of Fe (III) salts used for impregnation on the photocatalytic activity of P25 Degussa TiO_2 photocatalyst.

1.10.2. Photocatalytic reactivity of transition metal-exchanged ETS zeolites

TiO_2 is one of the most widely used photocatalyst in the pure form and as the supporting titania catalyst. These supporting materials include silica **[157-158]**, zeolites **[87, 159-160]**, fiber glass **[161-162]**, electrode **[163]** etc. However, the recovery is still a challenge even of supported photocatalyst. This problem can be short out by synthesizing a catalyst having in built TiO_2 network. The ETS-10 and ETS-4 photocatalyst were synthesized and transition metal ions were impregnated to improve the photocatalytic activity of these catalysts. These materials contains chains of $–O–Ti^{(IV)}–O–$ that exhibit quantum confinement effects and behave as one-dimensional semiconductor nanowires in its framework **[164-166]**.

1.10.3. Photocatalytic removal of *o*-tolidine over nano-TiO_2

Titanium dioxide has been promising as an excellent material for the photocatalysis of toxic compounds which are hazardous to health and many studies deal with photocatalytic degradation of organic pollutants from different class of compounds **[107, 1167-171]**. The photocatalytic applications are mainly influenced by the morphology, average particle size and size distribution, phase composition and porosity of titania powders. These are important factors governed by the synthesis methods and must be

controlled to achieve the desired photocatalytic activity. The different synthesis methods are responsible for different characteristics mentioned above. Thus the photocatalytic efficiency depends on the preparation method of the catalyst **[62]** that can influence significantly the composition and the size of the crystals and the surface distribution of hydroxyl groups **[172-174]**. This prompts us to synthesis of ultrafine TiO_2 particles with controlled size by different synthesis methods and their application for *o*-tolidine degradation. The mechanism of degradation is also studied.

1.10.4. Kinetic modeling of heterogeneous photocatalytic degradation reactions

There are so many parameters which can influence the photocatalytic activity of TiO_2 and the high surface area is one of the parameter. The high surface area results in higher catalytic active sites which is required for efficient adsorption and thus higher photocatalytic activity. This can be achieved by either synthesis of fine TiO_2 particles or dispersion of TiO_2 on a high surface supporting materials, such as zeolite. The pore characteristics of zeolite such as their shape, size and chemical aspects are responsible for the amount of adsorption **[175-178]**. Zeolite has the accessible cavities and can be modified through the incorporation of active species in pores by various techniques such as ion exchange and impregnation **[179-180]**. The kinetics of the photocatalytic oxidation of the *p*-nitrotoluene was successfully modeled by an approximation of the Langmuir-Hinshelwood (L-H) rate equation based on the hydroxyl radicals and direct hole attack. The reaction rate constants and adsorption constants were determined based on this L-H model.

1.10.5. TiO_2 coating on cenosphere surface towards industrial photocatalysis

The photocatalytic oxidation can be more successful if the catalyst is easily recoverable, reusable, employed to allow most rapid photooxidation possible and active under solar light. However, all the photocatalysts are having high density and they cannot float on the aqueous surface. The attempts has been done to overcome these problems and tried to prepare TiO_2 coated buoyant material such as polystyrene beads, sand, activated carbon, porcelain beads and ceramic microspheres **[181-185]**. These studies reported successful photooxidation but had lack of reusability. Thus the strong adhesion of TiO_2 on buoyant

surface is needed to solve this problem and the coating should stable even after multiple use. For the smart selection of buoyant, these should waste of some industrial process and environmental pollution free. In the study, the cenosphere particles are coated with TiO_2 via sol-gel method for the stable coating and the synthesized material was fully characterized by various instrumental techniques. The photocatalytic study of the synthesized materials was carried out by the photocatalytic degradation of MB, PNA, *n*-decane and *n*-tridecane under the solar light.

1.11. REFERENCES

[1] Ollis, D. F.; Al-Ekabi, H. Eds. Photocatalytic Purification and Treatment of Water and Air; *Elsvier Science Publishers B. V:Amsterdam*, **1993**.

[2] Hoffmann, M. R.; Martin, S. T.; Choi, W.; Bahnemann, D. W., *Chem. Rev.*, **1995,** *95*, 69-96.

[3] Stafford, U.; Gray, K. A.; Kamat, P.V., *Hetero. Chem. Rev.*, **1996,** *3*, 77-104.

[4] Hager, S.; Bauer, R.; Kudielka, G.; *Chemosphere*, **2000,** *41*, 1219-1225.

[5] Deng, X.; Yue, Y.; Gao, Z., *Appl. Catal. B Environ.*, **2002,** *39*, 135-147.

[6] Dunlop, P. S. M.; Byrne, J. A.; Manga, N.; Eggins, B. R., *J. Photochem. Photobiol. A. Chem.*, **2002,** *148*, 355-363.

[7] Balasubramanian, G.; Dionysiou, D. D.; Suidan, M.; Baudin, I.; Laîné; J.-M., *Appl. Catal. B Environ.*, **2004,** *47*, 73-84.

[8] Tayade, R. J.; Kulkarni, R. G.; Jasra, R. V., *Ind. Eng. Chem. Res.*, **2007,** *45*, 922-927.

[9] Al-Momani, F., *Ph. D. Thesis*, University De Baarcelona, **2003**.

[10] Braslavsky, S. E.; Houk, K. N., *Pure & Appl. Chem.*, **1988**, *60*, 1055-1106.

[11] Verhoeven, J. W., *Pure & Appl. Chem.*, **1996**, *68*, 2223-2286.

[12] Kim, Y. -C.; Sasaki, S.; Yano, K.; Ikebukuro, K.; Hashimoto, K.; Karube, I., *Anal. Chem.*, **2002**, *74*, 3858-3864.

[13] Carp, O.; Huisman, C. L.; Reller, A., *Prog. Solid State Ch.*, **2004**, *32*, 331-177.

[14] Florêncio, M. H.; Pires, E.; Castro, A. L.; Nunes, M. R.; Borges, C.; Costa, F. M., *Chemosphere*, **2004**, *55*, 345-355.

[15] Gratzel, M., Energy Resources through Photochemistry and Catalysis, *Acadmic Press Inc.* **1983.**

[16] Tseng, J. M.; Huang, C. P., *Wat. Sci. Tech.*, **1991,** *23*, 377-387.

[17] Huang C. P.; Dong, C.; Tang, Z. *Waste manage.*, **1993,** *13*, 361-377.

[18] Kolasinski, K., Surface Science: Foundations of Catalysis and Nanoscience; *John Wiley and Sons Ltd.: London*, **2002**.

[19] Rodríguez, M., *Ph. D. Thesis*, University De Baarcelona, **2003**.

[20] Stumm, W., Chemistry of the Solid-Water Interface, *John Wiley & Sons, New York, USA.* **1992.**

[21] Hagfeldt, A.; Grätzel, M.., *Chem. Rev.,* **1995,** *95*, 49-68.

[22] Linsebigler, A. L.; Lu, G.; Yates Jr., J. T., *Chem. Rev.*, **1995**, *95*, 735-758.

[23] Neppolian, B.; Choi, H. C.; Sakthivel, S.; Arabindoo, B.; Murugesan, V., *J. of Hazard. Mater.*, **2002**, *89*, 303-317.

[24] Comparelli, R.; Fanizza, E.; Curri, M. L.; Cozzi, P. D.; Mascolo, G.; Agostiano, A., *Appl. Catal. B – Environ.*, **2005**, *60*, 1-11.

[25] Serpone, N.; Maruthamuthu, P.; Pichat, P.; Pelizzetti, E.; Hidaka, H., *J. of Photochem. Photobio. A –Chem.*, **1995**, *85*, 247-255.

[26] Wu, C. H.; Chang-Chien, G. P.; Lee, W. S., *J. of Hazard. Mater.,* **2004**, *114*, 191-197.

[27] Andreozzi, R.; Caprio, V.; Insola, A.; Marotta, R., *Catal. Today*, **1999**, *53*, 51-59.

[28] Fox, M. A.; Dulay, M. T., *Chem. Rev.*, **1993**, *93*, 341-357.

[29] Serpone, N., *Sol. Energy Mat. Sol. Cell*., **1995**, *38*, 369-379.

[30] Munter, R.; Preis, S.; Kallas, J.; Traapido, M.; Veressinina, Y., *Kemia-Kemi*, **2001**, *28*, 354-362.

[31] Ilisz, I.; Dombi, A.; Mogyorósi, K.; Farkas, A.; Dékány, I., *Appl. Catal. B Environ.,* **2002,** *39*, 247-256.

[32] Kaneco, S.; Rahman, M. A.; Suzuki, T.; Katsumata, H.; Ohta, K., *J. Photochem. Photobiol. A Chem.,* **2004,** *163*, 419-424.

[33] Chen, Y.; Yang, S.; Wang, K.; Lou, L., *J. Photochem. Photobiol. A Chem.,* **2005,** *172*, 47-54.

[34] Bizani, E.; Fytianos, K.; Poulios, I.; Tsiridis, V., *J. Hazard. Mater.,* **2006,** *136*, 85-94.

[35] Augugliaro, V.; Loddo, V.; Palmisano, L.; Schiavello, M., *Sol. Energy Mat. Sol. Cells*., **1995**, *38*, 411-419.

[36] Chhor, K.; Bocquet, J. F.; Colbeau-Justin, C., *Mater. Chem. Phys.,* **2004**, *86*, 123-131.

[37] Uyguner, C. S.; Bekbölet, M., *Appl. Catal. B Environ.,* **2004,** *49*, 267-275.

[38] Surolia, P. K.; Lazar, M. A.; Tayade, R. J.; Jasra, R. V., *Ind. Eng. Chem. Res.,* **2008**, *47*, 5847–5855.

[39] Fujishima, A.; Honda, K., *Nature*. **1972**, *238*, 37-38.

[40] Fujishima, A.; Hashimoto, K.; Watanabe, T., "TiO2 Photocatalysis Fundamentals and Applications." *First Edition. Japan. BKC, Inc*., **1999**.

[41] Tiarks, F.; Frechen, T.; Kirsch, S.; Leuninger, J.; Melan, M.; Pfau, A.; Richter, F.; Schuler, B.; Zhao, C. -L., *Prog. Organ. Coating*. **2003**, *48*, 140-152.

[42] Schindler K-. M.; Kuns, M., *J. of Phys. Chem.*, **1990**, *94*, 8222-8226.

[43] Rivera, A.P.; Tanaka, K.; Hisanaga, T., *Appl. Catal. B Environ.*, **1993**, *3*, 37-44.

[44] Diebold, U., *Surf. Sci. Rep*., **2003**, 48, 53-229.

[45] Thompson, T. L.; Diwald O.; Yates, Jr. J. T., *Chem. Phys. Lett.*, **2004**, *393*, 28-30.

[46] Diwald, O.; Thompson, T. L.; Goralski, E.; Walck, S.; Yates, Jr. J. T., *J. Phys. Chem. B*., **2004**, *108*, 52-57.

[47] Ohtani, B.; Ogawa, Y.; Nishimoto, S., *J. Phys. Chem. B*., **1997**, *101*, 3746-3752.

[48] Thompson, T. L., *Ph. D. Thesis*, University of Pittsburgh, **2006**.

[49] Grela, M. A.; Coronel, M. E. J.; Colussi, A. J., *J. Phys. Chem.*, **1996**, *100*, 16940-16946.

[50] Bellu, E., *Ph. D. Thesis*, Robert Gordon University, **2007**.

[51] Mills, A.; Le Hunte, S., *J. of Photochem. Photobio. A: Chem*., **1997**, *108*, 1-35.

[52] Ollis, D. F., *The 1st International Conference on TiO2 Photocatalytic and Treatment of Water and Air*, London, Ontario, Canada. **1992**, 481-494.

[53] Riegel, G.; Bolton J. R., *J. Phys. Chem.*, **1995**, *99*, 4215-4224.

[54] Song, Y. -Z.; An, J. -Y.; Jiang, L. -J., *J. Photochem. Photobiol. A Chem.*, **1999**, *123*, 39-46.

[55] Legrini, O.; Oliveros, E.; Braun, A. M., *Chem. Rev.*, **1993**, *93*, 671-698.

[56] Scott, J. P.; Ollis, D. F., *Environ. Prog.*, **1995**, *14*, 88-103.

[57] Buettner, G. R.; in Greenwald, R. A. (Ed.), *CRC Press, Boca Raton*, **1985**, 151-155.

[58] Buxton, G. V.; Greenstock, C. L.; Helman, W. P.; Ross, A. B., *J. Phys. Chem. Ref. Data*, **1988**, *17*, 513-886.

[59] Fujishima, A.; Rao, T. N.; Tryk, D. A.; *J. Photochem. Photob. C – Photochem. Rev.*, **2000**, *1*, 1-21.

[60] Schmelling, D. C.; Gray, K. A.; Kamat, P. V.; *Wat. Res.*, **1997**, *31*, 1439-1447.

[61] Grzechulska, J.; Morawski, A. W., *Appl. Catal. B Environ.*, **2002**, *36*, 45-51.

[62] Sclafani, A.; Palmisano, L.; Schiavello, M., *J. Phys. Chem.*, **1990**, *94*, 829-832.

[63] Cheng, S.; Tsai, S. -J.; Lee, Y. -F., *Catal. Today*, **1995**, *26*, 87-96.

[64] Watson, S. S.; Beydoun, D.; Scott, J. A.; Amal, R., *Chem. Eng. J.*, **2003**, *95*, 213-220.

[65] Tanaka, K.; Capule, M. F. V.; Hisanaga, T., *Chem. Phy. Let.*, 1991, 187, 73-76.

[66] Bacsa, R. R.; Kiwi, J. *Appl. Catal. B Environ.*, **1998**, *16*, 19-29.

[67] Sumita, T.; Yamaki, T.; Yamamoto, S.; Miyashita, A., *Appl. Surf. Sci.*, **2002**, *200*, 21-26.

[68] Tsai, S. -J.; Cheng, S., *Catal. Today*, **1997**, *33*, 227-237.

[69] Ohno, T.; Sarukawa, K.; Tokieda, K.; Matsumura, M., *J. Catal.*, **2001**, *203*, 82-86.

[70] Sun, B.; Vorontsov, A. V.; Smirniotis, P. G., *Langmuir*, **2003**, *19*, 3151-3156.

[71] Dionysiou, D. D.; Burbano, A. A.; Suidan, M. T.; Baudin, I., *Environ. Sci. Technol.*, **2002**, *36*, 3834-3843.

[72] Goto, H.; Hanada, Y.; Ohno, T.; Matsumura, M., *J. Catal.*, **2004**, *225*, 223-229.

[73] Ku, Y.; Leu, R. -M.; Lee, K. -C., *Wat. Res.*, **1996**, *30*, 2569-2578.

[74] Deng, X.; Yue, Y.; Gao, Z., *Appl. Catal. B Environ.*, **2002**, *39*, 135-147.

[75] Davydov, L.; Smirniotis, P. G., *J. Catal.*, **2000**, *191*, 105-115.

[76] Emeline, A. V.; Smirnova, L. G.; Kuzmin, G. N.; Basov, L. L.; Serpone, N., *J. Photochem. Photobiol. A Chem.*, **2002**, *148*, 97-102.

[77] Sato, T.; Taya, M., *Biochem. Eng. J.*, **2006**, *28*, 303-308.

[78] Zhang, Q.; Gao, L.; Guo, J., *Appl. Catal. B Environ.*, **2000**, *26*, 207-215.

[79] Kawahara, T.; Konishi, Y.; Tada, H.; Tohge, N.; Ito, S., *Langmuir*, **2001**, *17*, 7442-7445.

[80] Hidalgo, M. C.; Colón, G.; Navío, J. A., *J. Photochem. Photobiol. A Chem.*, **2002**, *148*, 341-348.

[81] Qamar, M.; Muneer, M., *J. Hazard. Mater.*, **2005**, *120*, 219-227.

[82] Tariq, M. A.; Faisal, M.; Muneer, M., *J. Hazard. Mater.*, **2005**, *127*, 172-179.

[83] Tahiri, H.; Serpone, N.; Le van Mao, R., *J. Photochem. Photobiol. A. Chem.*, **1996**, *93*, 199-203.

[84] Carraway, E. R.; Hoffman, A. J.; Hoffmann, M. R., *Environ. Sci. Technol.,* **1994**, *28*, 786-793.

[85] Burgeth, G.; Kisch, H., *Coordin. Chem. Rev.,* **2002,** *230*, 41-47.

[86] Vamathevan, V.; Amal, R.; Beydoun, D.; Low, G.; McEvoy, S., *J. Photochem. Photobiol. A Chem.,* **2002**, *148*, 233-245.

[87] Tayade, R. J.; Kulkarni, R. G.; Jasra, R. V., *Ind. Eng. Chem. Res.,* **2007,** 45, 5231-5238.

[88] Wang, K.; Zhang, J.; Lou, L.; Yang, S.; Chen, Y., *J. Photochem. Photobiol. A Chem.,* **2004,** 165, 201-207.

[89] Dovranová, D.; Brevozá, V.; Mazúr, M.; Malati, M., *Appl. Catal. B Environ.,* **2002**, *37*, 91-105.

[90] Grzechulska, A.; Morawski, W. *Appl. Catal. B Environ.,* **2002,** *36*, 45-51.

[91] Surolia, P. K.; Tayade, R. J.; Jasra, R. V., *Ind. Eng. Chem. Res.,* **2007,** *46*, 6196-6203.

[92] Chen, D.; Ray, A. K., *Wat. Res.,* **1998,** *32*, 3223-3234.

[93] Herrmann, J. -M.; Disdier, J.; Pichat, P.; Malato, S.; Blanco, J., *Appl. Catal. B Environ.,* **1998**, *17*, 15-23.

[94] Alebbi, M.; Bignozzi C. A.; Heimer T. A.; Hasselmann, G. M.; Meyer, G. J., *J. Phys. Chem. B*, **1998**, *102*, 7577-7581.

[95] Haarstrick, A.; Kut, O. M.; Heinzle, E., *Environ. Scien. Technol.*, **1990**, *30*, 817-824.

[96] Sclafani, A.; Palmisano, L.; Davi, E., *J. Photochem. Photobio*., **1991**, *56*, 113-123.

[97] Choi, W.; Termin, A.; Hoffmann, M. R., *J. Phys. Chem.,* **1994**, *98*, 13669-13679.

[98] Litter, M. I., *Appl Catal B: Environ.*, **1999**, *23*, 89-114.

[99] Gurunathan, K.; Maruthamuthu, P.; Sastri, M. V. C., *Int. J. Hydrogen Energy,* **1997**, *22*, 57-62.

[100] Dhanalakshmi, K. B.; Latha, S.; Anandan, S.; Maruthamuthu, P., *Int. J. Hydrogen Energy,* **2001**, *26*, 669-674.

[101] Rideh, L.; Wehrer, A.; Ronze, D.; Zoulalian, A., *Catal. Today*, **1999**, *48*, 357-362.

[102] Aceituno, M.; Stalikas, C. D.; Lunar, L.; Rubio, S.; Pérez-Bendito, D., *Wat. Res.*, **2002**, *36*, 3582-3592.

[103] Obee, T. N.; Hay, S. O., *Environ. Sci. Technol.*, **1997**, *31*, 2034-2038.

[104] Davis, A. P.; Green, D. L., *Environ. Sci. Technol.*, **1999**, *33*, 609-617.

[105] Coleman, H. M.; Abdullah, M. I.; Eggins, B. R.; Palmer, F. L., *Appl. Catal. B Environ.*, **2005**, *55*, 23-30.

[106] McMurry, T. A.; Byrne, J. A.; Dunlop, P. S. M.; Winkelman, J. G. M.; Eggins, B. R.; McAdams, E. T., *Appl. Catal. A Gen.*, **2004**, *262*, 105-110.

[107] Alhakimi, G.; Studnicki, L. H.; Al-Ghazali, M., *J. Photochem. Photobiol. A Chem.*, **2003**, *154*, 219-228.

[108] Kaneco, S.; Rahman, M. A.; Suzuki, T.; Katsumata, H.; Ohta, K., *J. Photochem. Photobiol. A Chem.*, **2004**, *163*, 419-424.

[109] Zhang, T.; You, L.; Zhang, Y., *Dyes Pigment.*, **2006**, *68*, 95-100.

[110] Moser, J.; Punchihewa, S.; Infelta, P. P.; Grätzel, M., *Langmuir*, **1991**, *7*, 3012-3018.

[111] Palmer, F. L.; Eggins, B. R.; Coleman, H. M., *J. Photochem. Photobiol. A Chem.*, **2002**, *148*, 137-143.

[112] Trillas, M.; Peral, J.; Domènech, X., *Appl. Catal. B Environ.*, **1995**, *5*, 377-387.

[113] Augugliaro, V.; Palmisano, L.; Schiavello, M.; Sclafani, A., *Appl. Catal.*, **1991**, *69*, 323-340.

[114] Maurino, V.; Calza, P.; Minero, C.; Pelizzetti, E.; Vincenti, M., *Chemosphere*, **1997**, *35*, 2675-2688.

[115] Bekbölet, M; Balcioglu, I., *Wat. Sci. Tech*, **1996**, *34*, 73-80.

[116] Malato, S.; Blanco, J.; Maldonado, M. I.; Fernández-lbáñez, P.; Campos, A., *Appl. Catal. B Environ.*, **2000**, *28*, 163-174.

[117] Yoneyema. H.; Haga, S.; Yammaka, S., *J. Phys. Chm.*, **1989**, *93*, 4833-4837.

[118] Tanguay, J. F.; Suib, S. L.; Coughlin, R. W., *J. Catal.*, **1989**, *117*, 335-347.

[119] Chun, H. D.; Kim, J. S.; Yoon, S. –M.; Kim, C. G., *Kor. J. Chem. Eng.*, **2001**, *18*, 908-913.

[120] Fu, X; Clark, L. A.; Yang, *Q.;* Anderson, M. A-., *Environ.* Sci. *Tehnol.*, **1996**, *30*, 647-653.

[121] Torimoto, T.; Ito, S.; Kuwabata, S.; Yoaeyama, A., Environ. *Sci. Technol.*, **1996**, *30*, 1275-1281.

[122] Liu, X; Iu, K. K.; Thomas, J. K., *J. Chem. Soc. Faraday Trans.*, **1993**, *89*, 1810-1816.

[123] Green, K. J.; Rudham, R. J., *J. Chem . Soc. Faraday Trans,*. **1993**, *89*, 1867-1870.

[124] Moriguchi. L; Maeda, H.; Teraoka, Y.; Kagawa, S., *J. Am. Chem. Soc.*, **1995**, *117*, 1139-1140.

[125] Danion, A.; Disdier, J.; Guillard, C.; Abdelmalek, F.; Renualt, N. J-., Appl. Catal. B: Environ., **2004**, *52*, 213-223.

[126] Howe, R. F.; Krisnandi, Y. K., *Chem. Commun*. **2001**, 1588–1589.

[127] Agrios, A. G.; Pichat, P., *J. Appl. Electrochem*., **2005**, *35*, 655–663.

[128] Wang, R.; Hashimoto, K.; Fujishima, A.; Chikuni, M.; Kojima, E.; Kitamura, A.; Shimohigoshi, M.; Watanabe, T., *Adv. Mater.*, **1998**, *10*, 135-138.

[129] Mills, A.; Lepre, A.; Elliott, N.; Bhopal, S.; Parkin I. P.; O'Neill, S. A., *J. Photochem. Photobiol. A. Chem.*, **2003**, *160*, 213-224.

[130] Paz, Y.; Luo, Z.; Rabenberg, L.; Heller, A., *J. Mater. Res*. **1995**, *10*, 2842-2848.

[131] Puzenat, E.; Pichat, P., *J. Photochem. Photobiol. A. Chem*., **2003**, *160*, 127-133.

[132] Rome´as, V.; Pichat, P.; Guillard, C.; Chopin T.; Lehaut, C., Ind. Eng. Chem. Res. **1999**, *38*, 3878-3885.

[133] Rome´as, V.; Pichat, P.; Guillard, C.; Chopin, T.; Lehaut, C., *New J. Chem*. **1999**, *23*, 365-374.

[134] Pichat, P.; Disdier, J.; Hoang-Van, C.; Mas, D.; Goutailler G.; Gaysse, C., *Catal. Today*, **2000**, *63*, 363-369.

[135] Liang, H. –C.; Li, X. –Z.; Yang, Y. –H.; Sze, K. –H., *Chemosphere*, **2008**, *73*, 805-812.

[136] Robert, D.; Malato, S., *Sci. Total Environ.*, **2002**, *291*, 85-97.

[137] Malato, S.; Blanco, J.; Vidal, A.; Alarcon, D.; Maldonado, M. I.; Caceres, J.; Gernjak, W., *Solar Energy*. **2003**, *75*, 329-336.

[138] Pichat, P.; Vannier, S.; Dussaud, J.; Rubis, J. -P., *Solar Energy*, **2004**, *77*, 533-542.

[139] Hachem, C.; Bocquillon, F.; Zahraa, O.; Bouchy, M., *Dyes and Pigm*., **2001**, *49*, 117-125.

[140] http://www.purifics.com.

[141] Yin, J.; Zou, Z.; Ye, J., *J. Phys. Chem. B.*, **2003**, *107*, 4936-4941.

[142] Yin, J.; Zou, Z.; Ye, J., *J. Phys. Chem. B.*, **2003**, *107*, 61-65.

[143] Wang, D.; Zou, Z.; Ye, J., *Chem. Phys. Lett*., **2003**, *373*, 191-196.

[144] Nukumizu, K.; Nunoshige, J.; Takata, T.; Kondo, J. N.; Hara, M.; Kobayashi, H.; Domen, K., *Chem. Lett*., **2003**, *32*, 196-197.

[145] Ishikawa, A.; Takata, T.; Kondo, J. N.; Hara, M.; Koayashi H.; Domen, K., *J. Am. Chem. Soc.*, **2002**, *124*, 13547-13553.

[146] Iyonaga, M.; Chatouaki, E. M.; Sunada, K.; Ohnishi N.; Hashimoto, K., Energy saving system using super-hydrophilic TiO_2 surfaces induced by solar light, Photocatalysis: Fundamentals and Applications. *NIMS, Hayama, Kanegawa, Japan*, **2004**.

[147] Bechinger, C.; Ferrere, S.; Zaban, A.; Sprague, J.; Gregg, B. A.; *Natur*e, **1996**, *38*3, 608-610.

[148] Bonhoˆte, P.; Gogniat, E.; Gra¨tzel, M.; Ashrit, P. V., *Thin Solid Films*, **1999**, *350*, 269-275.

[149] Bonhoˆte, P.; Moser, J. E.; Humphry-Baker, R.; Vlachopoulos, N.; Zakeeruddin, S. M.; Walder, L.; Gra¨tzel, M., *J. Am. Chem. Soc*., **1999**, *121*, 1324-1336.

[150] Ohko, Y.; Saitoh, S.; Tatsuma, T.; Fujishima, A., *J. Electrochem. Soc.*, **2001**, *148*, B24-B28.

[151] Tatsuma, T.; Saitoh, S.; Ohko,Y.; Fujishima, A., *Chem. Mater*., **2001**, *13*, 2838-2842.

[152] Kulbacova, M.; Macak, J. M.; Schmidt,-Stein, F.; Mierke, C. T.; Schmuki, P., *Rapid Res. Lett*., **2008**, *2*, 194-196.

[153] Kubota, Y.; Niwa, C.; Ohnuma, T.; Ohko, Y.; Tatsuma, T.; Mori, T.; Fujishima, A., *J. Photochem. Photobiol. A.*, **2001**, *141*, 225-230.

[154] Ohko, Y.; Utsumi, Y.; Niwa, C.; Tatsuma, T.; Kobayakawa, K.; Satoh, Y.; Kubota Y.; Fujishima, A., *J. Biomed. Mater. Res.*, **2001**, *58*, 97-101.

[155] Li, X.; Yue P.; Kutal C., *New J. Chem*. **2003,** *27*, 1264-1269

[156] Martin, S. T.; Herrmann H.; Choi W.; Hoffmann M., *Faraday Trans*. **1994**, *90*, 3315-3322.

[157] Anpo, M.; Nakaya, H.; Kodama, S.; Kubokawal, Y.; Domen, K.; Onishi, T., *J. Phys. Chem.* **1986**, *90*, 1633-1636.

[158] Sato. S., *Langmuir*. **1988**, *4*, 1156-1159.

[159] Yoneyama, H.; Hag, S.; Yamanaka, S., *J. Phys. Chem*., **1989**, *93*, 4833-4837.

[160] Kim, Y. I.; Keller, S. W.; Krueger, J. S.; Yonemoto, E. H.; Saupe, G. B.; Mallouk. T. E., J. *Phys. Chem. B.*, **1997**, *101*, 2491-2500.

[161] Xu, Y.; Menassa, P. C.; Langford. C. H., *Chemosphere*, **1988**, *17*, 1971-1976.

[162] Mattews, R. W., *Solar energy*, **1987**, *38*, 405-413.

[163] Vinogopal, K.; Hotchandani, S.; Kamat, P. V., *J. Phys. Chem*., **1993**, *97*, 9040-9044.

[164] Tiscornia, T.; Irusta, S.; Pradanos, P.; Tellez C.;, Coronas, J.; Santamaria, J., *J. Phys. Chem.:C*., **2007**, *111*, 4702-4709.

[165] Kuznicki, S. M.; Bell, V. A.; Nair, S.; Hillhouse, H. W.; Jacubinas, R. M.; Braunbarth, C. M.; Toby, B. H.; Tsapatsis, M. A., *Nature*, **2001**, *412*, 720-724.

[166] Lamberti, C., *Micropor. Mesopor. Mater*., **1999**, *30*, 155-163.

[167] Assabane A.; Ichou, Y. A.; Tahiri, H.; Guillard, C.; Herrmann, J. -M., *Appl. Catal. B: Environ.*, **2000**, *24*, 71-87.

[168] Feng, W.; Nansheng, D., *Chemosphere*, **2000**, *41*, 1137-1147.

[169] Robert, D.; Dongui, B.; Weber, J. -V., *J. Photochem. Photobiol. A: Chem.*, **2003**, *156*, 195-200.

[170] Ao, C. H.; Lee, S. C.; Mak, C. L.; Chan, L. Y., *Appl. Catal. B: Environ.*, **2003**, *42*, 119-129.

[171] Koiminami, H.; Kumamoto, H.; Kera, Y.; Ohtani, B., *J. Photochem. Photobiol. A: Chem.*, **2003**, *160*, 99-104.

[172] Oosawa, Y.; Gr¨atzel, M., *J. Chem. Soc., Faraday Trans.*, **1988**, *84*, 197-206.

[173] Campostrini, R.; Carturan, G.; Palmisano, L.; Schiavello, M.; Sclafani A., *Mat. Chem. Phys.*, **1994**, *38*, 277-283.

[174] Boonstra, A. M.; Mutsaers, C. A. H. A., *J. Phys. Chem.*, **1975**, 79, 1694-1698.

[175] Bekkum, H. V; Flanige,n E. M.; Jansen, J. C. (Editors). Introduction to zeolite science and practice. *Elsevier Science Ltd., Amsterdam*. **1991.**

[176] Sing, K. S. W., *J. of Porous Mater.,* **1995**, *2*, 5-8.

[177] Matsumoto, A.; Zhao, J.; Tsutsumi, K., *Langmuir*, **1997**, *13*, 496-501.

[178] Tayade, R. J.; Kulkarni, R.G.; Jasra, R. V. , *Ind. Eng. Chem. Res.,* **2007,** *46*, 369-376.

[179] Keane, M. A., *Micropor. Mater*., **1996**, *7*, 51-59.

[180] Iu, K. K.; Thomas J. K., *Langmuir*, **1990**, *6*, 471-478.

[181] Nair, M.; Luo, Z.; Heller, A., *Ind. Eng. Chem. Res*. ,**1993**, *32*, 2318-2323.

[182] Fabiyi, M. E.; Skelton, R. L.; *J. Photochem. Photobiol. A.,* **2000**, *132*, 121-128.

[183] Matos, J.; Laine, J.; Hermann, J. M., *Appl. Catal., B Environ*., **1998**, *18*, 281-291.

[184] Piperata, G.; Meitchtry, J. M.; Litter, M. I., *Prog. Colloid & Polym. Sci*., **2004**, *128*, 303-308.

[185] Lohse, S.; Rosentreter, J. J., *Microchem. Journal*, **2006**, *82*, 66-72.

Chapter 2

Effect of Anions on the Photocatalytic Degradation

2.1. INTRODUCTION

The research efforts have been directed to enhance the activity of the photocatalysts using various methods such as increasing catalyst surface-to-volume ratio, sensitization of the catalyst using dye molecules [**1,2]** and doping the catalyst with non-metals such as nitrogen, carbon, and sulfur and catalyst impregnation of metal ions during the last one decade **[3-6]**. It has been demonstrated that the addition of a low percentage of metal ion such as those of Pt, Ag, Au, Cu, Ni, Co, Fe, Mg in TiO_2 improves its photocatalytic activity [**7-9]**. Fe metal ions impregnation has been studied for photocatalytic efficiency enhancement of the TiO_2 catalysts and varied results are reported [**10-13]**. This could be due to the different synthesis methods, percentage of ion impregnated, and source used for the impregnation of Fe. For example, Choi *et al*. [**10]** suggested that the ability of a dopant to function as an effective electron-hole trap is related to the dopant concentration and reported the highest activity at 0.5 atomic % of Fe (III). Li *et al*. [**11]** studied the photocatalytic oxidation of cyclohexane and found higher photocatalytic activity with Fe (III) ion impregnation. Vamathevan *et al*. [**12]** found lower activity of catalyst with 5 atomic % or higher loading of Fe (III) in TiO_2 particles for the degradation of sucrose. These studies concluded that increasing amount of iron could cause its agglomeration at surface of TiO_2 to form α-Fe_2O_3. This results into the reduction of catalytically active and electron relay sites and thereby negatively influencing the photocatalytic activity. The present work was carried out to specifically to study the effect of anion of Fe (III) salts used for impregnation on the photocatalytic activity of P25 Degussa TiO_2 photocatalyst. To study the photocatalytic activity, degradation of acetophenone in aqueous medium was used as a model organic compound with ultraviolet irradiation.

2.1.1. Photocatalyst deactivation

Deactivation of the photocatalyst is an important issue for practical applications of photocatalysts. During the photocatalytic reaction, TiO_2 may be deactivated by the formation of intermediates and byproducts, which have higher adsorption ability to the TiO_2 surface than the corresponding reactant or by "heavy products" that are difficult to decompose **[14-15]**. Another area of concern that has a significant impact on the rate of photocatalytic degradation is the presence of anions. Commonly encountered anions are

Cl^-, NO_3^-, HCO_3^-, SO_4^{2-}, PO_4^{3-}, ClO_4^-, HCO_3^- and CO_3^{2-}. These anions commonly found in neutral or polluted waters have a retarding effect on oxidation rate of organic compounds by competing for radicals or by blocking the active sites of the semiconductor photocatalyst such as TiO_2 photocatalyst **[16-17]**.

2.1.2. Aim of the study

The studies **[14-15]** indicated that inorganic anions affect the photocatalytic degradation of organic compounds by competitive adsorption that occurs on the surface of the photocatalyst. Moreover, the negative effect of these anions is also due to the scavenging of hydroxyl radicals those are active for degradation and mineralization. Such an adverse effect could have a great impact on the application of photocatalysis as a water treating method because anions such as chlorides, nitrates and bicarbonates are ever-present in natural waters and a removal of these ions will be necessary. The present work was carried out to specifically study the effect of anions on the photocatalytic activity of the Degussa P25 TiO_2 photocatalyst. The Fe (III) salts having different anions were used for impregnation on the P25 Degussa TiO_2 photocatalyst.

2.2. SYNTHESIS OF Fe (III) ION DOPED DEGUSSA P25 PHOTOCATALYST

2.2.1. Chemicals and Materials

Titanium dioxide (P25) was purchased from Degussa Corporation (Degussa AG, Frankfurt, Germany). Ferric nitrate, Ferric sulphate, and Ferric chloride were procured from, s. d. fine chem. Ltd., Mumbai, India. Acetophenone, AR grade was purchased from E. Merck, India. Deionised distilled water was used to make up the reaction mixture.

2.2.2. Catalysts preparation

Catalysts were prepared by wet impregnation method. P25 Degussa TiO_2 was suspended in aqueous solutions of the Fe (III) salt. The mixture was stirred for 36 h under normal room conditions to get the loading of Fe metal ion of 0.1, 0.5, 1.0, 5.0, 10.0 % (w/w) followed by the drying the slurry under vacuum using rotavapour and further drying in oven at 353 K for 12 h, Thus dried catalysts was thoroughly grounded with agate mortar

pestle and calcined at 723 K temperature for 4 h in presence of air. The impregnated TiO_2 catalysts with ferric nitrate were denoted as Ti-N1, Ti-N2, Ti-N3, Ti-N4, and Ti-N5, wherein numeral denotes the percentage (w/w) of iron as 0.1, 0.5, 1.0, 5.0, and 10.0 respectively, Similarly for Fe impregnated catalysts using ferric chloride and ferric sulphate were denoted as Ti-C1, Ti-C2, Ti-C3, Ti-C4, Ti-C5, Ti-S1, Ti-S2, Ti-S3, Ti-S4, and Ti-S5 respectively.

2.3. CHARACTERIZATION OF PREPARED PHOTOCATALYSTS

2.3.1. X-ray diffraction (XRD)

The catalysts were characterised by Powder X-ray Diffraction (XRD) recorded at 295 K using Phillips X'pert MPD system with CuKα1 radiation (λ = 0.15405 nm). Diffraction patterns were measured in 2θ range from 10°- 60° at a scan speed of 0.1°sec^{-1}. The XRD peaks of crystal plane 101 for anatase appeared at 25.3 (2θ) and at 27.4 (2θ) for 110 plane of rutile. These peaks were selected to determine the percentage of anatase and rutile phases [**19]** in TiO_2 sample. The percentage of anatase, A (%) was determined using the equation,

$$A\ (\%) = 100/(1 + 1.265 I_R/I_A) \quad (2.1)$$

Where I_R is the intensity of rutile peak at 2θ = 27.4 and I_A is the intensity of anatase peak at 2θ = 25.3. Crystallite size of TiO_2 was determined from the characteristic peak of 2θ = 25.3 (1 0 1) for anatase and 2θ = 27.4 (1 1 0) for rutile using the Scherrer formula [**20]**, with a shape factor (*K*) of 0.9

$$Crystallite\ size = K\lambda/WCos\theta \quad (2.2)$$

Where $W = W_b – Ws$, W_b is the broadened profile width of experimental sample. *W*s is the standard profile width of reference silicon sample, λ is the wavelength of X-ray radiation (CuKα1=0.15405nm). The crystallinity of the catalysts was calculated with reference to P25 Degussa as 100%, by taking the average of 5 major anatase peaks of the catalyst

(2θ= 25.3, 37.7, 47.9, 53.9 and 55.2). The unit cell volumes were calculated by crystal builder module in Cerius^2 ν. 4.1 (Accelrys Software Inc., USA).

Figure-2.1 shows the XRD patterns of Fe $(NO_3)_3$, $FeCl_3$ and Fe_2 $(SO_4)_3$ impregnated catalysts. The 2θ values at 25.3 and 27.4 correspond to anatase and rutile phase respectively. α-Fe_2O_3 show diffraction at 2θ value of 33.0 whereas SO_4^{2-} group show diffraction 2θ values of 14.75, 20.28, and 24.65. The confirmation of these peaks was done by comparing with XRD pattern of pure ferric sulphate. The peaks assigned to the Fe (III) were not observed in the XRD pattern of Fe impregnated TiO_2 samples below 5 %. However, the peak corresponds to α-Fe_2O_3 was observed in the all Fe(III) impregnated TiO_2 catalysts with impregnation higher than 5 %, indicating its presence on the external surface of the catalysts at higher loading of Fe(III) ion. X-ray diffraction analysis showed that TiO_2 structure is intact after iron salt impregnation. It has been reported [**9, 21]** that due to the small ionic size of Fe (III) (64pm) and low percentage of impregnation, Fe (III) could substitute to in TiO_2 lattice**.** All the samples have a tetragonal structure with space group, $D_{4h}^{19} - I4_1/amd$ and that the lattice parameters decrease along all three axes as the Fe (III) content is increased. The lattice constants for anatase phase of Degussa P25 were calculated a=b=3.7830Å and c=9.4940Å. The theoretical values for anatase phase of TiO_2 calculated using Cerius^2 software are a=b=3.7760Å and c=9.4860Å and similar values are reported by Diebold [**22]** with a=b=3.782Å and c=9.502Å. The values of the calculated lattice constants of Degussa P25 were found decreasing with increase in the Fe (III) ion content (**Table-2.1**) supporting substitution of Fe (III) ions in the lattice at lower Fe (III) loadings. **Figure-2.2** shows the change of V/Z with impregnation content, where V and Z are cell volume and the number of formulae per cell, respectively. The unit cell volumes were calculated by crystal builder module in Cerius^2 ν. 4.1 [**23]**. These data show that, for small amount of Fe (III) impregnation, there is a sharp decrease in V/Z ratio supporting substituting of Fe (III) ions in TiO_2 lattice. Nearly constant or gradual decrease in V/Z ratio at higher Fe(III) impregnation also support the observation that after certain impregnation, Fe(III) is residing on the external surface of TiO_2 as also seen from X-ray diffraction.

It is also seen in **Table-2.1** that there is no decrease in the anatase and rutile phase percentage but the intensity of all peaks was observed to reduce which could be attributed to formation of ferric oxide on the surface of TiO_2. A decrease in the percentage crystallinity was observed with increasing the loading of the Fe (III) ion. This decrease was seen to be higher in the case of Ti-S series of catalysts and at higher percentage loading of the Fe (III) ion. The pseudo-brookite peak is not observed, because there is a little tendency for bulk reactions between Fe_2O_3 and TiO_2 up to 823 K [**24]**.

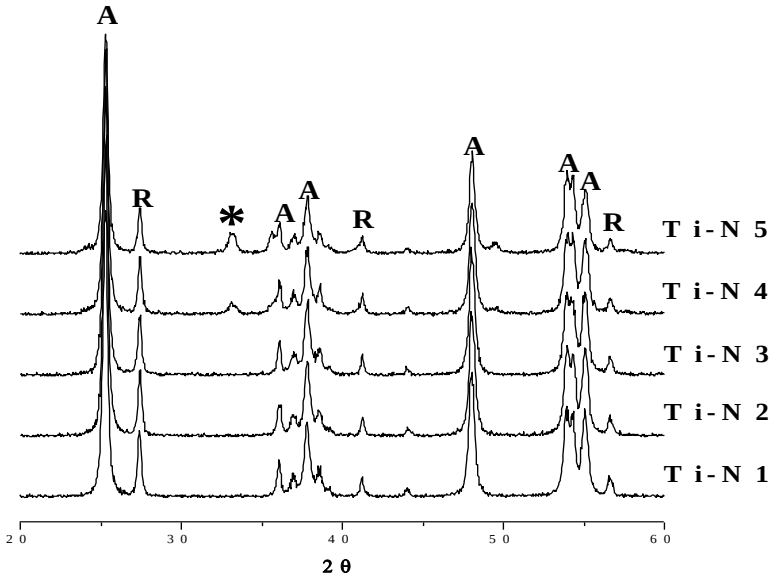

(a)

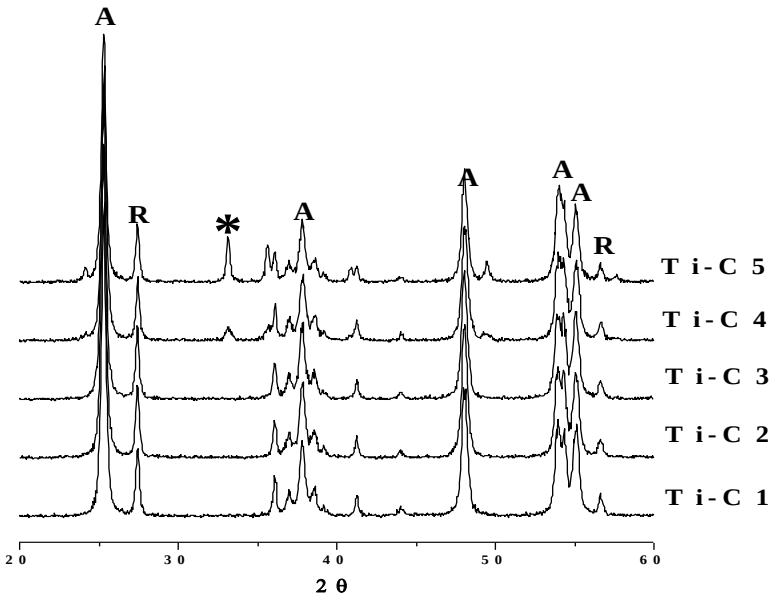

(b)

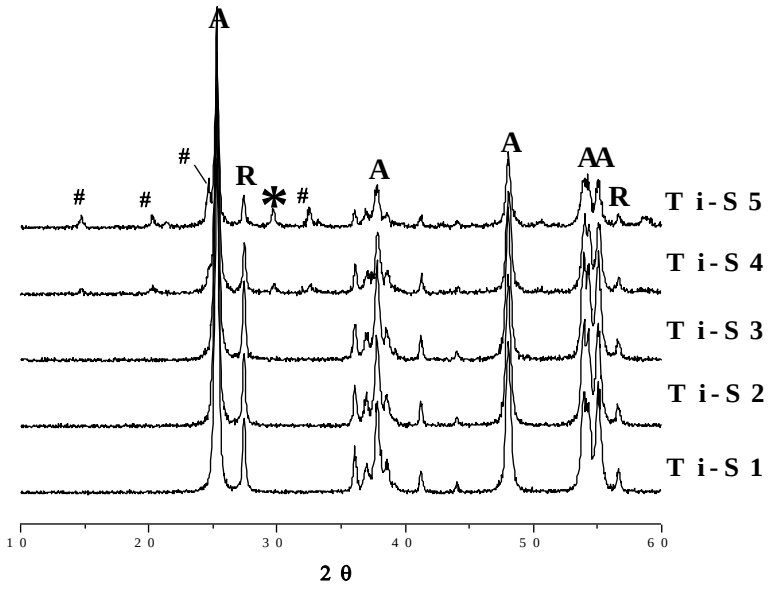

(c)

Figure-2.1. X-ray diffraction of Fe (III) salts impregnated TiO_2 (a) Ti-N series, (b) Ti-C series (c) Ti- S series

* show the α-Fe_2O_3 peak, # show the SO_4^{2-} peak

Table-2.1. XRD data of the catalysts

Catalyst	*Crystallite Size (nm)	Anatase (%)	Rutile (%)	**Crystallinity (%)	Lattice constants (Å)	
					a = b	c
P-25	25	80	20	100	3.7830	9.4940
Ti-N1	22	78	22	84	3.7811	9.4936
Ti-N2	22	78	22	85	3.7804	9.4880
Ti-N3	22	78	22	83	3.7802	9.4877
Ti-N4	22	79	21	78	3.7793	9.4850
Ti-N5	22	78	22	66	3.7787	9.4850
Ti-C1	23	78	20	86	3.7817	9.4920
Ti-C2	23	78	22	85	3.7797	9.4887
Ti-C3	22	78	22	84	3.7797	9.4885
Ti-C4	22	78	22	79	3.7787	9.4813
Ti-C5	22	78	22	67	3.7785	9.4812
Ti-S1	22	78	22	82	3.7810	9.4894
Ti-S2	22	78	22	81	3.7808	9.4893
Ti-S3	22	78	22	80	3.7807	9.4892
Ti-S4	22	78	22	57	3.7807	9.4890
Ti-S5	21	78	22	39	3.7806	9.4888

***** Calculated at 2θ = 25.3, the most intense peak

******Calculated by measuring the total peak area under five main peaks at 2θ = 25.3, 37.7, 47.9, 53.9 and 55.1

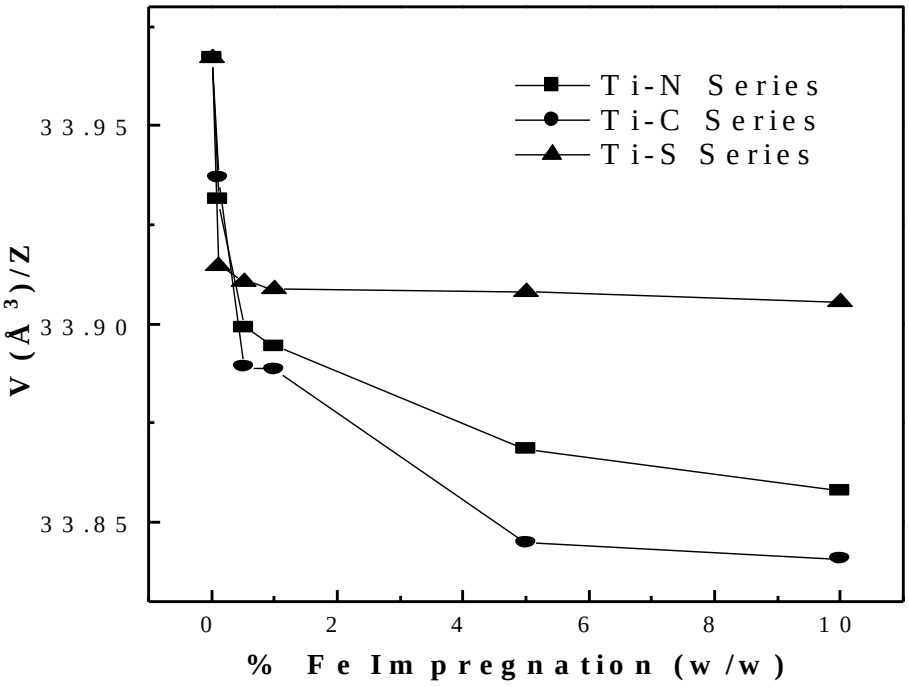

Figure-2.2. Change of V/Z with Fe impregnation content, where V and Z are the unit cell volume and the number of formulas per cell, respectively

2.3.2. Infra red spectroscopic measurement (FT-IR)

The FT-IR spectroscopic measurements were carried out using *Perkin-Elmer GX spectrophotometer*. The spectra were recorded in the range 400-4000 cm^{-1} with a resolution of 4 cm^{-1} as KBr pellets.

The FT-IR transmission spectra of catalysts are shown in **Figure-2.3**. The spectra show the Ti-O-Ti stretching band at 400-600 cm^{-1} **[25]**, α-Fe_2O_3 confirmed by XRD spectra also showed the vibrational band at 450-470 cm^{-1} **[24]** alongwith TiO_2 vibrational band. The FT-IR spectra of sulphated metal oxide show a broad band at 1200-900 cm^{-1}. This is the characteristic frequency band for SO_4^{2-}. The observed broad band resulted from the lowering of the symmetry in the free SO_4^{2-} (Td point group). The symmetry of bonded SO_4^{2-} to titania surface can be lowered either C_3V or C_2V point group. The peaks at 1220-1222, 1131 and 996-997 cm^{-1} are characteristic of inorganic chelating bidentate sulphates which are assigned to asymmetric and symmetric stretching frequencies of $S\overline{---}O$ and S – O bond [**26]**.

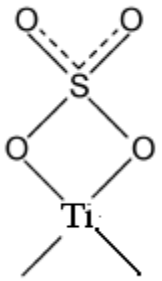

The peaks at 1622-1628 and 3372-3393 cm^{-1} are attributed to bending and stretching frequencies of water molecule occluded in the sample [**27]**.

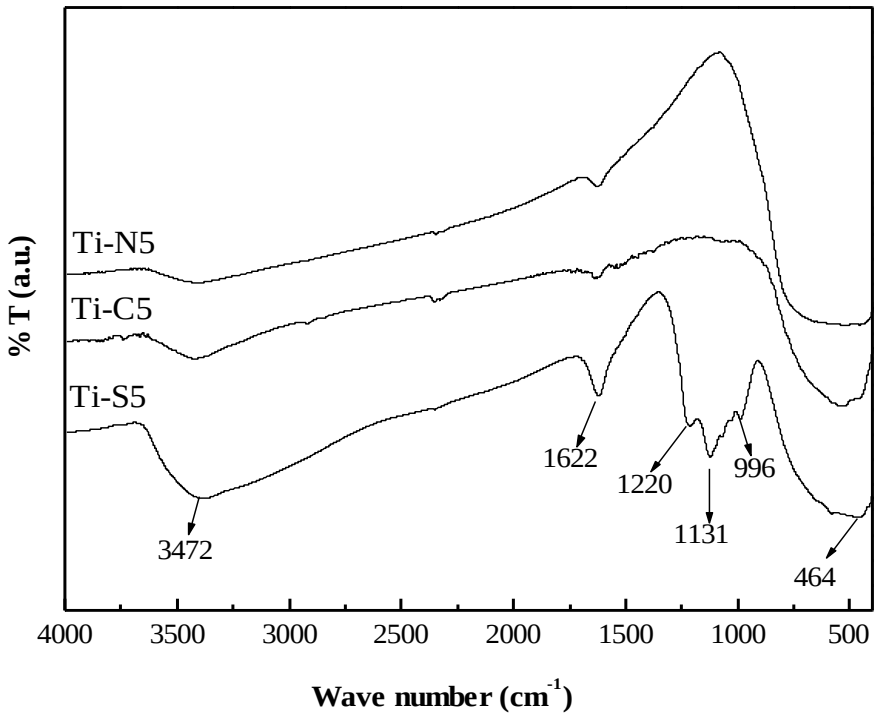

Figure-2.3. FT-IR spectra of 10% Fe (III) salts impregnated TiO_2 catalysts using different anionic sources

2.3.3. Surface area measurement (N_2 adsorption)

Specific single point surface area of catalysts were determined from N_2 adsorption at 77.4 K by using volumetric adsorption set-up *(ASAP 2010, Micromeritics, USA).* The catalysts were degassed under vacuum (10^{-2} Torr) at 623 K for 4 h, prior to adsorption measurement.

Single point surface areas of Fe (III) salt impregnated titania catalysts calcined at 723 K are shown in the **Table-2.2**. A slight decrease was observed in surface area of the catalysts in the case of Fe (III) ion impregnated P25 using ferric nitrate (47 m^2/g for Ti-N5) compared to Degussa P25 (surface area 50 m^2/g). The surface area of Fe (III) ion impregnated P25 using ferric chloride and ferric sulfate were found decreased up to 43 and 15 m^2/g respectively with increase the amount of ferric chloride and ferric sulfate. The result is different than the result observed previously where a considerable decrease in the BET surface area was observed with increase in the ferric nitrate concentration [**28]**. In case of Degussa P25, chlorination and sulphatation treatment produces a detrimental effect, decreasing the surface area values. In fact, these processes takes place in this case upon crystalline TiO_2 in contrast with that prepared from sol–gel route. Therefore, drop in surface area is observed when chlorination and sulphatation step takes places upon the crystalline oxide [**29]**. Along with this, the big anionic size of sulphate (0.38 nm in hydrated form) compared to nitrate (0.34 nm in hydrated form) and chloride (0.181 nm) is also responsible for higher decrease in surface area of Ti-S series. This indicates that the surface area of the catalysts get reduced by 3, 7, and 35 m^2/g using ferric nitrate, ferric chloride and ferric sulphate respectively by using wet impregnation method. The higher decrease in surface area using ferric sulphate of impregnated catalysts due to the plugging of pores would have occurred with higher sulphate loading [**30]**.

Table-2.2. Surface area of the synthesized catalysts

Catalyst	Surface area (m^2/g)	Catalyst	Surface area (m^2/g)	Catalyst	Surface area (m^2/g)
P-25	50	-	-	-	-
Ti-N1	47	Ti-C1	50	Ti-S1	48
Ti-N2	49	Ti-C2	48	Ti-S2	50
Ti-N3	47	Ti-C3	48	Ti-S3	48
Ti-N4	46	Ti-C4	44	Ti-S4	24
Ti-N5	47	Ti-C5	43	Ti-S5	15

2.3.4. Diffuse reflectance spectra (DRS)

The band gap energy of the catalysts was determined using the Diffuse Reflectance Spectroscopy (DRS). The spectrophotometer *(Shimadzu UV-3101PC)* was equipped with an integrating sphere and $BaSO_4$ was used as a reference **[31, 32]**. The spectra were recorded at room temperature in the wavelength range of 250-600 nm. The band gap energy of catalysts were calculated according to the equation,

$$Bandgap\ (EG) = hc/\lambda \qquad (2.3)$$

Where *EG* is the band gap energy (eV), *h* the Planck's constant, *c* the light velocity (m/s) and λ is the wavelength (nm).

The diffuse reflectance spectra are shown in **Figure-2.4**. In general, the absorption of Fe (III) in octahedral symmetry is known to appear above 430, 475, and 520 nm [**33]** while the absorption of Ti^{4+} tetrahedral symmetry appears at around 375-400 nm. In the case of catalysts prepared using ferric nitrate and ferric chloride, almost all bands assigned to the Fe (III) ion octahedral symmetry were broadly seen as long tails. This meant that the Fe (III) was physically connected to the external surface of the TiO_2 anatase structure. On

the other hand, in the catalysts prepared using ferric sulphate, the band slightly shows the blue shift without tail broadening reflecting that the Fe (III) ions were inserted into the pores of the TiO_2 anatase structure [**34]**. The absorption edge increases with increasing the amount of Fe (III) ion content along with changes on colour to pale yellow or reddish brown while the band gap region of the TiO_2 (391 nm) remains unaffected by the presence of Fe (III) ion. At higher concentration of Fe (III) ion, catalysts show absorption at about 584 nm with Ti-N and Ti-C series of catalysts and at about 437 nm with Ti-S series of the catalysts. The red shift of absorption edge in Fe (III) ion impregnated titania is attributed to the excitation of 3d-Fe^{3+} electrons to the TiO_2 conduction band (charge transfer transition). **[11, 24, 35-37]**. The band gap values and colours of the synthesized catalysts are given in the **Table-2.3**.

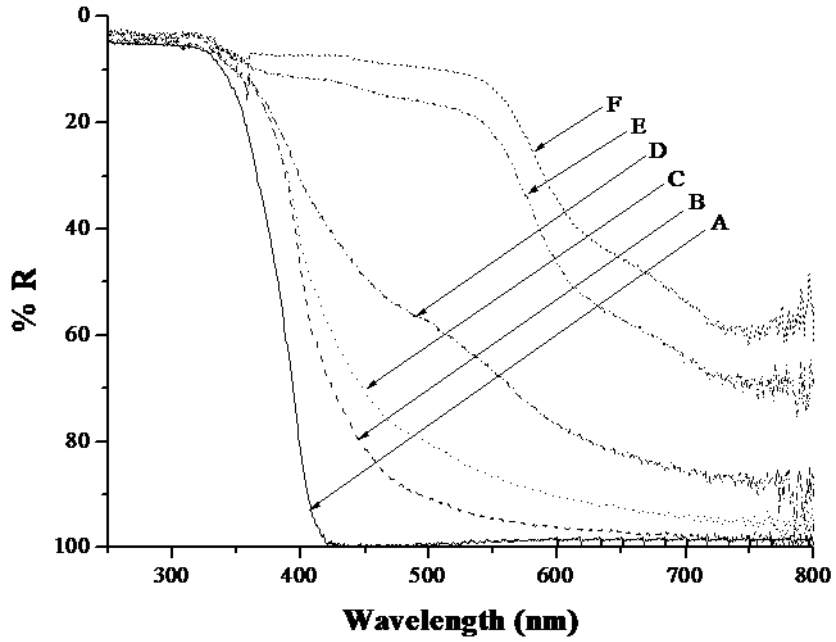

(a) A. P25 **B.** Ti-N1, **C.** Ti-N2, **D.**Ti-N3, **E.** Ti-N4, **F.** Ti-N5 Catalyst

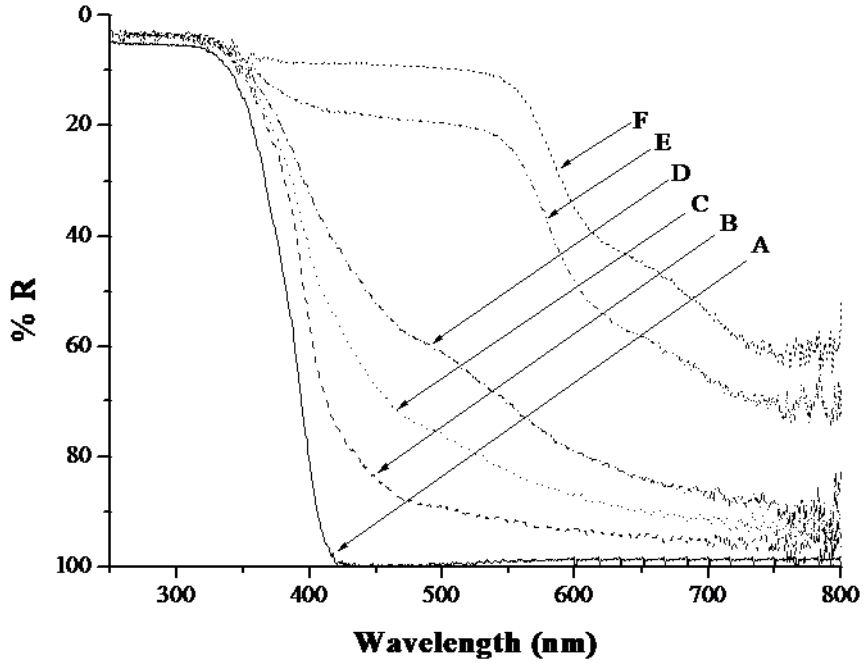

(b) A. P25 **B.** Ti-C1, **C.** Ti-C2, **D.**Ti-C3, **E.** Ti-C4, **F.** Ti-C5 Catalyst

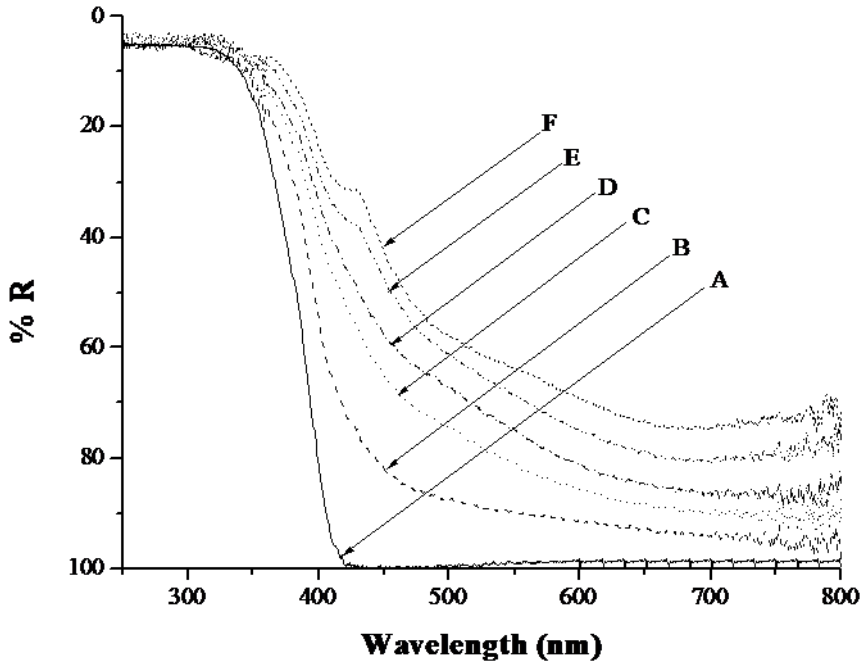

(c) A. P25 **B.** Ti-S1, **C.** Ti-S2, **D.**Ti-S3, **E.** Ti-S4, **F.** Ti-S5 Catalyst

Figure-2.4. DRS spectra of Fe (III) salts impregnated TiO_2 catalysts (a) Ti-N series (b) Ti-C series (c) Ti-S series

Table-2.3. Band gap values of the synthesized catalysts

Catalyst	Band gap (eV)	Colour
P-25	3.17	white
Ti-N1	3.17	white
Ti-N2	3.17	white
Ti-N3	3.17	brown
Ti-N4	3.17, 2.13	red-brown
Ti-N5	3.17, 2.13	red-brown
Ti-C1	3.17	white
Ti-C2	3.17	white
Ti-C3	3.17	brown
Ti-C4	3.17, 2.13	red-brown
Ti-C5	3.17, 2.13	red-brown
Ti-S1	3.17	white
Ti-S2	3.17	white
Ti-S3	3.17	white
Ti-S4	3.17, 2.84	pale-yellow
Ti-S5	3.17, 2.84	pale-yellow

2.3.5. Inductively coupled plasma (ICP)

An Inductively Coupled Plasma-optical emission spectrophotometer (ICP-OES, Optima 2000 DV, Perkin-Elmer, Eden Prarie, MN) was used to determine the percentage of the metal ion present in the degraded solution after performing photocatalytic experiments and for the actual loading of Fe (III) ion in the prepared catalyst samples (**Table-2.4**). The existence of chloride ion was confirmed by Brucker S4 Pioneer WD XRF Instrument. The value of Fe (III) ion in all the prepared catalysts shows the almost same Fe (III) values as per calculation.

Table-2.4. ICP analysis result of the prepared samples

Catalyst	% Fe	Catalyst	% Fe	Catalyst	% Fe
Ti-N1	0.13	Ti-C1	0.13	Ti-S1	0.11
Ti-N2	0.47	Ti-C2	0.52	Ti-S2	0.55
Ti-N3	1.21	Ti-C3	1.12	Ti-S3	0.98
Ti-N4	5.13	Ti-C4	5.05	Ti-S4	4.95
Ti-N5	9.87	Ti-C5	10.11	Ti-S5	10.07

2.4. PHOTOCATALYTIC DEGRADATION OF ACETOPHENONE

2.4.1. Acetophenone and its properties

Acetophenone is the simplest aromatic ketone. It is used as a polymerization catalyst for the manufacture of olefins, an intermediate for pharmaceuticals, agrochemicals and other organic compounds. It also has been used as a drug to induce sleep, in tear gas (especially as the form of chloro acetophenone) and warfare. The other applications are as a solvent for plastics, resins, cellulose ethers, and esters. The dimer (dipnone) is used as a plasticizer. Actophenone and its derivatives, having additionally substituted saturated alkyls, oxygenated alkyl groups, thio groups, additional aromatic groups, unsaturated aliphatic side chains, and other functional groups, are ingredients of flavor & fragrance for in soaps, detergents, cosmetics, and perfumes as well as in foods, beverages, and tobacco **[38-39]**. The properties of acetophenone are shown below:

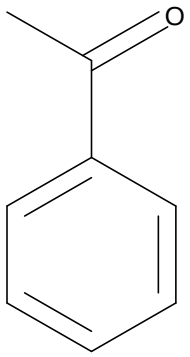	Molecular formula	$C_6H_5COCH_3$
	Physical state and appearance	Liquid
	Weight [g.mol^{-1}]	120.16
	Boiling point [°C]	201.7
	Melting point [°C]	19.7
	Specific gravity	1.03
	Solubility in water [mg.l^{-1}]	Partial soluble

2.4.2. Toxicological Information

The substance can be absorbed into the body by inhalation, through the skin and by ingestion. A harmful contamination of the air will be reached rather slowly on evaporation of this substance at 20 °C; on spraying or dispersing, however, much faster. The substance irritates the eyes. For the short term exposure, the substance may cause effects on the central nervous system. Exposure at high level may result in unconsciousness. The liquid defats the skin for the long term exposure. Material is irritating to mucous membranes and upper respiratory tract. It is narcotic in high concentrations **[38-39]**.

2.4.3. Photocatalytic experimental setup

Photocatalytic degradation of acetophenone was carried out using a reactor consisting of two parts as shown in **Figure-2.5**. The first part is the inner quartz double wall jacket with inlet and outlet for the water circulation to maintain the temperature of reaction mixture. This jacket has an empty chamber at the centre for immersion of mercury vapour lamp. UV irradiation is done with 125 W mercury vapour lamp *(Crompton Greaves Ltd. India)*. Second part is the outer borosilicate glass container (volume 250 ml after insertion of inner part) in which the reaction takes place. The magnetic stirrer was kept below the reactor for continuous stirring.

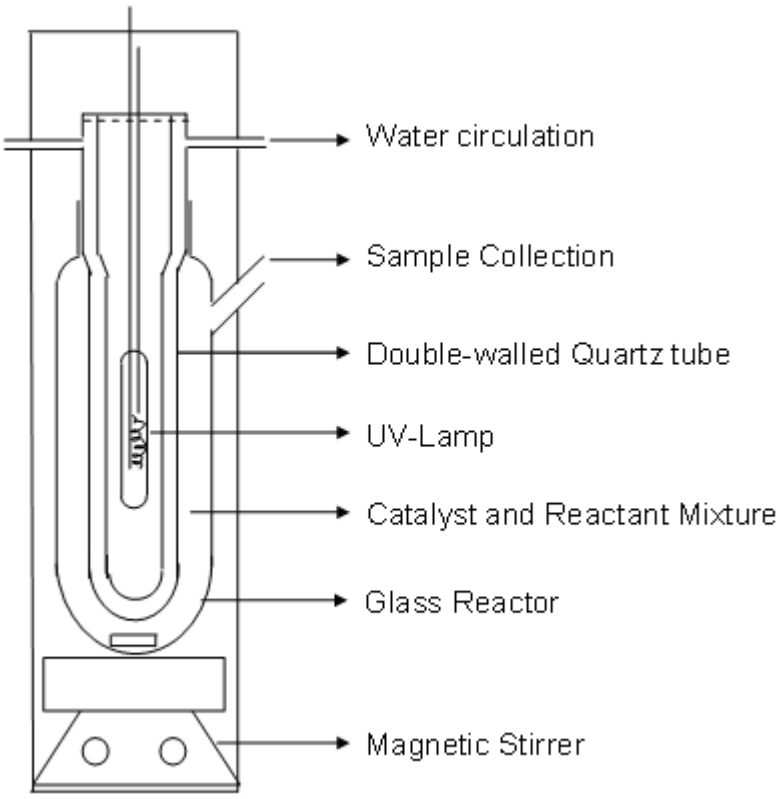

Figure-2.5. Photocatalytic degradation reactor set up

2.4.4. Photocatalytic degradation procedure

The photocatalytic activity of the catalysts was evaluated by measuring the decrease in concentration of acetophenone in the reaction solution. The decrease in the concentration of acetophenone was measured by using UV-Visible spectroscopy. The calibration curve was plotted for acetophenone and for the purpose the standard samples of acetophenone in distilled water was prepared. The concentrations of the standard samples were 5, 10, 20, 30, 40 and 50 ppm and the absorption of these samples were measured by UV-Visible spectroscopy. The calibration curves were plotted between absorption values of the samples with respect to their relevant concentrations. The slopes of the curves were calculated which were used for the calculation of acetophenone concentration. The calibration curve for acetophenone is shown in **Figures-2.6**.

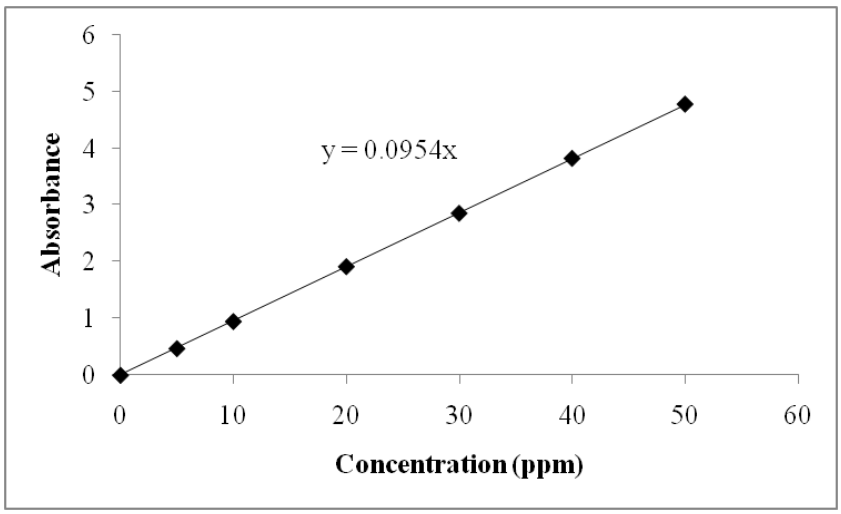

Figure-2.6. Calibration curve for the acetophenone

Prior to commencing irradiation, a suspension containing 50 mg of the catalyst and 250 ml aqueous solution of ca. 50 ppm of acetophenone was stirred continuously for 30 minutes in the dark followed by the collections of the sample and its analysis for acetophenone. Following this, solution was irradiated and samples were withdrawn for analysis by a syringe from the irradiated suspension at interval of 10 min for first one hour and every hour thereafter. The catalysts were separated by centrifugation from the aqueous solutions prior to analysing the samples. The concentrations of acetophenone in the solution were determined by UV-Visible spectrophotometer (Cary 500, Varian Palo Alto CA). The absorbance was measured at λ_{max} 246 nm for acetophenone.

The 5 ml reaction mixture was withdrawn from the port by syringe at different time intervals. The pH of the reaction mixture was measured by pH meter prior to reaction. The pH of the reaction mixture was observed in the range of 5.96-6.00. No acid and alkali was added to achieve the pH. It shows that no ion leaching is observed before irradiation and reaction mixture shows nearly constant pH.

2.5. RESULTS AND DISCUSSION

2.5.1. Photocatalytic degradation of acetophenone

The photocatalytic degradation of aqueous acetophenone solution was investigated by determining the concentration of acetophenone after irradiation at different time intervals. The adsorption of acetophenone on TiO_2 for first 30 minutes was determined without irradiation followed by photocatalytic degradation of acetophenone. In all the cases, the concentration of acetophenone after adsorption was taken as an initial concentration for calculating photocatalytic degradation. **Figure-2.7** shows the photocatalytic disappearance of the acetophenone during the degradation in the presence of 50 mg of the catalyst in 250 ml of aqueous solution having 50 ppm initial concentration of acetophenone as a function of irradiation time under near UV radiation.

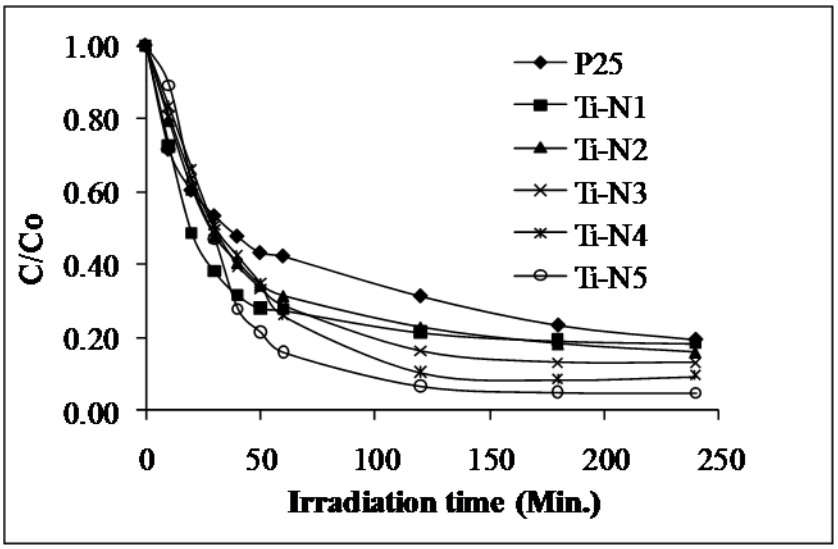

(a)

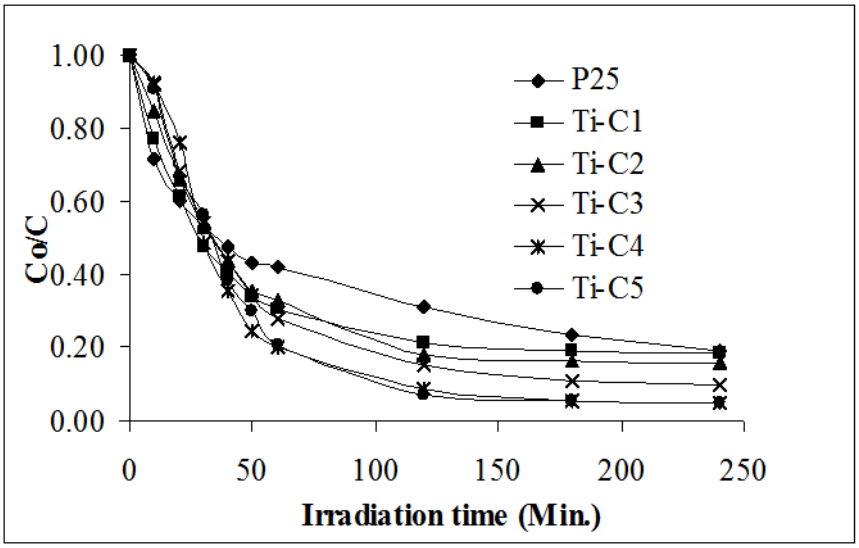

(b)

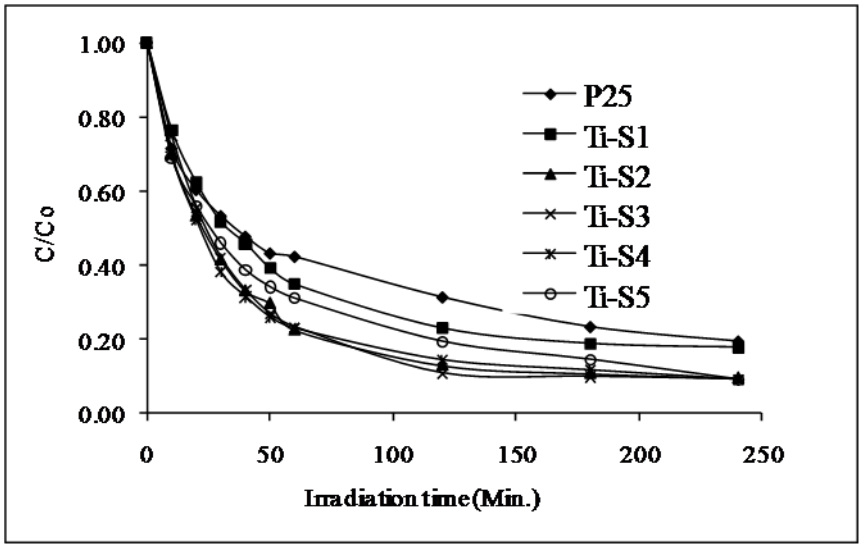

(c)

Figure-2.7. Photocatalytic degradation of acetophenone at different irradiation time with different Fe(III) salts impregnated TiO_2 catalysts (a) Ti-N Series (b) Ti-C Series (c) Ti-S Series

The progress of the reactions was followed by measuring the decrease in UV-visible absorption peaks corresponding to acetophenone in 200-400 nm range in the reaction solution obtained after the filtration of photocatalyst. Typical spectra obtained after irradiation at different times are shown in **Figure-2.8**.

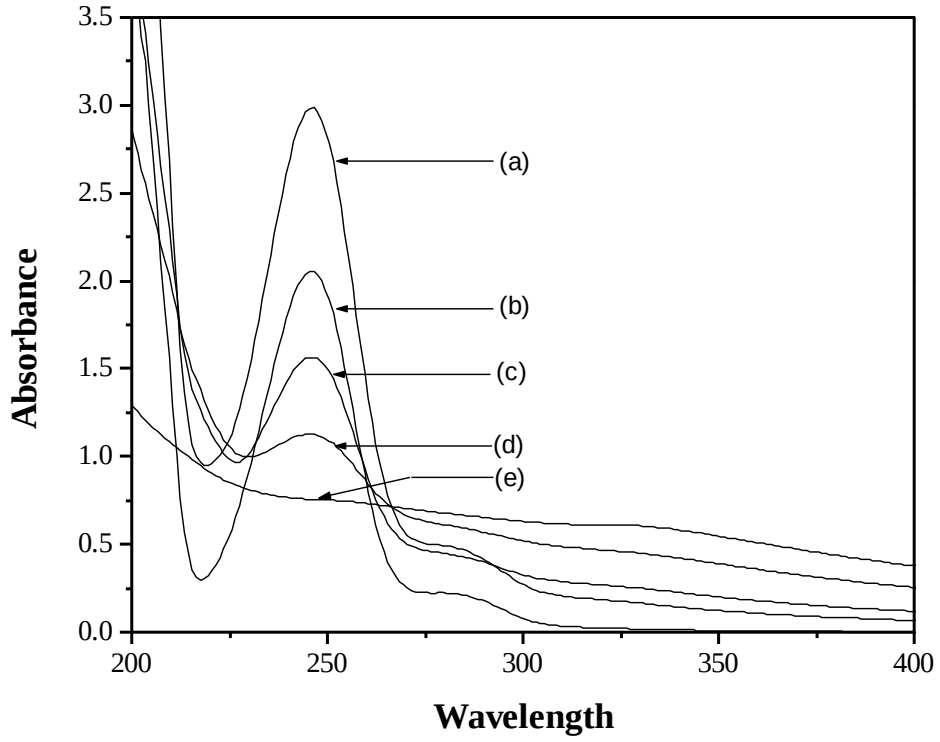

Figure-2.8. Typical UV spectrum profile during photocatalytic degradation of acetophenone, (a) 10 min. sample (b) double diluted 50 ppm original solution (c) 30 min. sample (d) 60 min. sample (e) 240 min. sample

2.5.2. Photocatalytic mechanism

The enhancement in photocatalytic activity with impregnation of the transition metal ion in the nanocrystalline TiO_2 is reported by various workers [**9, 24, 40-44]**. This enhanced activity is due to the charge trapping. The process of charge trapping in Fe (III) impregnated catalysts is as follows:

$$Ti^{4+} + e_{cb}^{-} \rightarrow Ti^{3+} \quad (2.4)$$

$$Fe^{3+} + e_{cb}^{-} \rightarrow Fe^{2+} \quad (2.5)$$

$$OH^{-} + h_{vb}^{+} \rightarrow OH^{\cdot} \quad (2.6)$$

This mechanism is supported by the visibly observed colour change of the solid catalysts on Fe^{3+} reduction to Fe^{2+}. The red brown and pale-yellow colours of the catalysts were

found to change to gray. The irradiation of semiconductor with UV light results in the formation of e^-/h^+ pairs which start redox reactions with species present in the solution. The occurrence of these redox reactions depends on the electrochemical potential of the species and redox level of the valence and conduction band-edges of the semiconductors. The life time of electrons and holes in the solution are very important and it can be increased either by trapping an electron or a hole. Transition metal impregnation helps to decrease the recombination rate by trapping the electrons and increase their lifetime. Consequently, the lifetime of free holes can be extended by moving the energy level of impregnated ion towards the conduction band edge because in this case the traps have a larger tendency to act as a shallow trap so that the holes generated by following photons cannot recombine with already trapped electrons **[9]**. The trapping of electrons makes it easy for holes to transfer onto the surface of TiO_2 and react with OH^- to form active $OH^\bullet$ radicals to participate in the acetophenone destruction.

Figure-2.9 shows the percentage degradation with increase the Fe (III) ion concentration in different catalysts after 4 h. It can be seen that the effectiveness of the catalysts increases with increase in the Fe (III) ion content. This may be due to the charge trapping by the impregnated metal. This charge trapping stops or minimizes the charge recombination and increase the effectiveness. Thus, the anion effect is not significant as far as the final degradation is concerned.

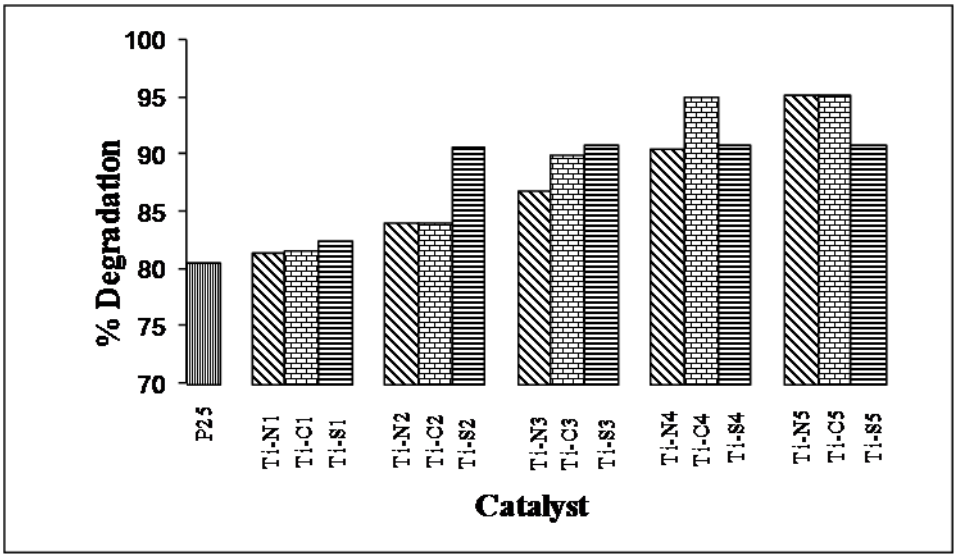

Figure-2.9. Photocatalytic degradation of acetophenone in aqueous suspension under UV irradiation using Fe (III) impregnated P25 TiO_2 samples

2.5.3. Kinetic study

The initial rate decreases continuously with increase in the Fe (III) ion impregnation with Ti-N and Ti-C series (**Table-2.5**). The initial rates observed are lower than that of pristine P25. The higher concentration of iron results into the agglomeration at surface of TiO_2 to form α-Fe_2O_3 as also evidenced by X-ray diffraction data (**Figure-2.1**). This causes in the reduction of catalytically active sites and electron relay sites, which would have a negative influence on the photocatalytic activity. The catalytic active sites may also be blocked by the anions [**45-46]**.

The scavenging feature of oxidizing radical species given by the Cl^- ion is also responsible in reducing the rate of degradation. The reactions were performed at pH = 6, and this pH, Cl^- ion can reduce TiO_2 valence band holes forming HClO or Cl_2 as follow [**47]**:

$$OX^{\cdot} + Cl^- \rightarrow Cl^{\cdot} \qquad \{Radical\ scavenging\} \tag{2.7}$$

$$h^+_{vb} + Cl^- \rightarrow Cl^{\cdot} \tag{2.8}$$

$$OH^{\cdot} + Cl^{\cdot} \rightarrow HOCl \tag{2.9}$$

$$Cl^{\cdot} + Cl^{\cdot} \rightarrow Cl_2 \quad (2.10)$$

NO_3^- ion may block the active sites of the catalysts. The decrease in rate was higher in presence of NO_3^- than the Cl^- ions. It may be because nitrate has large anionic size than chloride which could block the active sites more effectively. The existence of Cl^- was confirmed by X-Ray fluorescence (XRF) spectroscopy. The decreasing photoactivity in presence of anions was observed by others with photocatalytic degradation of humic acid [**45]**, *p*-hydroxy benzoic acid [**48]**, phenol [**49]**, nitrobenzene [**50]**, benzoic acid [**51]** and for the photocatalytic oxidation of organic carbon [**44]**.

In case of Ti-S series (**Table-2.5**), the initial rate was found lower than the P25 with Ti-S1, Ti-S2 and Ti-S3 catalysts but at higher impregnation of ferric sulfate, i.e., with Ti-S5 catalyst increased rates of degradation were observed. The initial rate decrease as SO_4^{2-} ions are introduced in P25 by ferric sulfate (catalyst Ti-S1) is due to the reason that the SO_4^{2-} ions are present on the surface of catalyst P25, deactivating a portion of the catalyst **[52]**. However, the observed rate increase with the increasing amount of SO_4^{2-} ions is explained in terms of the formation of reactive species such as $SO_4^{\bullet-}$ according to the reaction [**45-46]**.

$$h_{vb}^{+} + SO_4^{2-} \rightarrow SO_4^{\cdot-} \quad (2.11)$$

The increase in the percentage degradation after four hours may also be due to the leaching of anions from active sites of the catalysts. In case of ferric sulphate, the sulphate ions also enhance the degradation resulting into increase in photocatalytic activity while it is not the case for ferric nitrate and ferric chloride; as such chloride ions are known as inhibitor in photocatalytic activity.

Table-2.5. Kinetic data of the reactions performed

Catalyst	Initial Rate x 10^6 [mol.min.$^{-1}$]	Rate constant (k) x 10^{-2} [min.$^{-1}$]
P-25	8.00	2.64
Ti-N1	8.33	2.88
Ti-N2	6.93	2.25
Ti-N3	6.33	2.21
Ti-N4	5.80	2.19
Ti-N5	5.66	2.17
Ti-C1	7.13	2.19
Ti-C2	6.80	2.07
Ti-C3	6.40	2.07
Ti-C4	6.33	2.07
Ti-C5	6.13	2.07
Ti-S1	6.06	1.95
Ti-S2	7.46	2.56
Ti-S3	7.73	2.61
Ti-S4	8.00	2.64
Ti-S5	8.20	2.64

For photocatalysis, TiO_2 require UV-light only and the presence of Fe^{3+} does not affect or marginally affects this property. There is no visible light irradiated photocatalytic activity

observed for the iron impregnated titania samples [**28]**, which confirms lack of formation of e^-/h^+ pairs at these wavelengths.

The experimental kinetic data follow the first order kinetic expression,

$$\log[C_t] = -kt + \log[C_o] \quad (2.12)$$

Where $[C_o]$ and $[C_t]$ represents the concentration of the substrate in solution at time zero and time *t* of illumination respectively and *k* represents the apparent rate constant (min^{-1}). The constant *k* values for each reaction at every time suggest the applicability of the first order kinetics with respect to acetophenone. The photocatalytic degradation exhibited pseudo first order kinetics with respect to acetophenone concentration (**Figure-2.10**).

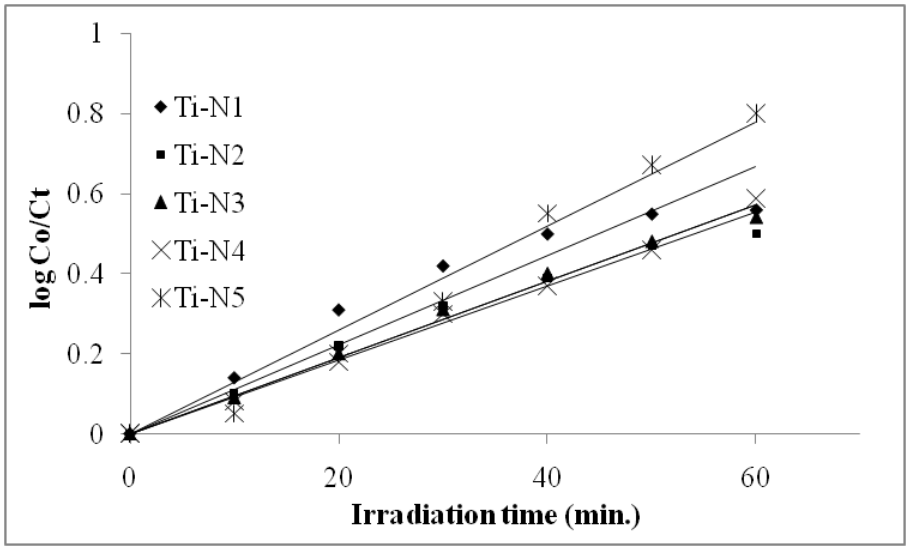

(a)

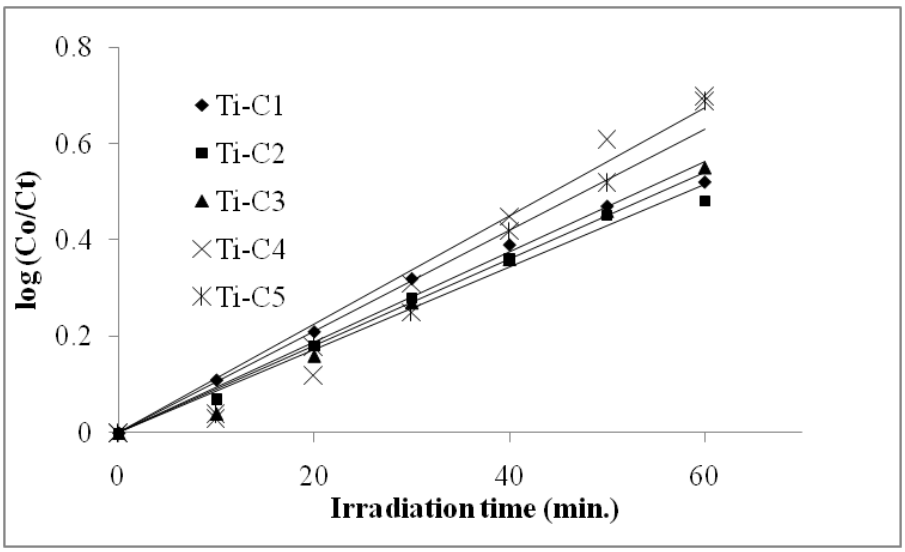

(b)

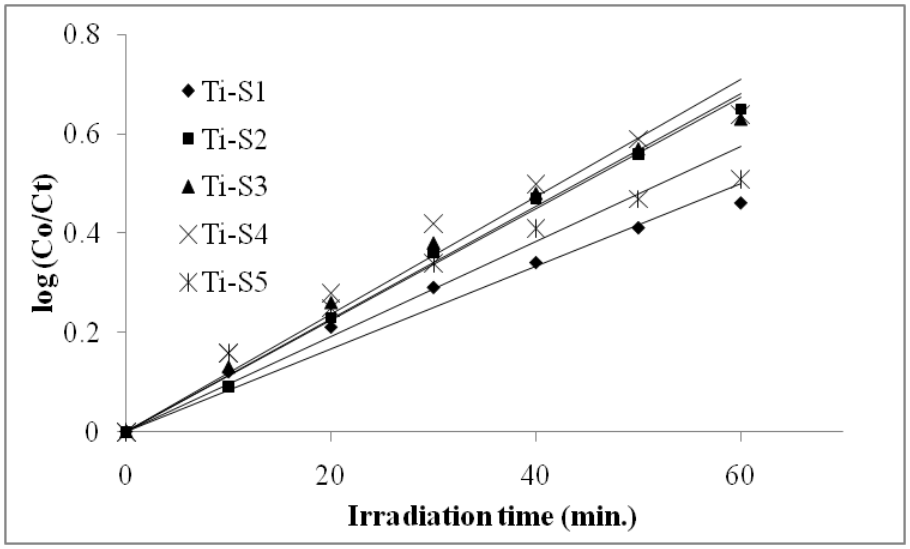

(c)

Figure-2.10. log Co/Ct vs. Irradiation time curves with (a) Ti-N series (b) Ti-C series and (c) Ti-S series catalysts

The rate constants were determined by linear regression of the data over the first 60 minutes of the reaction. The values of average rate constants obtained are represented in **Table-2.5**. The decreasing values of average rate constants are found to decrease in Ti-N series while increasing values of rate constants in Ti-S series shows an increase in the rate of acetophenone degradation. The average rate constant value is almost constant for Ti-C series showing not much difference in rates.

To find the leaching of the Fe (III) ion in the catalyst during the reaction, the reaction sample was filtered and analyzed after the completion of reactions and analyzed by ICP-AAS. The data showed the absence of any leaching of Fe (III) ion from the impregnated catalysts. No leaching was observed of the metal cation during the reaction.

Form this study we can conclude that, The impregnation of Fe (III) salts on Degussa P25 TiO_2 having different anions has been found to affect the activity of the photocatalyst for the degradation of acetophenone. The metal ion impregnation inhibits the recombination of the charge species electron and holes. It results in increase of the efficiency of catalyst which is observed in the form of increase in the final percentage degradation of acetophenone. The final percentage degradation increases continuously with increase in Fe (III) ion concentration and it was observed that anion effect is not significant in this case. On the contrary, the initial rate of degradation is reduced in presence of the Fe (III) ion impregnated catalyst prepared with ferric nitrate and ferric chloride. This decrease in the rate is possibly due to partial blockage of the active sites of the catalyst by anions. Cl^- ion can also reduce the rate of degradation by scavenging oxidizing radical species. In the case of Fe (III) ion impregnated catalyst prepared with ferric sulfate, first the initial rate was found to decrease as SO_4^{2-} ions are introduced in P25 by ferric sulfate. It is due to this reason that the SO_4^{2-} ions are present on the surface of catalyst P25 and deactivates a portion of the catalyst; however the rate was found to increase with the increasing amount of SO_4^{2-} ions, which could be due to the formation of reactive species such as $SO_4^{\bullet-}$ radicals.

2.6. References

[1] Li, B.; Wang, X.; Yan, M.; Li, L., *Mater. Chem. Phys.*, **2003,** *78*, 184-188.

[2] Nagaveni K.; Sivalingam, G.; Hegde, M. S.; Madras, G., *Appl. Catal., B: Environ.*, **2004,** *48*, 83-93.

[3] Irie, H.; Watanabe, Y.; Hashimoto, K., *Chem. Lett.*, **2003,** *32*, 772-773.

[4] Yang, S.; Gao, L., J. *Am. Ceram. Soc*., **2004**, *87*, 1803-1805.

[5] Liu, H.; GAO, L., *J. Am. Ceram. Soc*., **2004,** *87*, 1582-1584.

[6] Yu, J. C.; Yu, J. G.; Ho, W. K.; Jiang, Z. T.; Zhang, L. Z., *Chem. Mater.*, **2002,** *14*, 3808-3816.

[7] Litter, M. I., *Appl. Catal., B: Environ*., **1999,** *23*, 89-114.

[8] Brezová V.; Blažková A.; Karpinský,Ľ.; Grošková J.; Havlínová B.; Jorík V. and Čeppan M., *J. Photochem. Photobiol. A: Chem.*, **1997,** *109*, 177-183.

[9] Tayade R. J**.;** Kulkarni R. G.; and Jasra R. V., *Ind. Eng. Chem. Res*., **2006**, *45*, 5231-5238.

[10] Choi W.; Termin A.;Hoffmann M. R., *J. Phys. Chem.*, **1994**, *98*, 13669- 13679.

[11] Li X.; Yue P.; Kutal C., *New J.Chem*., **2003,** *27*, 1264-1269.

[12] Vamathevan V.; Tse H.; Amal R.; Low G.; McEvoy S., *Catal. today*, **2001,** *68*, 201-208.

[13] Martin S. T.; Herrmann H.; Choi W.; Hoffmann M., *Faraday Trans*., **1994**, *90*, 3315-3322.

[14] Herrmann J.-M.; Disdier J.; Pichat P.; Malato S.; Blanco J., *Appl. Catal. B Environ.*, **1998**, *17*, 15-23.

[15] Alebbi M.; Bignozzi C.A.; Heimer T.A.; Hasselmann G.M.; Meyer G.J., *J. Phys. Chem. B*, **1998**, *102*, 7577-7581.

[16] Grzechulska J.; Morawski A.W., *Appl. Catal. B Environ.*, **2002**, *36*, 45-51.

[17] Surolia P.K.; Tayade R.J.; Jasra R.V., *Ind. Eng. Chem. Res.*, **2007**, *46*, 6196-6203.

[18] Chen D.; Ray A.K., *Wat. Res.*, **1998**, *32*, 3223-3234.

[19] Spurr, R. A.; Myers H., *Anal. Chem.*, **1957**, *29 (9)*, 760-762.

[20] Cullity, B. D.; Stock, S. R., *Elements of X-ray Diffraction*, 3rd ed.; Prentice Hall Inc.: Upper Saddle River, NJ, **2001.**

[21] Shah, S. I.; Li. W.; Hung C.-P.; Jung U.; Ni, C., *Proc. Natl. Acad. Sci. U.S.A.*, **2003**, *99*, 6482-6486.

[22] Diebold U., The surface science of titanium dioxide. *Surface Science Reports*, **2003**, *48*, 53-229.

[23] Cerius2 v. 4.1; Accelrys, Inc.: San Diego, CA, **1999**.

[24] Litter M. I.; Navío J.A., *J. Photochem. Photobio. A: Chemistry*, **1996,** *98*, 171-181.

[25] Kim E. J.; Hahn S.-H., *Material Letters,* **2001,** *49***,** 244-249.

[26] Mishra M. K; Tyagi B.; Jasra R. V., *Ind. Eng. Chem. Res*., **2003**, *42*, 5727-5736.

[27] Lopez T.; Gomez R.; Sanchez E.; Tzompantzi F.; Vera L., *J. Sol-Gel Sci. and Technol.,* **2001,** *22*, 99–107.

[28] Navío J.A.; Colón G.; Litter M. I.; Bianco G. N., *J. Mol. Cat. A: Chem*., **1996,** *106*, 267-276.

[29] Colón G.; Hidalgo M.C.; Nav´ıo J.A., *Applied Catalysis B: Environ.*, **2003,** *45*, 39–50.

[30] Dalai A. K.; Sethuraman R.; Sai P. Katikaneni R.,; Idem R. O., *Ind. Eng. Chem. Res.*, **1998**, *37*, 3869-3878.

[31] Gratzel, M., *Heterogeneous Photochemical Electron Transfer*; CRC Press: Baton Rouge, LA, **1988**.

[32] Tayade, R. J.; Kulkarni, R. G.; Jasra, R. V., *Ind. Eng. Chem. Res*., **2006**, *45*, 922-927.

[33] Lee S.-H.; Sung M. K.; Cho M.; Han G. Y.; Kim B.-W.;Yoon K. J.; Chung C.-H., *J. Photochem. Photobiol. A: chem.*, **2001**, *146*, 121-128.

[34] Kang M.; Choung S.-J.; Park J. Y., *Catal. Today*, **2003**, *87*, 87–97.

[35] Zhu J.; Zheng W.; He B.; Zhang J.; Anpo M., *J. Mol. Cat. A: Chem.*, **2004**, *216*, 35-43.

[36] Borgarello E.; Kiwi J.; Pelizzetti E.; Visca M.; Graetzel M., *J. Am. Chem. Soc.* **1981**, *103*, 6324-6329.

[37] Wang Y.; Cheng H.; Hao Y.; Jiming M A.; Li W.; Cai S., *Journal of mater. sci.*, **1999**, *34*, 3721-3729.

[38] http://www.chemicalland21.com

[39] http://speclab.com

[40] Brezova, V.; Blazkova, A.; Karpinsky, L.; Groskova, J.; Havlinova, B.; Jorik, V.; Ceppan M., *J. Photochem. Photobiol. A: Chem.*, **1997**, *109*, 177-183.

[41] Ikeda, S.; Sugiyama, N.; Pal, B.; Marci, G.; Palmisano, L.; Noguchi, H.; Uosaki, K.; Ohtani, B., *Phys. Chem. Chem. Phys.* **2001**, *3*, 267-273.

[42] Fuerte, A.; Hernandez-Alonso, M. D.; Maria, A. J.; Martinez-Arias, A.; Fernandez-Garcia, M.; Conesa, J. C.; Soria, J., *Chem. Commun.* **2001**, *24*, 2718-2719.

[43] Chen, Y.-F.; Lee, C.-Y.; Yang, M.-Y.; Chiu, H.-T., *J. Cryst. Growth*, **2003**, *247*, 363-370.

[44] Liqiang, J.; Xiaojun, S.; Naifu, X.; Baiqi, W.; Weimain, C.; Honggang, F., *J. Solid State Chem.* **2004**, *177*, 3375-3382.

[45] Al-Rasheed R.; Cardin D. J., *Chemosphere,* **2003**, *51*, 925-933.

[46] Abdullah M.; Gary K.C., Low, Ralph W. Matthews, *J. Phys. Chem.* **1990**, *94(17),* 6820-6825.

[47] Boxall C.; Kelsall G. H., *Faraday Transaction*, **1991**, *87(21)*, 3537-3545.

[48] Subramanian V.; Pangarkar V. G.; Beenackers A. A. C. M., *Clean prod. proc.*, **2000**, *2*, 149-156.

[49] Yawalkar A. A.; Bhatkhande D. S.; Pangarkar V. G.; Beenackers A.A.C.M., *J. Chem. Technol. Biotechnol.* **2001**, *76*, 363-370.

[50] Bhatkhande D. S.; Pangarkar V. G.; Beenackers A. A. C. M., *Water research*, **2003**, *37*, 1223-1230.

[51] Ajmera A. A.; Sawant S. B.; Pangarkar V. G.;.Beenackers A.A.C.M., *Chem. Eng. Technol*. **2002**, *25 [2]*, 173-180.

[52] Houas A.; Lachheb H.; Ksibi M.; Elaloui E.; Guillard C.; Herrmann J.-M., *Applied catalysis B: Environ*. **2001**, *31*, 145-157.

Chapter 3

Photocatalytic Reactivity of Transition Metal-Exchanged ETS Zeolites

3.1. INTRODUCTION

Microporous titanosilicates comprise a new family of molecular sieve materials that possess zeolite-like properties such as catalysis, separation, absorption and ion-exchange **[1]**. As a new type of titanosilicate zeolite, ETS (Engelhard Titanium Silicate) has attracted much attention recently because of the structural uniqueness as well as potential applications in catalysis. ETS-4 and ETS-10 represent two of the earliest discovered microporous titanosilicates **[1-2]**. ETS-4 and ETS-10 has pore opening of 0.37 nm and 0.8 nm respectively. The first information on microporous titanosilicates dates back to 1967 when Young **[3]** reported the synthesis of titanium silicates under conditions similar to aluminosilicates. In 1973 a naturally occurring alkaline titanosilicate identified as zorite was discovered in trace quantities on the Siberian tundra. In 1989 and 1990 two independent reports by Kuznicki **[4-5]** and Chapman and Roe discussed synthetic structures that appeared to mimic zorite **[2]**. Unlike zeolites whose framework is built of tetrahedral [AlO_4^-] and [SiO_4^-] units, however, titanosilicates, especially those having higher Ti/Si ratios (>0.025) **[6]**. ETS zeolites including ETS-4 and ETS-10 have a porous structure comprising chains of corner-linked TiO_6 octahedron surrounded by SiO_4 tetrahedra units. Interestingly, this kind of zeolite, ETS-4 and ETS-10, comprises . . .–Ti–O–Ti–O– . . . quantum semiconductor nanowire (represented by cylinders with ca. 0.67 nm diameter) chains. Furthermore, it has been reported that ETS-10 has photocatalytic activity for oxidation of organic compounds owing to the embedded . . .–Ti–O–Ti–O–. . . nanowires **[7-11]**. For ETS-10, an electronic communication can occur between the –O–$Ti^{(IV)}$–O– semiconductor chains and guest species in the pores, and the photocatalytic activity for oxidation of organic compounds have been studied by some researchers **[7-8]**. Titania chains in ETS-10 have been shown to exhibit a blue shift **[10-11]** in its optical band gap. Both ETS-10 and ETS-4 are attractive systems for modeling properties of monatomic titania nanowires.

The three-dimensional 12-membered ring microporous framework offers many potential advantages in photocatalysis, such as excellent diffusion of reactant molecules, trapping, and in particular, shapes selectivity. In the perfect structure these quantum wires are surrounded by an envelope of SiO_4^- groups. These wires are characterized by full (O-

based: 2p) valence and empty (Ti based: 3d*xy* and 3dz^2) conduction bands **[11-12]**, separated by a band gap of about 4.03 eV, which is higher than that of TiO_2 (3.2 eV) due to confinement effects. They can act as an antenna-like system able to collect the light and to form electron-hole pairs in the -O-Ti-O-Ti- chain. Like in TiO_2, these pairs can recombine or diffuse toward the wire to its end originating photocatalytic activity. In a perfect crystal, this happens where the wires emerge on the external surface, but in the real material this can happen also at internal defects (Ti vacancies). The molecules entering the pore system can be protected from photocatalytic degradation, which occurred on the external surface. The interpretation that the active photocatalytic centers are Ti-OH species at defective sites well agrees by the parallel studies by Howe's group, **[7-13]** which have shown how a highly defective proton-exchanged sample of ETS-10 was much more active for the gas-phase photooxidation of ethylene than a well-crystalline as-synthesized sample.

A substantial difference between ETS-10 and TiO_2 modified systems, previously mentioned, **[14-16]** lies in the fact that surface nanostructuring is in one case (ETS-10) a structural property; while in the other cases it is the result of an external intervention modifying the original properties. A second difference is represented by the band gap, definitely higher in ETS-10 with respect to TiO_2. This implies that the synthesis of solids containing quantum wire affords a method to tailor the band gap and to modulate the response to photons activations. **[11]**. The titanosilicate zeolites ETS-4 and ETS-10 has in built photocatalytically active TiO_2 units. This structural property make it more suited to photocatalysis as it does not have the leaching problem of the photocatalytic active TiO_2 material from the support material.

3.1.1. Structural properties of ETS-4

ETS-4 has an approximate formula of $M_6Ti_3Si_8O_{25}.nH_2O$ (M=K or Na) **[17]** and is structurally similar to the rare titanosilicate mineral zorite (space group *Cmmm*) **[18-19]**. The framework of ETS-4 consists of chains of corner-sharing [TiO_6] octahedral along the *b* axis, with neighboring octahedral in a chain being laterally linked by [SiO_4] tetrahedral. Pairs of [SiO_4] tetrahedral connected to the adjacent [TiO_6] chains are further joined via a

structural unit containing one [TiO_6] surrounded by four [SiO_4] tetrahedral **[18]**. This topology ideally produces two orthogonal sets of channels that are defined by 12-membered rings perpendicular to the *c* axis and eight-member rings perpendicular to *b*. However, like zorite, ETS-4 commonly exhibits substantial stacking faults along the (100) and (001) planes and the faulted structure can be described as an intergrowth of four hypothetical ordered polymorphs **[20]**. As a result, the 12-ring channels along *c* become segmented, whereas the eight-ring channel along *b* is not affected. Correspondingly, the effective pore size of ETS-4 determined by absorption measurement is only about 3.7 Å, which is comparable to the pore size for a small pore zeolite.

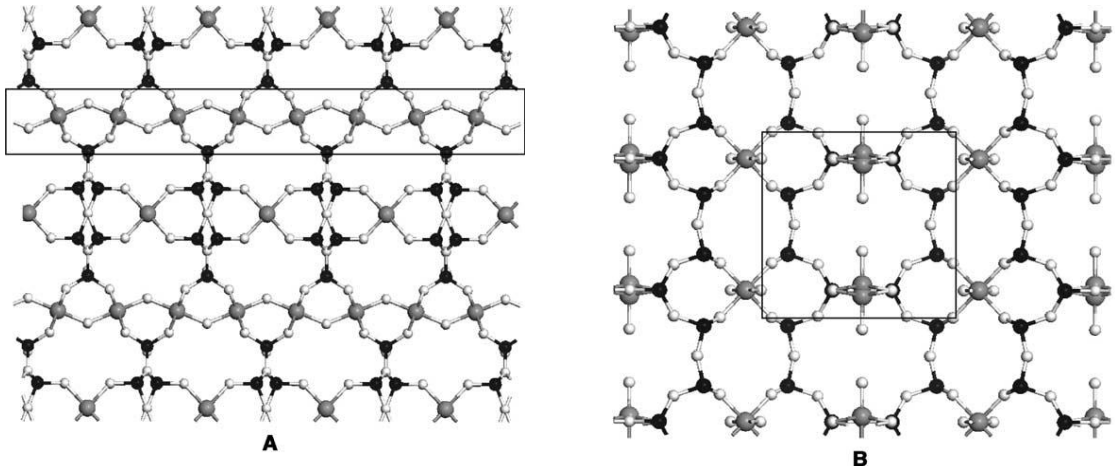

Figure-3.1. ETS-4 structure (A) In box Ti–O–Ti chains shown (a–b plane) and (B) eight-member rings (a–c plane) (black: Si; grey: Ti; white: O) [21-22]

3.1.2. Structural properties of ETS-10

ETS-10 has a tetragonal structure with the ideal composition $M_2TiSi_5O_{13}.nH_2O$ (M=K, Na) **[23-24]**. In this structure, chains of [TiO_6] octahedral are linked to two-folded chains of [SiO_4] tetrahedral, forming [$TiSi_4O_{13}$] columns **[24]**. These columns are packed into layers parallel to (001), with the columns in adjacent layers perpendicular to each other. The layers are further connected by [SiO_4] tetrahedral into a three-dimensional framework. This framework contains three orthogonal sets of channels, defined by 12-membered rings, along the *a*, *b* and *c* axes. As in ETS-4, considerable degree of stacking

disorder occurs in ETS-10 along its (001) plane; the disordered structure can be described as an intergrowth of two hypothetical polymorphs A and B, both of which exhibit a three dimensional 12-ring pore system. ETS-10 can exist as two ideal polymorphs that differ in the stacking sequence along the (001) direction. In polymorph A (tetragonal system, space group *P*41 or *P*43) zigzag channels in the *c* direction are present, while in polymorph B (monoclinic system, space group *C*2/*c*), they are diagonally arranged. The real ETS-10 is actually a virtually random intergrowth of both polymorphs, which results in a disordered material containing stacking faults and line defects. Because of this inherent disorder, the resolution of the structure of ETS-10 has been particularly challenging. A first structural model was proposed by Anderson et al. **[23, 25]** from a combination of electron microscopy, X-ray powder diffraction (XRPD) and electron diffraction, solid state NMR, and molecular modeling. The structure proposed by those authors was later confirmed by Wang and Jacobson using single-crystal diffraction. **[24]**.

Nevertheless, the stacking faults in ETS-10, unlike those in ETS-4, do not appear to cause blockage of the 12-ring channel systems. Thus, ETS-10 has a much higher adsorption capacity over ETS-4. Each titanium atom incorporates a net negative charge of -2 that is compensated by extra framework charge-balancing cations (Na^+ and K^+ in the as synthesized material).

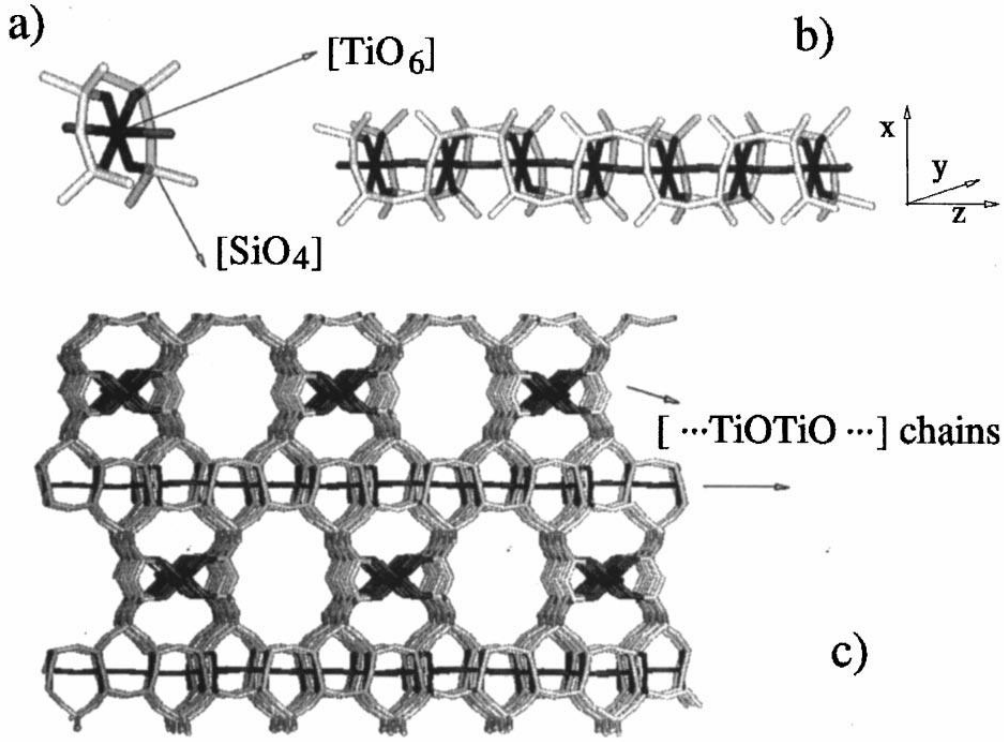

Figure-3.2. The framework structure of ETS-10 showing chains of corner-sharing TiO_6 octahedra which run along two perpendicular directions, and which are isolated by corner-sharing SiO_4 tetrahedra: (a) single element of the chain; (b) single chain; (c) three dimensional view [10, 23]

3.1.3. Ion-exchange in ETS materials

The high cation exchange capacity of ETS-4 and ETS-10 has attracted some attention **[5, 26-28]**. Owing to the high framework charge associated with the octahedral Ti, ETS zeolites have very high cation exchange capacity. In comparison with conventional aluminosilicate zeolites, however, the intrinsically disordered nature of the ETS-4 and ETS-10 structure may impose some limitations on practical applications. The photocatalytic reactivity of zeolites is strongly influenced by whether the material is as synthesized or transition metal ion exchanged. This has prompted us to investigate the effects of transition metal ion-exchange of ETS-4 and ETS-10, in the hope of better understanding variability of the photoactivity.

3.1.4. Aim of the work

The supporting titania catalyst have been tried to increase the photocatalytic activity. These supporting materials include silica **[29-30],** zeolites **[31-33],** fiber glass **[34-35]**, electrode **[36]** etc. However the recovery is still a challenge even of supported photocatalyst. In the present study, the bare and transition metal ion impregnated ETS-4 and ETS-10 zeolites were synthesized and their photocatalytic activity for nitrobenzene degradation under the UV-light irradiation was investigated. The mineralization of nitrobenzene in aqueous solution was confirmed by COD analysis. The low percentage (0.5 %) of ion exchange is chosen as these have shown promise for the improvement in photocatalytic activity **[37-38]**. The addition of transition metal ion offers a way to trap the charge carrier and extend the life time of one or both of charge carriers. The ions to be doped or exchanged must have the work function higher than that of the semiconductor providing a Schottky barrier **[33]**. Considering this characteristic of the transition metals, we chose five transition metals viz. Fe, Co, Ni, Cu and Ag for exchange.

3.2. SYNTHESIS OF ETS MATERIALS AND ION EXCHANGE

3.2.1. Chemicals and Materials

Titanium dioxide (P25) was purchased from Degussa Corporation (Degussa AG, Frankfurt, Germany). Titanium (IV) isopropoxide was purchased from *Aldrich* USA. Sodium silicate was procured from Aquagel, India. NaCl, KCl, Nitrobenzene (NB) and nitrates of all metals as metal source AR grade were purchased form s.d. fine-chem Ltd. Mumbai India. Deionised distilled water was used to make up the reaction mixture.

3.2.2. Catalysts preparation

3.2.2.1. *Synthesis of ETS-10 and transition metal ion exchange*

The synthesis of the catalysts was as per procedure reported by X. Yang et al. **[39]**. Degussa P25 was chosen as TiO_2 precursor. Typically 20 gm of sodium silicate solution

(24 wt.% SiO_2, 8 wt.% Na_2O) was diluted with 70 ml of water and then 13.8 gm of NaCl and 2.6 gm of KCl was dissolved in the solution. In the resultant translucent thick gel, 2.6 gm of Degussa P25 TiO_2 was added under vigorous stirring. The slurry was stirred for 30 min at room temperature and transferred to a Teflon-lined autoclave and heated statically at 200 °C for 42 h. The starting gel had the pH around 10.83. The solid product was isolated from mother liquor by filtration, washed with distilled water, dried overnight at 60 °C and then calcined at 450 °C for 5 h in air. Thus obtained ETS-10 had the stoichiometry of $(Na,K)_2$ Ti Si_5O_{13}.

For transition metal ion exchange in ETS-10, the weighed amount of ETS-10 (2 g) was stirred for 24 h with the metal salt solution in 100 ml water of the concentration calculated for 0.5 % (w/w) metal ion exchange at room temperature. In the ion exchange, some or most of the alkali metal ions (Na & K) would be replaced by transition metal ion from ETS-10 givens rise to composition $(Na,K)_{2-x}$ M_y Ti Si_5O_{13} (M = transition metal ion). After the ion exchange, the water was evaporated using rotavapor and the samples were dried at 120 °C for 12 h. The obtained samples were named as M-ETS-10, where M represents the transition metal.

3.2.2.2. *Synthesis of ETS-4 and transition metal ion exchange*

The initial chemical composition of the solution used for the synthesis of ETS-4 was Ti:Si:Na:H_2O_2:H_2O = 0.9:10:14:8:675 on a molar basis. Titanium (IV) butoxide was added to the aqueous solution of the sodium hydroxide followed and stirred for 20 min to make the solution homogeneous. The hydrogen peroxide was added to this white colour solution which turns it into yellow colour solution. The solution was again stirred for 10 min. The sodium silicate solution (24 wt. % SiO_2, 8 wt. % Na_2O) was added drop wise to this resultant solution producing a clear bright yellow solution. This solution was stirred for 15 min and transferred to autoclave for the hydrothermal synthesis. The hydrothermal synthesis was performed statically at 453 K for 72 h in an autoclave. The powder obtained was filtered, washed with distilled water, and dried at 40˚C temperature.

For transition metal ion exchange in ETS-4, the weighed amount of ETS-4 (2 g) was stirred for 24 h with the metal salt solution in 100 ml water of the concentration

calculated for 0.5 % (w/w) metal ion exchange at room temperature. In the ion exchange, Na ions would be replaced by transition metal ion from ETS-4. After the ion exchange, the water was evaporated using rotavapor and the samples were dried at 120 ℃ for 12 h. The obtained samples were named as M-ETS-4, where M represents the transition metal.

3.3. CHARACTERIZATION OF PREPARED PHOTOCATALYSTS

3.3.1. X-ray diffraction (XRD)

The X-ray diffraction data were collected on a Phillips X'pert MPD system using CuKα1 (λ = 0.15405 nm) radiation at 295 K. Diffraction patterns were taken over the 2θ range of 10°- 80° at the scan speed of 0.1°sec^{-1}.

The powder XRD patterns of pure ETS-10 and pure ETS-4 samples with their ion exchanged samples are shown in **Figure-3.3 (a)** and **(b)** respectively. The pattern of ion exchanged samples look similar to the parent ETS materials and are in good agreement for the peaks at their respective 2θ values. This implies the absence of any other impurities of silica or transition metal oxides during the metal ion exchange and also shows that the structures of ETS-10 and ETS-4 are retained after metal ion exchange. Another reason of the absence of any peak due to exchanged metal ion may be very small amount of ion exchange. The XRD pattern exhibits a high degree of disorder in ETS-10 **[23]** and ETS-4 structure.

The percent crystallinity of the modified ETS-4 samples was determined by taking bare ETS-4 as 100 % crystalline material. The crystallinity was found to decrease with transition metal ion exchange (**Table-3.1**). The crystallinity decreases due to presence of the transition metal ions at the surface of the ETS-4 sample. The main diffraction lines for the as synthesized ETS-4 were indexed with an orthorhombic unit cell with space group symmetry of *Cmmm* and cell parameters a = 23.2422 Å, b = 7.2021 Å**,** c = 6.9324 Å and $\alpha = \beta = \gamma = 90^{\circ}$ shown as in **Table-3.1**. The reported cell parameters in previous studies are a = 23.2272 Å, b = 7.1751 Å**,** c = 6.9727 Å and a = 23.24 Å, b = 7.23 Å**,** c = 6.95 Å respectively **[21, 40**]. The values of the calculated lattice constants of bare ETS-4

were found to decrease with increase in the metal ion content (**Table-3.1**) supporting exchange of transition metal ions in the lattice at metal exchange.

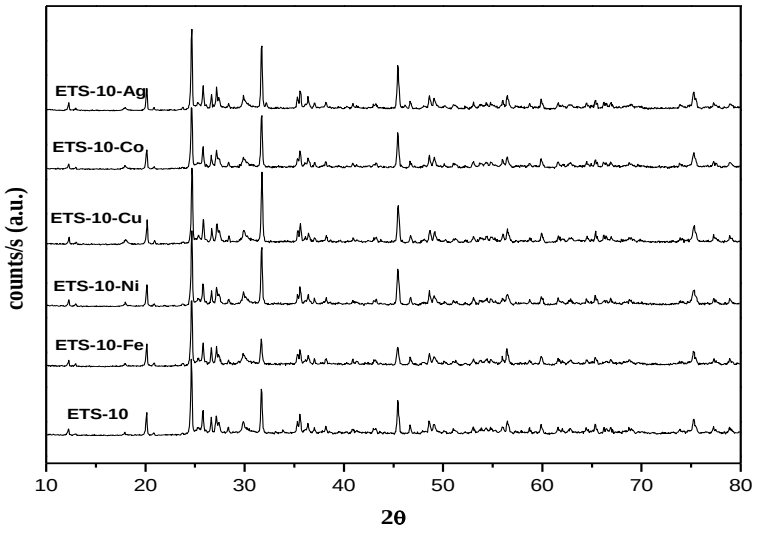

(a)

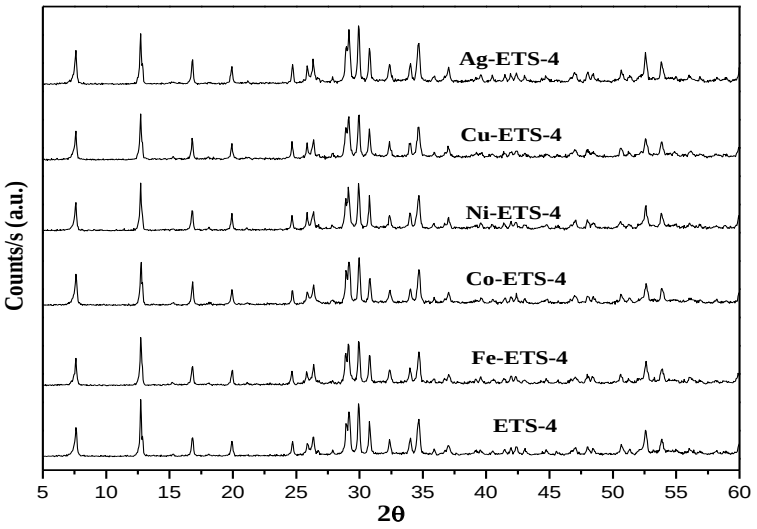

(b)

Figure-3.3. XRD patterns of (a) ETS-10 and (b) ETS-4 with metal exchanged ETS catalysts

Table-3.1. XRD data of the ETS-4 Catalysts

Catalyst	Crystallinity (%)	Lattice constants (Å)		
		a	**b**	**c**
ETS-4	100	23.2422	7.2021	6.9324
Fe-ETS-4	85	23.2420	7.1963	6.9187
Co-ETS-4	95	23.1635	7.1926	6.9182
Ni-ETS-4	89	23.2345	7.2000	6.9246
Cu-ETS-4	84	23.1543	7.1950	6.9252
Ag-ETS-4	96	23.1945	7.1950	6.9264

3.3.2. Infra red spectroscopic measurement (FT-IR)

The FT-IR spectroscopic measurements were carried out using *Perkin-Elmer GX spectrophotometer*. The spectra were recorded in the range 400-4000 cm^{-1} with a resolution of 4 cm^{-1} as KBr pellets.

The IR absorbance spectra of the samples were recorded in the frequency range 400-4000 cm^{-1} (**Figure-3.4**). The IR absorbance spectroscopy study of the samples demonstrated that the exchange of Na by different transition metal cation does not affect the framework and the water molecule at the surface. This may be because of small amount of metal exchange taken for the study (only 0.5%). The broad absorbance peak having values at around 3590 and 3350 cm^{-1} (3590, 3443 and 3216 cm^{-1} for ETS-4) are due to stretching vibrations while absorbance at 1650 is due to the bending vibration of water molecules and OH groups present at the surface of the prepared catalysts **[41-42]**. The absorbance at 1136 cm^{-1} is because of the asymmetric stretching vibrations of Si-O-Si bridges, while peak at 1020 cm^{-1} is the resultant of Si-O-Ti stretching vibrations. The stretching and bending vibrations of Ti-O-Ti give rise to the absorption peak at 750 and 661 cm^{-1}. The

comparison of the IR spectra of pure ETS and transition metal exchanged ETS catalysts showed that there is an additional peak around 1386 cm^{-1} in the IR spectra of transition metal exchanged ETS catalysts. This peak is because of vibrations of H^+ ion **[43]**.

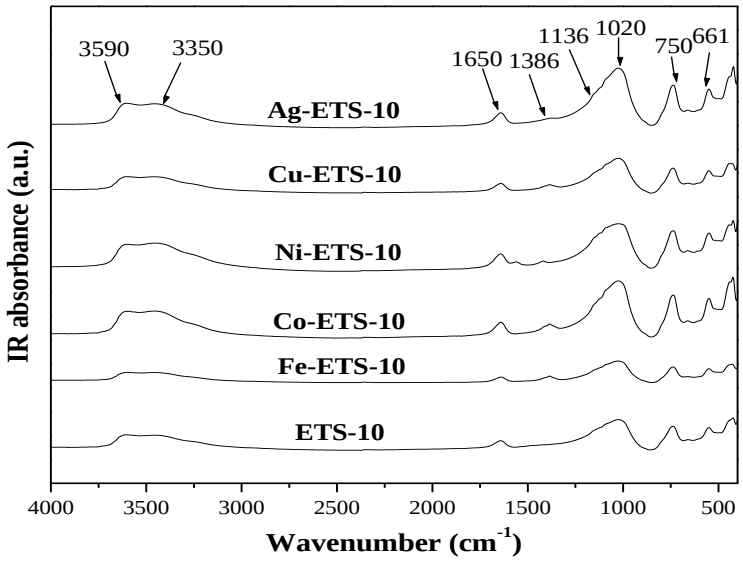

(a)

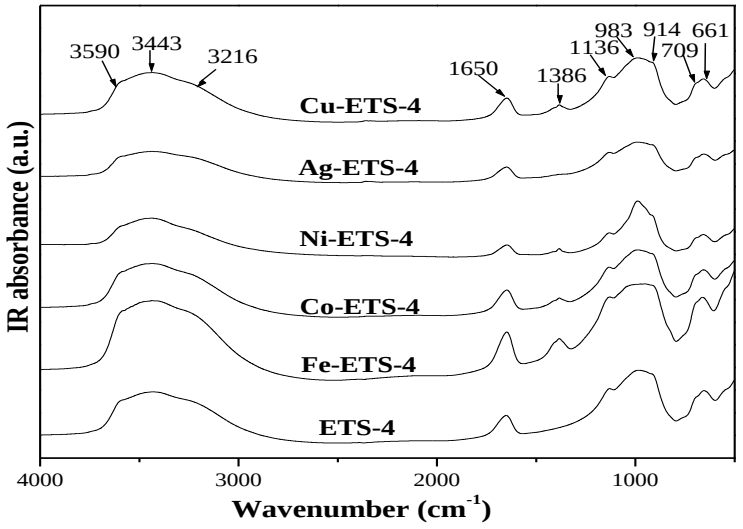

(b)

Figure-3.4. FT-IR spectra of (a) ETS-10 and (b) ETS-4 with metal exchanged ETS catalysts

3.3.3. Surface area measurement (N_2 adsorption)

The Brunauer-Emmett-Teller (BET) surface area of the catalysts was obtained from nitrogen adsorption data at 77.4 K measured using Micromeritics ASAP 2010 nitrogen adsorption apparatus. The surface areas of the synthesized bare ETS-10 and transition metal ion exchanged material are listed in **Table-3.2.** The surface areas of ion-exchanged catalysts were found decreased. The observed drop was minimum 16 m^2/g for Cu-ETS-10 catalyst and maximum 41 m^2/g for Fe-ETS-10. This could be due to the pore plugging of the starting material by ion exchange and/or by initial structure collapse **[44]**. However, surface area of ETS-4 could not be determined by N_2 adsorption as its pore size is smaller than the size of N_2 molecule.

Table-3.2. BET Surface area and Pore volume of ETS-10 Catalysts.

Catalyst	BET Surface area (m^2/g)	Pore Volume (cm^3/g)
ETS-10	232	0.134
Fe-ETS-10	191	0.125
Co-ETS-10	203	0.125
Ni-ETS-10	201	0.119
Cu-ETS-10	216	0.124
Ag-ETS-10	205	0.116

3.3.4. Diffuse reflectance spectra (DRS)

The band gap energy of the catalysts was determined using the Diffuse Reflectance Spectroscopy (DRS). The spectrophotometer (Shimadzu UV-3101PC) was equipped with an integrating sphere and $BaSO_4$ was used as a reference. The spectra were recorded at room temperature in the wavelength range of 250-600 nm. The band gap energy of catalysts were calculated according to the equation,

$$Bandgap\ (EG) = hc/\lambda \quad (3.1)$$

Where *EG* is the band gap energy (eV), *h* the Planck's constant, *c* the light velocity (m/s) and λ is the wavelength (nm).

The presence of transition metal ions in different M-ETS-10 and M-ETS-4 (ion-exchanged) samples could be seen from the UV– Vis diffuse reflectance spectra (**Figure-3.5**). Comparison of diffuse reflectance spectra of bare and ion exchanged catalysts showed change in the band gap due to ion exchange. The band gaps of bare and ion exchanged catalysts were calculated by using a differential calculation (**Table-3.3**). From the data it is evident that all the impregnated catalysts have extended a red shift except silver doped ETS-10 sample where slight blue shift of 2 nm was observed. The red shift was maximum 3.5 nm with cobalt metal ion impregnation in ETS-10 catalyst.

Figure-3.5 (b) shows the diffuse reflectance spectra of bare ETS-4 and transition metal exchanged ETS-4. The transition metal exchanged ETS-4 catalysts were found to show two band gaps. The values of these band gaps were same for all the samples. It is obvious that the band gap of ETS-4 is apparently blue-shifted compared to that of TiO_2 bulk (~3.2 eV). This blue shift in absorption of light by the prepared ETS-4 catalyst from TiO_2 bulk is attributable to the quantum size effect of the –Ti–O–Ti–O– nanowires embedded in the ETS-4 crystalline matrix **[45]** which arises from the confinement of charge carriers in a nanosized semiconductor **[46]**. However, this effect was not observed with ETS-10 where band gap was almost same as pure TiO_2 catalyst.

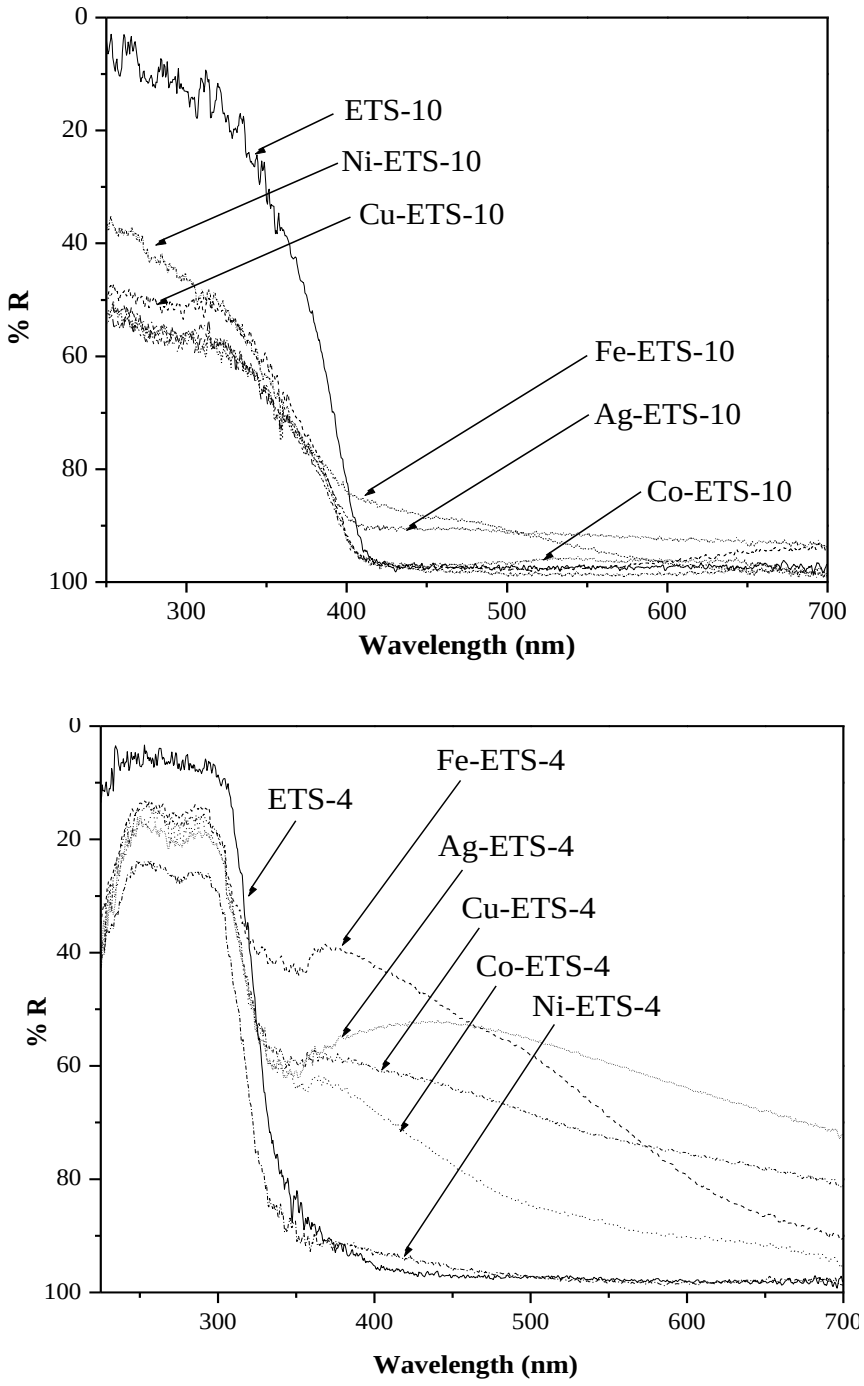

Figure-3.5. Diffuse reflectance UV/VIS spectra of (a) ETS-10 and (b) ETS-4 with metal exchanged ETS catalysts

Table-3.3. Electronic property of the catalysts

Catalyst	Band gap (eV)	Catalyst	Band gap (eV)
ETS-10	3.15	ETS-4	3.8
Fe-ETS-10	3.13	Fe-ETS-4	4.0/3.6
Co-ETS-10	3.12	Co-ETS-4	4.0/3.6
Ni-ETS-10	3.14	Ni-ETS-4	3.9/3.5
Cu-ETS-10	3.15	Cu-ETS-4	4.0/3.5
Ag-ETS-10	3.16	Ag-ETS-4	3.9/3.5

3.3.5. Scanning electron microscopy (SEM)

The morphology of the synthesized catalysts was studied using Scanning Electron Microscopy (Leo Series VP1430). The sample powder was supported on aluminium stubs prior to measurement.

The SEM pictures of the ETS-10 catalysts are given in **Figure-3.6**. All the catalysts are having identical morphology truncated bipyramidal that was observed in earlier studies **[39, 47]**. The longest dimension of the crystal is along 4-fold axis. The SEM image presented in **Figure-3.7** shows the crystals of the bare and transition metal exchanged ETS-4 in the form of intergrown and intertwined aggregates of plates as reported earlier **[48-49]**. All the catalysts are having identical morphology and the SEM images revealed that the bare ETS and M-ETS are indistinguishable suggesting no effect of transition metal exchange on the morphology of synthesized catalysts.

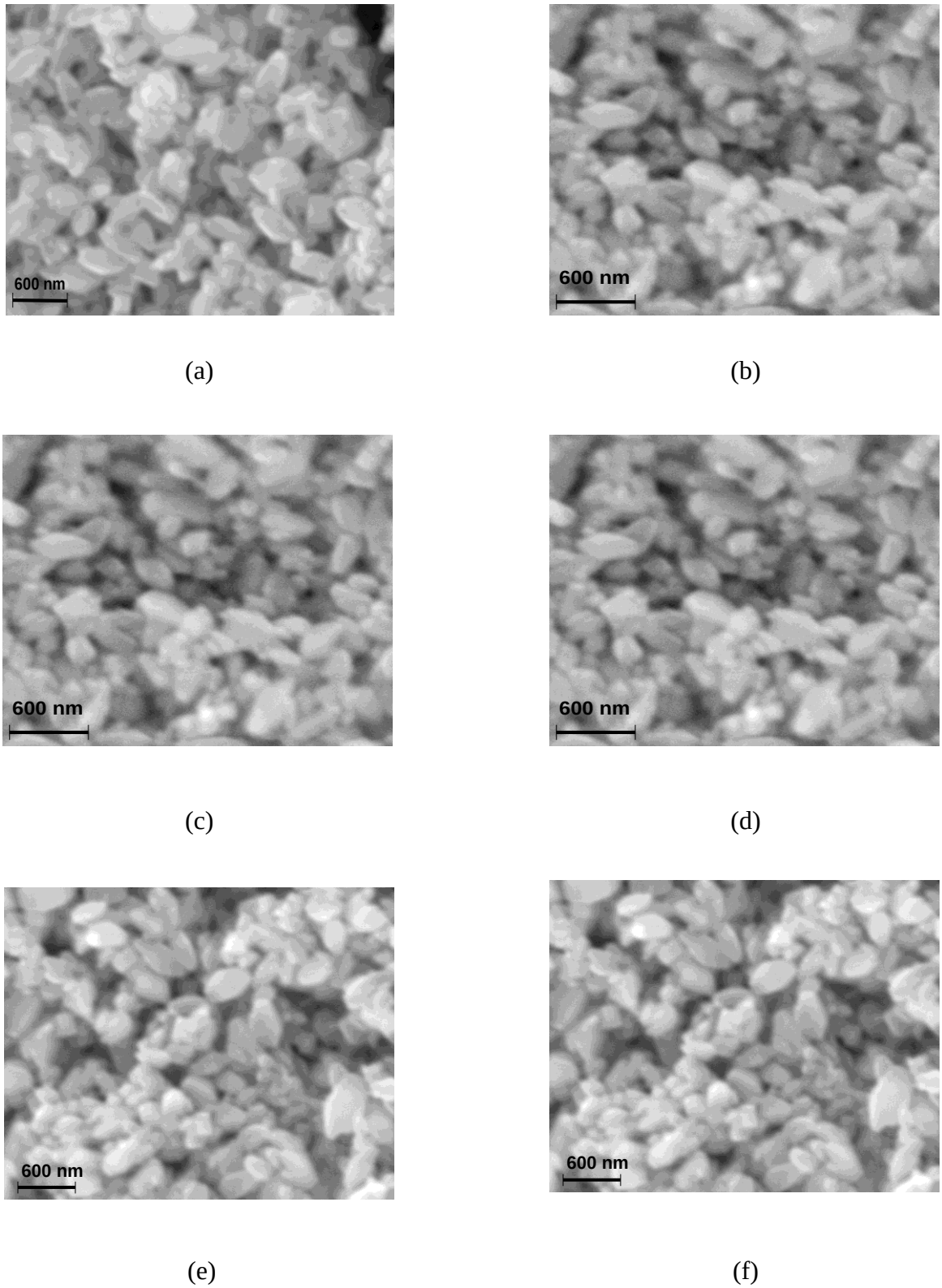

Figure-3.6. SEM images of the catalysts (a) Bare ETS-10 (b) Fe-ETS-10 (c) Co-ETS-10 (d) Ni-ETS-10 (e) Cu-ETS-10 (f) Ag-ETS-10 catalysts

(a)

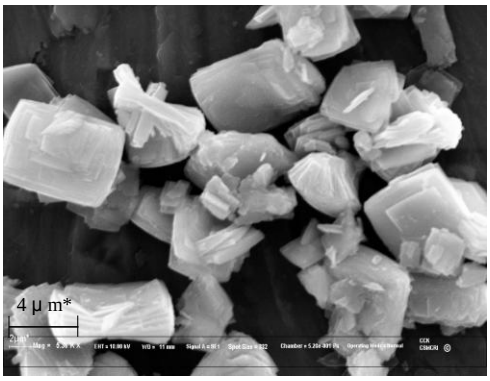

(b)

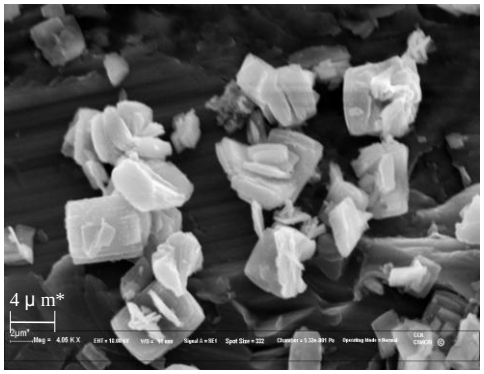

(c)

(d)

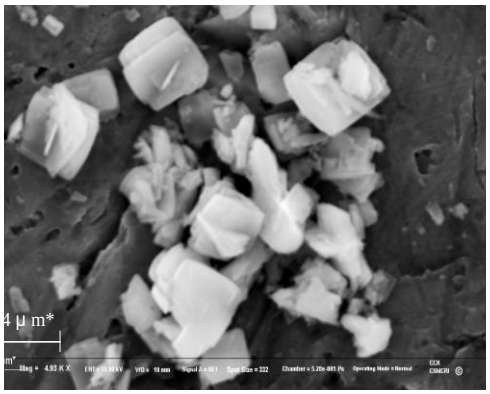

(e)

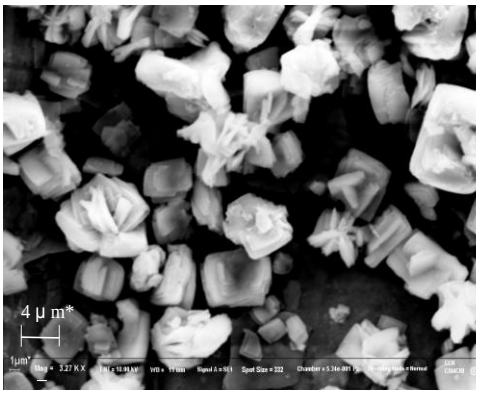

(f)

Figure-3.7. SEM images of the catalysts (a) Bare ETS-4 (b) Fe-ETS-4 (c) Co-ETS-4 (d) Ni-ETS-4 (e) Cu-ETS-4 (f) Ag-ETS-4 catalysts

3.3.6. Energy dispersive X-ray analysis (EDAX)

Scanning electron microscope (Leo series 1430 VP) equipped with INCA, Energy Dispersive System (EDX), Oxford instruments was used to confirm the presence of impregnated of metal on microporous ETS-10 and ETS-4 sample as well as to determine the morphology of catalysts.

The amount of Na, K ions and exchanged transition metal ion is given in **Table-3.4**. For the transition metal ion exchanged ETS-10, the ratio of Na and K to Ti was observed decreased after metal ion exchange. The ratio of Na to Ti was found decreased after the transition metal ion exchange for the ETS-4. This decrease confirms the metal ion exchange with Na and K ion. The EDAX analysis confirms the presence of transition metal ions in these samples as per calculations, which were vital for carrying out the photocatalytic studies. Moreover, the ICP analysis results also have good agreement with EDAX results as shown in **Table-3.4**.

Table-3.4. EDX analysis results

Catalyst	(Na+K)/Ti	% Metal (EDX)	Catalyst	Na/Ti	% Metal (EDX)
ETS-10	1.49	-	ETS-4	1.97	
Fe-ETS-10	1.30	0.53	Fe-ETS-4	1.67	0.74
Co-ETS-10	1.39	0.63	Co-ETS-4	1.93	0.50
Ni-ETS-10	1.35	0.53	Ni-ETS-4	1.72	0.52
Cu-ETS-10	1.30	0.61	Cu-ETS-4	1.62	0.63
Ag-ETS-10	1.37	0.47	Ag-ETS-4	1.60	0.47

3.3.7. Inductively coupled plasma (ICP)

An Inductively Coupled Plasma-optical emission spectrophotometer (ICP-OES, Optima 2000 DV, Perkin-Elmer, Eden Prarie, MN) was used to determine the percentage of the impregnated metal ion in the ETS materials. The values of metal ion are given in **Table-3.4**. The results have good agreement with EDAX results shown in **Table-3.4**.

Table-3.4. ICP analysis results

Catalyst	% Metal (ICP)	Catalyst	% Metal (ICP)
ETS-10	-	ETS-4	
Fe-ETS-10	0.55	Fe-ETS-4	0.68
Co-ETS-10	0.68	Co-ETS-4	0.53
Ni-ETS-10	0.59	Ni-ETS-4	0.50
Cu-ETS-10	0.65	Cu-ETS-4	0.58
Ag-ETS-10	0.41	Ag-ETS-4	0.49

3.3.8. Thermal stability analysis (TGA)

Thermogravimetry and differential thermal analysis were performed on a TGA/SDTA851^{e}, METTLER TOLEDO system in a temperature range of 50 to 700 °C with a heating rate of 5 °C min^{-1} under an air stream. The weight loss curves determined by thermal gravimetric analysis for as synthesized and transition metal exchanged ETS-4 is given in **Figure-3.8**. In the transition metal ion exchanged ETS-10 catalysts, The weight loss observed for Fe-ETS-10 was observed maximum almost 13% and for Ag-ETS-10, it was minimum almost 5%. All other samples showed weight loss almost constant value of 7-9%.

For the ETS-4 materials, the figure shows the maximum weight loss between 100-200 °C. This weight loss is attributed to loosely bound moisture present in the samples **[9, 50]**. The figure shows that Ni and Ag metal exchange leads to increase the dehydration temperature showing approximately 17 and 16 % respectively which are almost similar to bare ETS-4 (~18 % weight loss). Fe, Co and Cu lead to decrease the dehydration temperature showing the decrease in the stability by weight loss 25, 20 and 21 % respectively. The higher weight loss exhibit the more hydrated framework of the material. The more weight loss with these metals exchanged ETS-4 is because of the removal of strongly bounded water which allows the structure to begin to collapse **[50]**. This can be seen from the loss of crystallinity of these catalysts as shown in **Table-3.1**. The change in the dehydration temperature with transition metal exchange results in the stability change of ETS-4.

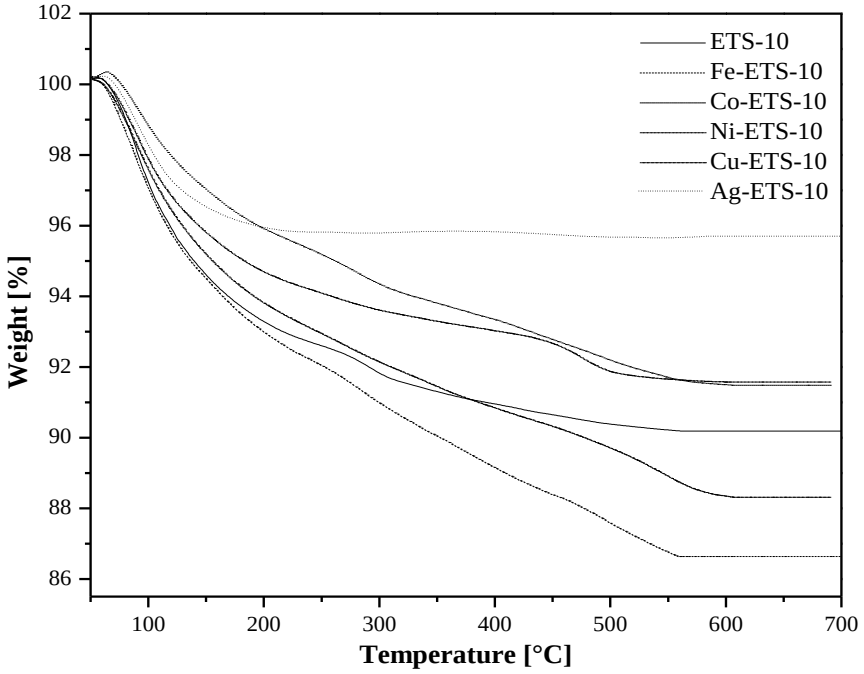

(a)

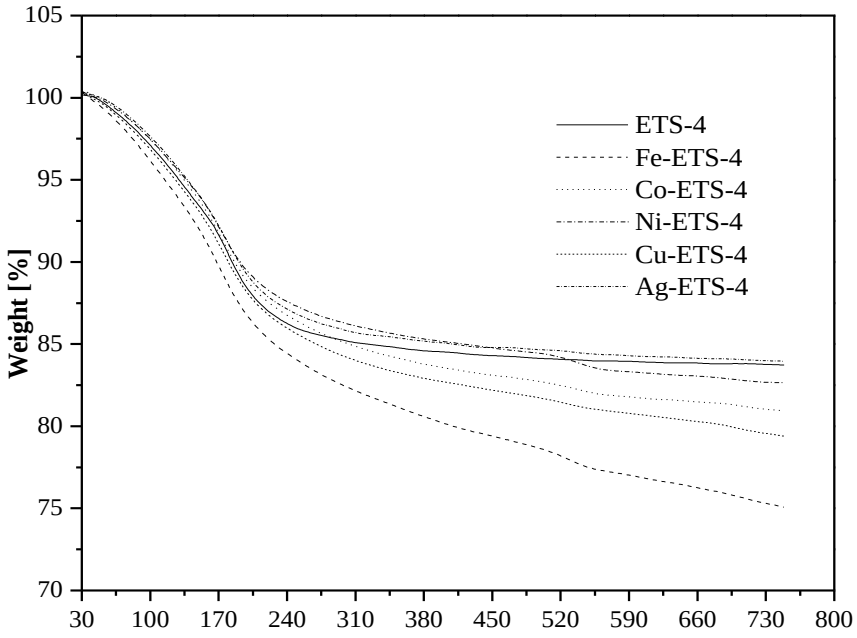

(b)

Figure-3.8. TGA pattern of (a) ETS-10 and (b) ETS-4 with metal exchanged ETS catalysts

3.4. PHOTOCATALYTIC DEGRADATION OF NITROBENZENE

3.4.1. Nitrobenzene and its properties

Aromatic nitro compounds are commonly used in industrial processes (manufacture of pesticides, dyes and explosives) and as a consequence they appear as contaminants in every kind of water (especially in surface waters) and industrial wastewaters **[51]**. The properties of nitrobenzene are shown below:

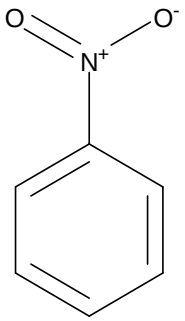

Molecular formula	$C_6H_5NO_2$
Physical state and appearance	Oily liquid
Weight [$g.mol^{-1}$]	123.11
Boiling point [°C]	210.8
Melting point [°C]	5.7
Specific gravity	1.2
Solubility in water [$mg.l^{-1}$]	Partial soluble

3.4.2. Toxicological Information

Nitrobenzene is a very toxic substance: the maximum allowable concentration for nitrobenzene is 1 ppm or 5 $mg.m^{-3}$. It is readily absorbed by contact with skin and by inhalation of vapor, and this start the conversion of hemoglobin to methemoglobin. This conversion eliminates hemoglobin from the oxygen-transport cycle. At the 15% methemoglobin level cyanosis appears. Nitrobenzene affects the central nervous system and produces fatigue, headache, vertigo, vomiting, general weakness, and in some cases unconsciousness and coma **[52]**.

3.4.3. Photocatalytic degradation procedure

The photocatalytic activities of the synthesized catalysts were determined for nitrobenzene degradation under UV irradiation using a reactor consisting two parts as mentioned in earlier chapter. The photocatalytic activity of the catalysts was evaluated by measuring the decrease in concentration of nitrobenzene in the reaction solution. The

decrease in the concentration of nitrobenzene was measured by using UV-Visible spectroscopy. The calibration curve was plotted for nitrobenzene and for the purpose the standard samples of nitrobenzene in distilled water was prepared. The concentrations of the standard samples were 5, 10, 20, 30, 40 and 50 ppm and the absorption of these samples were measured by UV-Visible spectroscopy. The calibration curves were plotted between absorption values of the samples with respect to their relevant concentrations. The slopes of the curves were calculated which were used for the calculation of nitrobenzene concentration. The calibration curve for nitrobenzene is shown in **Figure-3.9**.

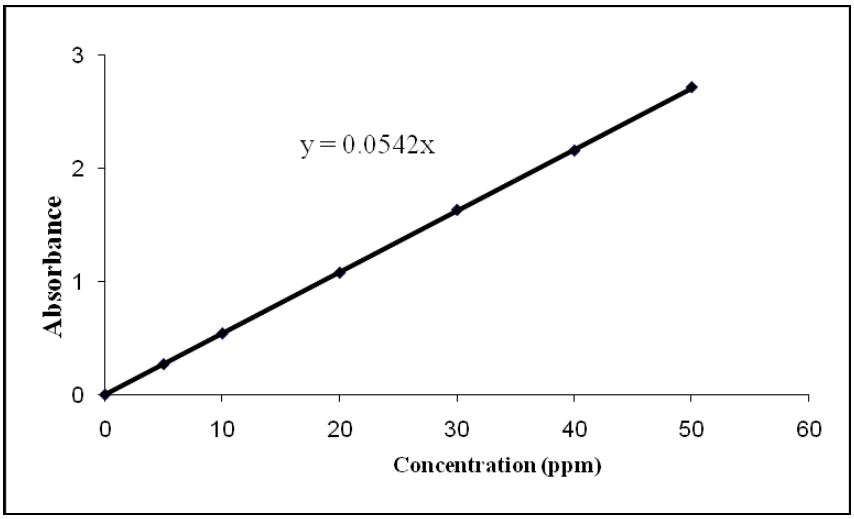

Figure-3.9. Calibration curve of nitrobenzene

Prior to commencing irradiation, a suspension containing 50 mg of the catalyst and 250 ml aqueous solution of ca. 50 ppm of nitrobenzene was stirred continuously for 30 minutes in the dark followed by the collections of the 5 ml sample and its analysis. After reaching the complete adsorption, the solution was irradiated and samples were withdrawn for analysis by syringe at interval of 10 min for first one hour and every hour thereafter for 4 h. The catalysts were separated by centrifugation from the samples prior to analysis. The absorbance was measured by a UV-Vis Spectrophotometer Cary 500 (Varian) at λ_{max} 267 nm for nitrobenzene. The 5 ml reaction mixture was withdrawn from the port by syringe at different time intervals. Photocatalytic activity was studied at pH of the initial reaction mixture and temperature was maintained at 293 K for all the reactions.

3.5. RESULTS AND DISCUSSION

3.5.1. Photocatalytic degradation of nitrobenzene

The photocatalytic degradation of aqueous nitrobenzene solution was investigated by determining the concentration of nitrobenzene after irradiation at different time intervals. The adsorption of nitrobenzene on different catalysts for first 30 minutes was determined without irradiation followed by photocatalytic degradation of nitrobenzene. **Figure-3.10** shows the spectral changes in absorption spectra of nitrobenzene in Ag-ETS-10 and Ag-ETS-4 under UV-light irradiation. The decrease at 267 nm shows the degradation of nitrobenzene, and was used as a measure of photocatalytic activity.

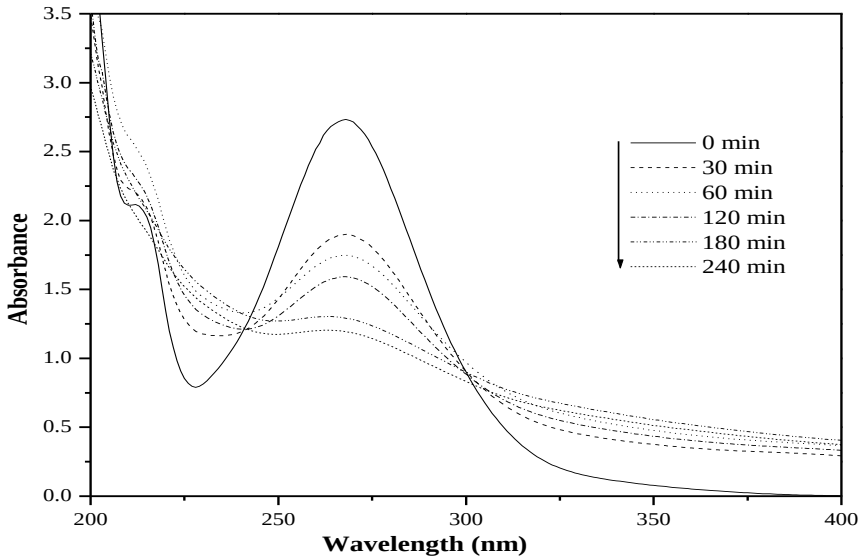

(a)

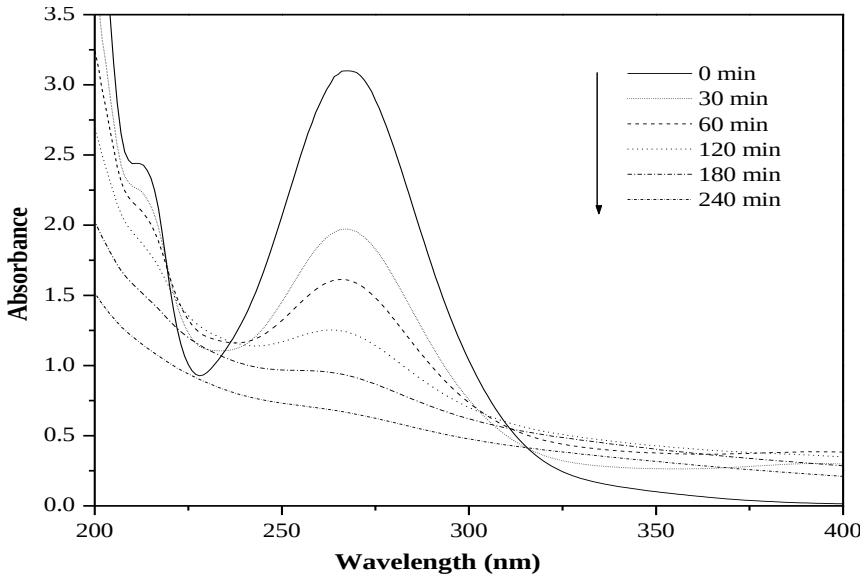

(b)

Figure-3.10. UV-Visible absorbance spectra of different reaction samples taken with (a) Ag-ETS-10 and (b) Ag-ETS-4 catalyst

The percentage degradation of nitrobenzene after 4 h reaction is shown in **Figure-3.11**. Comparison of the results from this figure shows that transition metal ion impregnated ETS-10 and ETS-4 samples exhibit more activity than pure ETS-10 and ETS-4. The percentage degradation after 4 h reaction was 33, 41, 38, 39, 47 and 57 for pure, Fe, Co, Ni, Cu and Ag metal ion exchanged ETS-10 respectively. Moreover, Ag-ETS-10 catalyst shows highest photocatalytic degradation (57 %) than bare ETS-10 (33 %) and among all other transition metal impregnated ETS-10 catalysts. The percentage degradation observed after 4 h reaction was 65, 69, 67, 68, 75 and 79 for bare, Fe, Co, Ni, Cu and Ag metal ion exchanged ETS-4 respectively. Ag-ETS-4 catalyst showed highest photocatalytic degradation (79 %) among all other transition metal impregnated ETS-4 catalysts. The photocatalytic active sites are titanols located on the external surfaces where the –O-Ti-O-Ti-O- chain emerges, exposing a surface Ti-OH titanol group **[53]**.

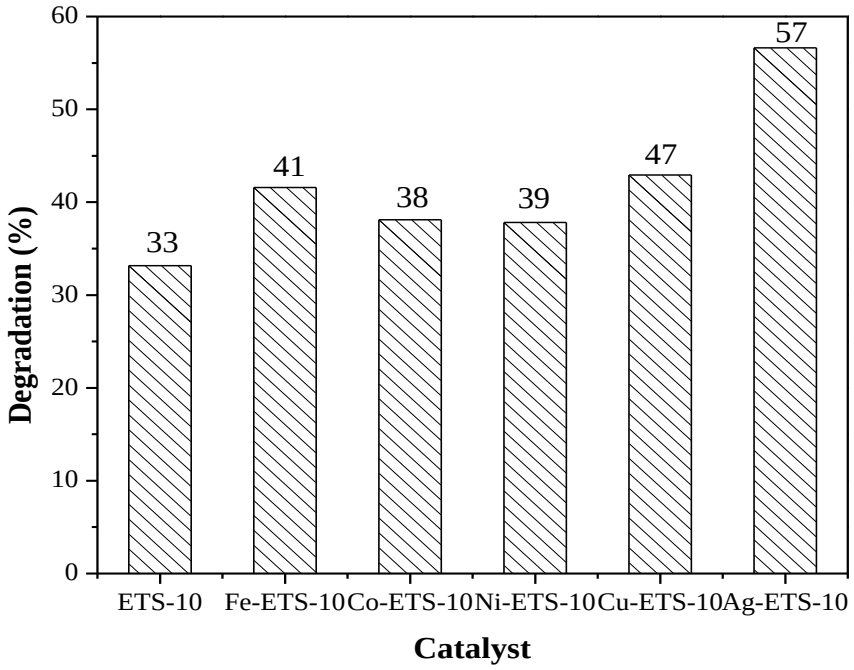

(a)

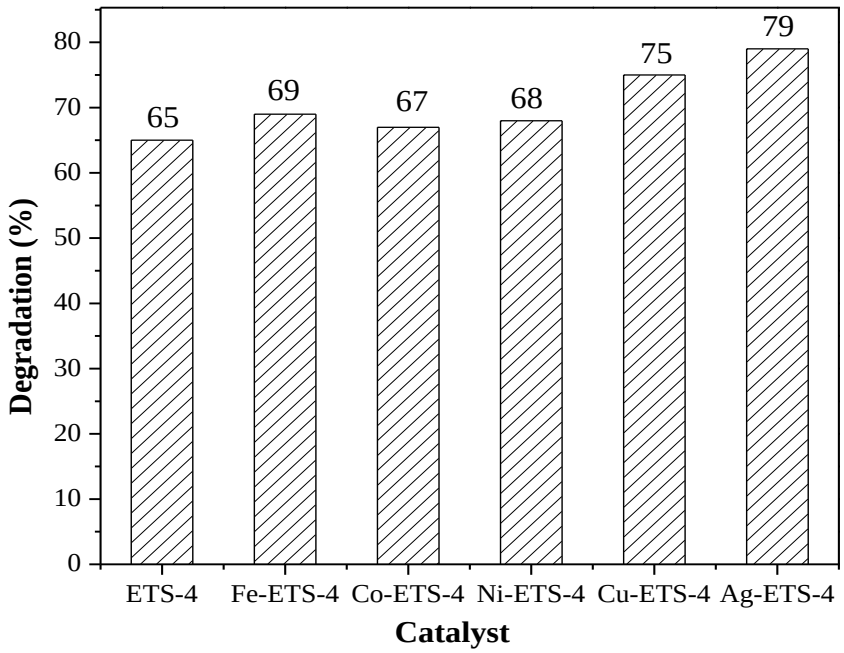

(b)

Figure-3.11. Percentage degradation of nitrobenzene after 4 h irradiation with different catalysts (a) ETS-10 and (b) ETS-4 series

3.5.2. Kinetic and mineralization study

Figure-3.12 shows the molar concentration vs. time graph and **Figure-3.13** shows the ln C_o/C_t vs. time graph.

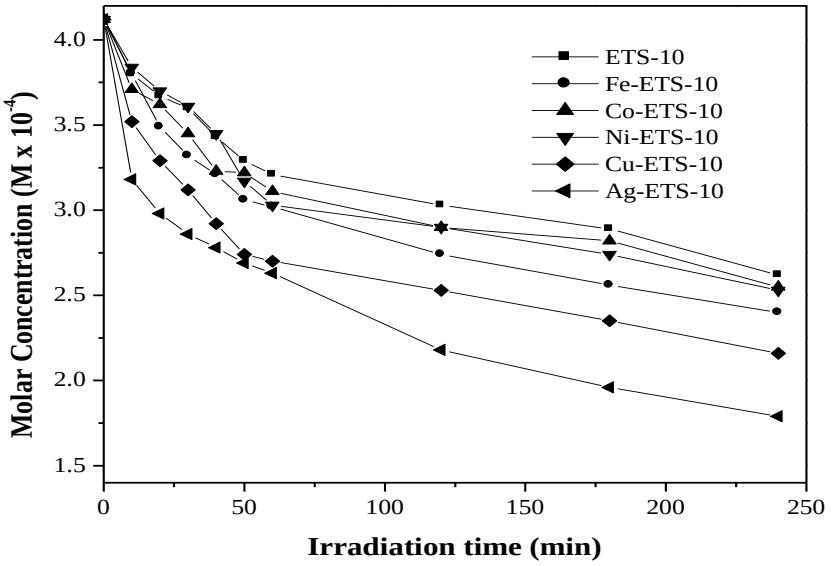

(a)

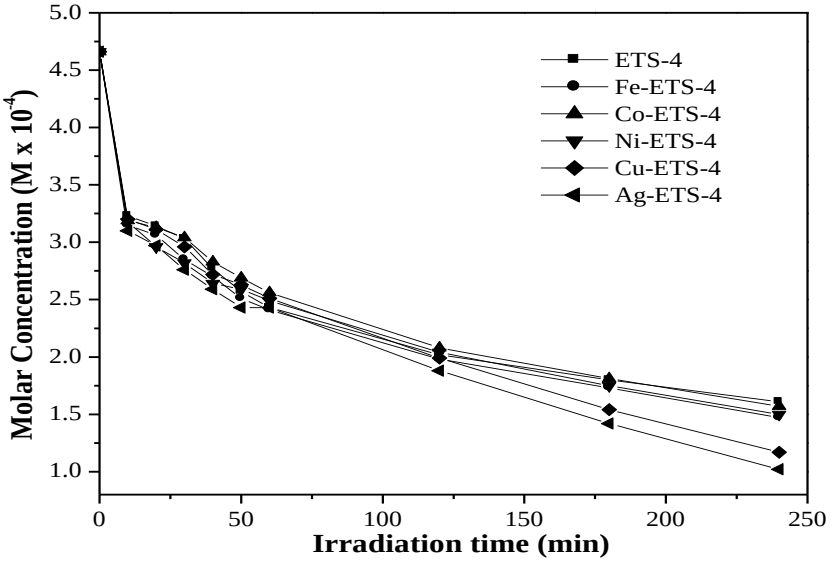

(b)

Figure-3.12. Photocatalytic disappearance of nitrobenzene using different catalysts (a) ETS-10 and (b) ETS-4 series

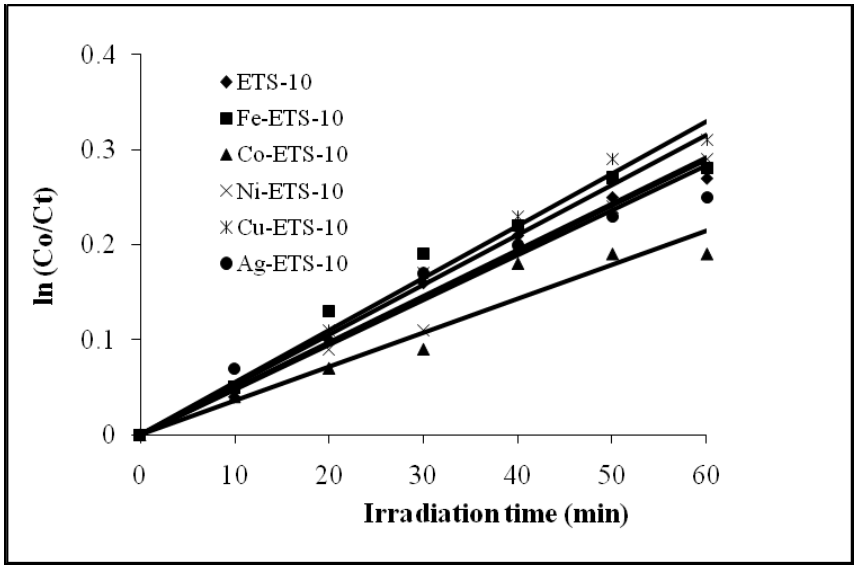

(a)

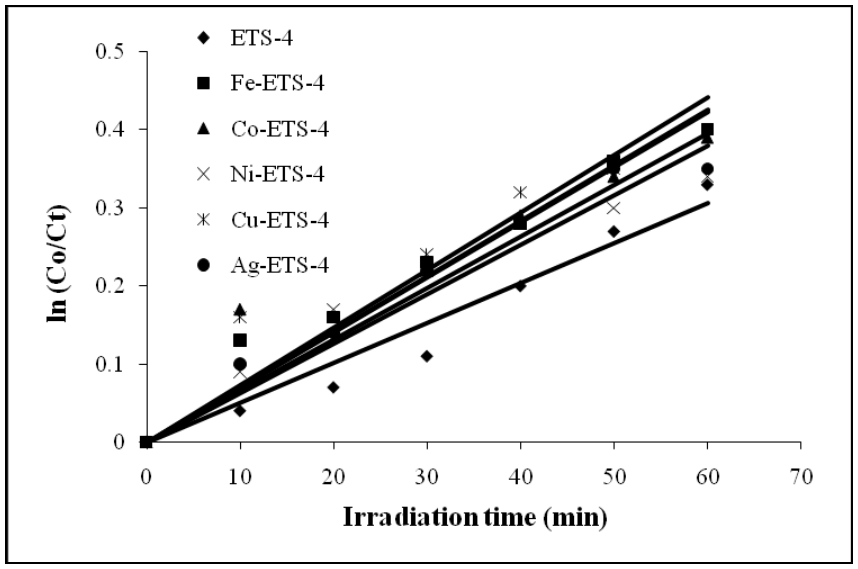

Figure-3.13. First-order kinetic plot for the synthesized catalysts (a) ETS-10 and (b) ETS-4 series

The straight line in **Figure-3.13** confirms the pseudo first order kinetics which follows the equation-

$$ln(C_o/C_t) = k_{app}t \qquad (3.2)$$

Here C_o is the initial concentration of nitrobenzene while C_t is the concentration at time'*t*'. The apparent first rate constant k_{app} was calculated by the linear regression of the slope of $ln\ C_o/C_t$ vs. time plot up to first 60 min. Thus the photocatalytic degradation process follows the Langmuir-Hinshelwood (L-H) law. The initial rates and apparent rate constants of photodegradation calculated for all catalyzed reactions are shown in **Table-3.5**. From initial rate, it can be concluded that M-ETS-10 and M-ETS-4 are better catalysts than bare ETS-10 and ETS-4 catalysts. Moreover, silver ion impregnated catalysts Ag-ETS-10 and Ag-ETS-4 are observed to be the best catalyst among all metal impregnated ETS-10 and ETS-4 catalysts.

Table-3.5 (a). Kinetic data of the performed reactions with ETS-10 catalyst series

Catalyst	Initial rate x 10^6 (mole litre^{-1}sec^{-1})	Rate constant (k x 10^3)	R^2 value	Standard redox potential E^0 (V) of metal
ETS-10	2.0	4.9	0.98	-2.71 (Na), -2.92 (K)
Fe-ETS-10	2.7	5.3	0.96	+0.33
Co-ETS-10	2.4	3.6	0.93	-0.28
Ni-ETS-10	2.3	4.8	0.97	-0.25
Cu-ETS-10	3.3	5.5	0.99	+0.68
Ag-ETS-10	3.7	4.7	0.92	+0.80

Table-3.5 (b). Kinetic data of the performed reactions with ETS-4 catalysts series

Catalyst	Initial rate x 10^6 (mole litre^{-1}sec^{-1})	Rate constant (k x 10^3)	R^2 value	Standard redox potential E^0 (V) of metal
ETS-4	4.6	5.1	0.96	-2.71 (Na)
Fe-ETS-4	5.1	7.1	0.96	+0.33
Co-ETS-4	5.3	7.0	0.86	-0.28
Ni-ETS-4	5.8	6.3	0.93	-0.25
Cu-ETS-4	4.8	7.4	0.89	+0.68
Ag-ETS-4	6.1	6.6	0.96	+0.80

The mineralization of nitrobenzene was analyzed by calculating COD values of the reaction mixture samples at different time interval (**Figure-3.14**). The COD values also confirm that silver metal impregnated ETS-10 and ETS-4 shows highest photocatalytic activity.

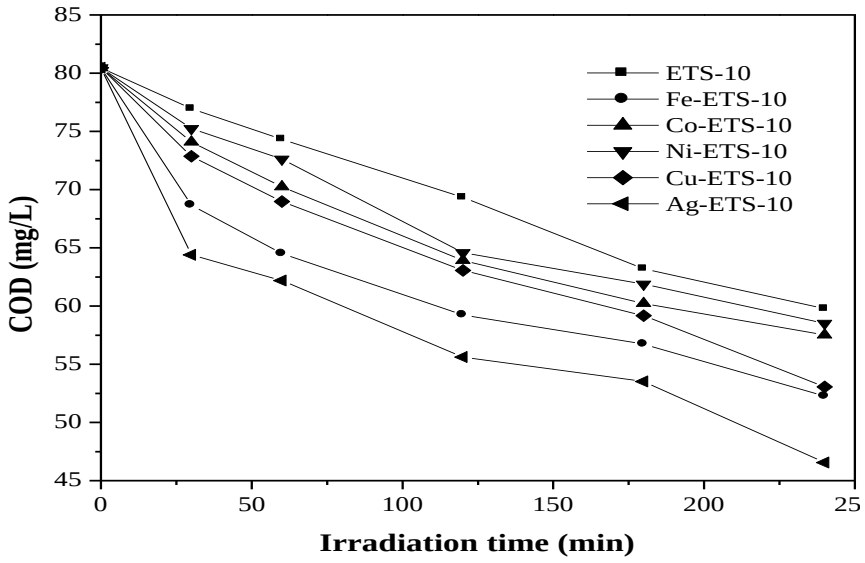

(a)

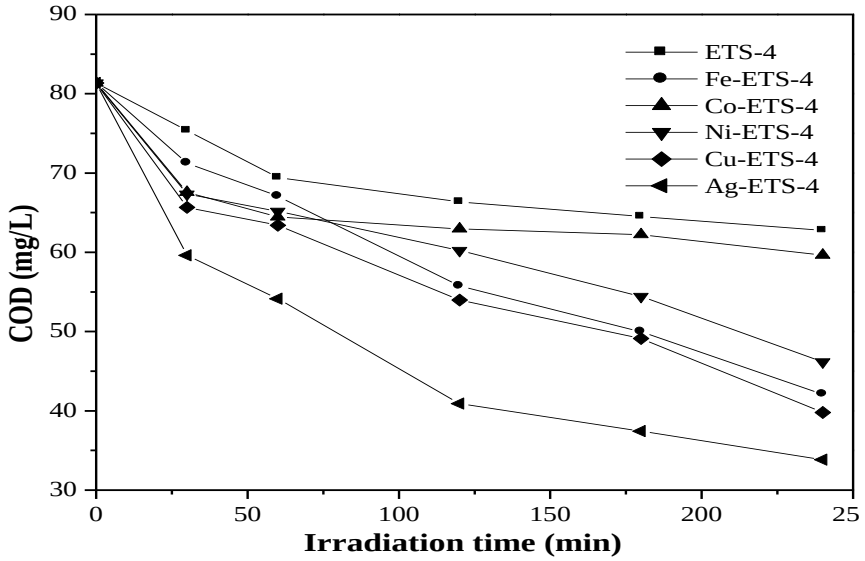

(b)

Figure-3.14. Reduction in COD value with different synthesized catalysts (a) ETS-10 and (b) ETS-4 catalysts series

Furthermore, the metal impregnated ETS-10 and ETS-4 catalysts shows higher photocatalytic activity than pure ETS-10 and ETS-4 catalyst. The transition metal incorporated in the pores of ETS-10 and ETS-4 could be reduced into M^0 by photogenerated electrons in the –O-$Ti^{(IV)}$-O- semiconductor nanowires under UV-irradiation. The reduction of transition metals by trapping photogenerated e^- over TiO_2 based photocatalysts is well known to occur and reported earlier and may also be possible for –O–$Ti^{(IV)}$–O– nanowires. Thus these transition metal acts as a sink for photogenerated electrons. This trapping of e^- by the transition metal ion minimize the e^-/h^+ recombination and assist the photocatalytic oxidation of nitrobenzene with oxidizing species free h^+ or $OH^\bullet$ radicals. The conduction band energy level of TiO_2 (E_c) is approximately –0.3 eV **[43]** and thus –O-$Ti^{(IV)}$-O- semiconductor unit of ETS is higher than that of reduction potential of transition metal as shown in **Table-3.5**. This makes thermodynamically feasible to transfer an e^- from conduction band to metallic particles. As the e^-/h^+ pair generation occurs in the semiconductor particle by the absorption of UV light, the electron in conduction band can be trapped by the exchanged transition metal particles due to their lower reduction potential. This trapping of electron makes free the oxidizing species for the photocatalytic oxidation. This above Fermi level of –O–$Ti^{(IV)}$–O– unit comparative transition metal results in the formation of Schottky barrier at metal-semiconductor contact region, which improves the charge separation and photocatalytic activity of microporous ETS-10 catalyst and ETS-4. On the other hand, Na^+ and K^+ ions in the original ETS-10 and ETS-4 cannot reduced into Na and K metal by photogenerated e^-s because the reduction potentials of these ions are much higher (**Table-3.5**), this causes the lower photocatalytic activity of ETS-10 and ETS-4 towards nitrobenzene degradation as compared to transition metal ion exchanged ETS-10 and ETS-4 catalysts.

3.6. REFERENCES

[1] Nyman, M.; Gu, B. X.; Wang, L. M.; Ewing, R. C.; Nenoff, T. M., *Micropor. Mesopor. Mater*., **2000**, *40*, 115-125.

[2] Chapman, D. M.; Roe, A. L.; *Zeolites*, **1990**, *10*, 730-737.

[3] Young, G., *U.S. Pat. No.* 3,329,481, **1967**.

[4] Kuznicki, S.M., *U. S. Pat. No*. 4,853, 202, **1989**.

[5] Kuznicki, S.M.; Thrush, A. K., *Eur Pat. No*. 0405978Al, **1990**.

[6] Jentys, A.; Catlow, C. R. A.; *Catal. Lett*., **1993**, *22*, 251-257.

[7] Howe, R. F.; Krisnandi, Y. K., *Chem. Commun*., **2001**, 1588–1589.

[8] Calza, P.; Paze, C.; Pelizzetti, E.; Zecchina, A., *Chem. Commun*., **2001**, 2130–2131.

[9] Kuznicki, S. M.; Bell, V. A.; Nair, S.; Hillhouse, H.W.; Jacubinas, R.M.; Braunbarth, C.M.; Toby, B.H.; Tsapatsis, M., Nature, **2001**, *412*, 720-724.

[10] Lamberti, C., *Micropor. Mesopor. Mater*., **1999**, *30*, 155-163.

[11] Bordiga, S.; Palomino, G. T.; Zecchina, A.; Ranghini, G.; Giamello, E. Lamberti, C., J. *Chem. Phys.*, **2000**, *112*, 3859-3867.

[12] Damin, A.; Xamena, F. X. L.; Lamberti, C.; Civalleri, B.; Zicovich-Wilson, C. M.; Zecchina, A. *J. Phys. Chem. B*, **2004**, *108*, 1328-1336.

[13] Krisnandi, Y. K.; Southon, P. D.; Adesina, A. A.; Howe, R. F. *Int. J. Photoenergy*, **2003**, *5*, 131-140.

[14] Inumaru, K.; Murashima, M.; Kasahara, T.; Yamanaka, S. *Appl. Catal., B,* **2004**, *52*, 275-280.

[15] Ghosh-Mukerji, S.; Haick, H.; Schvartzman, M.; Paz, Y. *J. Am. Chem. Soc.*, **2001**, *123*, 10776-10777.

[16] Ghosh-Mukerji, S.; Haick, H.; Paz, Y. *J. Photochem. Photobiol., A.*, **2003**, *160*, 77-85.

[17] Balmer, M. L.; Bunker, B. C.; Wang L. Q.; Penden, C. H. F.; Su, Y., *J. Phys. Chem. B.* **1997**, *101*, 9170-9179.

[18] Cruciani, G.; De Luca, P.; Nastro, A.; Pattison, P., *Micropor. Mesopor. Mater*., **1998**, *21*, 143-153.

[19] Philippou, A.; Anderson, M. W., *Zeolites*, **1996**, *16*, 98-107.

[20] Braunbarth, C.; Hillhouse, H. W.; Nair, S.; Tsapatsis, M., *Chem. Mater*., **2000**, *12*, 1857-1865.

[21] Nair, S.; Jeong, H. K.; Chandrasekaran, A.; Braunbarth, C. M.; Tsapatsis, M.; Kuznicki, S. M., *Chem. Mater*., **2001**, *13*, 4247-4254.

[22] Coutinho, D.; Losilla, J. A.; Balkus Jr. K. J., *Micropor. Mesopo. Mater*., **2006**, *90*, 229-236.

[23] Anderson M. W.; Terasaki, O.; Ohsuna, T.; Philippou, A.; Mackay, S. P.; Ferreira, A.; Rocha, J. Lidin, S. *Nature*, **1994**, *367*, 347-351.

[24] Wang, W.; Jacobson, A. J. *Chem. Chommun*., **1999**, 973-974.

[25] Anderson, M. W.; Terasaki, O.; Oshuna, T.; O'Malley, P. J.; Philippou, A.; Mackay, S. P.; Ferreira, A.; Rocha, J.; Lidin, S. *Philos. Mag. B*, **1995**, *71*, 813-841.

[26] Al-Attar, L.; Dyer, A.; Harjula, R. *J. Mater. Chem*., **2003**, *13*, 2963-2974.

[27] Zhao, G. S.; Lee, J. L.; Chia, P. A. *Langmuir*, **2003**, *19*, 1977-1979.

[28] Gervasini, A.; Picciau, C.; Auroux, A. *Micropo. Mesopor. Mater*., **2000**, *35-36*, 457-469.

[29] Anpo, M.; Nakaya, H.; Kodama, S. Kubokawal, Y.; Domen, K.; Onishi, T., *J. Phys. Chem*., **1986**, *90*, 1633-1636.

[30] Sato, S., Langmuir, **1988**, *4*, 1156-1159.

[31] Yoneyama, H.; Hag, S.; Yamanaka, S., *J. Phys. Chem*., **1989**, *93*, 4833-4837.

[32] Kim, Y. I.; Keller, S. W.; Krueger, J.S.; Yonemoto, E. H.; Saupe, G. B.; Mallouk, T. E., *J. Phys. Chem. B*., **1997**, *101*, 2491-2500.

[33] Tayade, R. J.; Kulkarni, R. G.; Jasra, R. V., *Ind. Eng. Chem. Res*., **2006**, *45*, 5231-5238.

[34] Xu, Y.; Menassa, P. C.; Langford, C. H., Chemosphere, **1988**, *17*, 1971-1976.

[35] Mattews, R. W., Solar *energy*, **1987**, *38*, 405-413.

[36] Vinogopal, K.; Hotchandani, S.; Kamat, P. V., J. *Phys. Chem*., **1993**, *97*, 9040-9044.

[37] Litter, M. I., *Appl. Catal., B*: *Environ.*, **1999**, *23*, 89-114.

[38] Brezova, V.; Blazkova, A.; Karpinsky, L.; Groskova, J.; Havlinova, B.; Jorik, V.; Ceppan, M., *J. Photochem. Photobiol., A: Chem.*, **1997**, *109*, 177-183.

[39] Yang, X.; Paillaud, J. –L.; Breukelen, H. F. W. J. V.; Kessler, H.; Duprey, E., *Micropor. Mesopor. Mater.*, **2001**, *46*, 1-11.

[40] Naderi, M.; Anderson, M. W., *Zeolites*, **1996**, *17*, 437-443.

[41] Usseglio, S.; Calza, P.; Damin, A.; Minero, C.; Bordiga, S.; Lamberty, C.; Pelizzetti, E.; Zecchina, A., *Chem. Mater.*, **2006**, *18*, 3412-3424.

[42] Kitiyanan A.; Yoshikawa S., *Materials Letters***, 2005,** *59*, 4038 – 4040.

[43] Krishnanandi, Y. K.; Howe, R. F., *Appl. Catal. A: General.*, **2006**, *307*, 62-69.

[44] Tiscornia, I.; Irusta, S.; Pradanos, P.; Tellez, C.; Coronas, J.; Santamaria, J., *J. Phys. Chem.:C.*, **2007**, *111*, 4702-4709.

[45] Guan, G.; Kida, T.; Kusakabe, K.; Kimura, K.; Fang, X.; Ma, T.; Abe, E.; Yoshida, A., *Chemical Physics Letters.*, **2004**, *385*, 319-322.

[46] Guan, G.; Kida, T.; Kusakabe, K.; Kimura, K.; Abe, E.; Yoshida, A., *Inorg. Chem. Communi.*, **2004**, *7*, 618-620.

[47] Damin, A.; Llabres i Xamena, F. X.; Lamberti, C.; Civalleri, B.; Zicovich-Wilson, C. M.; Zecchina, A., J. Phys. Chem. B., **2004**, *108(4)*; 1328-1336.

[48] Zubkova, N. V.; Pushcharovsky. D. Yu.; Giester, G.; Pekov, I. V.; Turchkova, A. G.; Chukanov, N. V.; Tillmanns E., *Crystallography Reports*, **2005**, *50*, 367-373.

[49] Kim, W. J.; Lee, M. C.; Yoo, J. C.; Hayhurst, D. T., *Micropor. Mesopor. Mater.*, **1999**, *41*, 79-88.

[50] Marathe, R. P.; Mantri, K.; Srinivasan, M. P.; Farooq, S., *Ind. Eng. Chem. Res.*, **2004**, *43*, 5281-5290.

[51] http://msds.chem.ox.ac.uk

[52] http://sciencelab.com

[53] Kitiyanan A.; Yoshikawa S., *Materials Letters*, **2005,** *59*, 4038 – 4040.

Chapter 4

Photocatalytic Removal of *o*-Tolidine over Nano-TiO_2

4.1. INTRODUCTION

The heterogeneous photocatalysis using semiconductor has been reported to promote the degradation and total mineralization for a wide range of pollutants both from water and air **[1-5]**. Titanium dioxide has emerged as an excellent material for the photocatalytic degradation of toxic compounds. Titanium dioxide has three kinds of phase structures, i.e., anatase, rutile and brookite and the photocatalytic activity of TiO_2 is phase dependent. The anatase phase is metastable but shows higher photocatalytic activity due to a low recombination rate of photo-generated electrons and holes. On the contrary, the thermodynamically most stable rutile phase is least active or not active at all **[6-7]**. Many studies **[8-13]** have reported that the surface properties such as porous structures, specific surface area, crystallinity, surface state and porosity obviously influence the photocatalytic activity of TiO_2. However, the estimation of exact contribution of each factor for the enhancement of photocatalytic activity is very difficult. For example, specific surface area and crystallinity usually appear to be two conflicting intrinsic properties for TiO_2 nanoparticles **[7]**. Nonetheless, the anatase TiO_2 powders with high BET specific surface areas, good crystallization and relative small crystallite size are desirable to improve the photocatalytic activity by creating more reactive sites on the surface of photocatalyst. Among various techniques available for the fabrication of TiO_2 nanoparticles, the sol-gel technique has been widely used due to its low cost equipment required, low temperatures and the homogeneous and high purity products produced. However, very high temperature (400 to 600^oC) is required for the crystallization of TiO_2. The high temperature leads to shrinkage or collapse of the mesostructure and is eventually followed by the increase in nanoparticle size and the decrease in specific surface area **[14-16]**. To prepare highly photoactive nanocrystalline TiO_2 powders, a reasonable route would be to reduce the temperature of the phase transformation of amorphous to anatase **[13, 17-18]**.

There are many studies dealing with photocatalytic degradation of organic pollutants from different class of compounds **[19-24]**. Most of these studies include a detailed examination of the primary processes of degradation, but provide little information on the reaction mechanism involved in the degradation and identification of major transient

intermediates. Also, the literature on the photocatalytic degradation of nitrogen containing-aromatic compounds is sparse **[25-27]**. The aromatics containing nitro and amino groups are toxic in nature **[28-30]** and act as inhibitor for the biodegradation of other compounds of waste **[31-34]**. These pollutants enter in the environmental during their manufacturing processes, their use as chemical intermediates in chemical processes. The aromatic amines could cause cyanosis and increased respiratory rate from methamoglobinamia **[35]**. Regardless of exposure route or length, all aromatic amines affect the blood as the primary target organ and needs to be stringently controlled.

4.1.1. Effect of TiO_2 synthesis method on the photocatalytic activity

In all the applications, the morphology, average particle size and size distribution, phase composition and porosity of titania powders are important factors to be controlled. Nanoparticles show a great tendency to aggregate due to high surface energy combined with their high surface area to volume ratio. This aggregation tendency impedes their use in a variety of applications. For these reasons, the synthesis of ultrafine particles with controlled size and surface chemistry is of technological interest. The different synthesis methods are responsible for different characteristics mentioned above. Thus the photocatalytic efficiency depends on the preparation method of the catalyst **[36]** that can influence significantly the composition and the size of the crystals and the surface distribution of hydroxyl groups **[37–39]**. Sol-gel method is a simple and versatile process for the synthesis of nanocrystalline materials. The solution combustion method is a single-step process and has been reported that this method give fine particles/large surface area oxide materials such as alumina, ceria, titania, and zirconia. Micelles and inverse micelles are commonly employed to synthesize TiO_2 nanomaterials **[40-42]**.

4.1.2. Aim of the present study

In the present study, the titania samples were synthesized using different synthesis processes **[40-42]** for the degradation of 3,3´-dimethylbiphenyl-4,4´-diamine (*o*-tolidine). The textural and electronic properties of catalysts were compared using different techniques. Their photocatalytic performance has been compared with commercial Degussa P25 sample. An attempt was made to correlate structural properties of titanium

dioxide to their photocatalytic activity. The mineralization achieved during the reaction, was determined by Total Organic Carbon Analyser (TOC). Electrospray ionization mass spectrometry (ESI–MS) **[43-44]** technique was used to identify possible major intermediates and photodegradation products and a possible reaction pathway for mineralization has been suggested.

4.2. SYNTHESIS OF TiO_2 SEMICONDUCTOR PHOTOCATALYST

4.2.1. Chemicals and Materials

Titanium dioxide (P25) was purchased from Degussa Corporation (Degussa AG, Frankfurt, Germany). Titanium (IV) tetraisopropoxide (97%) and glycine were procured from Sigma Aldrich India. *o*-tolidine (OT), *n*-hexanol and cyclohexane AR grade, were purchased from E. Merk, India. Deionised distilled water was used to make up the reaction mixture.

4.2.2. Catalysts preparation

4.2.2.1. *Sol-gel synthesis*

The TiO_2 was synthesized by sol-gel **[38]**, solution combustion **[41]** and microemulsion mediated hydrothermal synthesis **[42]**. For sol-gel synthesis procedure, the titanium (IV) tetraisopropoxide was taken with appropriate amount of dry ethanol in 500 ml round bottom flask. This mixture was stirred for 30 min (ca. 950 rpm) and then hydrolyzed by controlled drop by drop addition of water (1.5 mL min^{-1}). The resulting slurry was peptized for 12 h. The solvent was slowly removed by using rotavapor (*Buchi Rotavapor R-205*) at 343 K. Thus obtained sample was further calcined at 723 K for 4 h with heating rate of 5 °C min^{-1}. The reactant composition was 38 mL of titanium (IV) tetraisopropoxide, 120 mL of dry ethanol and 160 mL of water. This catalyst prepared was termed as SG.

4.2.2.2. *Solution combustion synthesis*

In solution combustion synthesis, a Pyrex dish (300 cm^3) containing an aqueous redox mixture of stoichiometric amounts of titanylnitrate (2.5 g), glycine (1.11 g) in 20 mL of distilled water was introduced into a muffle furnace preheated to 623 K. Titanylnitrate was obtained by adding concentrated HNO_3 in to titanium hydroxide, which, in turn, was made by sol-gel method, with stirring and reprecipitated by adding acetone. Inside the furnace, the solution initially undergoes dehydration and a spark appears at one corner which spreads throughout the mass, yielding predominant anatase titania. The glycine acts as a fuel to generate the spark. Thus obtained catalyst was further calcined under similar conditions as mentioned for sol-gel method. The catalyst thus obtained was termed as SC.

4.2.2.3. *Microemulsion synthesis*

For preparing microemulsion system, Triton X-100 was used as the surfactant, with *n*-hexanol as co-surfactant and cyclohexane as the continuous oil phase; the solution of tetrabutyl titanate dissolved in acid was employed as the dispersed aqueous phase. The transparent microemulsion was prepared by dispersing the aqueous phase (mixture of 5.4 ml tetrabutyl titanate and 6 ml of 5M HNO_3) in to the Triton X-100:n-hexanol: cyclohexane mixture of v/v ratio 5:3:8 with stirring. The stirring was continued for half an hour. The transparent feedstock was charged into a 75 ml Teflon-lined stainless autoclave, and the hydrothermal reaction was conducted at 120 ^oC in an oven for 12 h. The autoclave was cooled to room temperature and the nanocrystalline TiO_2 formed was separated by filtration followed by washing with ethanol and distilled water to remove the oil and surfactant, respectively. The catalyst was dried in air followed by calcination at 723 K at same heating rate applied in sol-gel and solution combustion method for 4 h. Thus obtained catalyst was termed as HT.

4.3. CHARACTERIZATION OF PREPARED PHOTOCATALYSTS

4.3.1. X-ray diffraction (XRD)

Powder X-ray diffraction patterns were recorded using CuKα1 (λ = 0.15405 nm) radiation at 295 K with *Phillips X'pert MPD system*. Diffraction patterns were taken over 2θ range of 10°- 70° at the scan speed of 0.1°sec^{-1}. The phase content of a sample can be calculated from the integrated intensities of anatase (101), rutile (110), and brookite (121) peaks using the following equations **[45]**.

$$W_A = \frac{K_A A_A}{K_A A_A + A_R + K_B A_B} \quad (4.1)$$

$$W_R = \frac{A_R}{K_A A_A + A_R + K_B A_B} \quad (4.2)$$

$$W_B = \frac{K_B A_B}{K_A A_A + A_R + K_B A_B} \quad (4.3)$$

Where W_A, W_R and W_B represent the mass fractions of anatase, rutile and brookite phases respectively. A_A, A_R and A_B are the integrated intensity of the anatase (101), rutile (110) and brookite (121) peaks respectively, and K_A and K_B are two coefficients and their values are 0.886 and 2.721, respectively.

The crystallite size of Degussa P25 and prepared catalyst were determined from the characteristic peak of 2θ=25.3 (101) for the anatase phase using the Scherrer formula, with a shape **[46]** factor (*K*) of 0.9:

$$Crystallite\ size = K\lambda / W Cos\theta \quad (4.4)$$

Where $W = W_b - Ws$, W_b is the broadened profile width of experimental sample. *W*s is the standard profile width of reference silicon sample, λ is the wavelength of X-ray radiation. The crystallinity of the catalysts was calculated with reference to P25 Degussa by taking the average of 5 major anatase peaks of the catalyst (2θ= 25.3, 37.7, 47.9, 53.9 and 55.2).

The X-ray diffraction patterns of TiO_2 catalysts are shown in **Figure-4.1**. The maximum intense peak at 2θ = 25.3 assigned to anatase structure, and those at 27.4 to the rutile of 101 and 110 plane respectively. The structural properties of the catalysts are reported in

Table-4.1. All the laboratory synthesized catalysts has observed small crystallite size compared to Degussa P25. As seen in **Table-4.1**, the smallest crystallites are obtained from catalyst prepared by solution combustion method. Crystallinity of all the synthesized catalysts is less than that of Degussa sample and it was observed lowest for HT catalysts. The XRD pattern confirms the highest 83 % anatase phase of the catalyst SG while the catalyst HT has minimum 50 % anatase phase content.

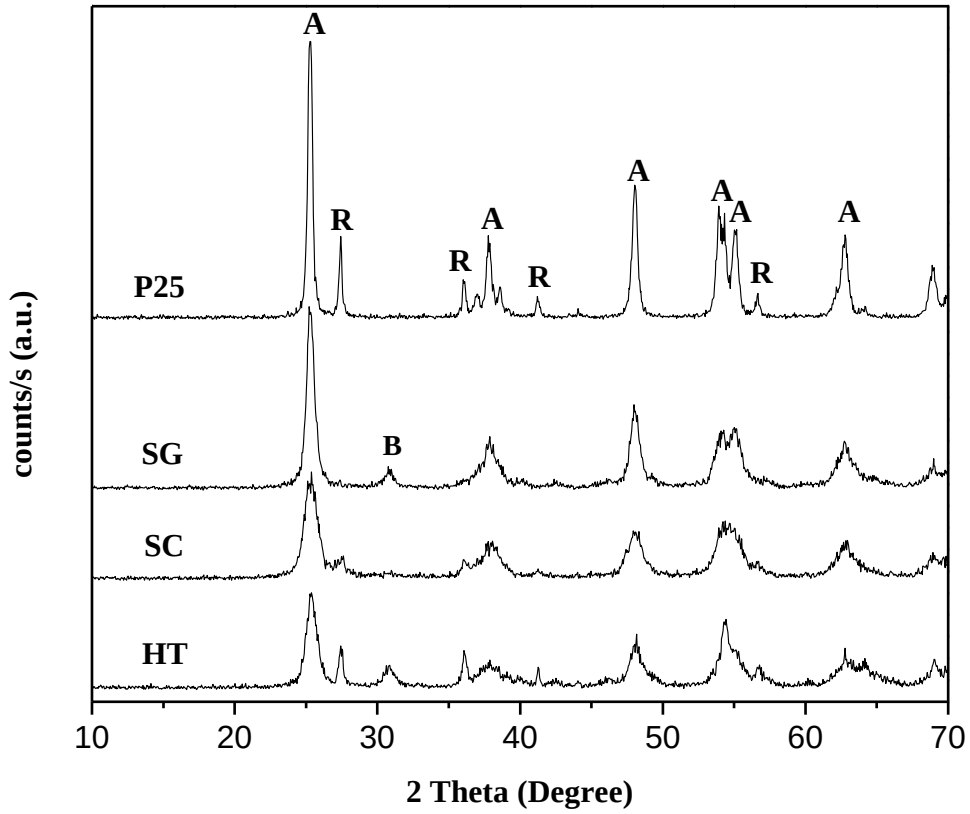

Figure-4.1. X-ray diffraction pattern for nanocrystalline titania catalysts (A = Anatase; R = Rutile; B = Brookite)

Table-4.1. Textural properties of synthesized and Degussa P25 TiO_2 catalysts by X-ray diffraction

Catalyst	Anatase[#] (%)	Rutile[#] (%)	Brookite[#] (%)	Average crystallite size[$] (nm)	Crystallinity[*] (%)
P25	80	20	0	25	100
SG	83	–	17	13	51
SC	82	18	0	08	40
HT	50	21	29	11	33

[*] Percentage Crystallinity was calculated by taking Degussa P25 as 100 % crystalline standard

[#] Percentage anatase, rutile and brookite were calculated by using their relative peak intensity at 2θ values 25.3, 27.4 and 30.8 respectively

[$] Calculated for anatase phase

4.3.2. Infra red spectroscopic measurement (FT-IR)

FT–IR spectroscopic analysis was carried out on a *Perkin-Elmer GX spectrophotometer*. The spectra were recorded in the range of 400–4000 cm^{-1} with a resolution of 4 cm^{-1} as KBr pellets. The FT–IR transmission spectra of catalysts produced under different synthesis conditions are shown in **Figure-4.2**. The spectra show the band at 400–600 cm^{-1} **[47-48]** including the stretching vibrations of Ti–O bonds at 550–653 cm^{-1} and Ti–O–Ti bonds at 436–495 cm^{-1}. Broad IR band at 3400–3437 cm^{-1} range is due to stretching of –OH groups and band at 1020 cm^{-1} which was observed in P25 and in SG is attributed to the Ti–OH deformation vibrations. All catalysts has IR band at 1622–1630 cm^{-1} range attributed to deformation vibrations of adsorbed water molecules. Intense band at 1020 cm^{-1} in P25 indicates the presence of higher amount of surface hydroxyl groups than in

other synthesized TiO_2 catalysts. The difference in the amount of hydroxyl groups may be due to the synthetic route used for the synthesis of nanocrystalline TiO_2.

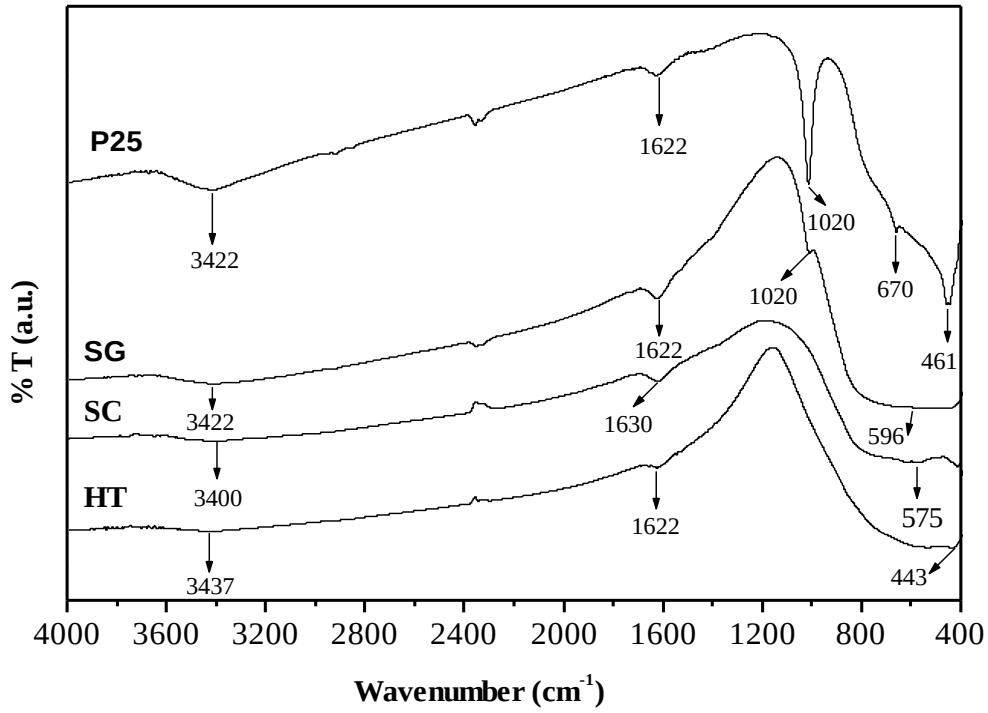

Figure-4.2. FT-IR spectra of nanocrystalline titania catalysts

4.3.3. Surface area measurement (N_2 adsorption)

The specific surface area, pore volume and pore size distribution of the calcined samples were determined from N_2 adsorption-desorption isotherms at 77.4 K using volumetric equation adsorption equipment (ASAP 2010, Micrometrics, USA), using BET and BJH models **[49]**. The specific surface area and average pore diameter has reported in **Table-4.2** show that the surface area of Degussa P25 which has highest crystallites size (25 nm) showed lowest surface area (54 m^2/g) and the catalyst prepared by solution combustion method having smallest size crystallites size (8 nm) has higher specific surface area (95 m^2/g).

Table-4.2. BET surface area and Pore diameter of synthesized and Degussa P25 TiO_2 catalysts

Catalyst	BET Surface area (m^2/g)	Pore diameter (nm)
P25	54	6, 12
SG	80	8
SC	95	5
HT	78	4

N_2 sorption isotherms for all catalysts are shown in **Figure-4.3**. The laboratory synthesized SG, SC and HT catalysts have shown type IV with a hysteresis typically observed for mesoporous solids. The BJH desorption pore size distribution determined from desorption branch of the isotherm as shown in **Figure-4.4 (a)**. Two types of mesopores are observed in P25 and hysteresis shown by P25 is slightly different from other synthesized catalysts. The values of pore diameter are given in **Table-4.2**.

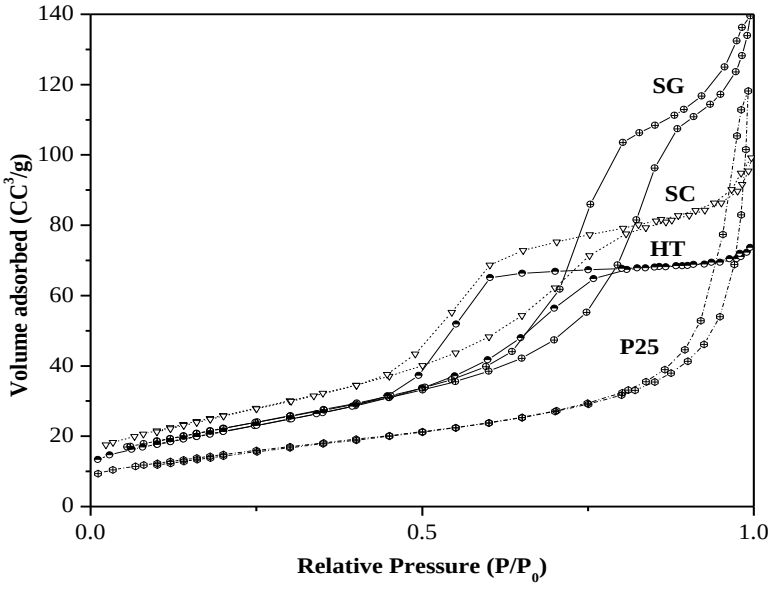

Figure-4.3. N_2 adsorption/desorption isotherm of the nanocrystalline TiO_2 catalysts

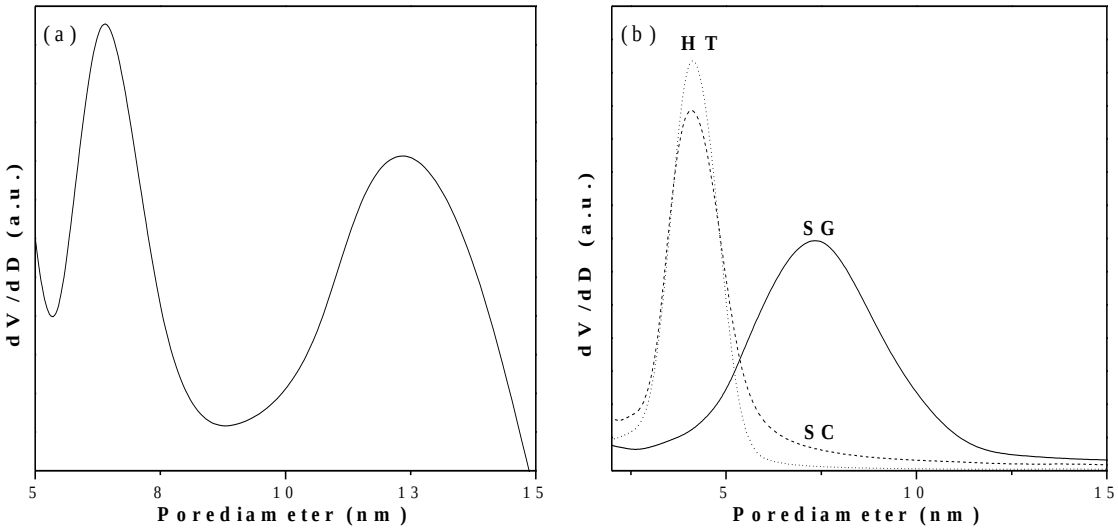

Figure-4.4. BJH pore size distribution plot of (a) Degussa P25 (b) SG, SC and HT TiO_2 catalysts

4.3.4. Diffuse reflectance spectra (DRS)

The Diffuse Reflectance Spectroscopy (DRS) was used to determine the band gap energy of the catalysts. The spectra were taken at room temperature in the range of 250-650 nm by *Shimadzu UV-3101PC* spectrophotometer. The spectrophotometer was equipped with an integrity sphere **[50-51]** and $BaSO_4$ was used as a reference. Band gap (EG) = hc/λ was calculated from the minimum of the DRS spectra shown in **Figure-4.5 (b) [51]**.

DR spectra of the catalysts are shown in **Figure-4.5 (a)**. Estimated band gap values were obtained from the minima in the differential of DR spectra shown in **Figure-4.5 (b)**. The band gap values of all nanocrystalline TiO_2 are in the range of 3.0 to 3.2 eV (**Table-4.3**). The difference in crystallite size and band gap was attributed due to the synthetic route used to prepare the catalysts.

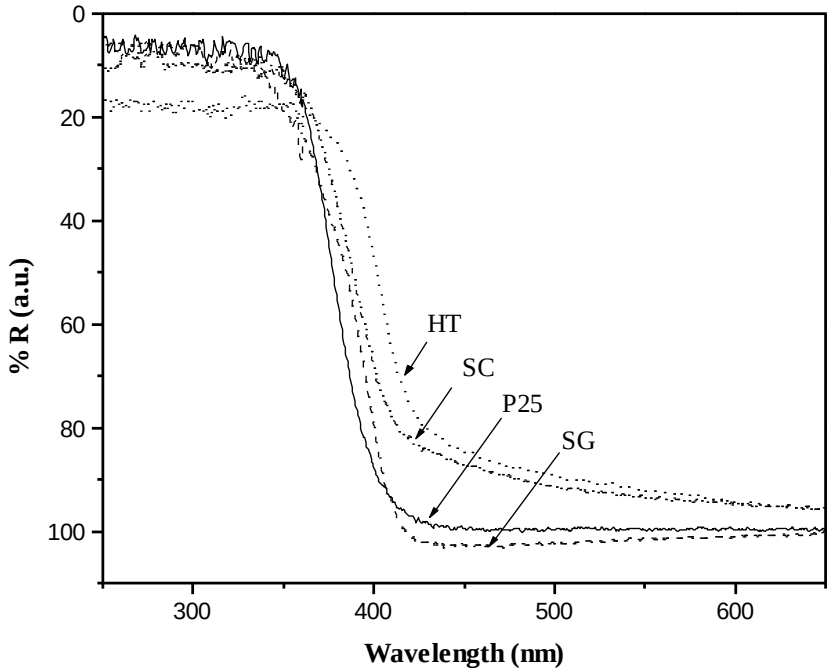

(a)

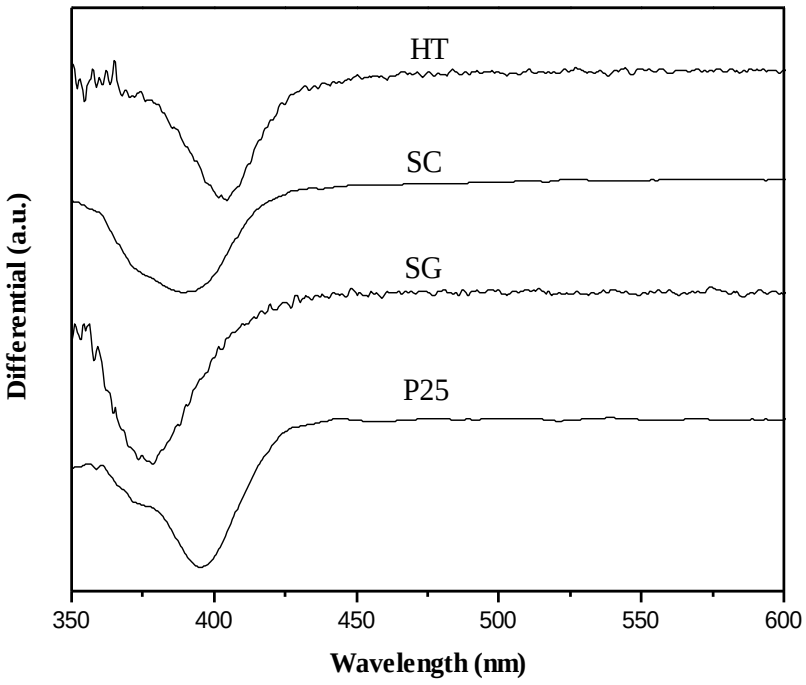

(b)

Figure-4.5. DRS spectra of nanocrystalline titania catalysts (a), and Differential spectra of DRS (b)

Table-4.3. Band gap values of the synthesized and Degussa P25 TiO_2 catalysts

Catalyst	Band gap, E_g (eV)	Catalyst	Band gap, E_g (eV)
P25	3.1	SC	3.1
SG	3.2	HT	3.0

4.3.5. Scanning electron microscopy (SEM)

Figure-4.6 shows the SEM images of all four catalysts. It is evident from the SEM images that synthesized catalysts are spherical particles in morphology in case of SC and SG while in case of HT there was no regular shape obtained. The reason for the irregularity in the shape of HT may because of its highly amorphous nature. The spherical shape of the catalysts provides more surface area of the active sites to carry out the reaction.

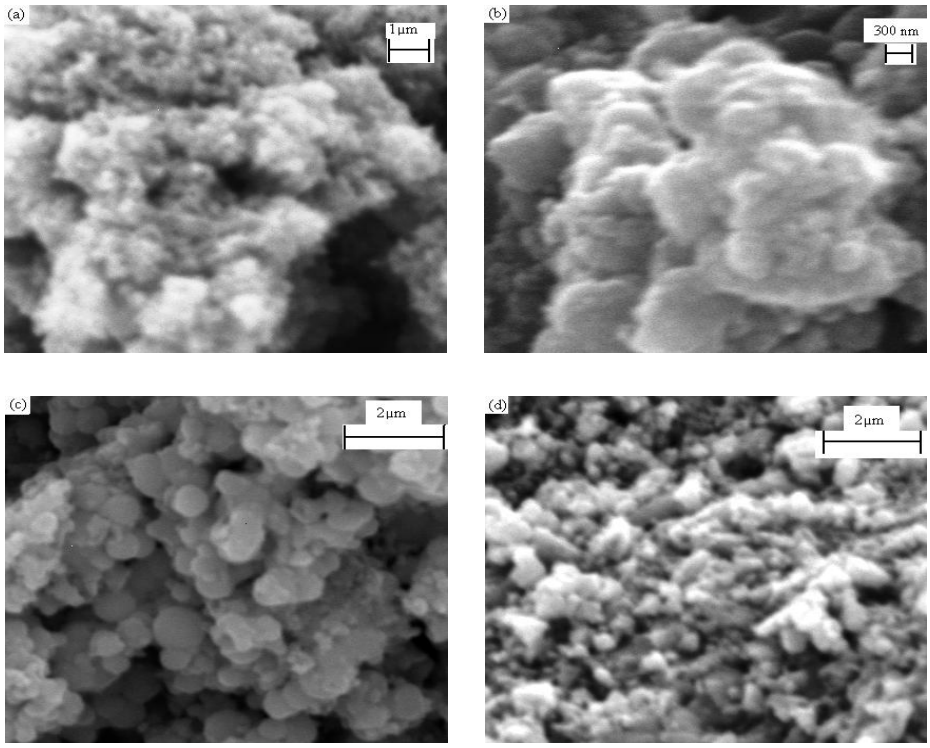

Figure-4.6. SEM images of (a) P25, (b) SG, (c) SC and (d) HT catalysts

4.4. PHOTOCATALYTIC DEGRADATION OF *o*-TOLIDINE

4.4.1. *o*-Tolidine and its properties

This is a nitro-aromatic compound having two benzene ring connected at para position. This can be formed in the manufacture of pesticides, dyes and explosives, and are often detected in industrial effluents, in ambient freshwater, in ambient environments and in the atmosphere. **[52]**. Physical properties are given below:

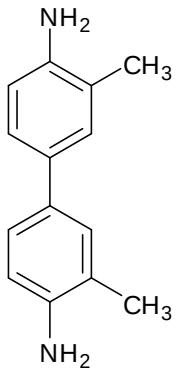

Molecular formula	$[(H_3C)C_6H_3(NH_2)]_2$
Physical state and appearance	Solid crystalline powder
Weight [$g.mol^{-1}$]	212.3
Boiling point [°C]	200
Melting point [°C]	129
Specific gravity	1
Solubility in water [$mg.l^{-1}$]	Partial soluble

4.4.2. Toxicological Information

The substance is toxic to lungs, the reproductive system, mucous membranes. Repeated or prolonged exposure to the substance can produce target organs damage. Repeated or prolonged inhalation of dust may lead to chronic respiratory irritation. The inhalation, ingestion and skin contact may cause severe gastrointestinal irritation, cyanosis, headache, dizziness, burns of mouth, esophagus and stomach. **[53]**.

4.4.3. Photocatalytic degradation procedure

Photocatalytic degradation reactions of *o*-tolidine were carried out using a reactor consisting of two parts which was designed and fabricated locally as mentioned earlier. The photocatalytic activity of catalysts was evaluated by measuring the decrease in

concentration of *o*-tolidine in the reaction solution. The decrease in the concentration of *o*-tolidine was measured by using UV-Visible spectroscopy. The calibration curve was plotted for *o*-tolidine and for the purpose the standard samples of *o*-tolidine in distill water was prepared. The concentrations of the standard samples were 5, 10, 20, 30, 40 and 50 ppm and the absorption of these samples were measured by UV-Visible spectroscopy. The calibration curves were plotted between absorption values of the samples with respect to their relevant concentrations. The slopes of the curves were calculated which were used for the calculation of *o*-tolidine concentration. The calibration curve for *o*-tolidine is shown in **Figures-4.7**.

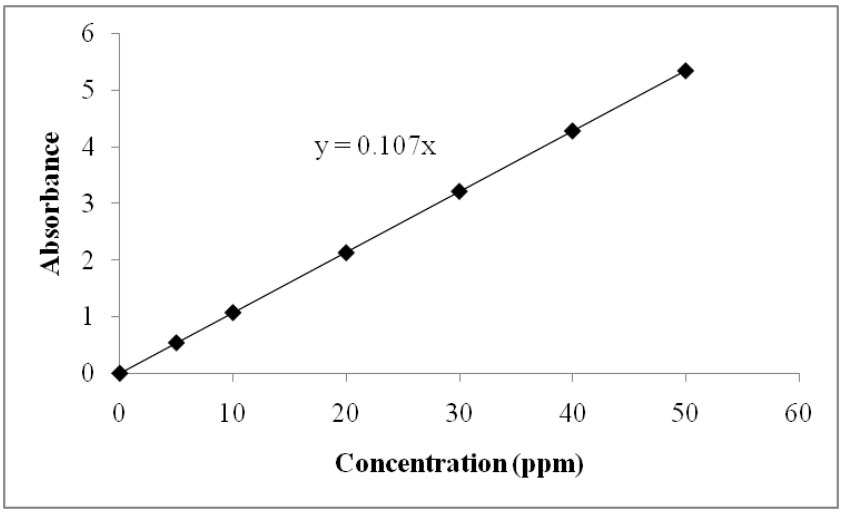

Figure-4.7. Calibration curve for *o*-tolidine

Prior to commencing illumination, a suspension containing 0.2 g lit^{-1} of the catalyst and 250 mL aqueous solution of ca. 50 ppm of *o*-tolidine was stirred continuously for 30 minute in the dark. After attaining the maximum adsorption, the solution was irradiated and the samples (5 mL) were withdrawn by syringe at time interval of 10 min for first one hour and every one hour thereafter. The centrifugation was applied to separate out the catalyst from the aqueous samples prior to analyse. The reaction solution was kept homogeneous throughout the reaction by applying continuous stirring using magnetic stirrer below the reactor. The stirring rate was 500 rpm throughout the reaction. All experiments were carried out without addition of any sacrificial agent**.** The irradiation source was cooled by circulating water to 293 K during experiment. The concentration of

o-tolidine was determined from the absorbance at λ_{max} = 281 nm using UV–Visible spectrophotometer *(Cary 500, Varian Palo Alto CA)*. The tentative fragmentation modes were determined by observing m/z values in mass spectra of the samples at different time intervals during the reaction.

4.5. RESULTS AND DISCUSSION

4.5.1. Photocatalytic degradation of *o*-tolidine in water/ TiO_2 /UV system

The photocatalytic experiments were performed using TiO_2 Degussa P25 and the laboratory prepared TiO_2 catalysts (SG, SC and HT) with *o*-tolidine. Catalyst amount used in all cases was 0.2 g/l for a 250 mL of 50 ppm reactant solution and reaction was carried out up to four hours. The amount of adsorption was observed approximate ca. 18 and 14% with P25 and SG catalysts respectively while it was observed only ca. 2 and 4 % with SC and HT catalysts respectively. The initial rate of degradation of *o*-tolidine was higher in case of SG catalyst as compared to other catalysts. The initial rate of degradation was in the order of SG>P25>SC>HT. The final percentage of degradation was obtained in the range of 82 to 99 % after 240 minutes which was measured by spectrophotometer (**Table-4.4**).

Table-4.4. % Degradation and %TOC values with different catalysts

Catalyst	% Degradation* (After 240min.)	% TOC removal	
		60 min	240 min.
P25	94	69	83
SG	99	66	80
SC	86	63	75
HT	82	58	71
Blank	32	12	16

The higher percentage of photocatalytic degradation was obtained for SG and P25 catalysts and it was 99 and 94 % respectively after four hours reaction. Lowest photocatalytic activity was attributed using HT catalyst. The molar concentration values were plotted as a function of duration of UV exposure as **Figure-4.8**.

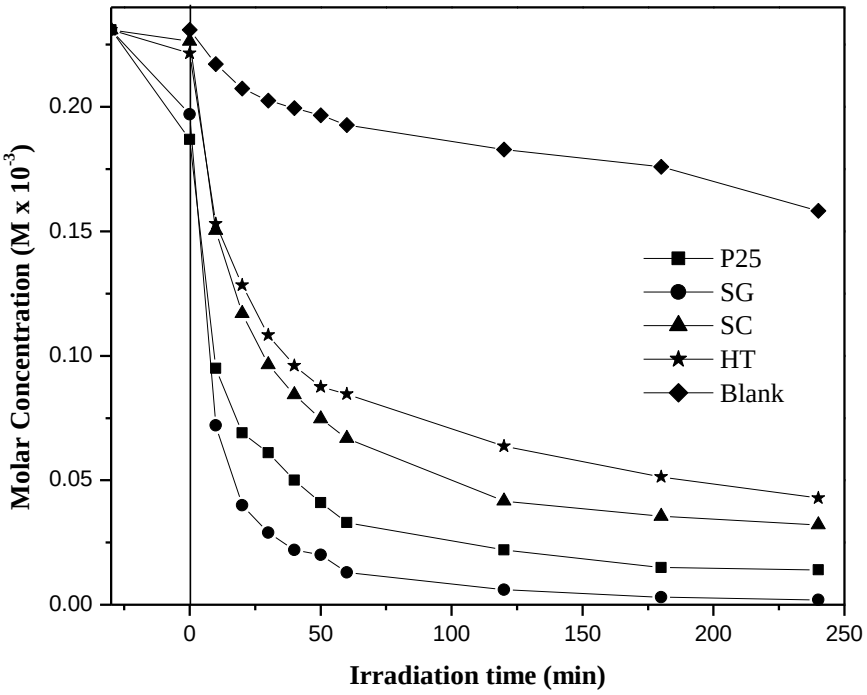

Figure-4.8. Decrease in concentration of *o*-tolidine as a function of irradiation time

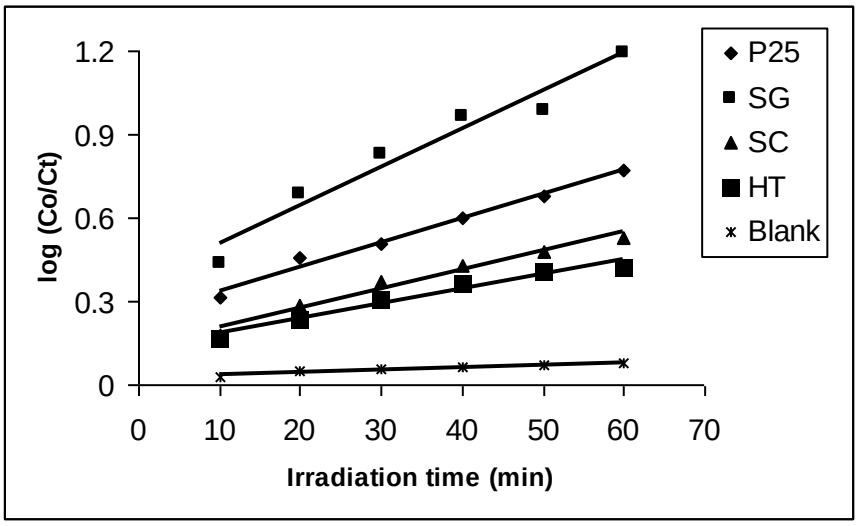

Figure-4.9. Kinetics of *o*-tolidine degradation

The initial rates of degradation and apparent rate constants are reported in **Table-4.5**. The initial rates of degradation of compounds were determined from the initial slope of the concentration profile.

Table-4.5. Kinetic data of the reactions with different catalysts

Catalyst	**Initial Rate* × 10^6 [mol min.$^{-1}$]**	**Rate Constant* (k_{app})×10^2 [min^{-1}]**	**R^2 (Degradation)**	**R^2 (TOC)**
P25	4.5	3.3	0.99	0.93
SG	5.2	5.1	0.96	0.88
SC	4.0	2.3	0.98	0.81
HT	3.6	1.9	0.96	0.90
Blank	1.2	0.15	0.95	0.80

* Calculated using UV–Visible absorbance data

Figure-4.2 shows that the presence of hydroxyl group in P25 and SG are higher as compared to SC and HT catalysts. The amino functional groups of *o*-tolidine can have some weak interaction with these hydroxyl groups. **Figure-4.4** shows the bimodal nature of pores in P25 with 6 and 12 nm pore diameter while the surface area of SG catalyst was attributed to 80 m^2g^{-1} with pore diameter of 8 nm. This may leads to higher adsorption of *o*-tolidine 18 and 14 % in case of P-25 and SG catalyst respectively. The higher adsorption of *o*-tolidine on the P25 and SG catalyst surface increase the probability of attack by radicals formed on the catalyst surface which results in higher degradation compared to SC and HT catalysts. A blank study was carried out only in presence of UV light without any catalyst. The concentration of *o*-tolidine was found decreased up to only 32 %, using UV-Visible spectroscopy**.**

4.5.2. Kinetics of *o*-tolidine degradation

The kinetics of *o*-tolidine degradation is represented using **Figures-4.8 and 4.9**. The **Figure-4.8** has an adsorption period of 30 min in dark. It follows pseudo first order kinetics in agreement with Langmuir-Hinshelwood mechanism with the rate r which is proportional to concentration C_t at any time *t*,

$$r = \frac{kKC_t}{1+KC_t} \approx k\,K\,C_t = k_{app}\,C_t \qquad (4.5)$$

Where *k* is the reaction rate constant, *K* is the reactant adsorption constant.

The apparent first order linear transform are given in **Figure-4.9**. The R^2 values of linearity and apparent rate constants calculated from slopes are given in **Table-4.5**. However at the low irradiation time, reaction was not initiated to follow the linearity shown in **Figure-4.9**, which is due to sharp decrease in concentration which was observed for first 10 min in all the reaction performed. The rate constants represent an index for how fast organic compounds can be converted to intermediates but not necessarily to ultimately CO_2.

4.5.3. Mineralization

Mechanistic explanation of semiconductor photocatalyzed oxidative degradation of organic materials in aqueous system can be specified by band-gap model of semiconductors **[26]**. Semiconductor is characterized by band structure, i.e., a filled valence band (VB) separated by an energy gap (Eg) from a vacant conduction band (CB).

$$TiO_2 + h\vartheta \rightarrow TiO_2(e_{cb}^- + h_{vb}^+) \qquad (4.6)$$

$$O_2 + TiO_2(e_{cb}^-) \rightarrow TiO_2 + O_2^{\cdot -} \qquad (4.7)$$

$$O_2^{\cdot -} + H_2O \rightarrow HOO^{\cdot} + OH^- \qquad (4.8)$$

$$OH^- + TiO_2(h_{vb}^+) \rightarrow TiO_2 + HO^{\cdot} \qquad (4.9)$$

$$TiO_2(h_{vb}^+) + H_2O \rightarrow TiO_2 + OH^{\cdot} + H^+ \qquad (4.10)$$

$$HOO^{\cdot} + H^{+} + TiO_2(e_{cb}^{-}) \rightarrow TiO_2 + HO^{\cdot} + H^{-} \quad (4.11)$$

$$> O_s^{-} + H_{aq} + TiO_2(h_{vb}^{+}) \rightarrow TiO_2 + HO_s^{\cdot} \quad (4.12)$$

$$HO^{\cdot} + o\text{-}tolidine \rightarrow Intermediate\ products \quad (4.13)$$

$$TiO_2(h_{vb}^{+}) + Intermediate\ products \rightarrow CO_2 + H_2O + NO_3^{-} \quad (4.14)$$

Absorption of a photon with energy equal or higher than band-gap energy (Eg) promotes an electron from valence band to conduction band, leaving an electron deficiency or hole in the valence band as shown in equation (4.6). This e^- and h^+ pair reacts with surface hydroxyl group or water **[54]** and dissolved oxygen to produce hydroxyl, peroxide and superoxide radical anion as shown from reaction steps (4.7) to (4.10). However P. Salvador has proposed that adsorbed hydroxyl groups and water molecule cannot be photooxidized with VB holes **[55]**. The structural $^{\bullet}$OH radicals can be photogenerated via electroreduction of $^{\bullet}$OOH with CB electrons as shown in equation (4.11). The hole generated can react with surface oxygen ions of TiO_2 lattice at pH below 7 to produce $^{\bullet}$OH radicals as step (2.12). These radicals generated further react with organic compound, producing a whole range of intermediates including radical and radical cations to achieve complete mineralization, i.e., carbon dioxide, water and inorganic nitrogen say nitrate ion formation.

The mineralization of the reaction mixture was determined by decrease in TOC values. The degradation of *o*-tolidine leads to conversion into harmless gaseous CO_2 and inorganic ions such as nitrite and ammonium respectively. The TOC disappearance for the organic molecules is represented in **Figure-4.10** as a function of irradiation time. The R^2 values of the first order kinetics for TOC disappearance are given in **Table-4.5**.

The decrease in TOC values was almost same for SC, SG and P25 catalyst after 4 h (**Table-4.4**). However Degussa P25 showed difference in efficiency to some extent compared to all other catalysts including SG catalyst for first hour. The blank study showed only 16 % decrease in the TOC value and 32 % degradation even after 4 h. The

values of percentage degradation and TOC removal confirm that degradation and mineralization are well pronounced in presence of catalyst.

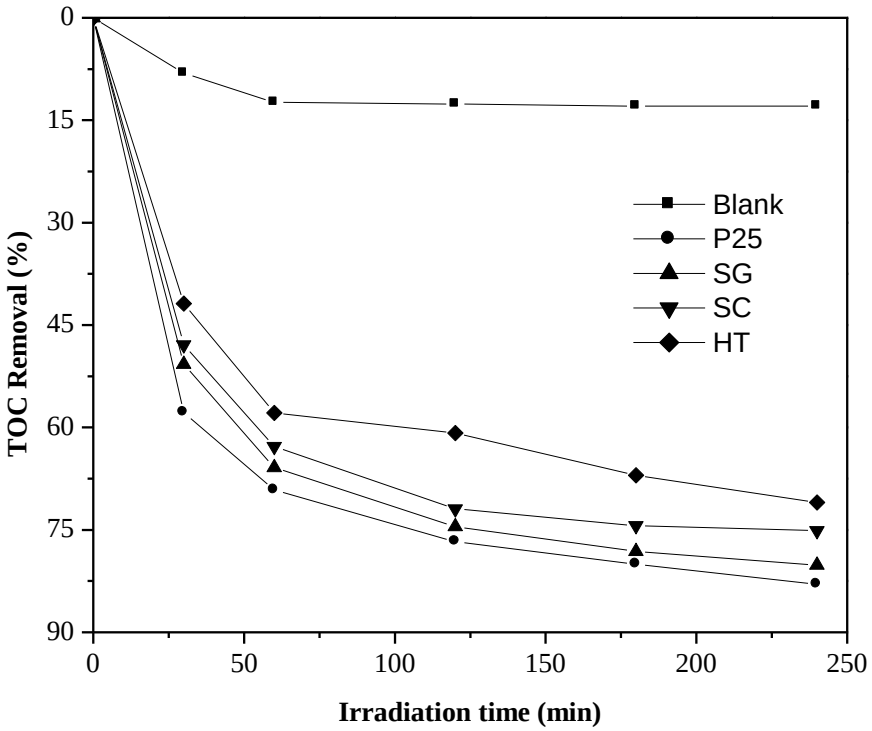

Figure-4.10. Percentage removal of TOC in the photocatalytic degradation of *o*-tolidine

4.5.4. Characterization of degradation products

To study the photodegradation pathway of *o*-tolidine under irradiation as well as to identify the possible degradation products, ESI-MS was used. For the purpose mass spectra of the sample taken at different reaction time intervals were observed. Major intermediates during the degradation process are proposed by using m/z values of the mass spectra (**Figure-4.11**). The plausible fragmentation path and intermediates are presented in the **scheme-4.1**. The scheme is proposed to start with two different ways. First path can start with the protonation of *o*-tolidine parent molecule. The peak at m/z = 213 is clearly observed in 30 and 60 min samples. Further removal of methyl radicals followed by hydroxylation may responsible for the peak at m/z = 217. The dehydration and dehydroxylation may provide the m/z values of 199 and 182 respectively.

The second path in scheme is proposed to start with the formation of parent molecule cation with m/z value 212. The replacement of amine groups with hydroxyl groups generated during the reaction can form 3,3′-dimethylbiphenyl-4,4′-diol molecule with m/z value 214. Further demethylation gives the peak at m/z = 186 value. These intermediates further reaches to mineralization by elimination of various hydrocarbon units, hydroxyl groups and other various possible radicals. The overall mineralization process is multi-step and multi-directional which involves various intermediates and radicals formed during the process.

The proposal for 3,3′-dimethylbiphenyl-4,4′-diol formation is feasible in aqueous media because in heterogeneous photocatalysis oxidation by oxidizing species such as hydroxyl, superoxide and reduction by hydrogen radicals are common.

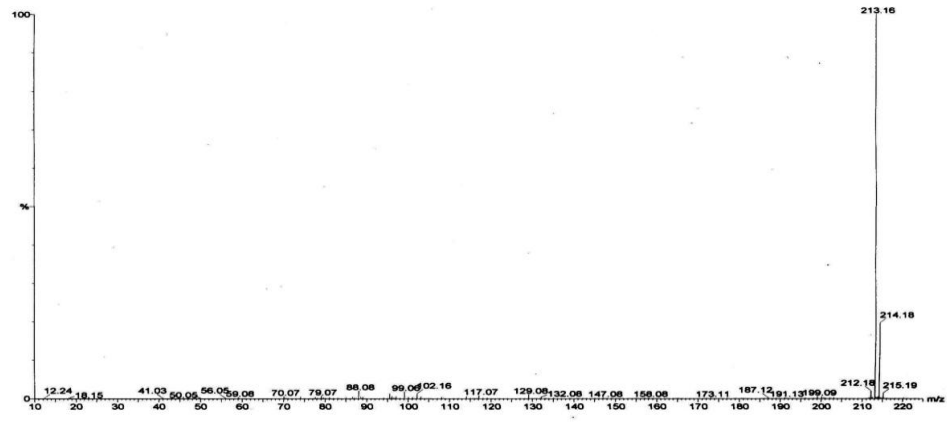
100
%
0
213.16
214.18
215.19
212.18
12.24
18.15
41.03
50.05
56.05
59.08
70.07
79.07
88.08
99.06
102.16
117.07
129.08
132.08
147.08
158.08
173.11
187.12
191.13
199.09
10
20
30
40
50
60
70
80
90
100
110
120
130
140
150
160
170
180
190
200
210
220
m/z

(a)

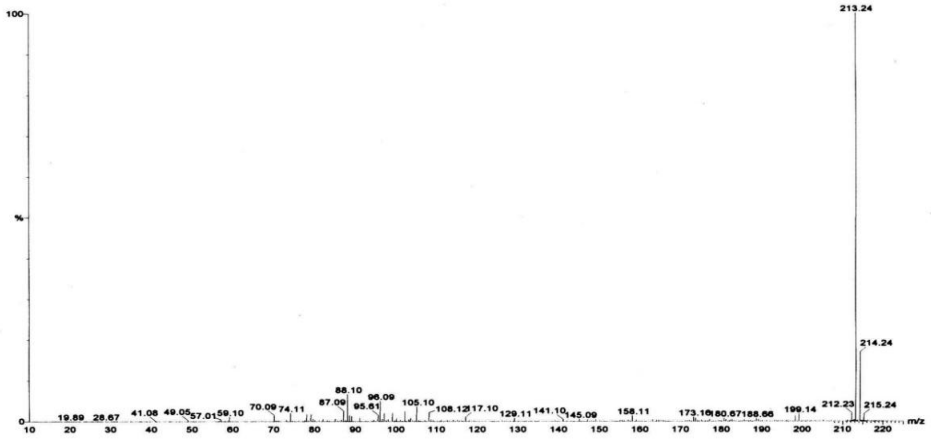
100
%
0
213.24
214.24
215.24
212.23
19.89
28.67
41.08
49.05
57.01
59.10
70.09
74.11
87.09
88.10
95.61
96.09
105.10
108.12
117.10
129.11
141.10
145.09
158.11
173.19
180.67
188.66
199.14
10
20
30
40
50
60
70
80
90
100
110
120
130
140
150
160
170
180
190
200
210
220
m/z

(b)

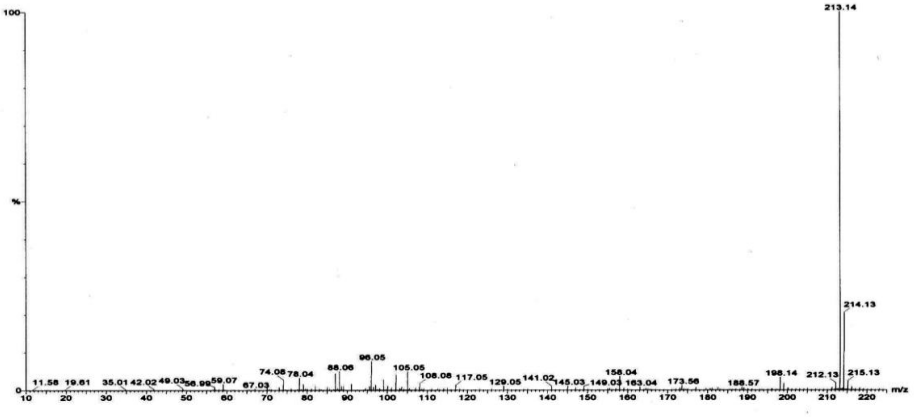
100
%
0
213.14
214.13
215.13
212.13
11.58
19.61
35.01
42.02
49.03
56.99
59.07
67.03
74.05
78.04
88.06
96.05
105.05
108.08
117.05
129.05
141.02
145.03
149.03
158.04
163.04
173.56
188.57
198.14
10
20
30
40
50
60
70
80
90
100
110
120
130
140
150
160
170
180
190
200
210
220
m/z

(c)

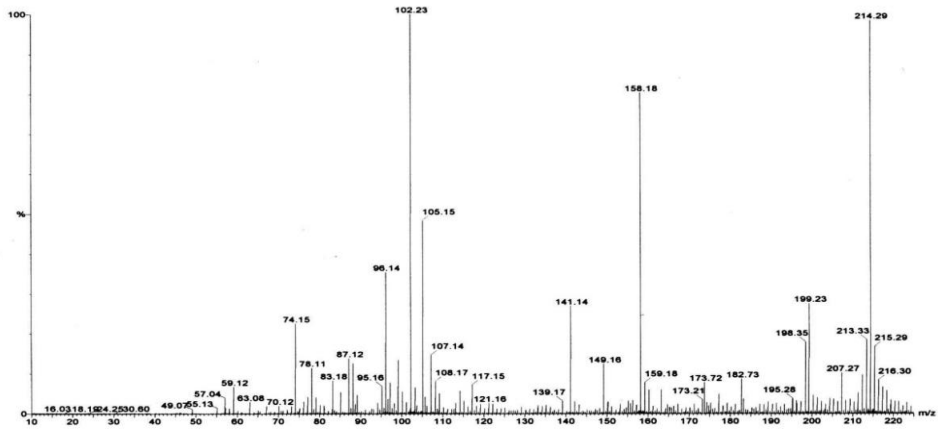
100
%
0
102.23
214.29
158.18
105.15
96.14
74.15
141.14
199.23
198.35
213.33
215.29
107.14
87.12
78.11
149.16
83.18
95.16
108.17
117.15
159.18
207.27
216.30
59.12
57.04
63.08
70.12
121.16
139.17
173.72
182.73
173.21
195.28
m/z

(d)

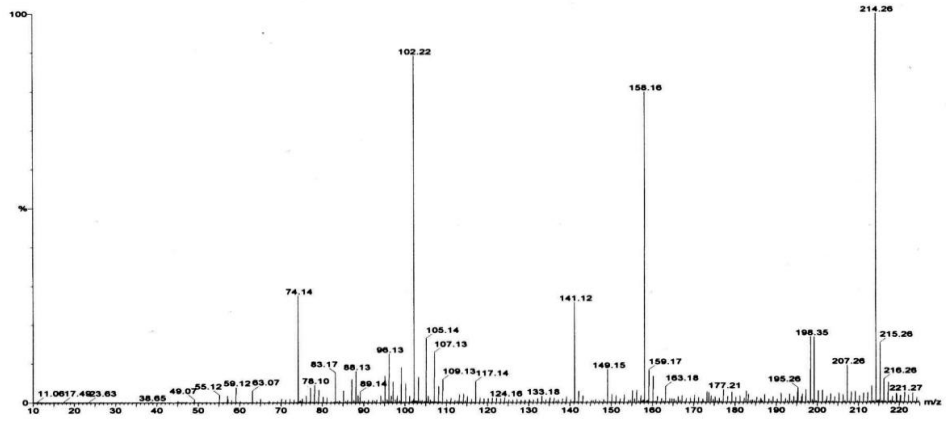
100
%
0
214.26
102.22
158.16
74.14
141.12
105.14
107.13
198.35
215.26
96.13
83.17
88.13
149.15
159.17
207.26
78.10
109.13
117.14
163.18
216.26
177.21
195.26
221.27
m/z

(e)

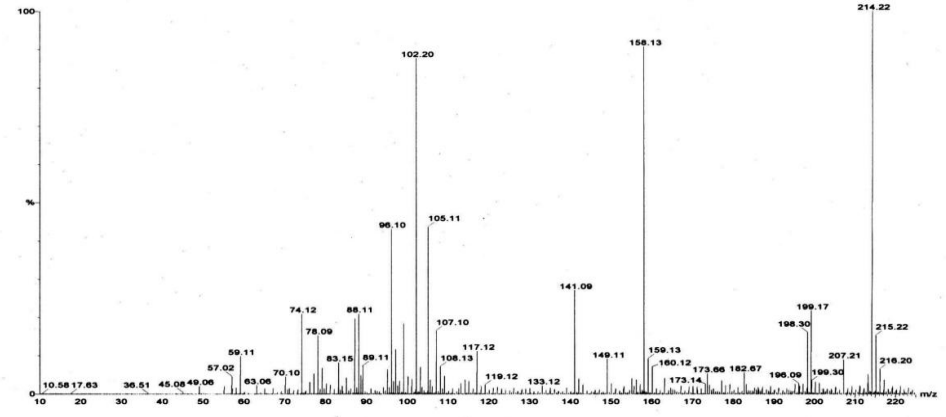
100
%
0
214.22
158.13
102.20
96.10
105.11
141.09
74.12
88.11
199.17
78.09
107.10
198.30
215.22
59.11
117.12
149.11
159.13
57.02
83.15
89.11
108.13
207.21
160.12
70.10
119.12
133.12
216.20
63.06
173.66
182.67
199.30
173.14
196.09
m/z

(f)

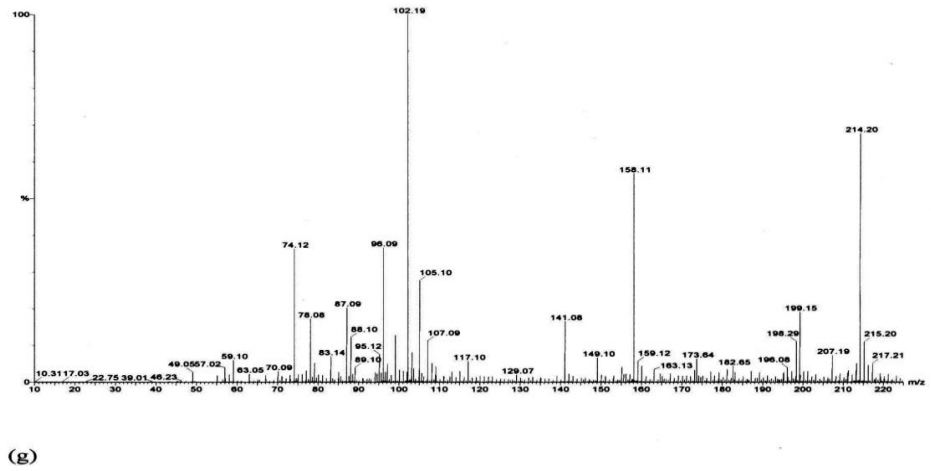

Figure-4.11. ESI mass spectra of *o*-tolidine at different time intervals of reaction (a) Original solution, 50 ppm concentration (b) After 30 min (c) After 60 min (d) After 5h (e) After 8 h (f) After 12 h (g) After 24 h

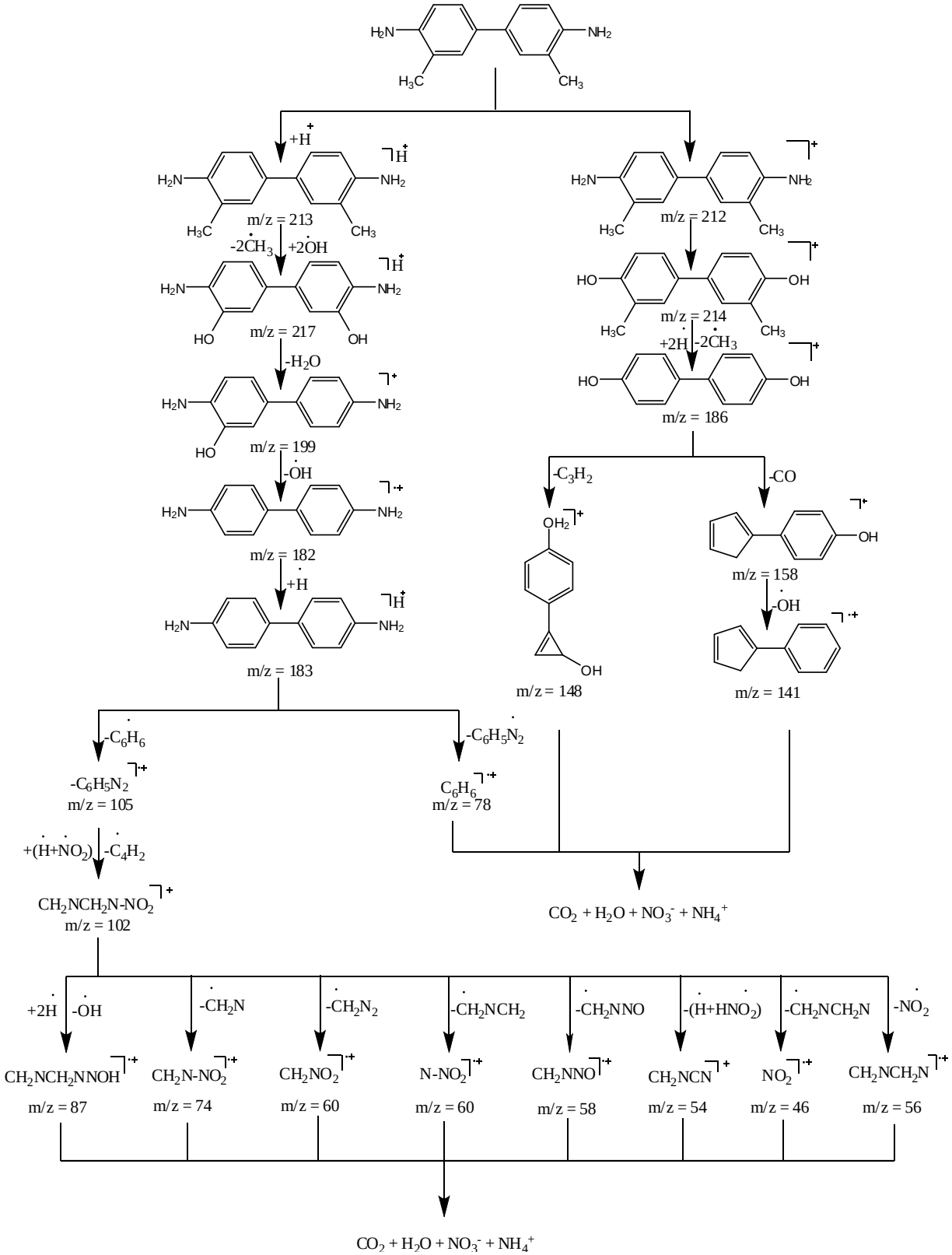

Scheme-4.1. Proposed fragmentation pattern of *o*-tolidine

4.6. REFERENCES

[1] Hoffmann, M. R.; Martin, S. T.; Choi,. W.; Bahnemann, D. W., *Chem. Rev.*, **1995**, *95*, 69-96.

[2] Fox, M. A.; Dulay, M. T., *Chem. Rev*., **1993**, *93*, 341-357.

[3] Litter, M. I., *Appl. Catal. B: Envron.*, **1999**, *23*, 89-114.

[4] Mills, A.; Hunte, S. L., *J. Photochem. Photobiol. A: Chem.*, **1997**, *108*, 1-35.

[5] Balasubramanian, G.; Dionysiou, D. D.; Suidian, M. T.; Subramanian, Y.; Baudin, I.; Laıˆne´, M., *J. Mater. Sci.*, **2003**, *38*, 823-831.

[6] Kolen'ko, Y. V.; Churagulov, B. R.; Kunst, M.; Mazerolles, L.; Colbeau-Justin, C., *Appl. Catal. B: Environ*., **2004**, *54*, 51-58.

[7] Liu, G.; Chen, Z. G.; Dong, C.L.; Zhao, Y. N.; Li, F.; Lu, G. Q.; Cheng, H. M., *J. Phys. Chem. B*, **2006**, *110*, 20823-20828.

[8] Yu, J. C.; Yu, J.; Zhao, J., *Appl. Catal. B*, **2002**, *36*, 31-43.

[9] Subramanian, V.; Wolf E. E.; Kamat, P. V., *J. Am. Chem. Soc*., **2004**, 126, 4943-4950.

[10] Yu, J. C.; Yu, J.; Ho, W.; Jiang, Z.; Zhang, L., *Chem. Mater*., **2002**, *14*, 3808-3816.

[11] Ohtani, B.; Ogawa, Y.; Nishimoto, S., *J. Phys. Chem. B*., **1997**, *101*, 3746-3752.

[12] Sibu, C. P.; Rajesh Kumar, S.; Mukundan, P.; Warrier, K. G. K., *Chem. Mater*., **2002**, *14*, 2876-2881.

[13] Yu, J.; Wang, G.; Cheng, B.; Zhou, M., *Appl. Catal. B*., **2006**, *69*, 171-180.

[14] Sheng, Q. R.; Cong, Y.; Yuan, S.; Zhang, J. L.; Anpo, M., *Micropor. Mesopor. Mater*., **2006**, *95*, 220-225.

[15] Li, Z. J.; Hou, B.; Xu, Y.; Wo D.; Sun, Y. H.; He, W.; Deng, F., *J. Solid State Chem.*, **2005**, *178*, 1395-1405.

[16] Lin, J.; Liu, P.; Meziani, M. J.; Allard, L. F.; Sun Y. P., *J. Am. Chem. Soc*., **2002**, *124*, 11514-11518.

[17] Sakai, H.; Kawahara, H.; Shimazaki, M.; Abe, M., *Langmuir,* **1998**, *14*, 2208-2212.

[18] Wilson, G. J.; Will, G. D.; Frost, R. L.; Montgomery, S. A., *J. Mater. Chem*., **2002**, *12*, 1787-1791.

[19] Assabane A.,; Ichou, Y. A.; Tahiri, H.; Guillard, C.; Herrmann, J.-M., *Appl. Catal. B: Environ.*, **2000**, *24*, 71-87.

[20] Feng, W.; Nansheng, D., *Chemosphere*, **2000**, *41*, 1137-1147.

[21] Alhakimi, G.; Studnicki, L. H.; Al-Ghazali, M., *J. Photochem. Photobiol. A: Chem.* **2003**, *154*, 219-228.

[22] Robert, D.; Dongui, B.; Weber, J.-V., *J. Photochem. Photobiol. A: Chem.*, **2003**, *156*, 195-200.

[23] Ao, C. H.; Lee, S. C.; Mak, C. L.; Chan, L. Y., *Appl. Catal. B: Environ.*, **2003**, *42*, 119-129.

[24] Koiminami, H.; Kumamoto, H.; Kera, Y.; Ohtani, B.,. *J. Photochem. Photobiol. A: Chem.*, **2003**, *160* , 99-104

[25] Piccinini, P.; Minero, C.; Vincenti, M.; Pelizzetti E., *Faraday Trans.*, **1997**, *93*, 1993-2000.

[26] Yang, Y.; Ma, J.; Qin, Q.; Zhai, X., *J. Mol. Catal. A: Chem,* **2007**, *267*, 41-48.

[27] Tayade, R. J.; Surolia, P. K.; Kulkarni, R. G.; Jasra, R. V., *Sci. Technol. Adv. Mater.*, **2007**, *8*, 455-462.

[28] Ikeda, S.; Sugiyama, N.; Pal, B.; Marci, G.; Palmisano, L.; Noguchi, H.; Uosaki, K.; Ohtani, B. *Phys. Chem. Chem. Phys.*, **2001**, *3*, 267-273.

[29] Fuerte, A.; Hernandez-Alonso, M. D.; Maria, A. J.; Martinez-Arias, A.; Fernandez-Garcia, M.; Conesa, J. C.; Soria, J., *Chem. Commun*., **2001**, *24*, 2718-2719.

[30] Haigler, B. E.; Spain, J. C., *Appl. Environ. Microbiol.*, **1991**, *57*, 3156-3162.

[31] Chou, W. L.; Speece, R. E.; Siddiqi, R. H., *Biotechnol. Bioeng. Symp.*, **1978**, *8*, 391-414.

[32] Hallas, L. E.; Alexander, M., *Appl. Environ Microbiol.*, **1983**, *45*, 1234-1241.

[33] Davis, E. M.; Murray, H. E.; Liehr, J. G.; Powers, E. L., *Water Res.*, **1981**, *15*, 1125-1127.

[34] Rodriguez, M. ; Timokhin, V. ; Michl, F.; Contreras, S. ; Gimenez, J. ; Esplugas S., *Catal. Today*, **2002**, *76*, 291-300.

[35] Toxicological Profile for nitrobenzene; U.S. Department of Health and Human Services: Atlanta, GA, **1990**. website: http:// www.atsdr.cdc.gov/taxfaq.html.

[36] Sclafani, A.; Palmisano, L.; Schiavello, M., *J. Phys. Chem.*, **1990**, *94*, 829-832.

[37] Oosawa, Y.; Gr¨atzel, M., *J. Chem. Soc., Faraday Trans.*, **1988**, *84*, 197-206.

[38] Campostrini, R.; Carturan, G.; Palmisano, L.; Schiavello, M.; Sclafani A., *Mat. Chem. Phys.*, **1994**, *38*, 277-283.

[39] Boonstra, A. M.; Mutsaers, C. A. H. A., *J. Phys. Chem.*, **1975**, *79*, 1694-1698.

[40] Andersson, M.; Osterlund, L.; Ljungstrom, S.; Palmqvist, A., *J. Phys. Chem. B.*, **2002**, *106*, 10674-10679.

[41] Nagaveni, K.; Sivalingam, G.; Hegde, M. S.; Madras, G., *Appl. Catal. B: Environ.*, **2004**, *48*, 83-93.

[42] Wu, M.; Long, J.; Huang, A.; Luo, Y.; Feng, S.; Xu, R., *Langmuir*; **1999**, *15(26)*, 8822-8825.

[43] Madeira, P.; Nunes, M. R.; Borges, C.; Costa, F. M. A.; Florêncio, M. H., *Rapid Commun. Mass Spectrom.*, **2005**, *19*, 2015-2020.

[44] Florêncio, M. H.; Pires, E.; Castro, A. L.; Nunes, M. R.; Borges, C.; Costa, F. M., *Chemosphere*, **2004**, *55*, 345-355.

[45] Yu, J.; Yu, J. C.; Leung, M. K. -P.; Ho, W.; Cheng, B.; Zhao X.; Zhao J., *J. Catas.*, **2003**, *217*, 69-78.

[46] Cullity, B. D.; Stock, S. R., Elements of X-ray Diffraction, 3rd ed.; *Prentice Hall Inc. Upper Saddle River, NJ*, **2001**.

[47] Surolia, P. K.; Tayade, R. J.; Jasra, R. V., *Ind. Eng. Chem. Res*., **2007**, *46*, 6196-6203

[48] Kim, E. J.; Hahn, S. -H., *Mater. Lett.*, **2001**, *49*, 244-249.

[49] Gregg, S. J.; Sing, K. S. W., Adsorption, Surface Area and Porosity, *2nd ed.; Academic Press: New York*, **1982.**

[50] Tayade, R. J.; Kulkarni, R. G.; Jasra, R. V., *Ind. Eng. Chem. Res*., **2006**, *45*, 922-927.

[51] Gratzel, M., Heterogeneous Photochemical Electron Transfer; *CRC Press: Baton Rouge, LA*, **1988**.

[52] http://www.poolwaterproducts.com

[53] http://www.carolina.com

[54] Poulios, I.; Makri, D.; Prohaska, X., *Global Nest the Int. Journal*, **1999**, *1*, 55-62.

[55] Salvador, P., *J. Phys. Chem. C.*, **2007,** *111*, 17038-17043.

Chapter 5

Kinetic Modeling of Heterogeneous Photocatalytic Degradation Reactions

5.1. INTRODUCTION

Adsorption of molecules on porous adsorbents strongly depends on their surface functionalities and textural characteristics such as surface area, pore dimension and shape and also pore size distribution **[1-4]**. Zeolites are microporous materials consisting anionic silico-alumina framework and extra framework exchangeable cations. Such anion-cation pairs from strong electrostatic fields strongly interact with polar adsorbates **[5-6]**. These attributes of zeolites make them good adsorbents and catalytic support materials **[7-10]**. Because of the presence of accessible molecular sized cavities, zeolites can be modified through the incorporation of active species in pores by various techniques such as ion exchange and impregnation **[11-12]**. Photocatalysis has emerged a valuable technique for degradation and mineralization of organic and inorganic pollutants. TiO_2 is a widely studied photocatalyst for decomposition of organic molecules and dyes **[10-13]**. The photocatalytic activity of TiO_2 is significantly influenced by its crystallite structure and crystallite size, surface area, porosity and band gap **[14]**. The high surface area results in higher catalytic active sites which is required for efficient adsorption and thus higher photocatalytic activity. This can be achieved by either synthesis of fine TiO_2 particles or dispersion of TiO_2 on high surface support materials, such as zeolite. Furthermore, the intermediates formed during degradation process may be adsorbed and retained for complete mineralization to CO_2 and water. The zeolite framework also could participate actively in electron transfer processes, either as electron accepter or electron donor **[15-16]**. Ag^+ ion exchanged zeolites have been reported to exhibit higher photocatalytic activity for decomposition, photochemical cleavage of water, photodimerization, photo-oxygen production from water and photocatalytic degradation of various organic compounds and dyes **[17-24]**. The photocatalytic activity of silver doped titania was found increased significantly for the degradation of oxalic acid, sucrose, methyl orange and phenol while the activity was observed mildly enhanced for 4-chlorophenol , 1,4-dicholorobenzene and some dyes **[25]**.

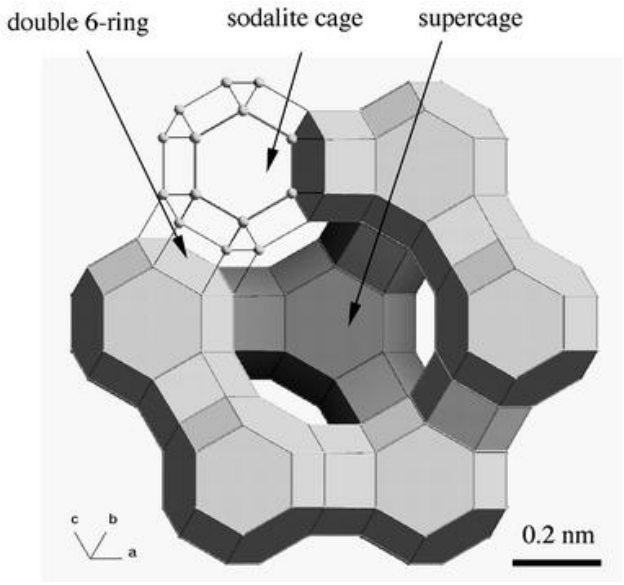

Figure-5.1. Schematic diagram of the zeolite-Y structure

5.1.1. Kinetic and Mechanistic Study

Photoassisted heterogeneous catalysis has been gaining attention as a technique for total destruction of hydrocarbon, chlorocarbon and nitrocarbon contaminants in water. The investigation of any chemical reaction has often followed a three-step sequence: determination of reaction stoichiometry, description of the observed kinetics, and finally, development of plausible mechanisms. Thus far, the first step has accounted for most research in heterogeneous photocatalysis. However, reaction mechanisms and kinetics which are consistent with the observed stoichiometry, and known physical and electronic properties of the illuminated semiconductor- water system are sparsely studied. Study of the reaction mechanism is significant as it will promote an increased understanding of the photocatalytic reaction. While many typical water pollutants and related compounds have been successfully mineralized via photocatalysis **[26-28]**, the establishment of kinetic models with a wide range of validity has been somewhat slow.

5.1.2. Aim of present study

In the view of above, an attempt has done to study the impregnation of titania as well as silver ion exchange in zeolite Y for preparaing photocatalysst for degradation of *p*-nitrotoluene [PNT]. A possible reaction path for mineralization has been suggested on the

basis of the analytical results of HPLC and ESI–MS well which are recognized analytical tool for the characterization and identification of a wide range of compounds even at trace level **[29-30]**. Langmuir-Hinshelwood kinetic model has been proposed for the degradation and the reaction rate constant values were determined from the experimental data using the model. TiO_2 loading was optimized from the percentage degradation, rate constant and mineralization values.

5.2. SYNTHESIS OF CATALYSTS

5.2.1. Chemicals and Materials

Titanium (IV) tetraisopropoxide (97%) was procured from Sigma Aldrich, India. Zeolite NaY with Si/Al ratio 5.5 was procured from United Catalysis India Ltd., Vadodara, India. Silver nitrate, AR grade, was procured from Ranbaxy, India were used for the silver ion exchange. COD standard chemical reagents and *p*-nitrotoluene (PNT), AR grade were purchased from E. Merck, India. *p*-aminophenol, *p*-nitrophenol, phenol and toluene from RANKEM, benzene from Qualigens, India, benzaldehyde, nitrobenzene, benzoic acid and *p*-toluidine from s. d. fine-chem. Ltd., India, Hydroquinone and benzoquinone from S.D.S. Lab chem. Industry, India were used as standards for HPLC analysis. Deionised distilled water was used for catalyst synthesis as well as for reaction and analysis purposes.

5.2.2. Catalysts preparation

The catalysts were synthesized as following earlier reported procedure **[24]**. Prior to the TiO_2 impregnation, the zeolite $NaY_{5.5}$ was activated by calcination at 723 K for 4 h under nitrogen flow to remove the adsorbed water present in the zeolite cavities. The solutions of appropriate amount of titanium tetra isopropoxide for 1, 2, 4, 10 w/w % TiO_2 in $NaY_{5.5}$ zeolite were prepared in dry ethanol. The solutions were stirred for 30 min followed by addition of calculated amount of activated zeolite. This slurry was stirred for 2 h and then solvent was removed by using rotavapour (*Buchi Rotavapour R-205*). The samples were dried in oven at 393 K for 12 h. The hydrolysis was done by adding water to this sample and then samples were dried for a second time in oven at 393 K for 12 h. Thus obtained

samples were calcined at 723 K for 11 h. These catalysts were named as $TiO_2/NaY_{5.5}$-1, $TiO_2/NaY_{5.5}$-2, $TiO_2/NaY_{5.5}$-4 and $TiO_2/NaY_{5.5}$-10 for 1, 2, 4 and 10 (w/w %) coating of TiO_2 on $NaY_{5.5}$ zeolite respectively.

The above TiO_2 coated catalysts were treated with silver nitrate solution at 353 K for 4 h in dark. The residue was filtered and washed with distilled water several time. This cycle was repeated three times to get complete silver ion exchange. Thus obtained samples were dried at 353 K for 12 h and calcined at 753 K for 6 h. These catalysts were named as $TiO_2/AgY_{5.5}$-1, $TiO_2/AgY_{5.5}$-2, $TiO_2/AgY_{5.5}$-4 and $TiO_2/AgY_{5.5}$-10 for 1, 2, 4 and 10 (w/w %) coating of TiO_2 respectively.

5.3. CHARACTERIZATION OF PREPARED PHOTOCATALYSTS

5.3.1. X-ray diffraction (XRD)

Powder X-ray diffraction patterns were recorded using CuKα1 (λ = 0.15405 nm) radiation at 295 K with *Phillips X'pert MPD system*. Diffraction patterns were taken over 2θ range of 5°- 40° at the scan speed of 0.1°sec^{-1}. The crystallinity of the catalysts was calculated with reference to pure $NaY_{5.5}$ zeolite by taking the average of 6 major peaks of the catalyst (2θ = 6.28, 15.72, 20.42, 23.70, 27.10 and 31.45).

Figure-5.2 shows the X-ray diffraction pattern of TiO_2 coated $NaY_{5.5}$ and $AgY_{5.5}$ zeolite catalysts. The XRD patterns of all Ag^+ ion exchanged zeolite catalysts agree with that of pure $NaY_{5.5}$ zeolite and no extra peak was observed. This indicates that the zeolite framework is unaltered during the ion exchange process. Furthermore, XRD diffraction of TiO_2 modified Ag-exchanged $NaY_{5.5}$ catalysts showed the diffraction peak assigned to $NaY_{5.5}$ zeolites. However, the crystallinity of the zeolite was found to decrease with the amount of incorporated TiO_2 **(Table-5.1)**. The decrease in crystallinity could be due to leaching of Al in the zeolite structure **[31-32]** or due to occupation of cavities by TiO_2 particles. The later seems to be the main reason for that as leaching of Al from the framework under TiO_2 coating or silver ion exchange conditions seems unlikely. The diffraction peak due to TiO_2 was not observed in the XRD pattern even at 10 % impregnation, which may be because of low amount of TiO_2 relative to zeolite.

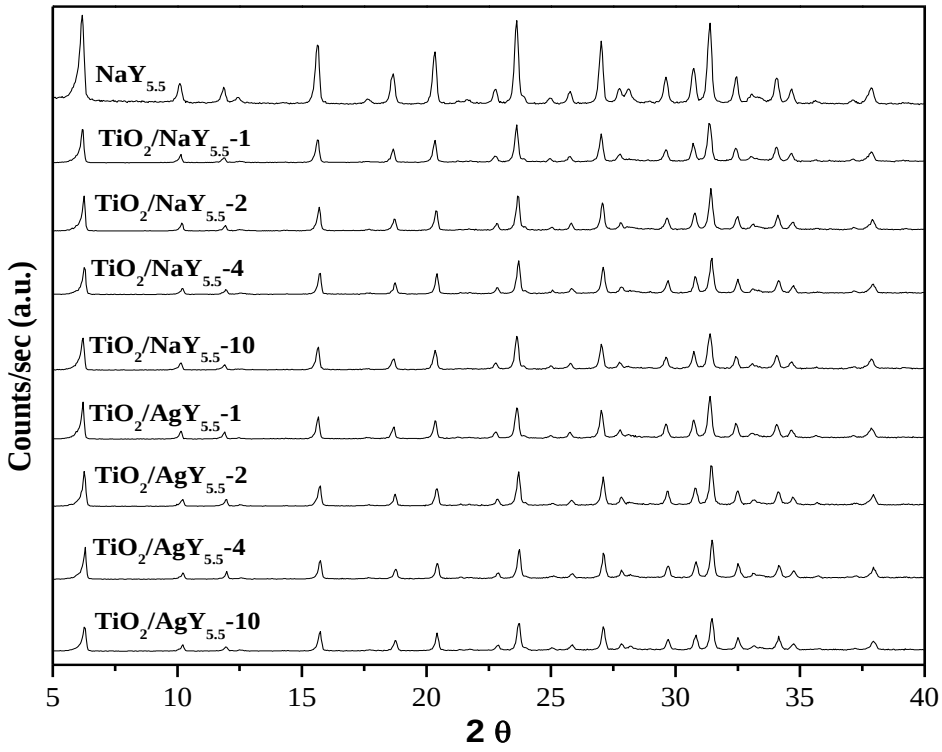

Figure-5.2. XRD patters of the synthesized catalysts

Table-5.1. Crystallinity of the catalysts by X-ray diffraction

Catalyst	Crystallinity [%]	Catalyst	Crystallinity [%]
$NaY_{5.5}$	100	-	-
$TiO_2/NaY_{5.5}$-1	99	$TiO_2/AgY_{5.5}$-1	99
$TiO_2/NaY_{5.5}$-2	98	$TiO_2/AgY_{5.5}$-2	89
$TiO_2/NaY_{5.5}$-4	90	$TiO_2/AgY_{5.5}$-4	80
$TiO_2/NaY_{5.5}$-10	87	$TiO_2/AgY_{5.5}$-10	74

5.3.2. Surface area measurement (N_2 adsorption)

The BET surface area of the calcined samples was determined from N_2 adsorption-desorption data measured at 77.4 K using volumetric set-up (ASAP 2010, micrometrics,

USA). The BET surface area of all catalysts after coating of TiO_2 and modification with Ag-ion exchange was observed to decrease as compared to bare $NaY_{5.5}$ zeolite sample **(Table-5.2)**. The decrease in the surface area was lower at the lower amount of TiO_2 impregnation but was observed to sharply decrease at 4-10% of TiO_2. This decrease suggests the occupation of zeolite pores by TiO_2 particles. The decrease in the surface area was very high after the Ag ion exchange **(Table-5.2)**. This decrease in surface area may due to replacement of Na^+ ion (0.89 Å) with Ag^+ ion (1.29 Å).

Table-5.2. BET surface area of the synthesized catalysts

Catalyst	Surface Area ($m^2 g^{-1}$)	Catalyst	Surface Area ($m^2 g^{-1}$)
$NaY_{5.5}$	737	-	-
$TiO_2/NaY_{5.5}$-1	688	$TiO_2/AgY_{5.5}$-1	506
$TiO_2/NaY_{5.5}$-2	682	$TiO_2/AgY_{5.5}$-2	505
$TiO_2/NaY_{5.5}$-4	676	$TiO_2/AgY_{5.5}$-4	502
$TiO_2/NaY_{5.5}$-10	639	$TiO_2/AgY_{5.5}$-10	494

5.3.3. Diffuse reflectance spectra (DRS)

Diffuse Reflectance Spectroscopy (DRS) was used to determine the band gap energy as well as the oxidation state of silver in the catalysts. The spectra were taken at room temperature in the range of 225-700 nm by *Shimadzu UV-3101PC* spectrophotometer. The spectrophotometer was equipped with an integrating sphere **[33-34]** and $BaSO_4$ was used as a reference.

The DRS spectra of Ag-exchanged TiO_2 encapsulated zeolite $NaY_{5.5}$ and bare $NaY_{5.5}$ are shown in **Figure-5.3**. All catalysts show a band in wavelength regions larger than 250 nm that is at around 288 nm and 322 nm. No absorption was observed at 190 nm. This shows that silver is present as Ag_n^0 and Ag_m^{n+} clusters and not fully as isolated Ag^+ ions. This indicates that the reduction and aggregation of Ag^+ ions have occurred in zeolite the

zeolite cavities. However, the absence of band at 410 nm confirms the lack of aggregation of the metallic silver particles up to several nano-meter or larger size **[18, 35-37]**.

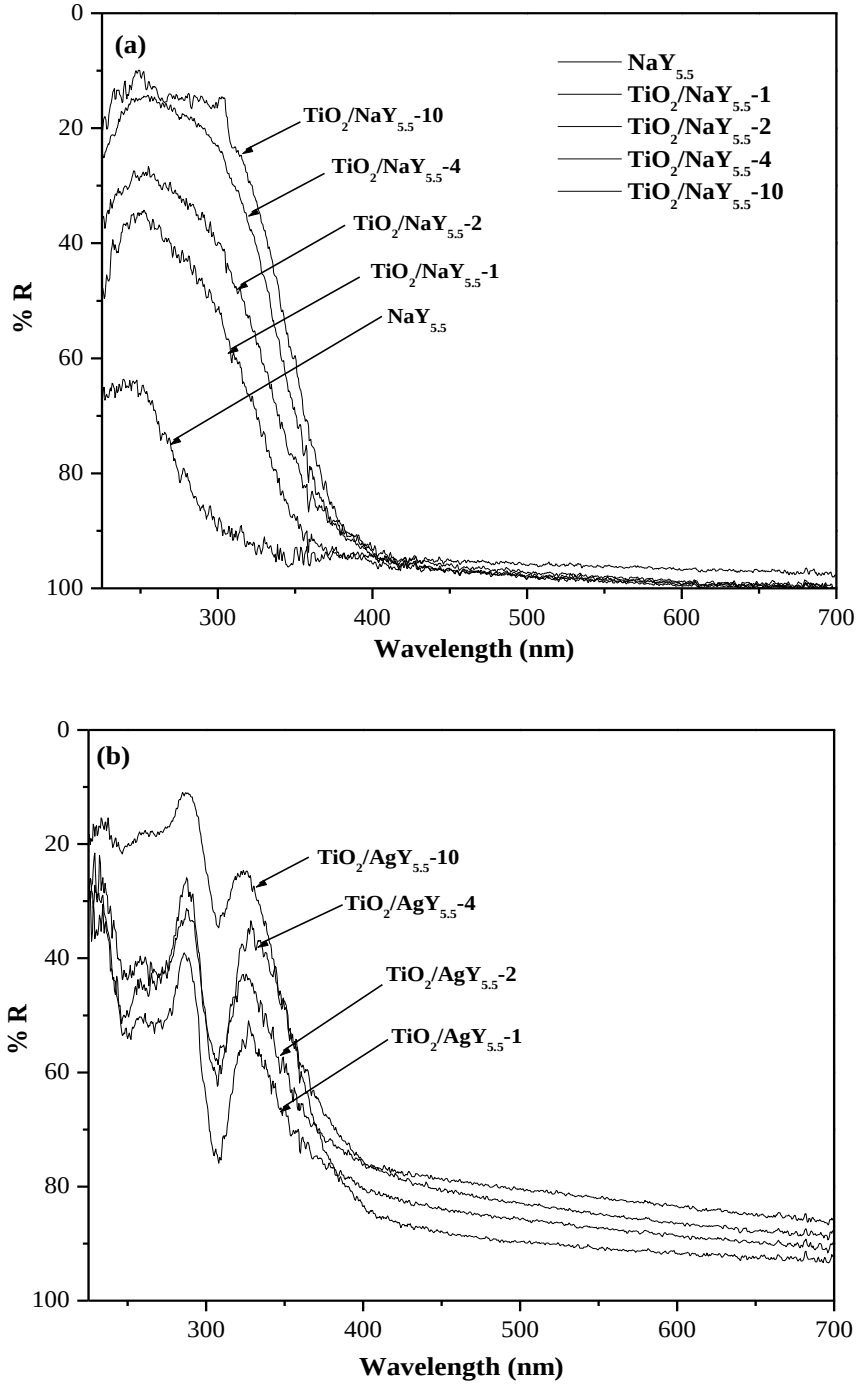

Figure-5.3. Diffuse reflectance spectra of TiO_2 impregnated (a) without Ag exchanged and (b) Ag exchanged NaY zeolite catalysts

5.3.4. Scanning electron microscopy (SEM)

The morphology of the synthesized catalysts was studied using Scanning Electron Microscopy (Leo Series VP1430). The morphology of synthesized catalysts is shown in **Figure-5.4**. The figure confirms that the morphology of the synthesized catalysts was not changed after the silver exchange. The particles were hexagonal in shape and some agglomeration occurred with increase amount of TiO_2 in the zeolite material.

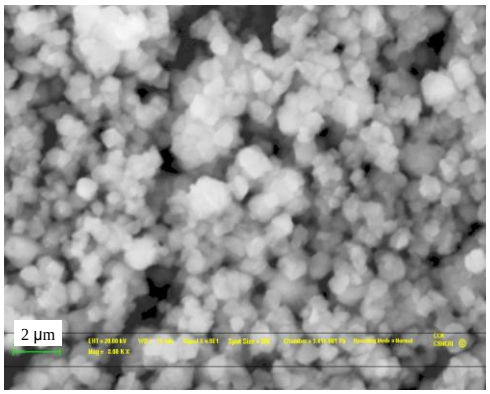

(a)

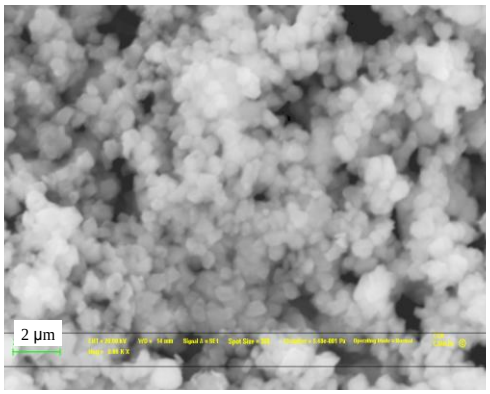

(b)

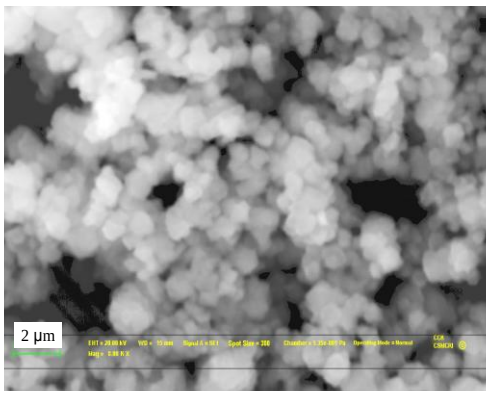

(c)

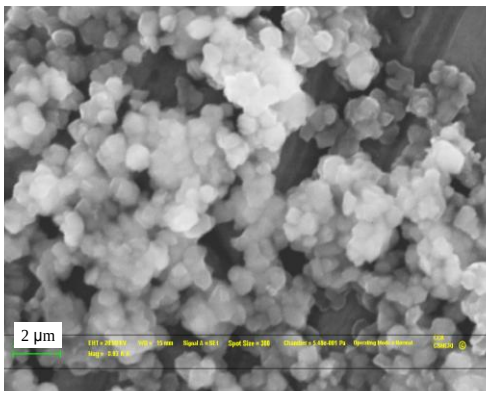

(d)

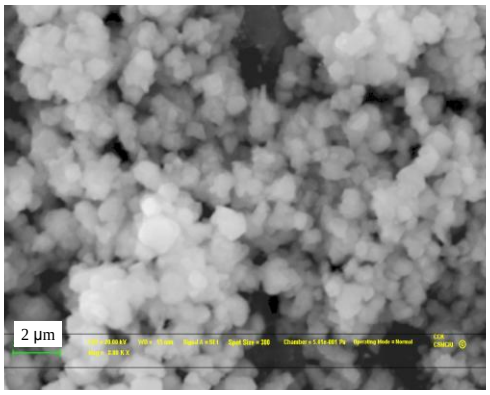

(e)

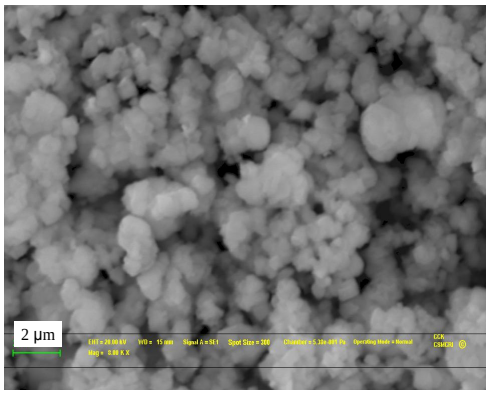

(f)

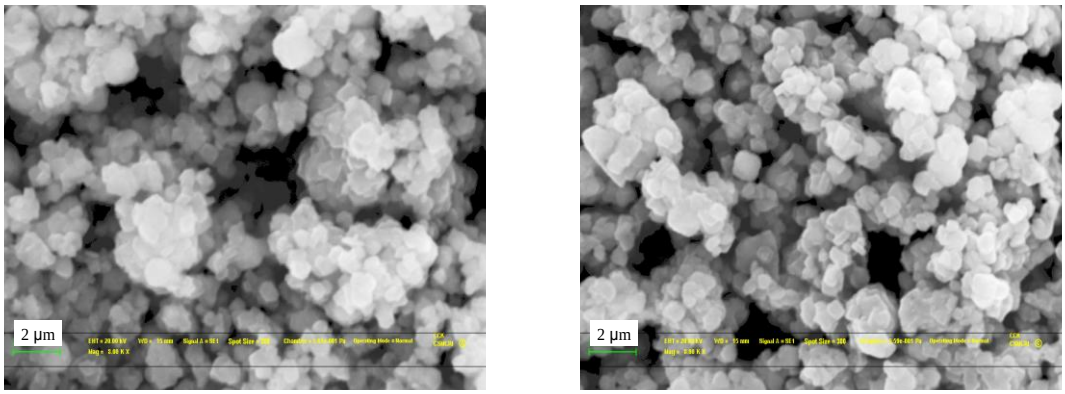

(g) (h)

Figure-5.4. SEM images of synthesized catalysts (a) $TiO_2/NaY_{5.5}$-1, (b) $TiO_2/NaY_{5.5}$-2, (c) $TiO_2/NaY_{5.5}$-4, (d) $TiO_2/NaY_{5.5}$-10 (e) $TiO_2/AgY_{5.5}$-1, (f) $TiO_2/AgY_{5.5}$-2, (g) $TiO_2/AgY_{5.5}$-4, (h) $TiO_2/AgY_{5.5}$-10

5.3.5. Energy dispersive X-ray analysis (EDAX)

Scanning electron microscope (Leo series 1430 VP) equipped with INCA, Energy Dispersive System (EDX), Oxford instruments was used to confirm the presence of Ti impregnated of metal on microporous ETS-10 sample as well as to determine the morphology of catalysts. The EDX results are shown in **Table-5.3** were used to confirm the percentage loading of Ti, Ag, Si and Na present in the zeolite material. The results confirm silver ions exchange with extra framework zeolite sodium ions. The Si:Al ratio also found constant with increase in Ti content and silver exchange in zeolite material.

Table-5.3. Elemental analysis results by EDX

Catalysts	Percentage of metal ion (weight %)				
	Na	**Ag**	**Si**	**Ti**	**O**
$TiO_2/AgY_{5.5}$-1	5.02	1.12	29.44	0.56	54.74
$TiO_2/AgY_{5.5}$-2	4.94	1.10	28.74	1.25	55.06
$TiO_2/AgY_{5.5}$-4	5.13	1.15	28.68	2.83	56.54
$TiO_2/AgY_{5.5}$-10	5.20	1.06	27.41	5.84	69.74

5.3.6. Inductively coupled plasma (ICP)

An Inductively Coupled Plasma-optical emission spectrophotometer (ICP-OES, Optima 2000 DV, Perkin-Elmer, Eden Prarie, MN) was used to determine the percentage of the different elements in the synthesized materials. The values of elements are given in **Table-5.4**. The results have good agreement with EDAX results shown in **Table-5.3**.

Table-5.4. Elemental analysis results by ICP

Catalysts	Percentage of metal ion (weight %)			
	Na	**Ag**	**Si**	**Ti**
$TiO_2/AgY_{5.5}$-1	5.16	1.08	28.94	0.96
$TiO_2/AgY_{5.5}$-2	5.23	1.05	28.56	1.86
$TiO_2/AgY_{5.5}$-4	5.15	1.13	29.25	3.95
$TiO_2/AgY_{5.5}$-10	5.20	1.00	28.96	6.21

5.4. PHOTOCATALYTIC DEGRADATION OF *p*-NITROTOLUENE

5.4.1. *p*-nitrotoluene and its properties

p-Nitrotoluene is an intermediate for *p*-toluidine, stilbene, dinitrotoluene, *p*-nitrobenzaldehyde and *p*-nitrobenzoic acid which are basic raw materials for dye stuff, paint, medicine and agricultural chemicals. **[38]**. The properties are given below:

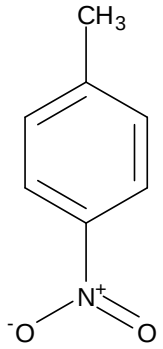

Molecular formula	$H_3C\ (C_6H_4)NO_2$
Physical state and appearance	Colorless or yellow color
Weight [$g.mol^{-1}$]	137.14
Boiling point [°C]	238.3
Melting point [°C]	53-54
Specific gravity	1.10
Solubility in water [$mg.l^{-1}$]	442 (30 °C)

5.4.2. Toxicological Information

The major hazards encountered in the use and handling of *p*-nitrotoluene stems from its toxicological properties and explosivity. Toxic by all routes (i.e., inhalation, ingestion,

and dermal absorption), exposure to this bitter-almond-smelling, white-to-yellowish, crystalline substance may occur from its manufacture and use in the synthesis of dinitrotoluene, trinitrotoluene, and various azo and sulfur dye intermediates such as *p*-toluidine, *p*-nitrobenzaldehyde and 4-nitro-2-chlorotoluene. Effects from exposure may include contact burns to the skin and eyes, headache, weakness, dizziness, nausea, shortness-of-breath, tachycardia, and methemoglobinemia **[39]**.

5.4.3. Photocatalytic degradation procedure

The photocatalytic activities of the synthesized catalysts were determined for *p*-nitrotoluene degradation under UV irradiation using a reactor consisting of two parts as reported in our earlier work. The photocatalytic activity of the catalysts was evaluated by measuring the decrease in concentration of nitrobenzene in the reaction solution. The decrease in the concentration of *p*-nitrotoluene was measured by using UV-Visible spectroscopy. The calibration curve was plotted for *p*-nitrotoluene and for the purpose the standard samples of nitrobenzene in distilled water was prepared. The concentrations of the standard samples were 5, 10, 20, 30, 40 and 50 ppm and the absorption of these samples was measured by UV-Visible spectroscopy. The calibration curves were plotted between absorption values of the samples with respect to their relevant concentrations. The slopes of the curves were calculated which were used for the calculation of *p*-nitrotoluene concentration. The calibration curve for *p*-nitrotoluene is shown in **Figures-5.5**.

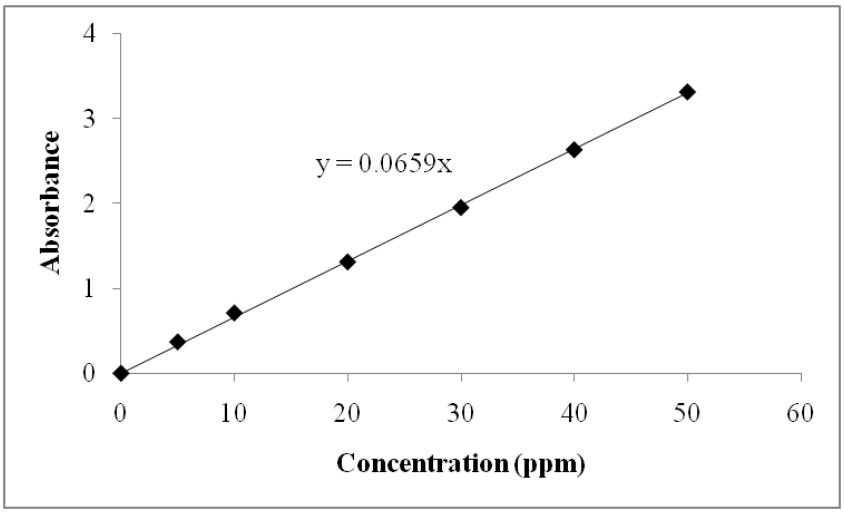

Figure-5.5. Calibration curve for *p*-nitrotoluene

Prior to commencing irradiation, a suspension containing 50 mg of the catalyst and 250 ml aqueous solution of ca. 50 ppm of *p*-nitrotoluene was stirred continuously for 30 minutes in the dark followed by the collections of the 5 ml sample and its analysis. After reaching the complete adsorption, the solution was irradiated and samples were withdrawn for analysis by syringe at interval of 10 min for first one hour and every hour thereafter for 4 h. The catalysts were separated by centrifugation from the samples prior to analysis. The absorbance was measured by a UV-Vis Spectrophotometer Cary 500 (Varian) at λ_{max} 284 nm for *p*-nitrotoluene. The 5 ml reaction mixture was withdrawn from the port by syringe at different time intervals. Photocatalytic activity was studied at pH of the initial reaction mixture and temperature was maintained at 293 K for all the reactions.

Adsorption studies in the dark were performed separately using an aqueous 50 ppm solution of nitrobenzene with all the catalyst for 1 h at the same reaction condition to find out the decrease in the concentration due to the adsorption. The decrease in concentration was observed by using UV-Visible spectroscopy. The mineralization of nitrobenzene in aqueous solution was confirmed by COD analysis of the samples taken at different reaction time interval by using HACH Instrument DR 2800 Photometer.

5.4.4. Kinetic Modeling

The mechanism of the photocatalytic oxidation can be described with consecutive steps initiating with illumination of a photoactivity with UV light generating charge carriers,

$$> TiO_2 \xrightarrow{h\upsilon} h^+_{VB} + e^-_{CB} \qquad (5.1)$$

$>TiO_2$ is the active catalyst surface. This e^-/h^+ pair can undergo charge transfer to the adsorbate on photocatalyst surface. However these e^- and h^+ can recombine to each other and results in low quantum yield of photocatalytic reaction.

$$h^+_{VB} + e^-_{CB} \longrightarrow heat \qquad (5.2)$$

The photocatalyst TiO_2 exist in hydroxylated form in aqueous suspension with coverage of 5-15 mol/nm^2 **[40]**. The generated hole can react with these surface hydroxyl group or water to produce strong oxidizing agents hydroxyl radicals.

$$> TiO_2 - OH^- \left(or > TiO_2 - H_2O\right) + h_{VB}^+ \longleftrightarrow > TiO_2 - OH^\bullet \left(or > TiO_2 - OH^\bullet + H^+\right) \tag{5.3}$$

This oxidation reaction is thermodynamically favorable throughout the entire pH range and thus can be expected under both acidic and basic conditions **[41]**. However, initially the original compounds and later intermediate species also compete with $OH^\bullet$ radical and can be adsorb on photocatalyst surface as

$$> TiO_2 + PNT \longleftrightarrow > TiO_2 - PNT \tag{5.4}$$

$$> TiO_2 + I \longleftrightarrow > TiO_2 - I \tag{5.5}$$

$$> TiO_2 + OH^\bullet \longleftrightarrow > TiO_2 - OH^\bullet \tag{5.6}$$

The generated hole can also be captured by adsorbed PNT or intermediate compound on catalyst surface as the competition with the step (3).

$$> TiO_2 - PNT + h_{VB}^+ \longrightarrow > TiO_2 - PNT^{\bullet +} \longrightarrow Mineralized\ \ species \tag{5.7}$$

$$> TiO_2 - I + h_{VB}^+ \longrightarrow > TiO_2 - I^{\bullet +} \longrightarrow Mineralized\ \ species \tag{5.8}$$

The $OH^\bullet$ radical can attack on adsorbed organic species at catalyst surface which either may be PNT or intermediate. This attacking $OH^\bullet$ radical may be free or adsorbed on catalyst surface.

$$> TiO_2 - PNT + > TiO_2 - OH^\bullet \longrightarrow > TiO_2 + > TiO_2 - PNT^{\bullet +} + OH^- \longrightarrow Mineralized\ species \tag{5.9}$$

$$> TiO_2 - I + > TiO_2 - OH^\bullet \longrightarrow > TiO_2 + > TiO_2 - I^{\bullet +} + OH^- \longrightarrow Mineralized\ species \tag{5.10}$$

$$> TiO_2 - PNT + OH^{\bullet} \longrightarrow > TiO_2 - PNT^{\bullet +} + OH^{-} \longrightarrow Mineralized\ species \quad (5.11)$$

$$> TiO_2 - I + OH^{\bullet} \longrightarrow > TiO_2 - I^{\bullet +} + OH^{-} \longrightarrow Mineralized\ species \quad (5.12)$$

The kinetics of the organic compound degradation can be determined by the applying elementary stoichiometric balance and steady state approximation on the intermediates and radicals formed during the process. The rate expression obtained by these processes is as expressed in equation (A5.14) as given in appendix;

$$r_{PNT} = \frac{k\ K\ [PNT]}{1 + K\ [PNT] + \sum_{i=1}^{n} K_i [I]}$$

The L-H parameters can be evaluated by simplify and linearizing this equation as equation (A5.17) shown in appendix;

$$\frac{1}{r_{PNT}} = \frac{1}{k} + \frac{1}{k\ K} \cdot \frac{1}{[PNT]_0}$$

Here r_{PNT} is initial rate while $[PNT]_0$ is initial concentration of PNT. From the plot of $1/r_{PNT}$ vs. *1/* $[PNT]_0$, we can find the values of *k* and *K*. The intercept determines the reaction kinetic constant '*k*' that varies with the rate of degradation and the value of adsorption constant '*K*' can be obtained by the slope of the curve. The higher value of *k* implies the higher rate of degradation. The value of *k* is a function of catalyst properties and reaction conditions and hence its value is independent of the organic pollutant taken for degradation [**41]**.

5.5. RESULTS AND DISCUSSION

5.5.1. Photocatalytic activity results of *p*-nitrotoluene

The photocatalytic activities of the synthesized catalyst were monitored at natural pH value, at catalyst dose of 200 mg/L and 293 K temperature, while initial concentration of PNT was varied as 30 (2.2×10^{-4} M), 50 (3.7×10^{-4} M) and 75 ppm (5.5×10^{-4} M).

The progress of the reaction was studied from the decrease in the absorption peak values at different time intervals in UV-Visible spectra at λ_{max} = 284 nm. The degradation reaction data follows Langmuir-Hinshelwood rate equation

$$\frac{1}{r_{PNT}} = \frac{1}{k} + \frac{1}{k\,K} \cdot \frac{1}{[PNT]_0}$$

The values of reaction kinetic constants, adsorption constants and initial rates are listed in **Table-5.5**. The initial rates of degradation of compounds were determined from the initial slope of the concentration profile. When the direct photolysis reaction was carried out (without catalyst), the concentration of PNT was found reduced with low extent with less percentage degradation value **(Figure-5.6)**.

Table-5.5. Initial rates of different reactions (r x 10^6 mol L^{-1} min^{-1}), Reaction rate constants (k x 10^6) and Adsorption constants (K x 10^{-3})

Catalyst	Initial rates with initial Concentration			Reaction rate constant (k x 10^6) [mol L^{-1} min^{-1}]	Adsorption constant (K x 10^{-3}) [L mol^{-1}]
	2.2 x 10^{-4} mol L^{-1} (30ppm)	3.7 x 10^{-4} mol L^{-1} (50ppm)	5.5 x 10^{-4} mol L^{-1} (75ppm)		
Blank	1.93	2.60	2.87	-	-
$NaY_{5.5}$	2.06	3.13	3.40	6.08	2.56
$TiO_2/NaY_{5.5}$-1	2.93	3.80	5.23	9.55	1.97
$TiO_2/NaY_{5.5}$-2	3.57	5.00	5.70	9.98	2.56
$TiO_2/NaY_{5.5}$-4	3.32	4.90	5.30	9.86	2.36
$TiO_2/NaY_{5.5}$-10	3.10	4.30	5.10	9.17	2.33
$TiO_2/AgY_{5.5}$-1	4.00	5.87	6.00	10.25	3.00
$TiO_2/AgY_{5.5}$-2	4.53	6.00	6.80	10.48	3.49
$TiO_2/AgY_{5.5}$-4	3.80	5.67	5.80	10.30	2.74
$TiO_2/AgY_{5.5}$-10	3.37	4.93	5.30	9.57	2.53

From the data in **Table-5.5**, it is clear that initial rate and final degradation was highest for the reaction using $TiO_2/AgY_{5.5}$-2 as a catalyst. The percentage degradation was observed 92, 84 and 74 % with 30, 50 and 75 ppm initial concentration of PNT respectively using $TiO_2/AgY_{5.5}$-2 catalyst. These values were highest among all other values observed using other catalysts and the blank study **(Figure-5.6)**. The decreases in the concentrations due to adsorption are reported in **Table-5.6**.

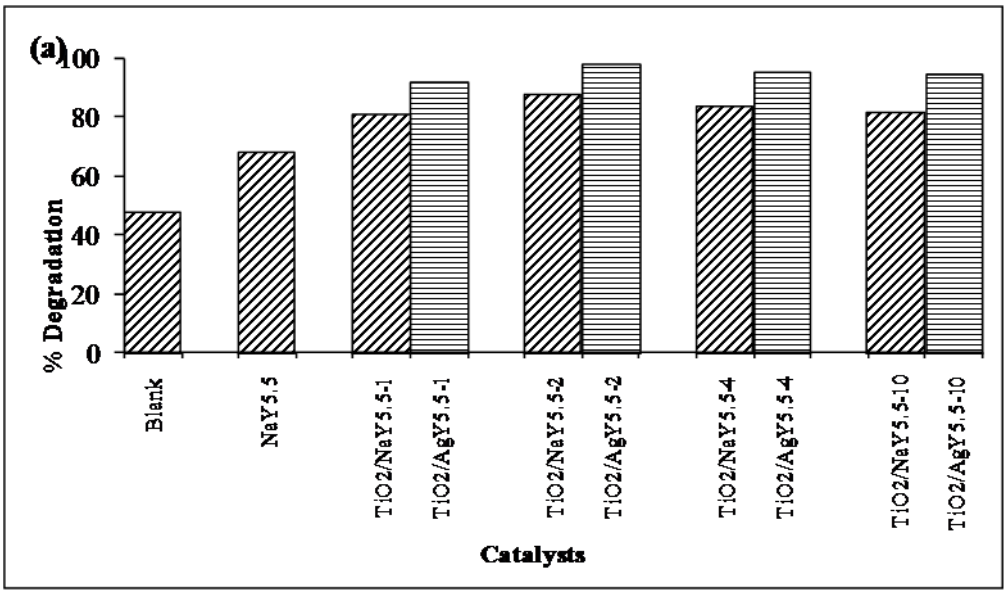
(a)
% Degradation
0
20
40
60
80
100
Blank
NaY5.5
TiO2/NaY5.5-1
TiO2/AgY5.5-1
TiO2/NaY5.5-2
TiO2/AgY5.5-2
TiO2/NaY5.5-4
TiO2/AgY5.5-4
TiO2/NaY5.5-10
TiO2/AgY5.5-10
Catalysts

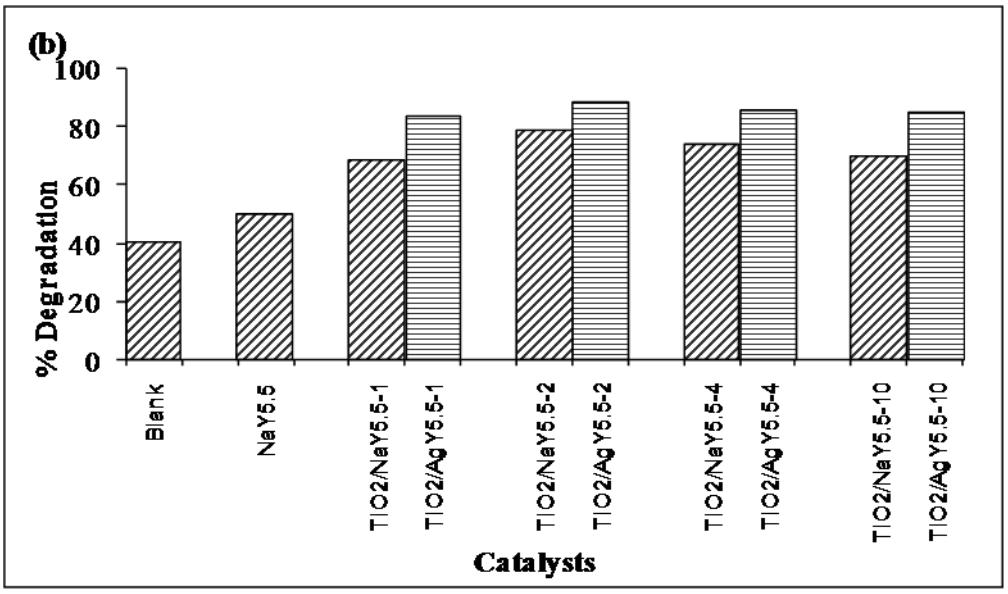
(b)
% Degradation
0
20
40
60
80
100
Blank
NaY5.5
TiO2/NaY5.5-1
TiO2/AgY5.5-1
TiO2/NaY5.5-2
TiO2/AgY5.5-2
TiO2/NaY5.5-4
TiO2/AgY5.5-4
TiO2/NaY5.5-10
TiO2/AgY5.5-10
Catalysts

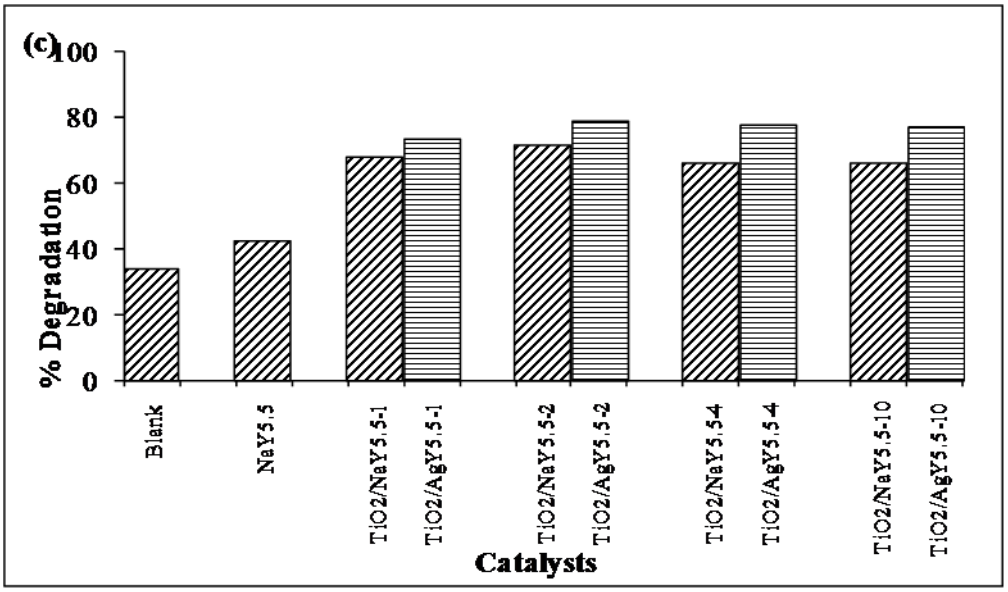

Figure-5.6. Percentage degradation of the *p*-nitrotoluene (a) 30 ppm (b) 50 ppm and (c) 75 ppm concentration in the presence of different synthesized catalysts after 4 h reaction

Table-5.6. Adsorption properties of the catalysts

Catalyst	Decrease in concentration with adsorption [%]		
	30 ppm	**50 ppm**	**75 ppm**
$NaY_{5.5}$	27	14	10
$TiO_2/NaY_{5.5}$-1	25	12	09
$TiO_2/NaY_{5.5}$-2	24	12	09
$TiO_2/NaY_{5.5}$-4	22	11	09
$TiO_2/NaY_{5.5}$-10	21	11	08
$TiO_2/AgY_{5.5}$-1	16	11	09
$TiO_2/AgY_{5.5}$-2	15	10	08
$TiO_2/AgY_{5.5}$-4	13	10	08
$TiO_2/AgY_{5.5}$-10	12	09	07

These values suggested that the adsorption was highest with bare zeolite because of its higher surface area. As the surface area decrease in TiO_2 impregnated and silver exchanged catalysts, the adsorption values also decrease as compared to bare zeolite. Moreover, the % concentration decrease by adsorption decreased with the increase in initial concentration of PNT. However, there was no considerable difference observed in the adsorption values for the same initial concentration of PNT with different catalysts. This suggests that adsorption does not make any difference in the photocatalytic activity among these catalysts. This increased surface area of the supported titania results into enhanced concentration of substrate molecules near TiO_2 particles which increases the rate of photocatalysis as compared to the bare TiO_2 catalyst.

5.5.1.1. *Effect of substrate concentration*

The influence of initial concentration of substrate on disappearance and mineralization kinetics of PNT was studied using three initial concentration, viz., 30, 50 and 75 ppm **(Table-5.5)**. It is clear from the data that as the initial concentration increases, the rate of disappearance of PNT also increases but the final percentage degradation after 4 h decreases as shown in **Figure-5.6**. In all the cases, catalyst $TiO_2/AgY_{5.5}$-2 exhibited the highest photocatalytic activity. The similar results were observed in mineralization processes also **(Table-5.7)**. At higher initial concentration of PNT, all catalytic sites of the semiconductor catalyst surface are occupied by the reactant molecules. Furthermore, increase in initial concentration does not affect the actual catalyst surface concentration. Therefore, this decreases the catalyst surface to reactant ration and may result in the decrease of observed final degradation at higher initial concentration.

The second factor which governs the degradation is generation and migration of the photogenerated e^-/h^+ pair, and reaction between these photogenerated h^+ ($OH^\bullet$ radical) and organic substrate molecules. Both the processes occur in series and each step may become the rate determining step for overall process. At low concentration the latter process dominants resulting high degradation values while at higher concentration, the former process dominants, and resulting into low degradation values.

5.5.1.2. *Effect of TiO_2 concentration*

At all the initial substrate concentrations, the catalyst $TiO_2/AgY_{5.5}$-2 showed the highest photocatalytic activity. The removal efficiency of PNT was observed to decrease with increased TiO_2 concentration. It could be because at certain concentration level, the TiO_2 particles block the pores of zeolite material which results in decrease in adsorption capacity of the catalyst towards organic substrate molecules. This could make the decomposition less effective. According to the principle of the photocatalytic reaction, the main step in process occurs on the surface of solid semiconductor photocatalyst, so the adsorption of organic compounds on the catalyst surface certainly affects the reaction and usually high adsorption capacity favors the reaction.

5.5.1.3. *Effect and role of silver*

The Ag particle in contact with TiO_2 surface can act as e^-/h^+ separation center **[42-43]** as the Fermi level of TiO_2 is higher than that of silver metal. This makes it feasible to thermodynamically transfer an e^- from conduction band to metallic silver particles, enhancing the e^-/h^+ separation and the subsequent transfer of the trapped e^- to the adsorbed O_2 acting as e- acceptor. This above Fermi level of TiO_2 than that of Ag metal results in the formation of Schottky barrier at metal-semiconductor contact region, which improves the stability of charge separation and thus enhances the photocatalytic activity of TiO_2 **[25]**. There are different oxidizing entities responsible for breaking the bonds of the organic species. These entities may either be hydroxyl radicals **[44]** or valence band holes **[45]**. In the present case, where zeolite framework also acts to discourage recombination, the primary species to attack the organic molecule are e^- and h^+. The silver ion and zeolite framework both act to stop the recombination of primary attacking species e^- and h^+.

5.5.1.4. *The role of zeolite framework*

The zeolite with higher surface area increases the adsorption of the substrate and hence increases its efficiency towards degradation by taking either e^- or h^+. Upon irradiation of TiO_2 on $TiO_2/AgY_{5.5}$ zeolite by UV light (band gap energy 3.2 eV), the conduction band electron generated can be react with adsorbed PNT from TiO_2 site before charge recombination. The electron rich zeolite surface functions as an h^+ scavenger to stop the e^-/h^+ recombination. This increases the electron donor capacity of TiO_2 site for reduction of adsorbed species **[16]**.

5.5.2. Mineralization

The mineralization during the photocatalytic process of PNT was confirmed by COD value determination given in **Table-5.7**. The decrease in COD values was found least when blank experiment was run, and observed highest when $TiO_2/AgY_{5.5}$-2 was used as a catalyst. The decrease in COD values with the blank study were 28, 26 and 21 % while using $TiO_2/AgY_{5.5}$-2 catalyst the observed decrease in the COD values were 67, 45 and 60 % with 30, 50 and 75 ppm *p*-nitrotoluene respectively. The presence of silver ion in

zeolite framework was found to increase the mineralization capacity. In all the cases, COD values could not reach to zero in 4 h irradiation. These COD values with values obtained from UV-Visble spectra confirm that an optimum amount of TiO_2 on zeolite material required for higher photocatalytic activity. However COD decrease was less than degradation values observed form UV analysis. It confirms that some organic and nitro-intermediates are still present in reaction samples.

Table-5.7. COD of reaction mixture with respect to irradiation time (mg/L) using different catalysts

Initial concentration	Catalysts	Irradiation time (min)					
		0	**30**	**60**	**120**	**180**	**240**
30 ppm	Blank	69	66	65	60	56	50
	$NaY_{5.5}$	69	63	61	55	52	45
	$TiO_2/NaY_{5.5}$-1	69	50	47	45	38	33
	$TiO_2/NaY_{5.5}$-2	69	47	44	42	34	28
	$TiO_2/NaY_{5.5}$-4	69	48	46	44	36	31
	$TiO_2/NaY_{5.5}$-10	69	49	48	45	39	36
	$TiO_2/AgY_{5.5}$-1	69	44	42	41	31	26
	$TiO_2/AgY_{5.5}$-2	69	43	40	39	24	23
	$TiO_2/AgY_{5.5}$-4	69	38	37	35	34	29
	$TiO_2/AgY_{5.5}$-10	69	55	48	46	41	40
50 ppm	Blank	100	96	92	88	82	74
	$NaY_{5.5}$	100	90	85	78	74	71
	$TiO_2/NaY_{5.5}$-1	100	85	81	76	69	65
	$TiO_2/NaY_{5.5}$-2	100	81	76	70	64	61
	$TiO_2/NaY_{5.5}$-4	100	82	77	73	68	64
	$TiO_2/NaY_{5.5}$-10	100	84	78	74	69	66
	$TiO_2/AgY_{5.5}$-1	100	78	70	69	66	58
	$TiO_2/AgY_{5.5}$-2	100	62	61	57	56	55
	$TiO_2/AgY_{5.5}$-4	100	62	61	60	59	58
	$TiO_2/AgY_{5.5}$-10	100	65	64	61	58	57
75 ppm	Blank	145	140	132	124	119	115
	$NaY_{5.5}$	145	137	126	118	110	103
	$TiO_2/NaY_{5.5}$-1	145	95	88	81	77	74
	$TiO_2/NaY_{5.5}$-2	145	80	74	72	69	65
	$TiO_2/NaY_{5.5}$-4	145	90	83	79	76	74
	$TiO_2/NaY_{5.5}$-10	145	93	86	79	74	68
	$TiO_2/AgY_{5.5}$-1	145	83	75	73	72	70
	$TiO_2/AgY_{5.5}$-2	145	70	68	64	60	57
	$TiO_2/AgY_{5.5}$-4	145	78	77	74	73	72
	$TiO_2/AgY_{5.5}$-10	145	101	99	93	89	88

5.5.3. Tentative mechanism of PNT photocatalytic degradation

ESI-MS and HPLC technique was used to identify the photocatalytic degradation pathway of PNT and possible degradation products. The mass spectra (**Figure-5.7**) of the samples taken at different time intervals of the reaction performed. The m/z values present in these mass spectra are used to propose the major intermediates while the HPLC analysis was used to confirm some of the suggested intermediates (**Figure-5.8**). Scheme 1 and 2 demonstrate the plausible fragmentation path and intermediates. First scheme starts with the parental PNT molecule. The mineralization of this parental molecule can occur by both oxidation and reduction processes as these are possible in heterogeneous photocatalysis in aqueous media.

The oxidation can result in the formation of the intermediates shown in path 'a' by removal and addition of different radicals mainly hydrogen and hydroxyl radicals which are very common in this aqueous photocatalytic system. The oxidation of this parent compound can give the 4-nitrobenzaldehyde and 4-nitrobenzoic acid of m/z = 151 and 167 respectively. Further oxidation and decarboxylation of this 4-nitrobenzoic acid can give 4-nitro phenol (m/z = 139), phenol (m/z = 94) and nitrobenzene (m/z = 123) respectively. These compounds are believed to mineralize in CO_2, H_2O and NO_3^- by oxidation and removal of various possible radicals respectively.

The intermediates resultants of reduction process are shown in path 'b'. The first step is the reduction of nitro group into amino group giving the m/z value 107. These intermediates also approach to complete mineralization by subsequently addition and removal of hydrogen, hydroxyl and amino radicals. The intermediates suggested in this process are 4-hydroxytoluene, toluene, 4-aminophenol and aniline having m/z values 108, 94, 109 and 93 respectively.

However, the peak at m/z = 213 is observed in all mass spectra. This peak is mass spectra is proposed by the formation of 4-methyl-4'-nitrobiphenyl. The proposal for 4-methyl-4'-nitrobiphenyl formation is feasible in aqueous media because in photocatalytic degradation of 4-nitrotoluene (PNT), formation of toluene and nitrobenzene radicals and their combination is common. The protonation of this compound followed by removal of

methyl and hydroxyl groups gives the m/z values 198 and 197 respectively. The peak of m/z = 197 further by removal of $NO^{\bullet}$ radical can give the m/z value 167 and by hydroxylation of this compound at 184.The proposed compound of peak at 198 can further can give peaks at 123 and 77 by removal of benzene and nitrobenzene radicals respectively. These intermediates further attain mineralization by elimination of hydrocarbons, nitroso, nitro and hydroxyl groups. The overall mineralization process is a multi-step and multi-directional which involves various intermediates and radicals formed during the process. The HPLC analysis was carried out to confirm the intermediates suggested in the proposed fragmentation pathway. The compounds were confirmed on the basis of their retention time in the HPLC analysis. The suggested intermediates which were defined are nitrobenzene, 4-aminophenol, benzoic acid, benzaldehyde, 4-aminotoluene, toluene, benzoquenone and hydroquenone. However, all the compounds could not be confirmed as their standards were not available. The HPLC analysis revealed that, after few minutes irradiation, some UV absorbing intermediates were present together with the unreacted substrate.

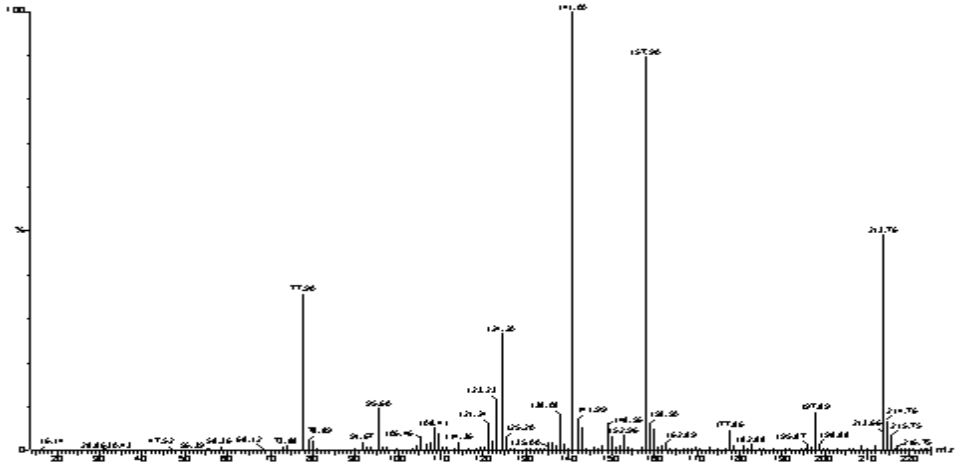

(a)

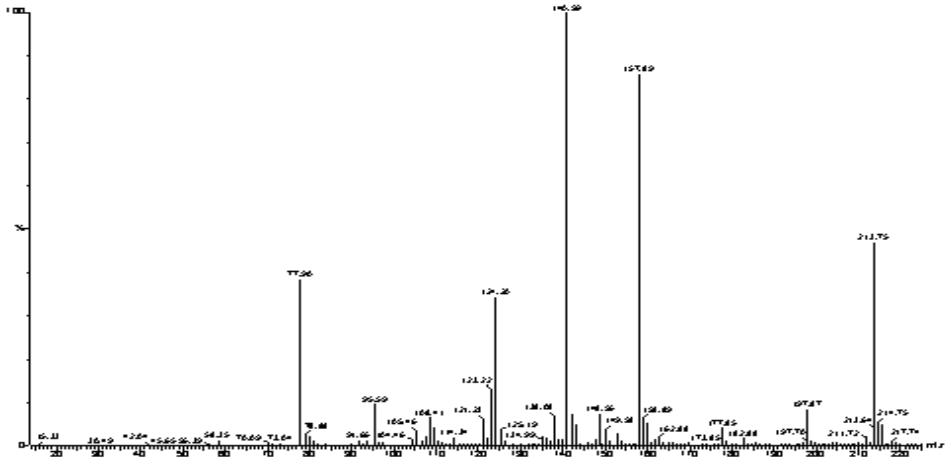

(b)

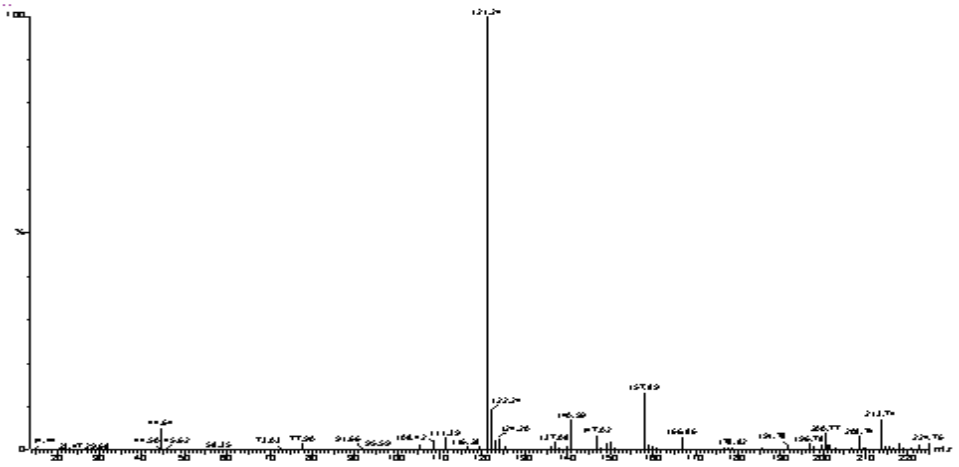

(c)

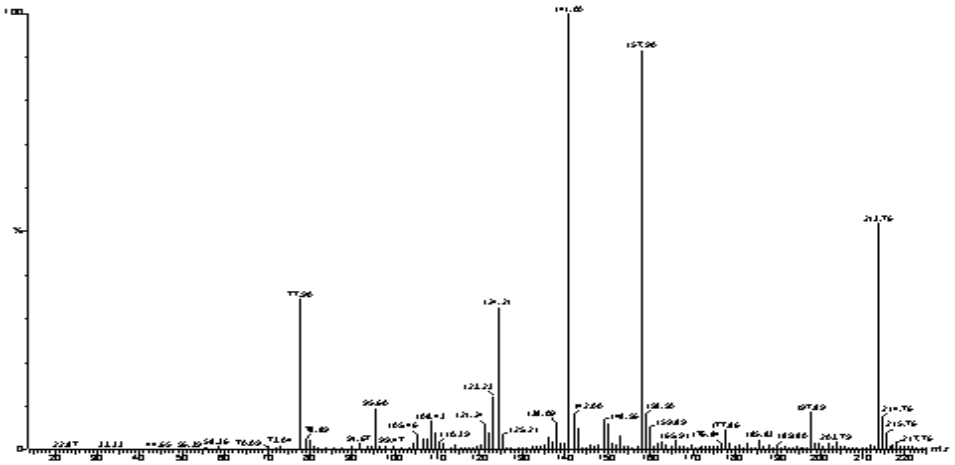

(d)

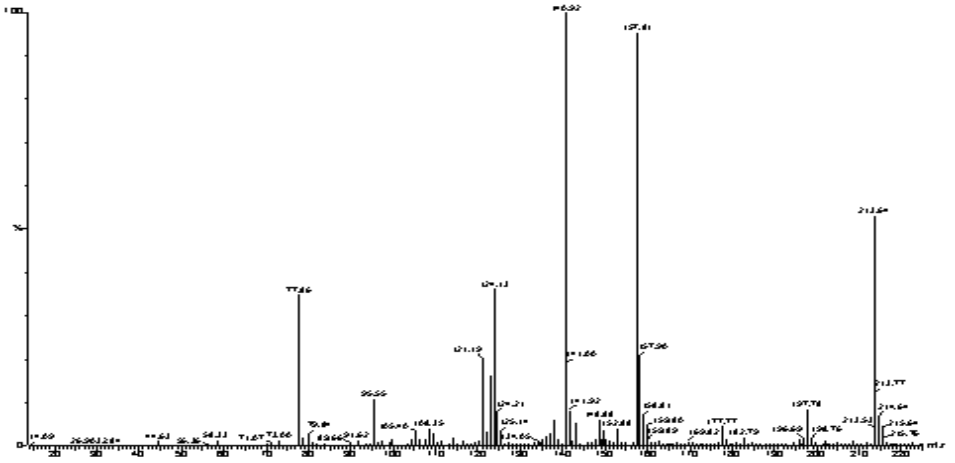

(e)

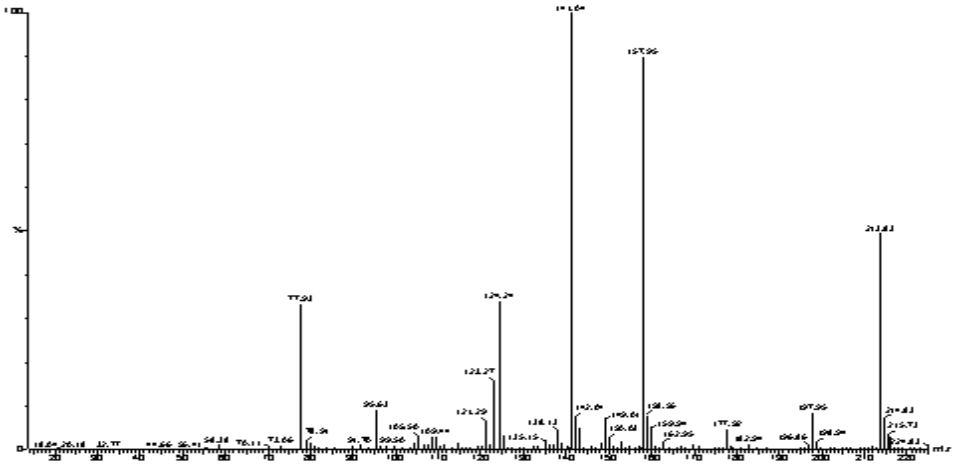

(f)

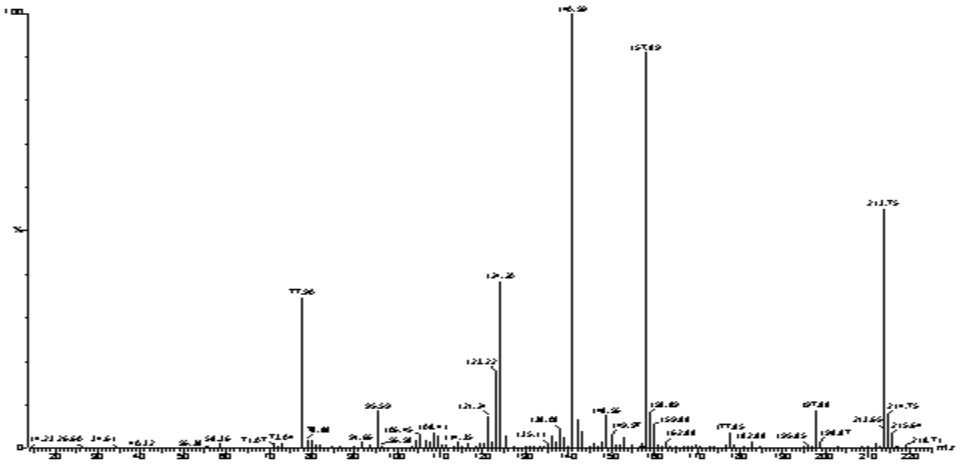

(g)

Figure-5.7. ESI mass spectra of *p*-nitrotoluene at different time intervals of reaction (a) After 30 min (b) After 60 min (c) After 4 h (d) After 6 h (e) After 8 h (f) After 12 h (g) After 24 h

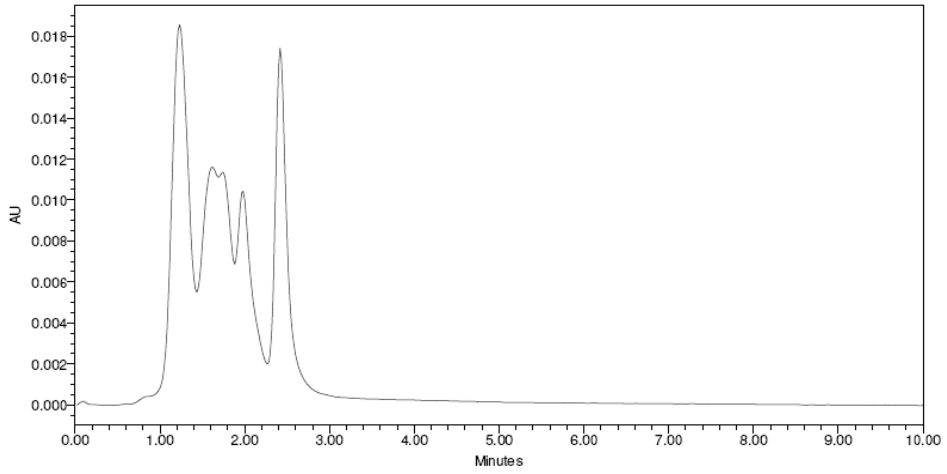

(a) PNT 30 min sample (RT = 1.23, 1.62, 1.99 and 2.42 min)

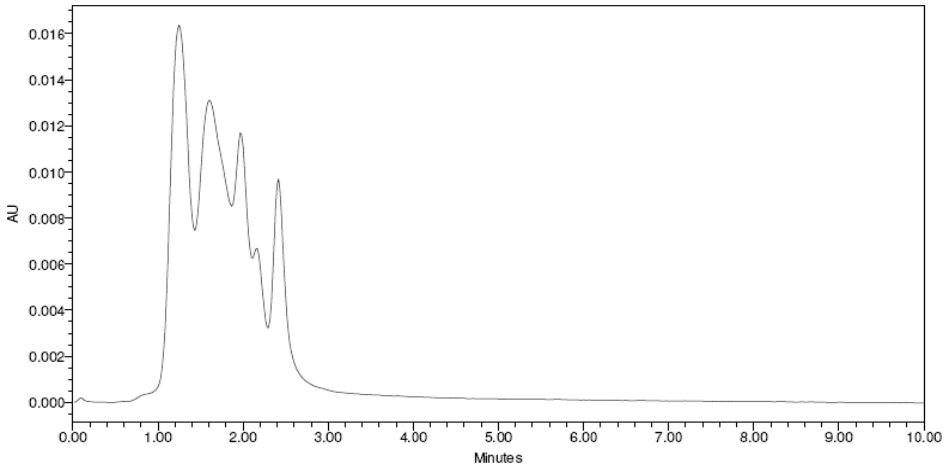

(b) PNT 60 min sample (RT = 1.25, 1.61, 1.97, 2.23 and 2.42 min)

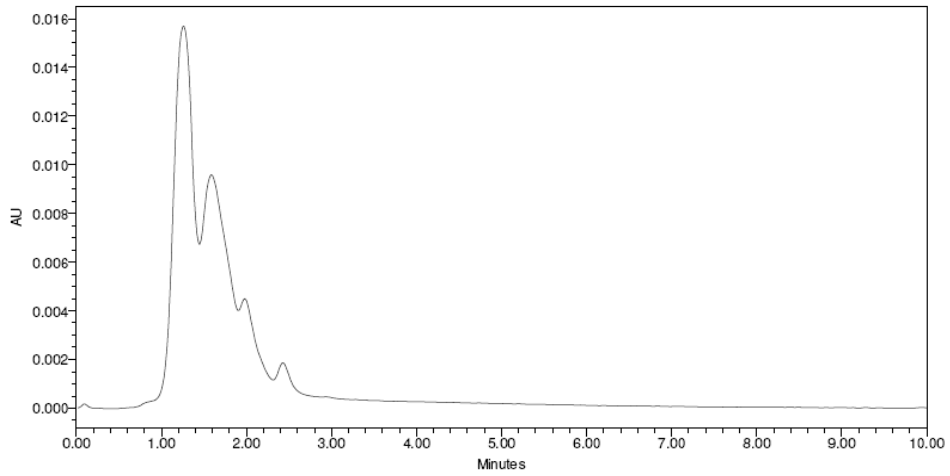

(c) PNT 4 h sample (RT = 1.26, 1.59, 2.03 and 2.42 min)

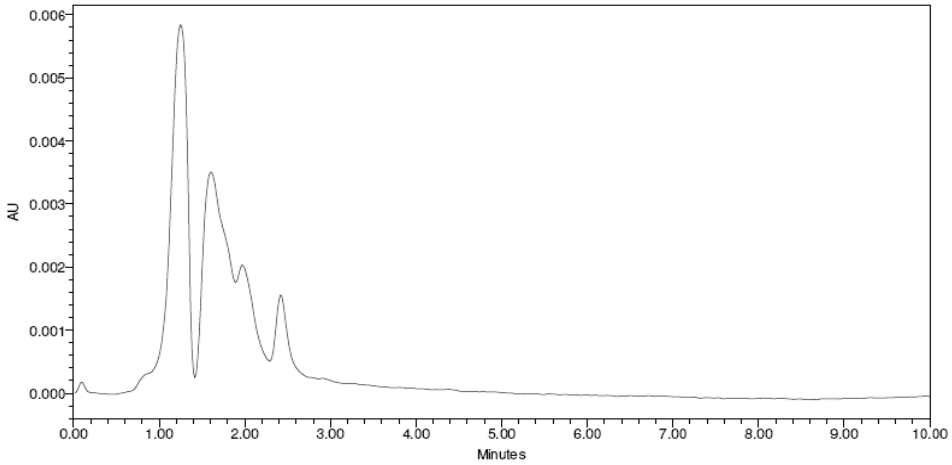

(d) PNT 8 h sample (RT = 1.25, 1.60 and 2.42 min)

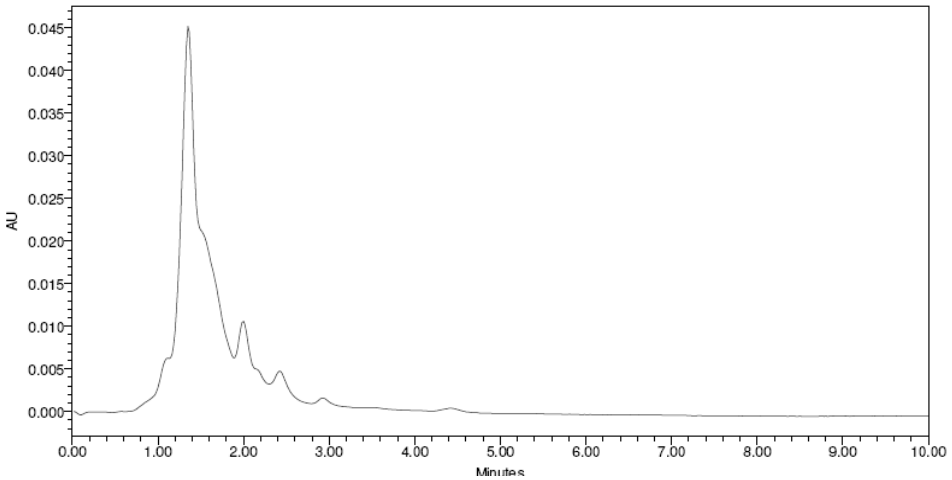

(e) PNT 12 h sample (RT = 1.35, 2.00, 2.42 and 2.93 min)

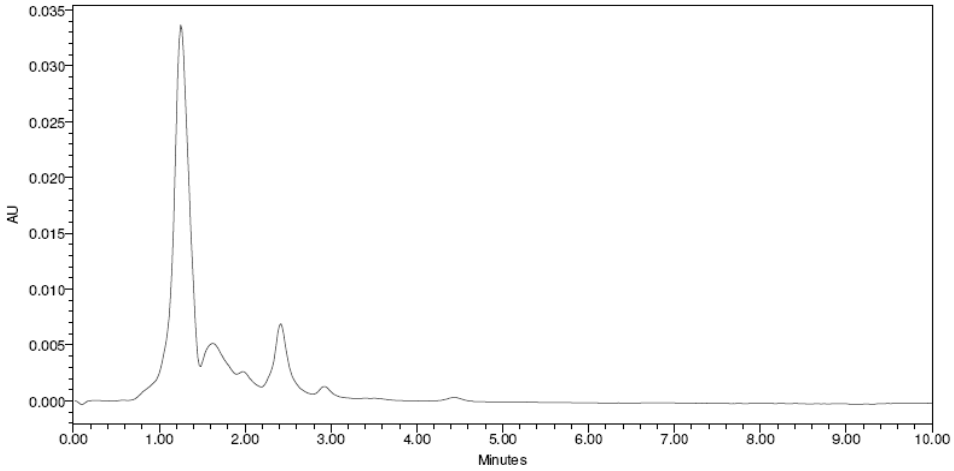

(f) PNT 24 h sample (RT = 1.26, 1.62, 2.42 and 2.92 min)

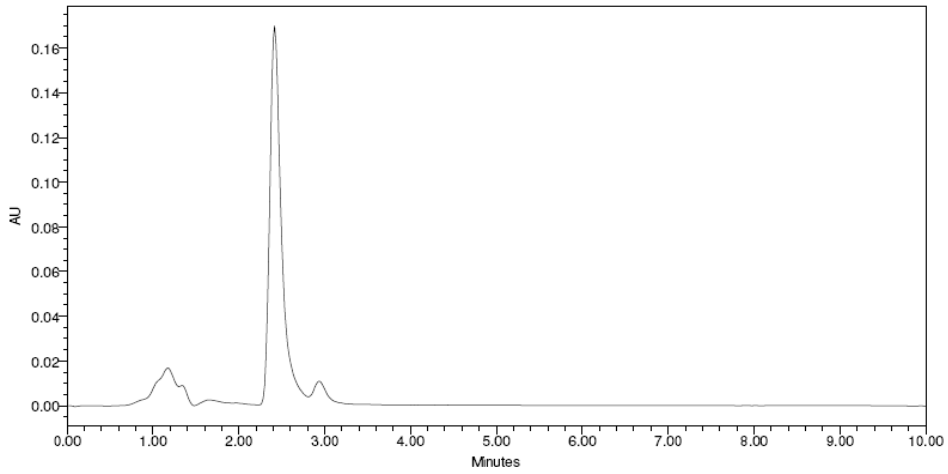

(g) PNT standard sample (RT = 1.17, 1.66 and 2.42 min)

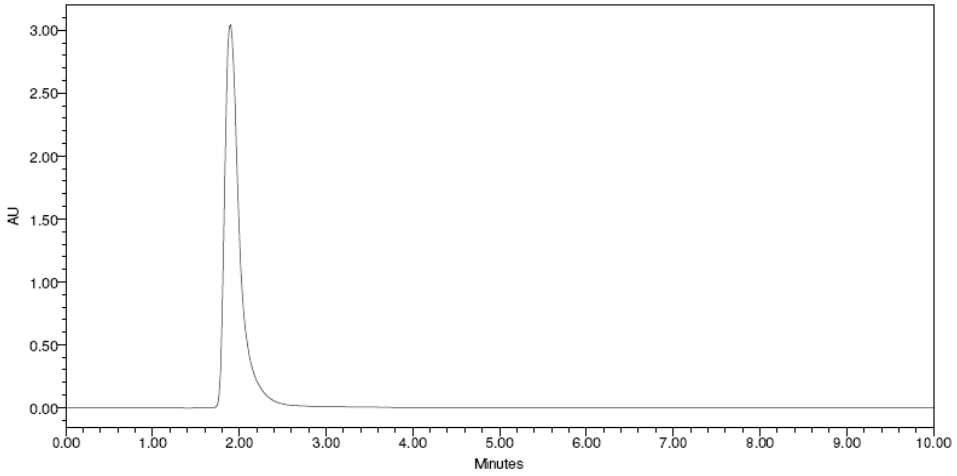

(h) Aniline standard sample (RT = 1.90 min)

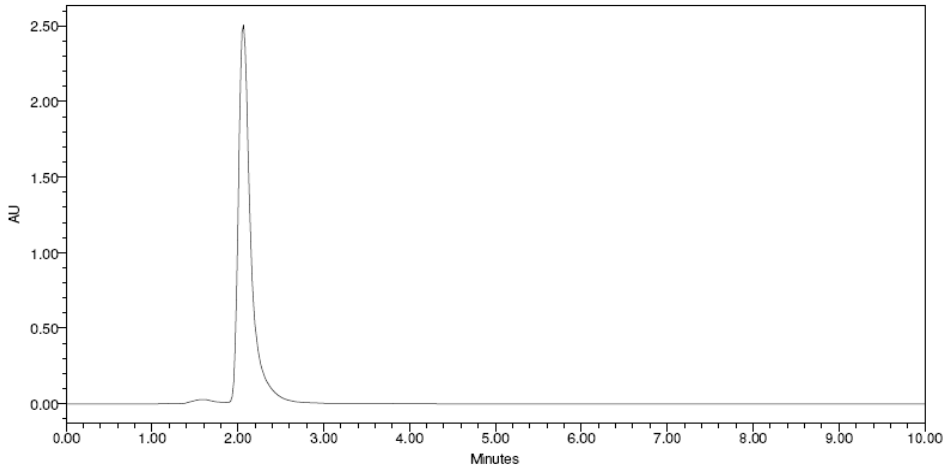

(i) Benzeldehyde standard sample (RT = 1.27, 1.59 and 2.06 min)

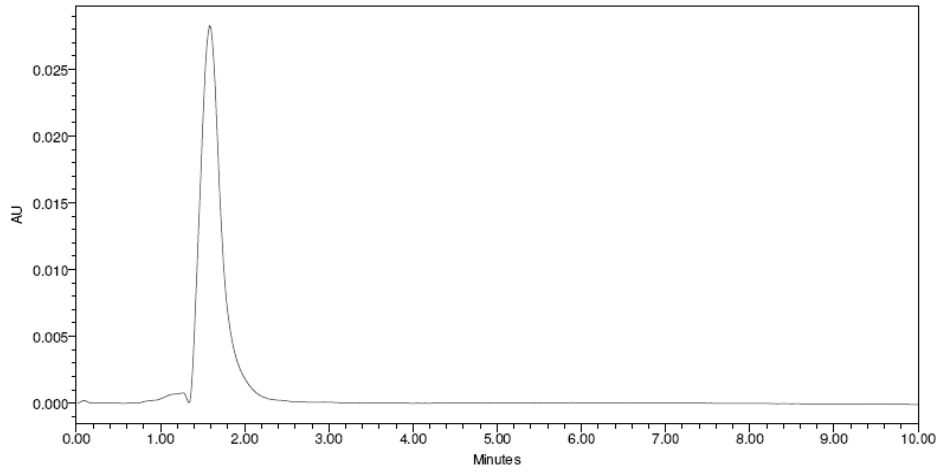

(j) Benzoic acid standard sample (RT = 1.59 min)

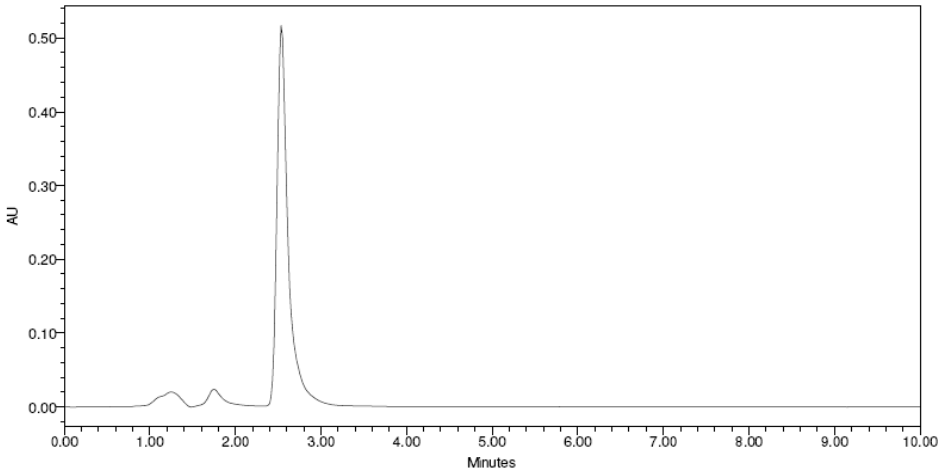

(k) Benzene standard sample (RT = 1.25, 1.75 2.54 min)

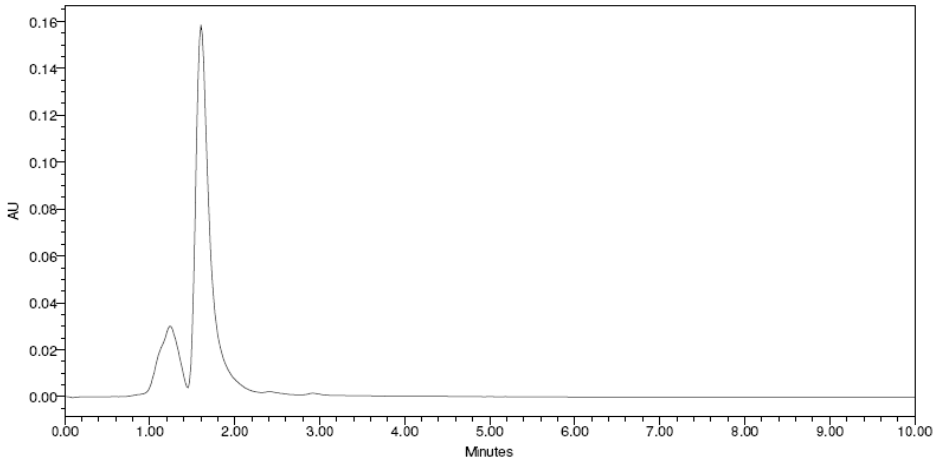

(l) Benzoquenone standard sample (RT = 1.24, 1.60 and 2.92 min)

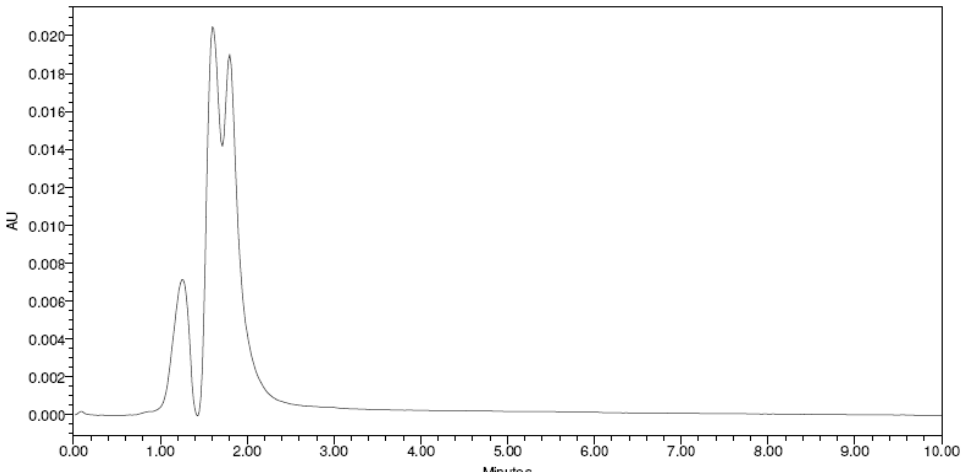

(m) Hydroquenone standard sample (RT = 1.26, 1.61 and 1.80 min)

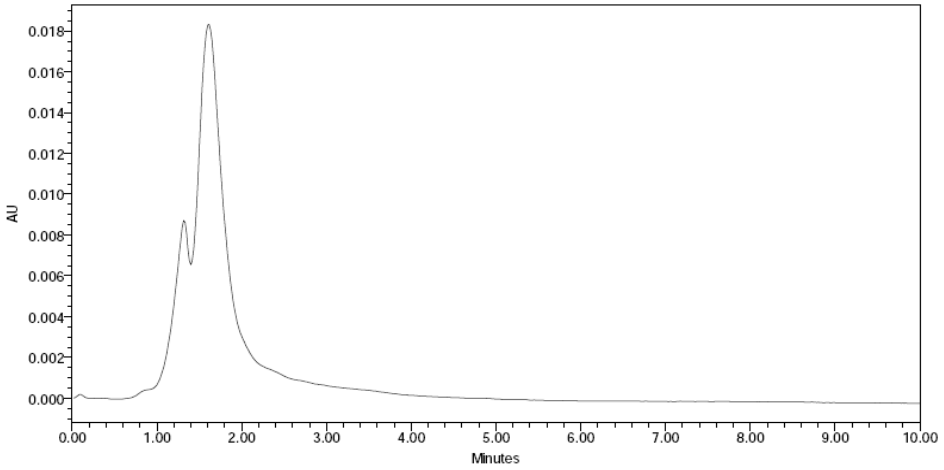

(n) *p*-aminophenol standard sample (RT = 1.32 and 1.61 min)

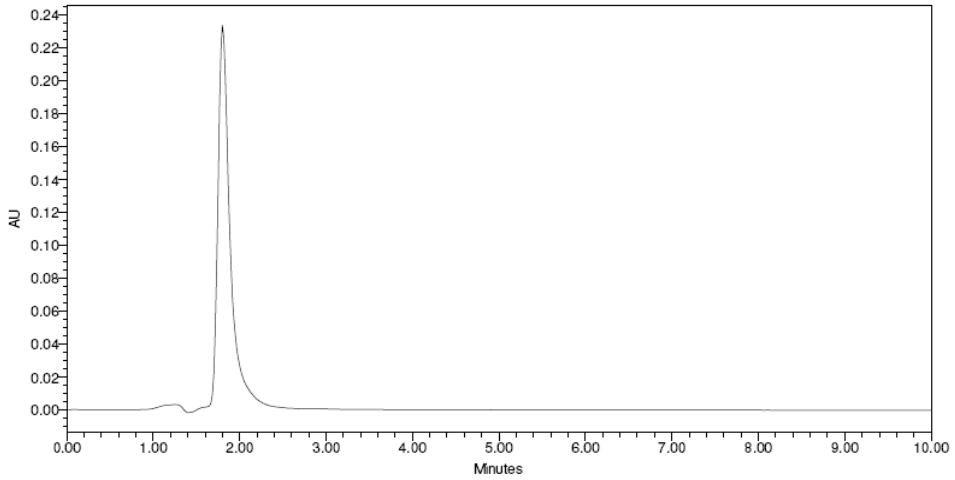

(o) Phenol standard sample (RT = 1.26 and 1.80 min)

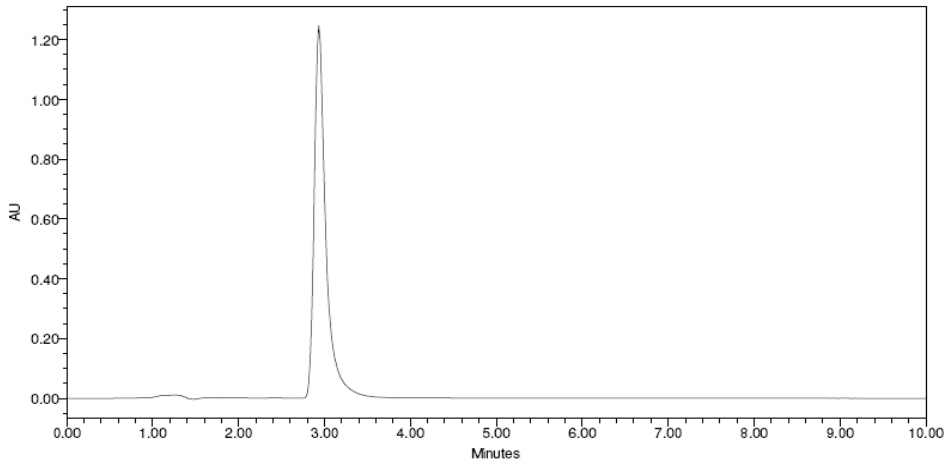

(p) Toluene standard sample (RT = 2.94 min)

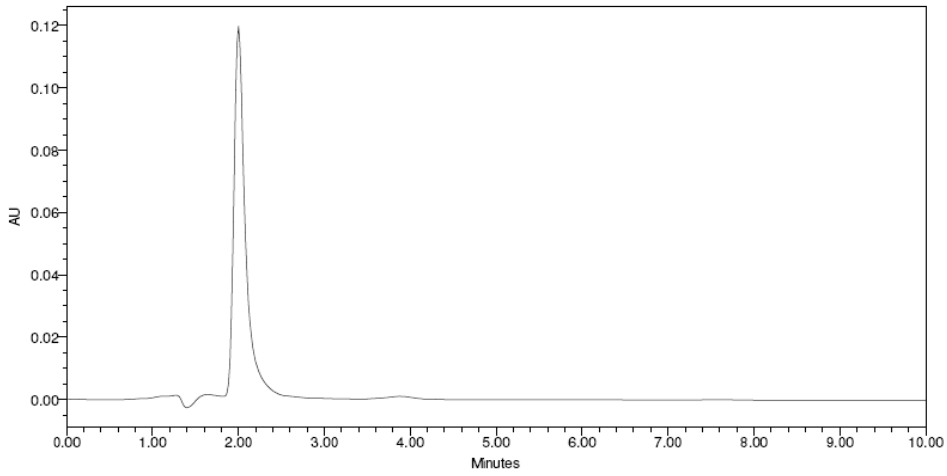

(q) *p*-toluidine standard sample (RT = 2.00 min)

Figure-5.8. HPLC chromatogram of *p*-nitrotoluene at different time intervals of reaction and standard samples (a) – (q)

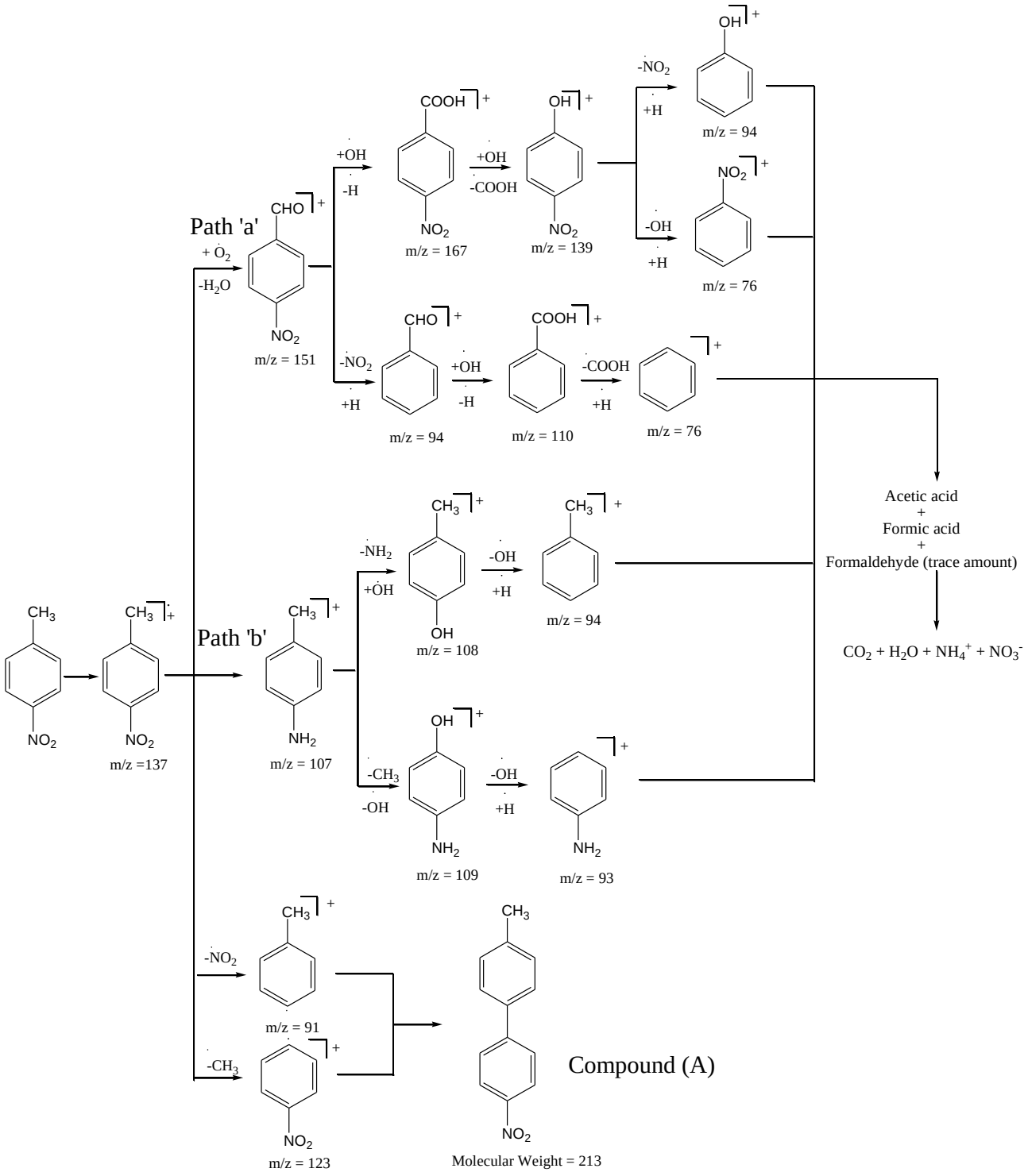

Scheme-5.1. Proposed fragmentation pattern of *p*-nitrotoluene

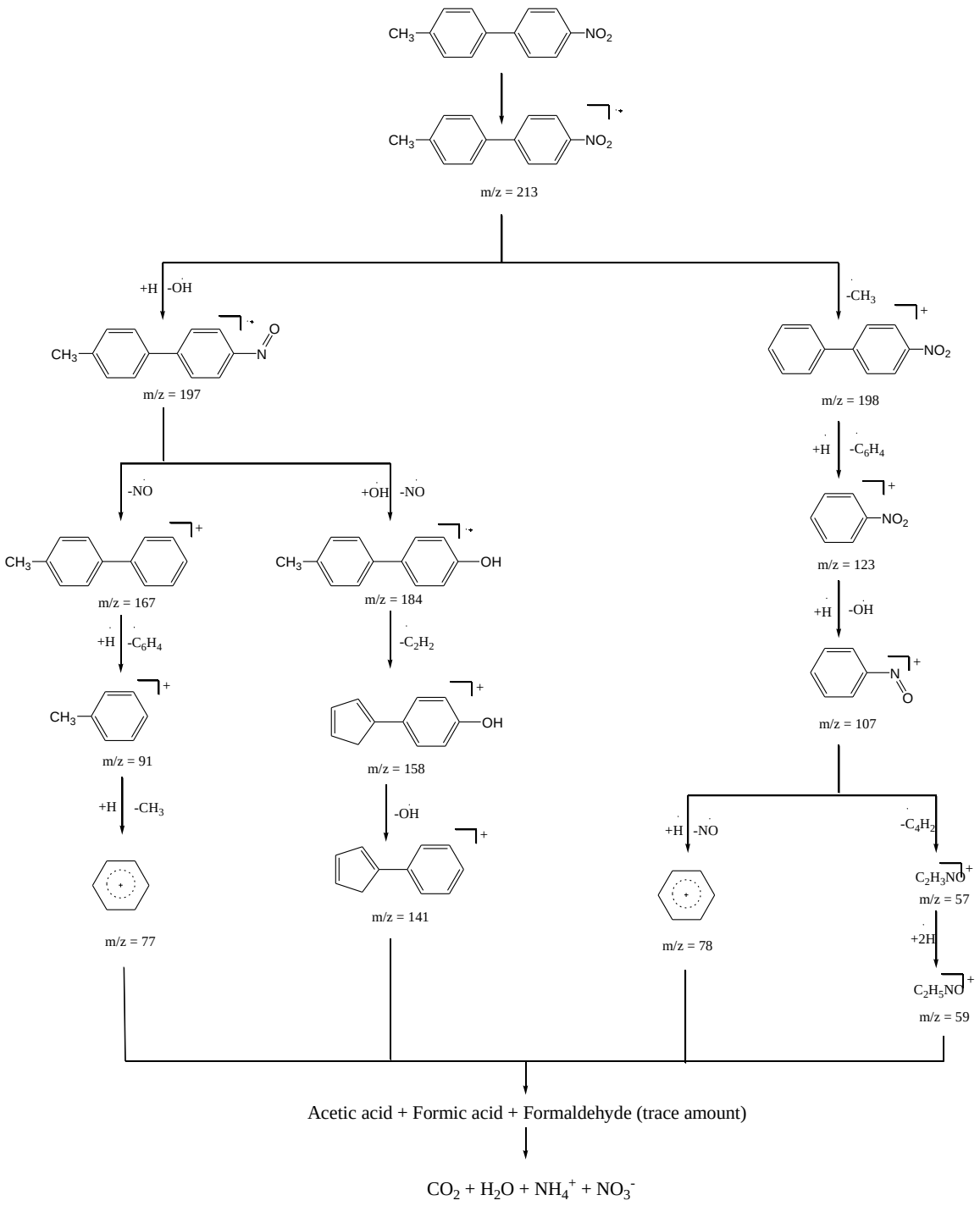

Scheme-5.2. Proposed fragmentation pattern of 4-methyl-4′-nitrobiphenyl

Appendix

In the mechanism presented in section 5.4.4, there are four possibilities of the mineralization shown from equation (5.9) to (5.12). Out of these four possibilities, we can select equation (5.11) for kinetic study. There are two reasons behind it:

(1) The intermediates are in very less concentration as compare to initial compound PNT, showing the less possibility of reaction (5.10) and (5.12).

(2) By the reaction–diffusion model, the average rate of reaction between photogeneration $OH^{\bullet}$ and semiconductor surface is far less than the diffusion rate. Thus, it is plausible for the radical to diffuse away from the surface and to react subsequently in solution with less possibility of equation (5.9).

So the case of equation (5.11) is a typical mechanism since the surface $OH^{\bullet}$ group must diffuse into solution and the organic reactant PNT must adsorb on catalytic surface after generation in bulk phase. Thus the rate disappearance of reactant PNT may be represented as:

$$r_{PNT} = k_{11}\left[OH^{\bullet}\right]\left[>TiO_2 - PNT\right] \tag{A5.1}$$

The balance for the total $OH^{\bullet}$ radical concentration from above discussion can be written as

$$\frac{d\left[OH^{\bullet}\right]}{dt} = k_3\left[TiO_2 - OH^{-}\right]\left[h_{VB}^{+}\right] - k_{-3}\left[TiO_2 - OH^{\bullet}\right] - k_{11}\left[TiO_2 - PNT\right]\left[OH^{\bullet}\right] - \sum_{i=1}^{n} k_i\left[TiO_2 - I\right]\left[OH^{\bullet}\right] \tag{A5.2}$$

However the concentration of $[>TiO_2\text{-}OH^{-}]$ should be relatively constant in aqueous media as in equation (5.3), equilibrium lies far to right. So taking this-

$$\frac{d\left[OH^{\bullet}\right]}{dt} = k_3^{'}\left[h_{VB}^{+}\right] - k_{-3}\left[TiO_2 - OH^{\bullet}\right] - k_{11}\left[TiO_2 - PNT\right]\left[OH^{\bullet}\right] - \sum_{i=1}^{n} k_i\left[TiO_2 - I\right]\left[OH^{\bullet}\right] \tag{A5.3}$$

The surface concentration of PNT, intermediates and $OH^{\bullet}$ radical can be obtained by the adsorption equilibrium so from equation (5.4), (5.5) and (5.6):

$$> TiO_2 - PNT = K_P \left[> TiO_2\right]\left[PNT\right] \tag{A5.4}$$

$$> TiO_2 - I = K_I \left[> TiO_2\right]\left[I\right] \tag{A5.5}$$

$$> TiO_2 - OH^{\bullet} = K_{OH} \left[> TiO_2\right]\left[OH^{\bullet}\right] \tag{A5.6}$$

Where $K_P = k_4/k_{-4}$, $K_I = k_5/k_{-5}$ and $K_{OH} = k_6/k_{-6}$

Using the values of (A5.4), (A5.5) and (A5.6), equation (A5.3) can be written as

$$\frac{d\left[OH^{\bullet}\right]}{dt} = k_3^{'}\left[h_{VB}^{+}\right] - k_{-3}\, k_{OH}\left[TiO_2\right]\left[OH^{\bullet}\right] - k_{11}\, k_P\left[TiO_2\right]\left[PNT\right]\left[OH^{\bullet}\right] - \sum_{i=1}^{n} k_i\, k_{OH}\left[TiO_2\right]\left[I\right]\left[OH^{\bullet}\right] \tag{A5.7}$$

Thus the bulk $OH^{\bullet}$ radical can be obtained by applying quasi steady state approximation on equation (A5.7)

$$\left[OH^{\bullet}\right] = \frac{k_3^{'}\left[h_{VB}^{+}\right]}{k_{-3}\, K_{OH}\left[> TiO_2\right] + k_{11}\, K_P\left[> TiO_2\right]\left[PNT\right] + \sum_{i=1}^{n} k_i\, K_I\left[> TiO_2\right]\left[I\right]} \tag{A5.8}$$

Here 'n' represents the number of different organic intermediate species present. Similarly, the h^+ concentration balance by quasi steady state approximation can be written as

$$\frac{d\left[H^{+}\right]}{dt} = k_1\left[> TiO_2\right] - k_2\left[h_{VB}^{+}\right]\left[e_{CB}^{-}\right] - k_3\left[> TiO_2 - OH^{-}\right]\left[h_{VB}^{+}\right] + k_{-3}\left[> TiO_2 - OH^{\bullet}\right] \tag{A5.9}$$

However, the photogenerated holes remove by recombination faster than any other traping process **[42, 46]**, so considering this equation (A5.9) can be written as

$$\frac{d\left[H^{+}\right]}{dt} = k_1\left[> TiO_2\right] - k_2\left[h_{VB}^{+}\right]\left[e_{CB}^{-}\right] \tag{A5.10}$$

As the photogeneration rate of h^+ and e^- are equal, then we can assume that $[h^+] = [e^-]$, using this and by applying quasi steady state approximation, the hole concentration from equation (A5.10)

$$\left[h_{VB}^{+}\right] = \left[k_1 / k_2\right]^{1/2} \left[> TiO_2\right]^{1/2} \tag{A5.11}$$

Putting this value in equation (A5.8)

$$\left[OH^{\bullet}\right] = \frac{k_3^{'} \left[k_1 / k_2\right]^{1/2} \left[> TiO_2\right]^{1/2}}{k_{-3}\ K_{OH} \left[> TiO_2\right] + k_{11}\ K_P \left[> TiO_2\right]\left[PNT\right] + \sum_{i=1}^{n} k_i\ K_I \left[> TiO_2\right]\left[I\right]} \tag{A5.12}$$

Using the equation (A5.12), the rate of PNT degradation

$$r_{PNT} = \frac{k_{11}\ K_{PNT} \left[> TiO_2\right]\left[PNT\right] \cdot k_3^{'} \left[k_1 / k_2\right]^{1/2} \left[> TiO_2\right]^{1/2}}{k_{-3}\ K_{OH} \left[> TiO_2\right] + k_{11}\ K_P \left[> TiO_2\right]\left[PNT\right] + \sum_{i=1}^{n} k_i\ K_I \left[> TiO_2\right]\left[I\right]} \tag{A5.13}$$

$$r_{PNT} = \frac{k\ K \left[PNT\right]}{1 + K \left[PNT\right] + \sum_{i=1}^{n} K_i \left[I\right]} \tag{A5.14}$$

Where $k = k_3^{'} \left[k_1 / k_2\right]^{1/2} \left[> TiO_2\right]^{1/2}$, $K = \frac{k_{11}\ K_{PNT}}{k_{-3}\ K_{OH}}$, $K_i = \frac{k_i\ K_I}{k_{-3}\ K_{OH}}$

k is the reaction kinetic constant (mol L^{-1} s^{-1}) and K (L mol^{-1}) is the adsorption constant of reactant PNT. K_i (L mol-1) is the adsorption constant of intermediate products adsorbed on catalyst surface.

Since the adsorption constant and concentration on intermediates are difficult to measure, two distinct approximations can be made **[47-48]**:

Approximation (1): The concentration of intermediates adsorbed on the catalyst surface can be neglected as compared to primary substrate PNT, and then equation (A5.14) can be simplified as

$$r_{PNT} = \frac{k\,K\left[PNT\right]}{1 + K\left[PNT\right]} \qquad \text{(A5.15)}$$

This is assumed to be valid for very low degree of conversion.

Approximation (2): The photocatalytic degradation process is a stepwise process where adsorption constant of intermediates and main substrate (PNT) are the same

$K_{i=1} = K_{i=2} =$ ---------- $= K_{i=n} = K$, thus equation (A5.14) becomes

$$r_{PNT} = \frac{k\,K\left[PNT\right]}{1 + K\left[PNT\right]_0} \qquad \text{(A5.16)}$$

Where $[PNT]_0$ represent the initial concentration of reactant PNT.

Since in initial condition $[PNT] = [PNT]_0$, then using equation (A5.15)

$$\frac{1}{r_{PNT}} = \frac{1}{k} + \frac{1}{k\,K} \cdot \frac{1}{\left[PNT\right]_0} \qquad \text{(A5.17)}$$

From the plot of $1/r_{PNT}$ vs. $1/[PNT]_0$, we can get the values of k and K. All the parameters were determined using the initial rates and initial concentration data where the effect of the intermediates can be conveniently neglected (Approximation 2). The intercept determines the reaction kinetic constant '*k*' that varies with the rate of degradation and the value of adsorption constant '*K*' can be obtained by the slope of the curve.

5.6. REFERENCES

[1] Bekkum H. V; Flanigen E.M.; Jansen J.C. (Editors). *Introduction to zeolite science and practice.* Elsevier Science Ltd., Amsterdam. **1991**.

[2] Sing K. S. W., *J. of Porous Mater.* **1995**, *2*, 5-8.

[3] Matsumoto A.; Zhao J.; Tsutsumi K., *Langmuir*, **1997**, *13*, 496-501.

[4] Tayade R.J.; Kulkarni R.G.; Jasra R.V., *Ind. Eng. Chem. Res.* **2007,** *46*, 369-376.

[5] Tsutsumi K.; Takahashi H., *J. of Phys. Chem*. **1970**, *74*, 2710-2713.

[6] Tsutsumi K.; Takahashi H., *J. Phys. Chem*. **1972**, *76*, 110-115.

[7] Iu, K. K.; Thomas J. K., *J. Phys. Chem*. **1991**, *95*, 506-509.

[8] Uchida H.; Itoh S.; Yoneyama H., *Chem. Lett*. **1993**, *22*, 1995-1998.

[9] Dagan G.; Tomkiewich M., *J. Phys. Chem*. **1993**, *97*, 12651-12655.

[10] Augustynski J., *Electrochim Acta*. **1993**, *38*, 43-46.

[11] Keane M. A., *Microporous Mater*. **1996**, *7*, 51-59.

[12] Iu, K. K.; Thomas J. K., *Langmuir*. **1990**, *6*, 471-478.

[13] Al-Ekabi H.; Seone N., *J. Phys. Chem.* **1988**, *92*, 5726-5731.

[14] Akurati K.K.; Bhattacharya S.S.; Winterer M.; Hahn, H., *J. Phys. D: Appl. Phys.* **2006**, *39*, 2248–2254.

[15] Corma A.; Garcia H., *Chem. Commun.*, **2004**, 1443-1459.

[16] Kim Y.; Yoon M., *J. of Mol. Catal. A: Chemical*, **2001**, *168*, 257-263.

[17] Patterson H. H.; Gomez R. S.; Lu H.; Yson R. L., *Catalysis Today*, **2007**, 120, 168–173.

[18] Matsuoka M.; Ju W. -S.; Yamashita H.; Anpo M., *J. Photochem. Photobio. A: Chem.* **2003**, *160*, 43–46.

[19] Kanan S. M.; Kanan M. C.; Patterson H. H., *J. Phys. Chem. B.* **2001**, *105*, 7508-7516.

[20] Gachard, E.; Belloni, J.; Subramanian, M. A., *J. Mater. Chem.* **1996**, *6*, 867-870.

[21] Anpo, M.; Kondo, M.; Coluccia, S.; Che, M., *J. Am. Chem. Soc.* **1989**, *111*, 8791-8799.

[22] Sun T.; Seff K., *Chem. Rev*. **1994**, *94*, 857-870.

[23] Anpo M.; Zhang S.G.; Matsuoka M.; Yamashita H., *Catal. Today.* **1997,** *39*, 159-168.

[24] Tayade R. J.; Surolia P. K.; Lazar M. A.; Jasra R. V., *Ind. Eng. Chem. Res. Ind. Eng. Chem. Res.* **2008,** *47*, 7545-7551.

[25] Tran H.; Chiang K.; Amal R., *Photochem. Photobiol. Sci.* **2005**, *4*, 565-567.

[26] Ollis, D. F., *Environ. Sci. Technol*. **1985**, *19*, 480-484.

[27] Matthews, R., *J. Catal*. **1988**, *111*, 264-272.

[28] Pelizzetti, E., Barbeni, M., Pramauro, E., Serpone, N., Borgarello, E., Jamieson, M., and Hidaka, H., *Chim. Ind. (Milan.)* **1985**, *67*, 623-625.

[29] Madeira, P.; Nunes, M. R.; Borges, C.; Costa, F. M. A.; Florêncio, M. H., *Rapid Commun. Mass Spectrom*. **2005**, *19*, 2015-2020.

[30] Florêncio, M. H.; Pires, E.; Castro, A. L.; Nunes, M. R.; Borges, C.; Costa, F. M., *Chemosphere*. **2004**, *55*, 345-355.

[31] Chen H.; Matsumoto A.; Nishimiya N.; Tsutsumi K., *Colloids and Surfaces*. **1999**, *157*, 295-305.

[32] Ray G. J.; Nerheim A. G.; Donohue J. A., *Zeolites*. **1988**, *8*, 458-463.

[33] Tayade, R. J.; Kulkarni, R. G.; Jasra, R. V., *Ind. Eng. Chem. Res*. **2006**, *45*, 922-927.

[34] Gratzel, M., Heterogeneous Photochemical Electron Transfer; *CRC Press: Baton Rouge, LA*, **1988**.

[35] Shi C.; Cheng M.; Qu Z.; Bao X., *Appl. Catal. B: Environ.* **2004,** *51*, 171–181.

[36] Shimizu K.–i.; Shibata J.; Yoshida H.; Satsuma A.; Hattori T., *Appl. Catal. B: Environ.* **2001**, *30*, 151–162.

[37] Shimizu K.-i.; Satsuma A., *Phys. Chem. Chem. Phys.*, **2006**, 8, 2677–2695.

[38] http://www.cameochemicals.noaa.gov.

[39] http://www.meti.go.jp.

[40] Naskar S.; Pillay S. A.; Chanda M., *J. Photochem. Photobio. A: Chem.* **1998**, *113*, 257–264.

[41] Turchi C. S.; Ollis F. D., *J. Catal*. **1990**, *122*, 178-192.

[42] Sung-Suh H. M.; Choi J. R.; Hah H. J.; Koo S. M.; Bae Y. C., *J. Photochem. Photobio. A: Chem.* **2004**, *163*, 37–44.

[43] Andersson M.; Birkedal H.; Franklin N. R.; Ostomel T.; Boettcher S.; Palmqvist A. E. C.; Stucky G. D., *Chem. Mater*. **2005**, *17*, 1409-1415.

[44] Mills G.; Hoffman M. R., *Environ. Sci. Technol*. **1993**, *27*, 1661-1689.

[45] Mao Y.; Schoneich C.; Asmus K.D., *J. Phys. Chem.* **1991**, *95*, 10080-10089.

[46] Rothenberger G.; Moser J.; Grätzel M.; Serpone N.; Sharma D. K., *J. Amer Chem.* **1985**, *107*, 8054-8059.

[47] Gora A.; Toepfer B.; Puddu V.; Puma G. L., *Appl. Catal. B: Environ.* **2006**, *65*, 1–10.

[48] Turchi C. S.; Ollis F. D., *J. Catal*. **1989**, *119*, 483-496.

Chapter 6

TiO_2 Coating on Cenosphere Surface towards Industrial Photocatalysis

6.1. INTRODUCTION

The photocatalytic oxidation has been attracted a great deal of attention as a potential method for the remediation of aqueous organic environmental contaminants **[1-4]** and occurs most rapidly in the presence of powdered catalyst. These powdered catalysts are very fine and cumbersome to recover them. However, to make photocatalytic oxidation suited to practical situations, the catalyst must be easily recovered, reusable, employed to allow most rapid photooxidation possible and active under solar light. Moreover, most of the photocatalysts studied have high density and cannot float on the aqueous surface. The attempts have been done to overcome these problems by preparing TiO_2 coated buoyant material such as polystyrene beads, sand, activated carbon, porcelain beads and ceramic microspheres **[5-9]**. These studies reported did show successful photooxidation but had lack of reusability due to leaching of photocatalyst. Thus the strong adhesion of TiO_2 on buoyant surface is needed to overcome the problem of catalyst leaching so that coating is stable even after multiple uses. For the smart selection of buoyant support, inexpensive material is preferred so that the prepared catalyst is cost effective.

Fly-ash cenospheres are hollow inorganic mixed inorganic oxide having nearly spherical shapes spheres and are the by-products of coal-fired power generation plants. The hollow spheres have trapped nitrogen or other gases inside and are very light material and thus can be used as buoyant support material for photocatalyst. Thus fly-ash cenospheres those are stable, non-toxic, non-metallic hollow particles those can float on water surface. However, still only a very few studies are reported involving the cenosphere as a catalyst or catalytic support material **[5]**.

Figure-6.1. Cenosphere particles and fly-ash removal at coal thermal power plants

The photooxidation of petroleum constituents is the key factor in the weathering processes in the marine environment [**10-11**]. Photocatalytic reactions transform the hydrocarbons to more water soluble and hazardless, small more mobile compounds. Some investigations concern the photocatalytic transformation of hydrocarbons and possible application in the cleaning up of marine oil spills [**5, 12-13**].

6.1.1. Coating of the semiconductor on supporting surface

The coating of the semiconductor materials on the support surface is a great deal of concern due to the spontaneous aggregation of TiO_2 nanoparticles in the aqueous reaction system **[14]**. Recent research interest has been focused on nonporous solid supports because light penetration is into the pore surface to access the TiO_2 particles dispersed on the pore surface [**15-20**] is not always facile and it is the external surface of the porous support on which supported TiO_2 is effective in photocatalytic decomposition of organic compounds. Several strategies have been described for coating of TiO_2 films on SiO_2 materials including sol-gel **[21]**, chemical vapour deposition **[22-25]** and liquid-phase deposition methods **[26-28]**.

6.1.2. Aim of the work

In this study, we synthesized the buoyant TiO_2 coated cenosphere particles via sol-gel method for the stable coating. The synthesized material was fully characterized by analytical instrumental techniques. The photocatalytic study of the synthesized materials was carried out by the photocatalytic degradation of Methylene blue (MB), *p*-nitroaniline (PNA) and saturated hydrocarbons; *n*-decane and *n*-tridecane under the solar light. In the solar light, very small part consist of photons that have sufficient energy to promote the valence band electron to conduction band of TiO_2 but still solar light assisted clean up can be quite fast even with the residual photons in the wavelength range 300-390 nm.

The benefit of this type of coating is its stability which is due to the covalent bonding between the cenosphere surface and the TiO_2 framework and thus it results in the stable coating. This material can be used for the photocatalytic oxidation of the saturated hydrocarbons which form a layer on the water surface. Such hydrocarbon layers can be

very perilous to the aquatic ecology. Thus prepared catalysts promise aspects of the photocatalysis relevant to the marine environment.

6.2. TiO_2 COATING ON CENPSPHERE SURFACE

6.2.1. Chemicals and Materials

Titanium (IV) isopropoxide was purchased from *Aldrich* USA. Fly-ash cenospheres were taken from NTPC, Shaktinagar, U.P., India. Methylene blue (MB), *p*-nitroaniline (PNA), *n*-decane and *n*-tridecane AR grade were purchased form s.d. fine-chem Ltd. Mumbai India. Deionised distilled water was used to make up the reaction mixture.

6.2.2. Coating process

Titanium tetraisopropoxide was chosen as TiO_2 precursor for the coating on Fly-ash cenospheres. The coating process is shown in the **scheme-6.1**. The 0.1 M solution of titanium tetraisopropoxide was prepared in the 100 ml dry ethanol and this solution was stirred for 30 min to make the solution homogeneous. 5 gm cenospheres were added to this solution and allowed to stir for 12 h. This slurry was hydrolyzed with distilled water followed by solvent evaporation using rotavapor. The sample was dried in oven at 120 °C and calcined at 450 °C for 5 h under the air.

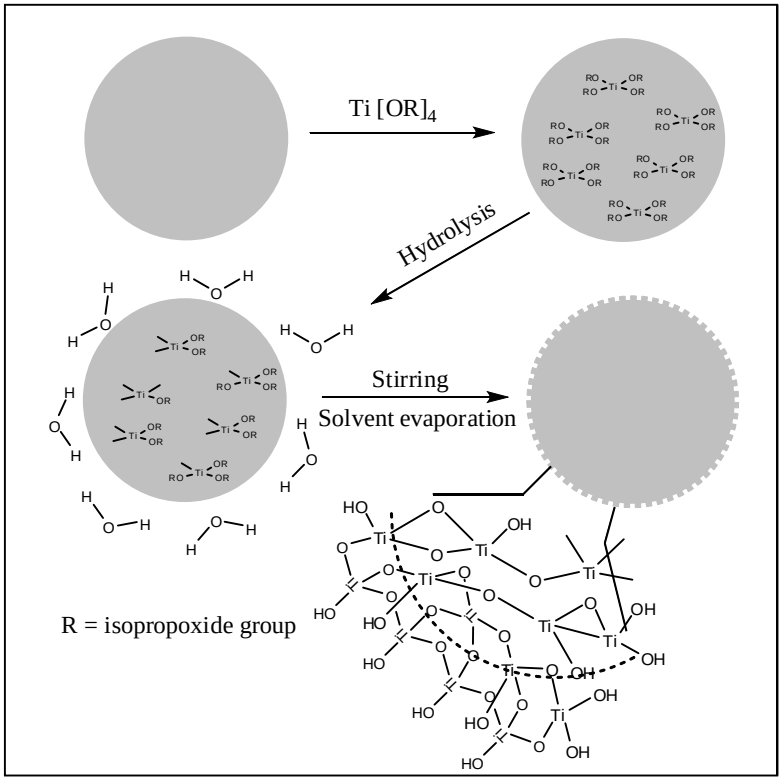

Scheme-6.1. The TiO_2 coating process on cenospheres surface

6.3. CHARACTERIZATION OF PREPARED PHOTOCATALYSTS

6.3.1. X-ray diffraction (XRD)

The X-ray diffraction data were collected on a *Phillips X'pert MPD system* using CuKα1 (λ = 0.15405 nm) radiation at 295 K. Diffraction patterns were taken over the 2θ range of 10°- 70° at the scan speed of 0.1°sec^{-1}. The X-ray diffraction of the coated and uncoated samples was carried out to confirm the TiO_2 coating and the components of cenosphere. The obtained X-ray powder diffraction patterns of bare and coated cenosphere are presented in **Figure-6.1.** All sharp peaks in the Figure can be identified mainly to either mullite M, ($3Al_2O_3.2SiO_3$) or quartz Q, (SiO_2) **[29]** which confirm that the cenosphere particles are mainly composed of mixture of mullite and quartz. The TiO_2 coated samples exhibit a peak at 2θ = 25.3° corresponding to anatase phase of the titania. The anatase phase is responsible for photocatalytic activity of the catalyst. The broad diffraction peak

maxima centered at around 2θ = 24° indicates the presence of amorphous (glassy) aluminosilicate phase in the fly-ash sample **[30]**. The crystallinity of the bare and coated cenosphere was found almost same from this figure.

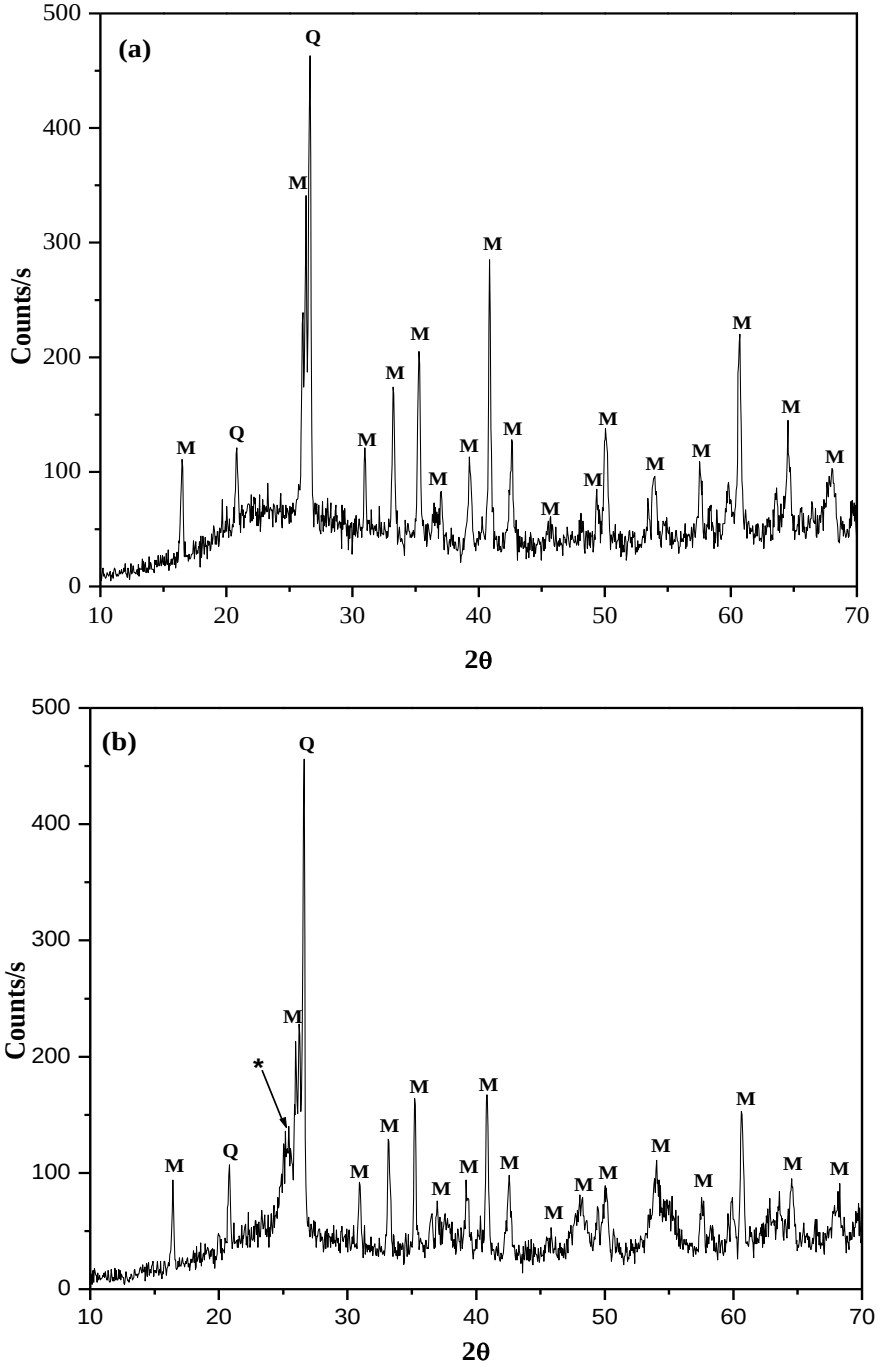

* show the peak for TiO_2 at 2θ = 25.3

Figure-6.1. XRD pattern of (a) bare cenosphere (b) TiO_2 coated cenosphere catalyst

6.3.2. The Scanning Electron Microscopy (SEM)

The morphology of the synthesized catalysts was studied using Scanning Electron Microscopy (Leo Series VP1430). The sample powder was supported on aluminium stubs prior to measurement. The SEM images of the uncoated and coated fly-ash cenospheres particle shows that the particles are spherical in shape and TiO_2 particles has formed a uniformly layer on it (**Figure-6.2**). The cenosphere are spherical in shape caused by the surface tension forces acting on the melt to minimize surface free energy during cooling. This coating is due to the development of TiO_2 network on the cenosphere particle surface as shown in **scheme-6.1**. The SEM images of the used TiO_2 coated cenosphere catalysts also show the presence of TiO_2 on the cenosphere surface which confirms the stability of the coating. Some clusters can also be seen to be deposited on the surface.

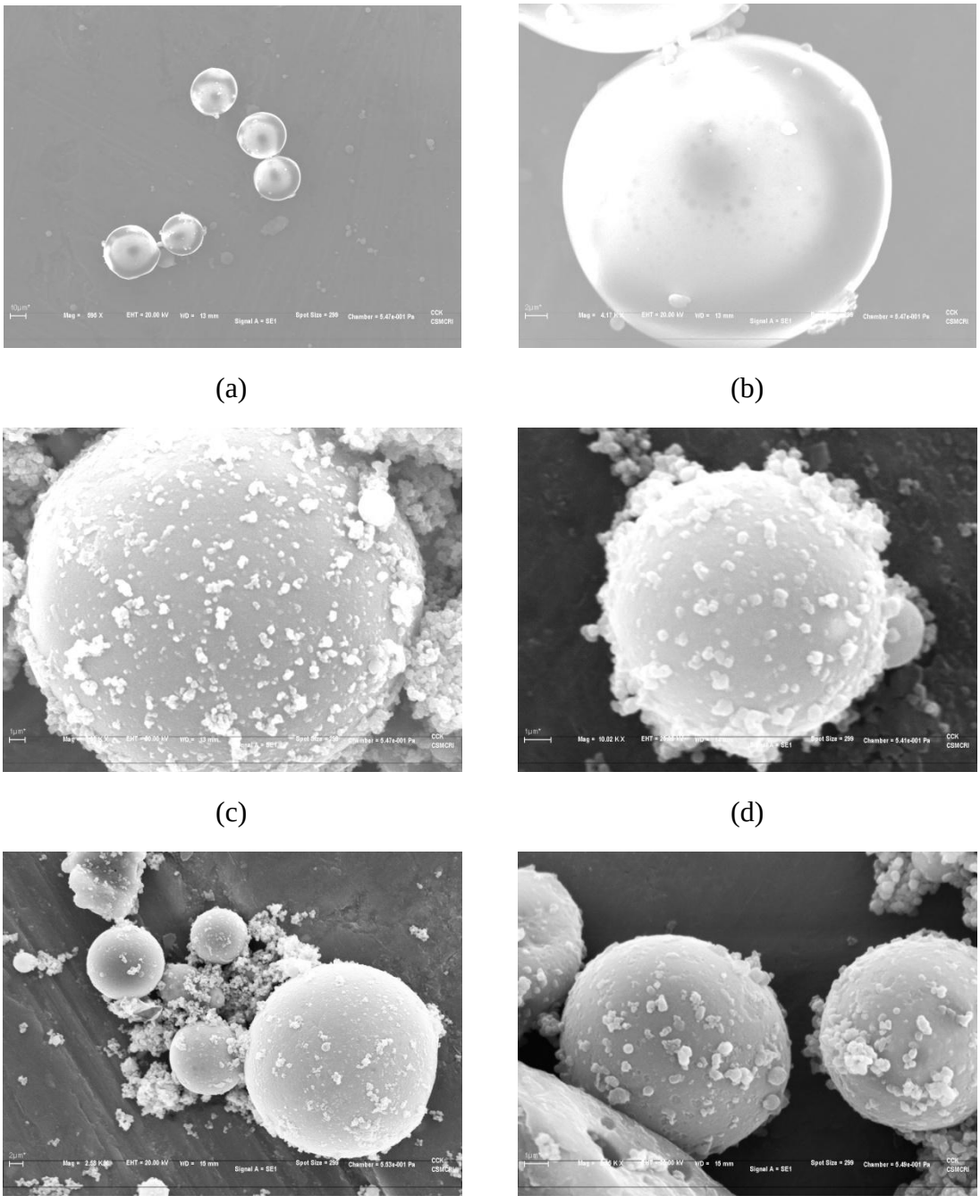

(a) (b)

(c) (d)

(e) (f)

Figure-6.2. SEM images of cenosphere (a), (b) bare cenospheres; (c), (d) TiO_2 coated cenospheres and (e), (f) TiO_2 coated cenospheres after reaction performed

6.3.3. Energy dispersive X-ray analysis (EDAX)

Scanning electron microscope *(Leo series 1430 VP)* equipped with INCA, Energy Dispersive System (EDX), Oxford instruments was used to confirm the elements present in the cenosphere, the increased Ti element concentration at the cenosphere surface and to determine the morphology of catalysts.

The EDAX analysis was carried out to find out the chemical composition of these particles (**Figure-6.3**). These results with X-ray analysis confirm that these particles are mainly composed of a mixture of oxides of Si and Al and the main components are mullite and quartz, while other oxides of trace elements such as K, Fe, Ca, Ti and Mg are also present. The peaks corresponding to 'Ti' and 'O' were found increased after coating process indicating successful TiO_2 nano particle network formation on the cenosphere particles. The Si:Al ratio was observed constant before and after coating. The weight and atomic % values are given in **Table-6.1**. The SEM and EDAX analysis suggest the successful TiO_2 coating on the surface of fly-ash cenosphere particles by the sol-gel process.

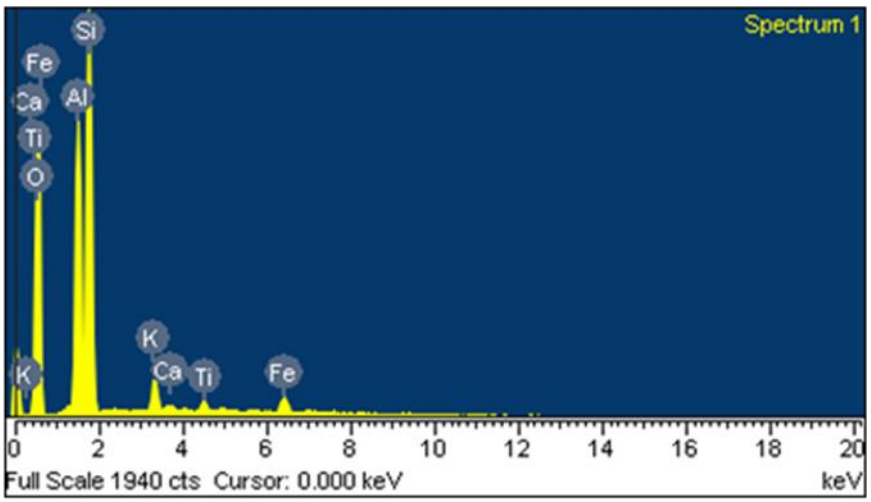

(a)

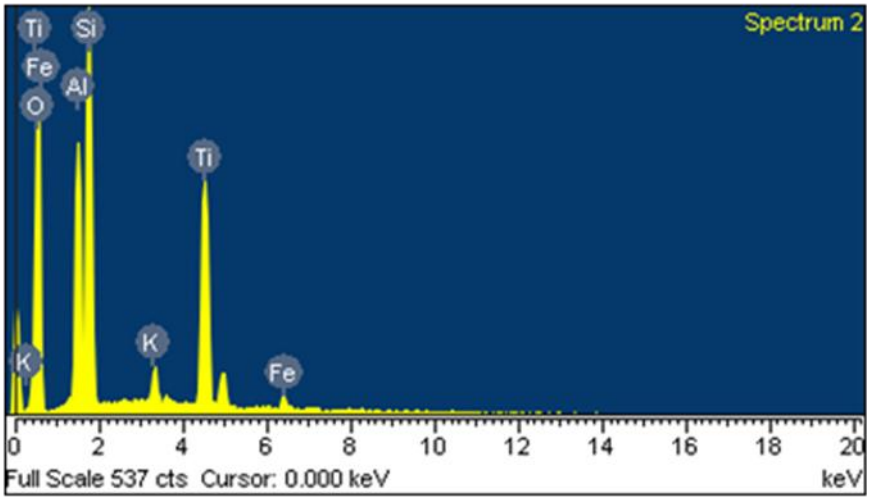

(b)

Figure-6.3. EDAX results of (a) bare cenosphere (b) TiO_2 coated cenosphere

Table-6.1. Elemental values (Weight % and Atomic %) of the uncoated and coated cenospheres particles by EDAX analysis

Element	Bare cenospheres		TiO_2 coated cenosphere	
	Weight %	Atomic %	Weight %	Atomic %
Si	22.86	16.24	13.98	10.17
Al	13.91	10.29	9.07	6.86
Fe	3.00	1.07	1.19	0.43
K	2.23	1.14	1.42	0.74
Ca	0.31	0.15	-	-
Ti	1.00	0.42	15.47	6.60
O	56.70	70.70	58.88	75.19

6.3.4. Transmission Electron Microscopy (TEM)

Phase identification and the coating were also conducted using transmission electron microscopy (JEOL JEM 2100 Model 794). The coating and presence of TiO_2 layer on the cenosphere particles was studied more thoroughly using TEM analysis, and typical micrographs and selected area electron diffraction pattern of the synthesized catalyst are shown in **Figure-6.4 (a)-(d)** and **Figure-6.4 (e)-(f)** respectively. The selected area electron diffraction patterns were taken at the position A and B shown in the circles in the **Figure-6.4 (d)**. The TEM images show the hexagonal morphology of the TiO_2 particles. The **Figure-6.4 (e)** shows the selected area electron diffraction pattern of TiO_2 particles on the cenosphere surface while **Figure-6.4 (f)** shows the TiO_2 particles from the side of the cenosphere particles. This selected area electron diffraction pattern has shown the planes 101, 004, 200 and 105 which indexed to anatase crystalline phase of TiO_2.

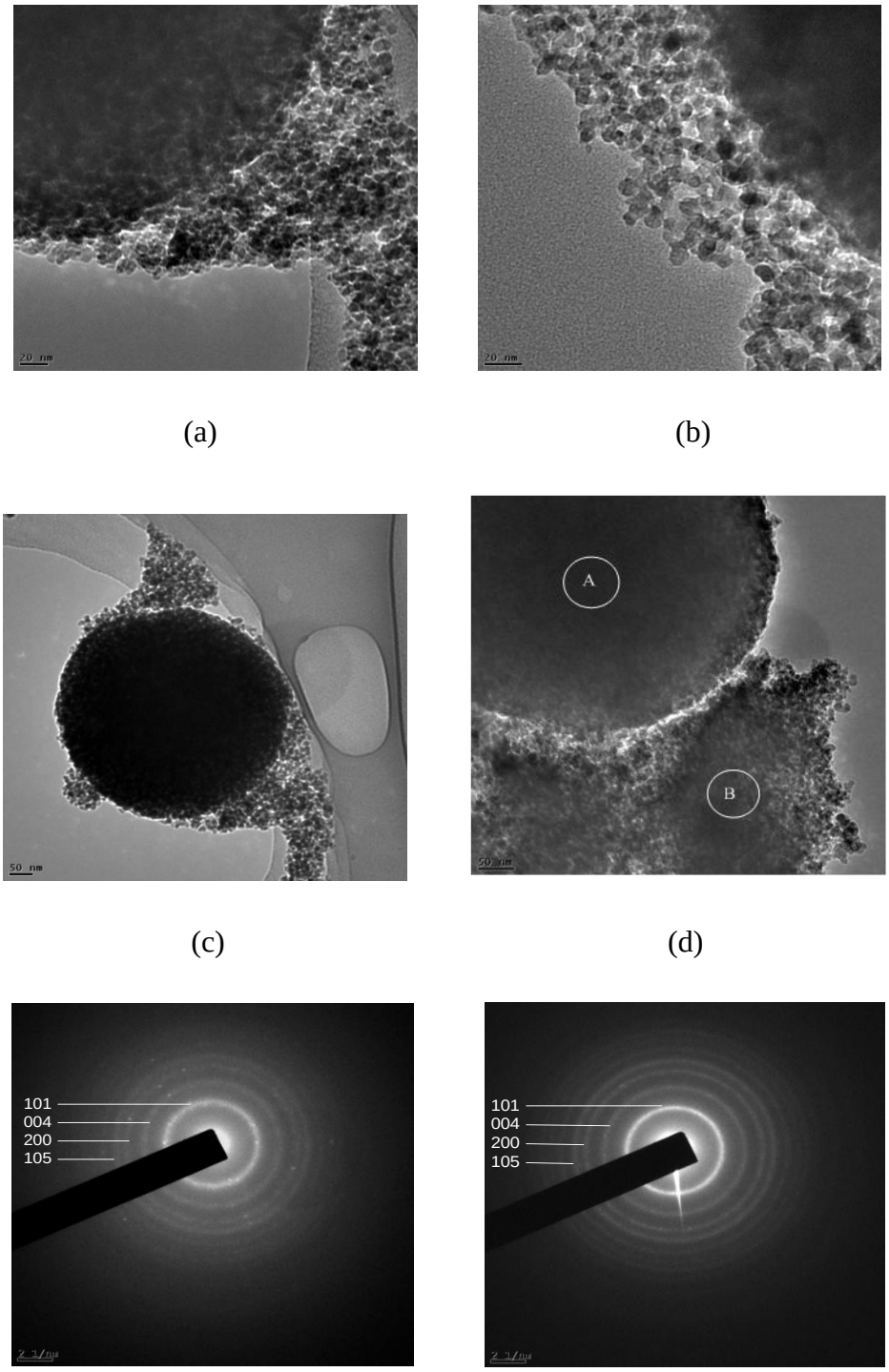

Figure-6.4. Transmission electron micrographs (a)-(d) and selected area electron diffraction pattern (e)-(f) of TiO_2 coated cenosphere

6.3.5. Optical Micrograph analysis

The optical micrographs were viewed under a light microscope (Carl Zeiss Axion imager). The optical micrographs were taken to confirm shape of the particles and the stability of the coating towards the mechanical forces. The ultrasonication was applied as mechanical force. The micrographs of the prepared catalyst are shown in **Figure-6.5**. The coated TiO_2 particles were found at the cenospheres surface even after applying the ultrasonication force as shown in **Figure-6.5 (c)**. This confirms the stability of the coating towards the mechanical forces.

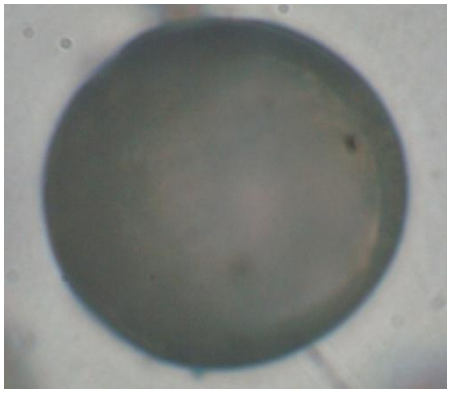

(a)

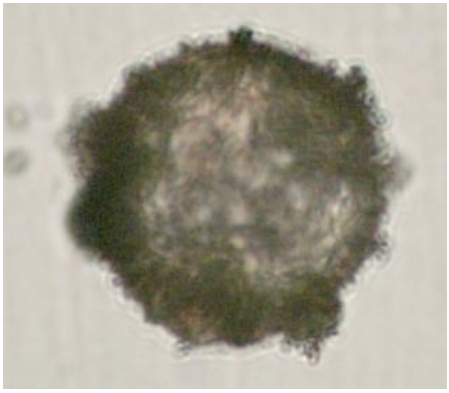

(b)

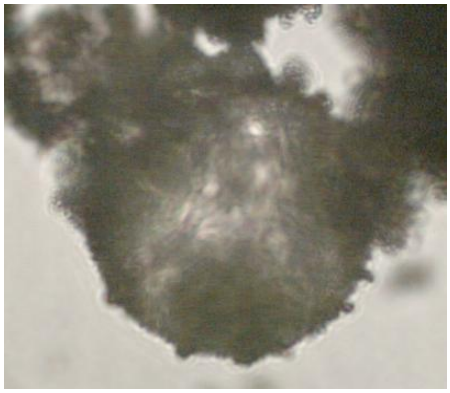

(c)

Figure-6.5. Optical micrograph of (a) bare cenospheres (b) TiO_2 coated cenospheres and (c) TiO_2 coated cenospheres after ultrasonication treatment

6.3.6. Infra red spectroscopic measurement (FT-IR)

The FT-IR spectroscopic measurements were carried out using *Perkin-Elmer GX spectrophotometer*. The spectra were recorded in the range 400-4000 cm^{-1} with a resolution of 4 cm^{-1} as KBr pellets.

The bonding of the coated and uncoated cenospheres particles were confirmed by FT-IR analysis. The FT-IR spectra of coated and uncoated fly-ash cenosphere are shown in **Figure-6.6**. The **Figure-6.6 (a), 6.6 (b), 6.6 (c) and 6.6 (d)** shows the FT-IR spectra of uncoated, coated, used for first cycle and used for second cycle respectively. The uncoated fly-ash cenosphere showed FT-IR bands at 1095 and 451 cm^{-1} with shoulders at 1189 and 552 cm^{-1}. The band 1095 and 1189 cm^{-1} are attributed to symmetric stretching vibration of Si-O-Si and asymmetric vibration of Al-O-Si respectively, while the band at 451 cm^{-1} is attributed to bending vibration of Si-O-Si. An additional band is observed at 552 cm^{-1} in case of tectosilicate such as quartz, crystobalite etc. The peaks at 800 and 720 cm^{-1} are due to the asymmetric stretching vibration and symmetric vibration of Si-O-Si and Al-O-Si respectively. The peaks at 3441 and 1692 cm^{-1} are due to the OH-stretching and bending vibrations of the adsorbed water or surface hydroxyl groups. The silicate bands are broad and diffuse because of the overlapping of different types of silicate molecular vibration resulting from various silicate minerals. Hence, only those vibrations that are unique and do not interfere with other silicate minerals are observed distinctly in the spectrum. After coating of TiO_2 on the cenosphere surface, the peaks due to the Si-O-Si and Al-O-Si get diminished. This is due to the formation of Si-O-Ti and Al-O-Ti bonds at the surface of cenosphere. However, the band of Si-O-Ti and Al-O-Ti near at 450 cm^{-1} cannot identify individually. The surface water molecule and hydroxyl groups remain almost same after the coating. The FT-IR spectra were also recorded after the use of TiO_2 coated cenosphere for first and second reaction cycles. These spectra bear a resemblance to fresh TiO_2 coated cenosphere which confirms the stability of the coating. This stability is due to formation of strong covalent bonding of Si-O-Ti and Al-O-Ti.

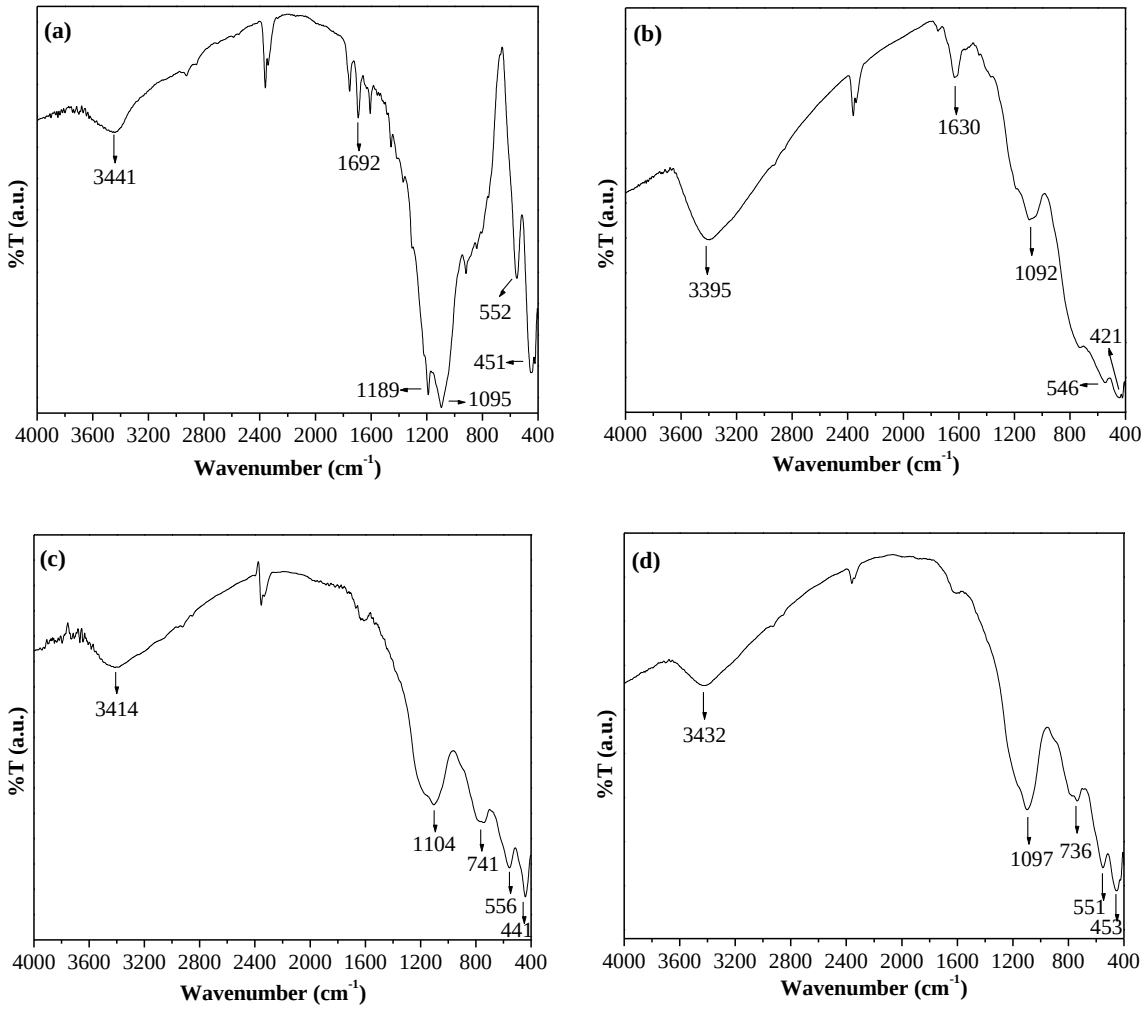

Figure-6.6. FT-IR spectra of (a) bare cenosphere, (b) TiO_2 coated cenosphere, (c) TiO_2 coated cenosphere after first cycle and (d) TiO_2 coated cenosphere after second cycle

6.3.7. Diffuse Reflectance spectra (DRS)

The band gap energy of the TiO_2 network developed on the cenosphere surface was determined using the Diffuse Reflectance Spectroscopy (DRS). The spectrophotometer *(Shimadzu UV-3101PC)* was equipped with an integrating sphere and $BaSO_4$ was used as a reference. The spectra were recorded at room temperature in the wavelength range of 225-800 nm. The band gap energy of catalysts were calculated according to the equation,

$$Band\ gap\ (EG) = hc/\lambda \qquad (6.1)$$

Where *EG* is the band gap energy (eV), *h* the Planck's constant, *c* the light velocity (m/s) and λ is the wavelength (nm). The semiconductor nature of the TiO_2 network grown at the cenospheres surface was confirmed by diffuse reflectance spectra. The diffuse reflectance spectra of uncoated and TiO_2 coated cenosphere are shown in **Figure-6.7**. The **Figure-6.7 (b)** shows the differential spectra of the diffuse reflectance spectra. In the differential spectra of TiO_2 coated cenosphere, a minimum was observed at 367 nm and the calculated band gap was 3.3 eV. This spectrum confirms the presence of TiO_2 at the cenosphere surface and the formed TiO_2 network exhibit the semiconductor nature. The minimum was not observed in the differential spectra of bare cenosphere material.

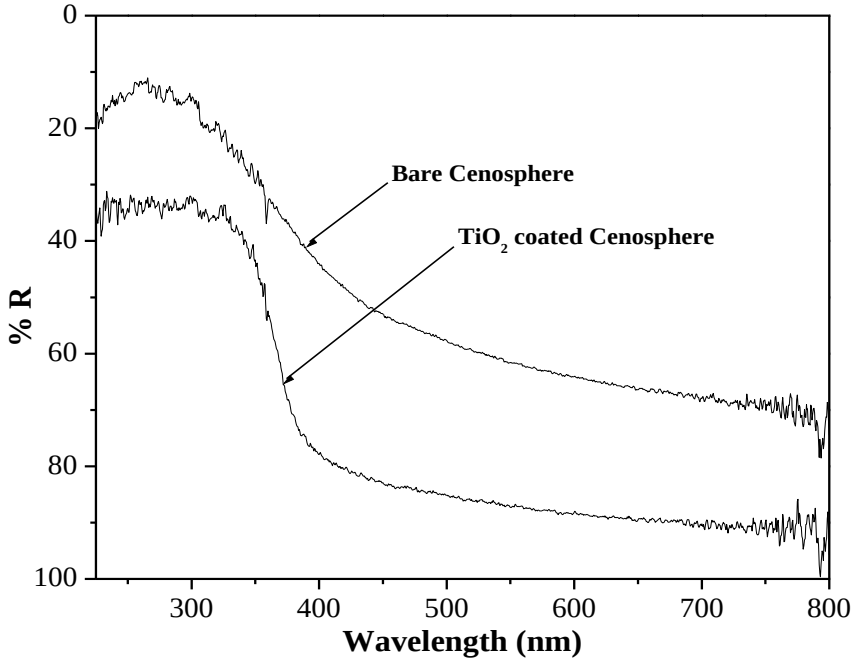

(a)

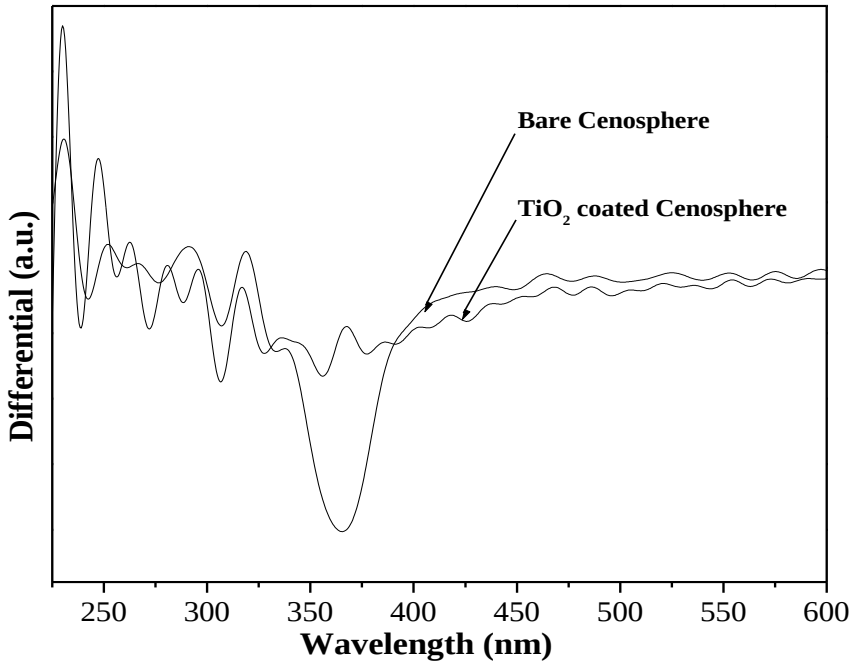

(b)

Figure-6.7. DRS spectra (a) and differential DRS spectra (b) of bare and TiO_2 coated cenosphere

6.3.8. Surface area measurement (N_2 adsorption)

The Brunauer-Emmett-Teller (BET) surface area of the catalysts was obtained from nitrogen adsorption data at 77.4 K measured using Micromeritics ASAP 2010 nitrogen adsorption apparatus.

The BET surface area of the uncoated and TiO_2 coated cenosphere particles were analyzed. The surface area of uncoated fly-ash cenospheres was observed only 0.72 $m^2 g^{-1}$, which confirms the nonporous material. After the TiO_2 coating, BET surface area was found increased to 45 $m^2 g^{-1}$ which is due to the porosity of TiO_2 network developed on cenosphere surface. The surface area was observed to decreased up to 26 $m^2 g^{-1}$ after the calcination. This decrease may be due to the shrinkage of TiO_2 network after the calcination.

6.3.9. Particle Size Distribution

The measured particle size distribution of the uncoated cenosphere and TiO_2 coated cenosphere particles are presented in **Figure-6.8**. In the uncoated cenosphere the average particle size is 47 μm with the 3.38 and 8.65 % particles below 4.5 and 10 μm sizes respectively. The TiO_2 coated cenosphere particle size distribution is ranging 9.04 and 18.82 % particles below 4.5 and 10 μm sizes respectively. The average particle size was observed decreased which is due to the development of TiO_2 nanoparticle network on the cenosphere surface. Thus the coated cenosphere particles have finer TiO_2 particles in the form of network with bulky cenosphere particles and thus for a given amount of powder provide more surface area than provide by uncoated cenosphere. In the TiO_2 coated cenospheres, the smaller particle size exhibit the higher volume percent as compare to uncoated cenosphere. This is due to the formation of TiO_2 particle network on the cenosphere surface.

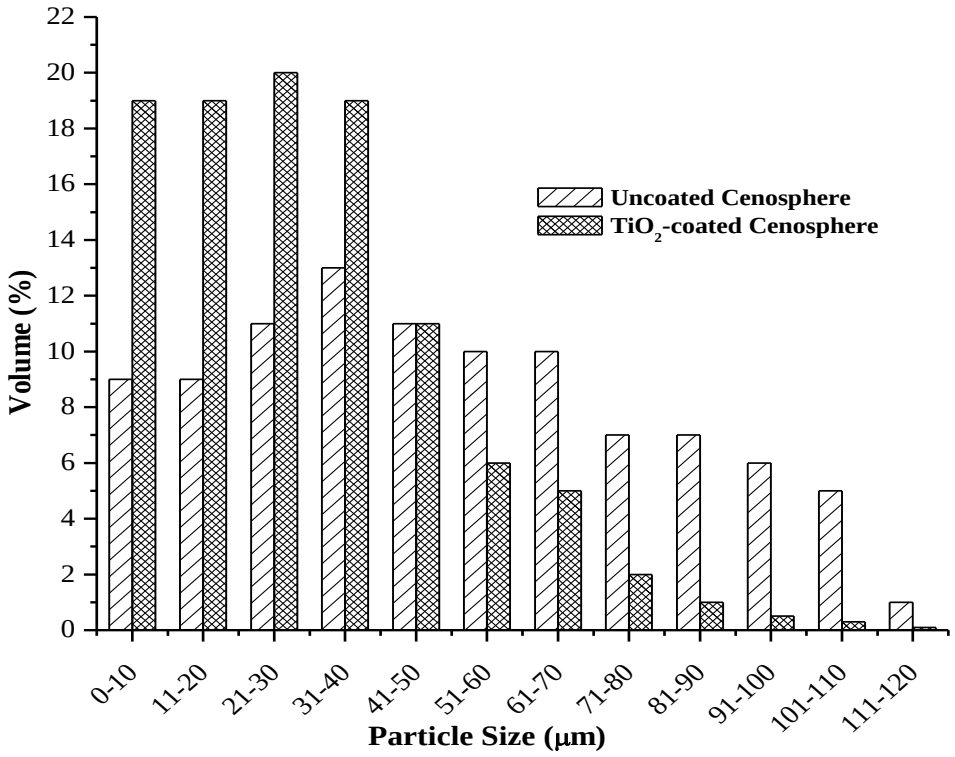

Figure-6.8. Particle size distribution of bare and TiO_2 coated cenospheres

6.4. PHOTOCATALYTIC DEGRADATION OF ORGANIC COMPOUNDS

6.4.1. Irradiation Experiments

The photocatalytic activities of the prepared catalysts were determined under solar light. The experiments were carried out in the Petri dish of the inner diameter 90 mm and outer diameter 93 mm. These Petri dishes were covered with another Petri dish of inner diameter 96 mm and outer diameter 99 mm to stop the loss of water due to evaporation. The 50 ml of reactant solution was taken in the Petri dish and 1 gm of catalyst was spread over it. The initial concentrations of the MB and PNA taken for the study were 10 and 25 ppm. The activity of the catalyst was determined by the observation of concentration decrease of the methylene blue (MB) and *p*-nitroaniline (PNA) at different time intervals. An independent experiment was carried out for every sample that was stopped at the required time and analyzed to determine the MB and PNA content of the solution. The reactions were carried out at Bhavnagar city in Gujarat state of India. This city is situated

at Latitude: 21° 26′ North and Longitude: 72° 09′ East. The sample time, the day and reaction time performed and conditions of the reactions are given in the **Table-6.2**.

Table-6.2 (a). The day conditions of the reaction performed with 10 ppm MB

Time*	**Solar light intensity (Lux)**			
	Reaction Cycle			
	1	**2**	**3**	**Blank**
	March 01, 2008 (Saturday)	**March 04, 2008 (Tuesday)**	**March 05, 2008 (Wednesday)**	**March 01, 2008 (Saturday)**
11:00 AM	60500	61300	60800	60500
11:30 AM	67800	67200	67500	67800
12:00 noon	68300	68500	71000	68300
12:30 PM	70100	71000	71200	70100

*Time = Indian Standard Time

Table-6.2 (b). The day conditions of the reaction performed with 25 ppm MB

Time*	**Solar light intensity (Lux)**			
	Reaction Cycle			
	1	**2**	**3**	**Blank**
	February 26, 2008 (Tuesday)	**March 02, 2008 (Sunday)**	**March 03, 2008 (Monday)**	**February 29, 2008 (Friday)**
11:00 AM	61500	61400	61100	62000
12:00 noon	68800	68200	70300	70500
13:00 PM	71500	72000	72000	72000
14:00 PM	72100	72400	72500	72700

*Time = Indian Standard Time

Table-6.2 (c). The day conditions of the reaction performed with 10 ppm PNA

Time*	**Solar light intensity (Lux)**			
	Reaction Cycle			
	1	**2**	**3**	**Blank**
	April 14, 2008 (Monday)	**April 16, 2008 (Wednesday)**	**April 18, 2008 (Friday)**	**April 14, 2008 (Monday)**
11:00 AM	61000	61500	61000	61100
12:00 noon	68300	67000	67500	68000
13:00 PM	72300	72500	72700	72500
14:00 PM	72500	72500	72500	72600

*Time = Indian Standard Time

Table-.2 (d). The day conditions of the reaction performed with 25 ppm PNA

Time*	**Solar light intensity (Lux)**			
	Reaction Cycle			
	1	**2**	**3**	**Blank**
	April 08, 2008 (Tuesday)	**April 11, 2008 (Friday)**	**April 12, 2008 (Saturday)**	**April 10, 2008 (Thursday)**
11:00 AM	60500	61000	61000	60700
12:00 noon	68000	67000	67500	67700
13:00 PM	72500	72000	72200	71500
14:00 PM	72500	72000	72300	72000

*Time = Indian Standard Time

Table-6.2 (e). The day conditions of the reaction performed with *n*-decane

Time*	**Solar light intensity (Lux)**		
	3 ml	**8 ml**	**12 ml**
	March 21, 2008 (Friday)	**March 25, 2008 (Tuesday)**	**April 02, 2008 (Wednesday)**
10:00 AM	60000	57500	56500
11:00 AM	65000	60000	60500
12:00 noon	71000	63500	65500
13:00 PM	71000	70500	71000
14:00 PM	62500	62500	71000
15:00 PM	57500	58500	64000

*Time = Indian Standard Time

Table-6.2 (f). The day conditions of the reaction performed with *n*-tridecane

Time*	**Solar light intensity (Lux)**		
	3 ml	**8 ml**	**12 ml**
	May 02, 2008 (Friday)	**May 12, 2008 (Monday)**	**May 22, 2008 (Thursday)**
10:00 AM	64500	62400	63800
11:00 AM	68700	67800	68400
12:00 noon	70100	69500	69900
13:00 PM	72000	71900	72200
14:00 PM	67500	65400	69300
15:00 PM	62300	59300	64000

*Time = Indian Standard Time

The decrease due to adsorption on the catalyst was considered by keeping one reaction sample under dark for the time equal to maximum solar light illumination time for the degradation, for example, the adsorption time was given 1.5 h for 10 ppm MB and 3 h for the remaining reaction mixtures. The degradation due to solar light was studied by running one blank run without catalyst for the equal to maximum solar light illumination time for the degradation (1.5 h for 10 ppm MB and 3 h for remaining). The catalyst was separated by filtration for reusability.

The initial amounts of *n*-decane and *n*-tridecane were 3, 8 and 12 ml on the aqueous phase. The total 50 ml of reactant solution having both water and hydrocarbon was taken in the Petri dish and 1 gm of catalyst was spread over it. The activity of the catalyst was determined by the observation of amount decrease of the *n*-decane and *n*-tridecane at different time intervals.

An independent experiment was carried out for every sample that was stopped at the required time and analyzed to determine the *n*-decane and *n*-tridecane content of the solution. The sample time, the day and reaction time performed and conditions of the reactions are given in the **Table-6.2**. The time given in the table is the Indian standard time. The decrease in the amount due to solar light was studied by running one blank run without catalyst for the equal to maximum solar light illumination time for the degradation (6 h for each).

6.4.2. Analytical determination

The concentration of MB and PNA was analyzed by UV-Visible spectroscopy. The absorbance of the samples taken at different time interval were measured which was used to determine the concentration.

For the hydrocarbon analysis, after the irradiation the samples were taken in the dark and remaining amount of the hydrocarbon in the samples was extracted with CH_2Cl_2. The CH_2Cl_2 was removed by solvent evaporation using rota-vapour. The obtained hydrocarbon was mixed with the constant 10 ml amount of the toluene and analyzed by Gas chromatography (GC-14, Shimadzu) with packed column.

The mineralization of MB and PNA in aqueous solution was confirmed by COD analysis of the samples taken at different reaction time interval.

6.4.3. The studied organic compounds

6.4.3.1. *Methylene blue, its properties and Toxicological Information*

The textile activities release large volume of waste waters that contain high organic charge and strong colouration. Many dyes used in textile processes show toxicity to the aquatic biota and could cause interference in natural photosynthetic processes. The major environmental associated with the use of reactive dyes is their loss during the dyeing process. The most commonly practiced technology for the removal of dyestuffs from aqueous solution is chemical coagulation followed by sedimentation which generates massive amounts of sludge and leaves further problems to be solved. Methylene blue is a heterocyclic aromatic chemical compound with molecular formula: $C_{16}H_{18}ClN_3S$. It has many uses in a range of different fields, such as biology or chemistry. **[31]**. The properties of methylene blue are shown below:

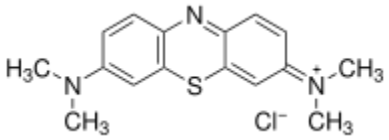

Molecular formula	$C_{16}H_{18}N_3ClS$
Physical state and appearance	Solid
Weight [g.mol^{-1}]	319.85
Boiling point [°C]	Decomposes
Melting point [°C]	100-110
Specific gravity	-
Solubility in water [mg.l^{-1}]	Soluble

Methylene blue is a monoamine oxidase inhibitor **[32]**, and if infused intravenously at doses exceeding 5 mg/kg, may precipitate serious serotonin toxicity, serotonin syndrome, if combined with any selective serotonin reuptake inhibitors (SSRIs) or other serotonin reuptake inhibitor (e.g., duloxetine, sibutramine, venlafaxine, clomipramine, imipramine) [33].

6.4.3.2. *p-nitroaniline, its properties and Toxicological Information*

These are intermediate during the synthesis of pesticides, dyes and explosives and are also the basic raw materials for dye stuff, paint, medicine and agricultural chemicals. This often detected in industrial effluents, in ambient freshwater, in ambient environments and in the atmosphere to pollute the ecosystem. **[34]**. The properties of *p*-nitroaniline are shown below:

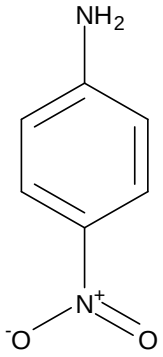	Molecular formula	$NH_2(C_6H_4)NO_2$
	Physical state and appearance	Solid
	Weight [$g.mol^{-1}$]	138.12
	Boiling point [°C]	331.7
	Melting point [°C]	148.7
	Specific gravity	1.424
	Solubility in water [$mg.l^{-1}$]	Slightly soluble

Inhalation and skin contact are expected to be the primary routes of occupational exposure to *p*-nitroaniline. *p*-nitroaniline is readily absorbed through human skin. Although *p*-nitroaniline is considered to be only slightly toxic on the basis of single exposure animal tests, human experience has shown that man is much more sensitive to methemoglobinemia caused by aromatic amino compounds than the rat or the rabbit. Cyanosis may occur and, as oxygen deficiency increases, there may be associated headache, weakness, irritability, drowsiness, shortness of breath, and unconsciousness. The appearance of methemoglobinemia may be delayed 0 to 12 hours after exposure. Because of the high potential for this material to cause methemoglobin formation, *p*-nitroaniline should be considered hazardous by all routes of exposure and exposures should be tightly controlled **[35]**.

6.4.3.3. *n-decane, its properties and Toxicological Information*

n-decane is a colorless liquid saturated hydrocarbon. It is less dense than water and insoluble in water. In high concentrations its vapors may be narcotic. It is used as a solvent and to make other chemicals. Contact with eyes may produce mild irritation. Contact with skin may cause defatting, redness, scaling, and hair loss. Ingestion may cause diarrhea, slight central nervous system depression, difficulty in breathing and fatigue. Inhalation of high concentrations may cause rapid breathing, fatigue, headache, dizziness, and other CNS effects.

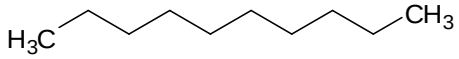

Molecular formula	$H_3C(CH_2)_8CH_3$
Physical state and appearance	Colorless liquid
Weight [$g.mol^{-1}$]	142.29
Boiling point [°C]	174
Melting point [°C]	-30
Specific gravity	0.73
Solubility in water [$mg.l^{-1}$]	Not soluble

6.4.3.4. *n-tridecane, its properties and Toxicological Information*

n-tridecane is a colourless liquid. It is irritant and may be harmful by inhalation, ingestion or through skin contact.

Molecular formula	$H_3C(CH_2)_{11}CH_3$
Physical state and appearance	Colorless liquid
Weight [$g.mol^{-1}$]	184.3
Boiling point [°C]	234
Melting point [°C]	-5
Specific gravity	-
Solubility in water [$mg.l^{-1}$]	Not soluble

6.4.4. Calibration curves by UV-Visible spectroscopy

6.4.4.1. *Calibration curves for MB and PNA*

The decrease in the concentration of MB and PNA was measured by using UV-Visible spectroscopy. The calibration curves were plotted for MB and PNA and for the purpose the standard samples of MB and PNA were prepared in distilled water. The concentrations of the standard samples were 5, 10, 20, 30, 40 and 50 ppm and the absorption of these samples were measured by UV-Visible spectroscopy. The calibration curves were plotted between absorption values of the samples with respect to their relevant concentrations. The slopes of the curves were calculated which were used for the calculation of MB and PNA concentration. The calibration curves for MB and PNA are shown in **Figures-6.9**.

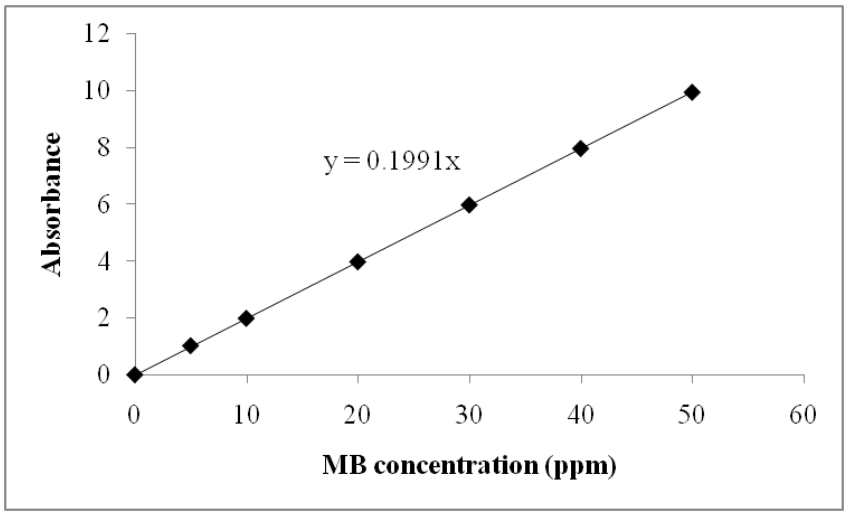

(a)

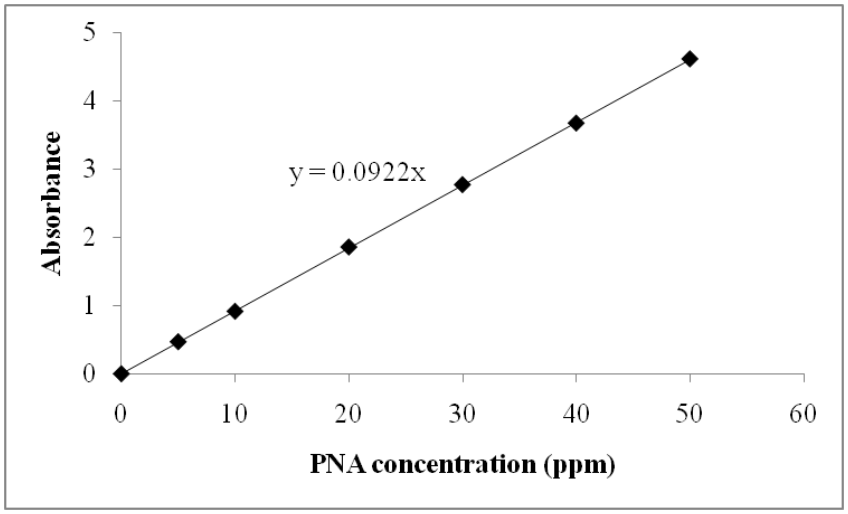

(b)

Figure-6.9. Calibration curves for (a) Methylene blue and (b) *p*-nitroaniline

6.4.4.2. *Calibration curves for n-decane and n-tridecane*

The progress of the reaction was studied by considering the decrease in the initial amount of the hydrocarbon. The analysis was done using gas chromatography. The calibration curves were plotted for both the hydrocarbons and for the purpose the standard mixtures of the hydrocarbons with the toluene were prepared. The amounts of hydrocarbon were taken 0.1, 0.2, 0.4, 0.6, 0.8, 1.0, 2.0, 3.0 and 4.0 ml with the constant amount of 10 ml of toluene and these mixtures were analyzed with GC. The calibration curves were plotted

between peak area ratio of hydrocarbon with toluene and the amount of hydrocarbon taken in the samples. The slopes of the curves were calculated which were used for the calculation of hydrocarbon amount. The calibration curves are shown in **Figures-6.10** for *n*-decane and *n*-tridecane.

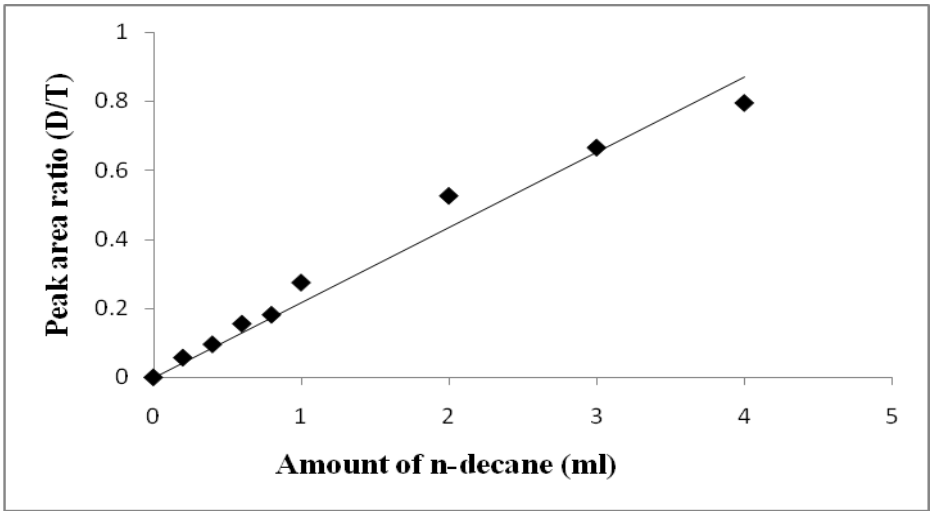

(a)

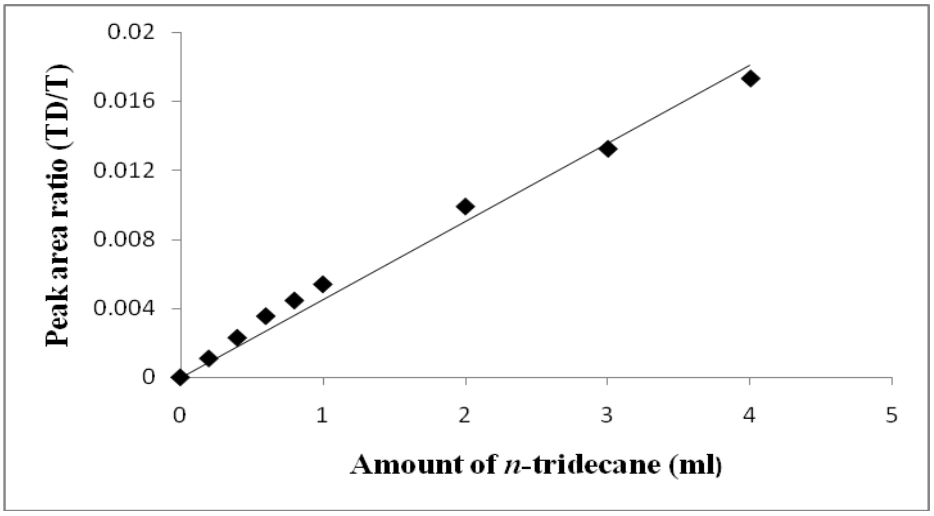

(b)

Figure-6.10. Calibration curves for (a) *n*-decane and (b) *n*-tridecane

6.5. RESULT AND DISCUSSION

6.5.1. Photocatalytic degradation of MB and PNA

The photocatalytic activity of the synthesized TiO_2 coated cenosphere catalyst was assessed for the degradation of aqueous MB and PNA solution of the initial concentration 10 and 25 ppm under the solar irradiation. The sample time, the day and reaction time performed and conditions of the reactions were noted as given in **Table-6.2**. The schematic diagram of the e^-/h^+ pair generation process is given in the **Scheme-6.2**.

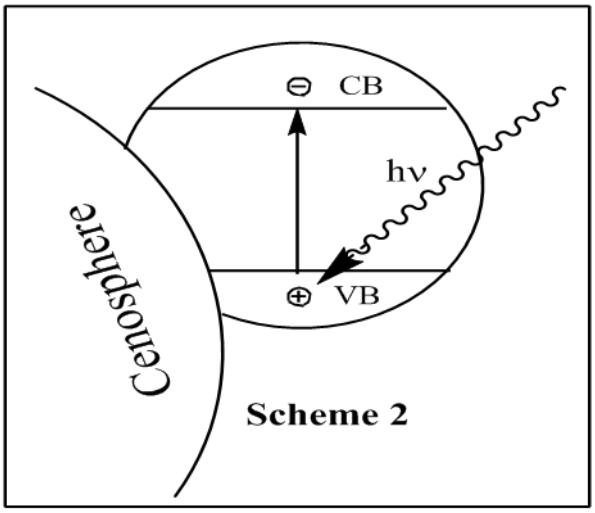

Scheme-6.2. The e^-/h^+ pair generation process in semiconductor at cenospheres surface

The two main parameters used to rank the photocatalytic activity of the prepared catalyst material were the final degradation percentage and the mineralization after 3 h of irradiation. However, the almost complete degradation was observed for the 10 ppm MB within 1.5 h only. The reusability of the catalyst was studied for three consecutive cycles. For the recycling, the catalyst was filtered and dried under the solar light and then reused again for the reaction. The decrease in the concentration due to adsorption and blank study (only under solar light and absence of catalyst) was also considered. The **Figure-6.11, 6.12 and 6.13** shows the concentration vs. solar light irradiation curves, COD decrease and % degradation respectively of MB and PNA. Each data point in these plots

corresponds to an independent experiment that was stopped at the required time and analyzed to determine the MB and PNA content of the solution.

6.5.1.1. *Removal of Methylene blue (MB)*

The **Figure-6.11 (a),** 6.11 **(b), Figure-6.12 (a), 6.12 (b)** and **Figure-6.13 (a), 6.13 (b)** shows the concentration vs. solar light irradiation time, COD decrease and % degradation after the 3 h reaction time with MB.

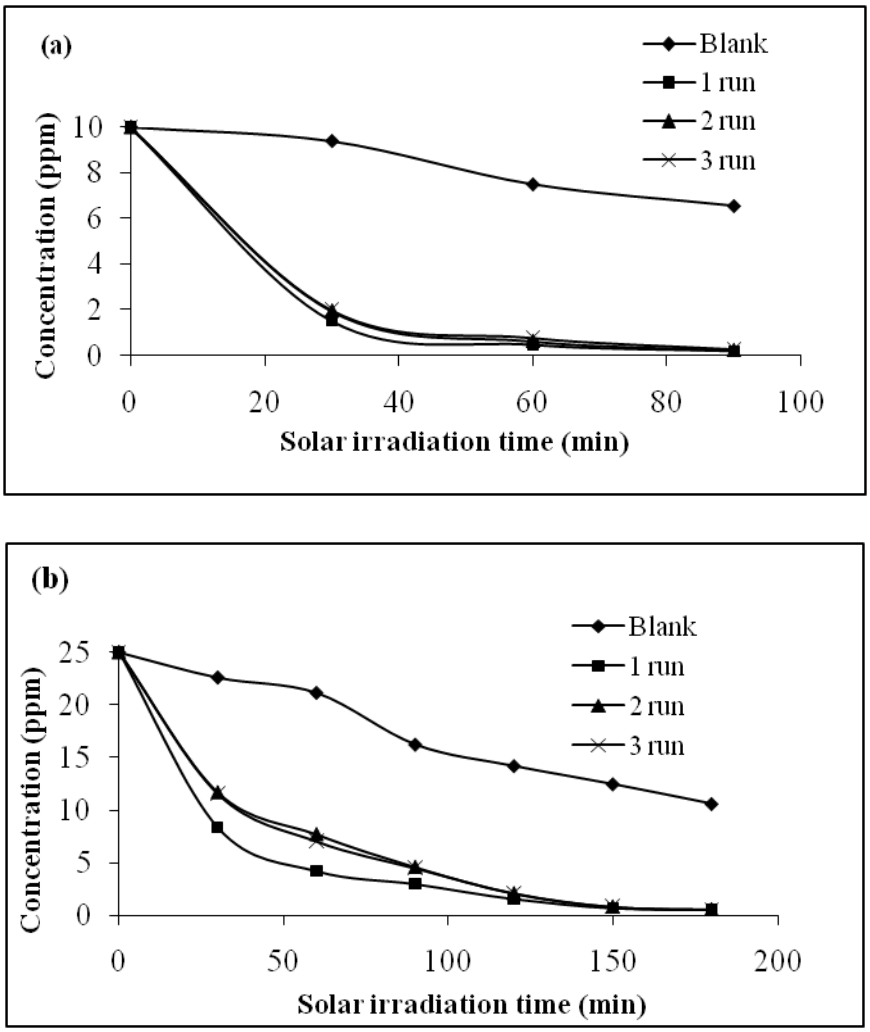

Figure-6.11. Concentration vs. Solar irradiation time for (a) 10 ppm MB and (b) 25 ppm MB

The degradation was observed 99 % after the 3 h for 25 ppm initial concentration of MB **(Figure-6.12)**. However, the reaction was stopped after 1.5 h only for the 10 ppm initial concentration of MB as 98 % degradation was observed within this time period. The concentration of MB was decreased with 58 % and 45 % after the same reaction time 3 h and 1.5 h as in the blank study for 25 and 10 ppm initial concentration of MB. The decrease in the concentration due to adsorption was 29 and 36 % for 25 and 10 ppm initial concentration. But these values are far behind the degradation values which were observed in the presence of catalyst (99 and 98 % respectively). The reusability of the catalyst was also observed and second and third run were also carried out under the same reaction conditions.

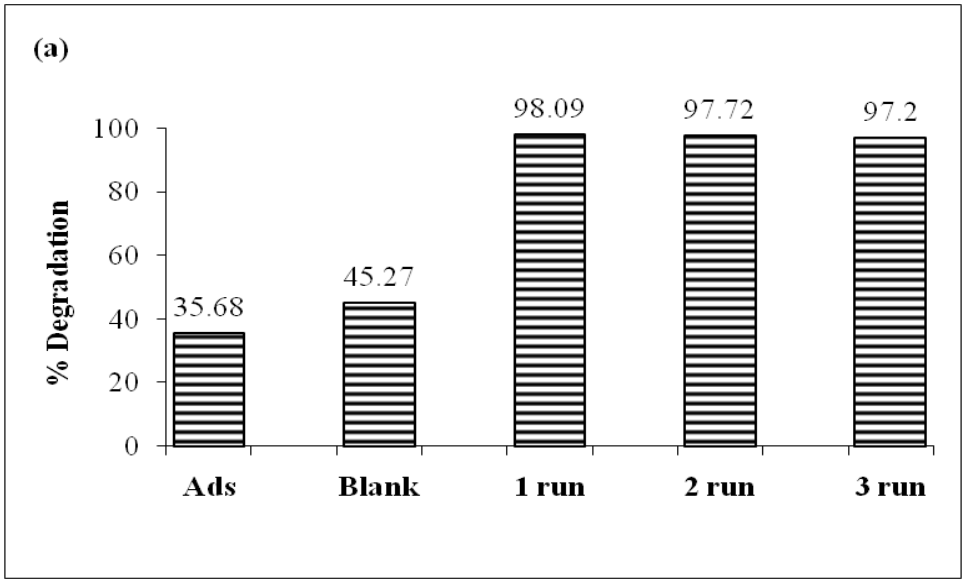

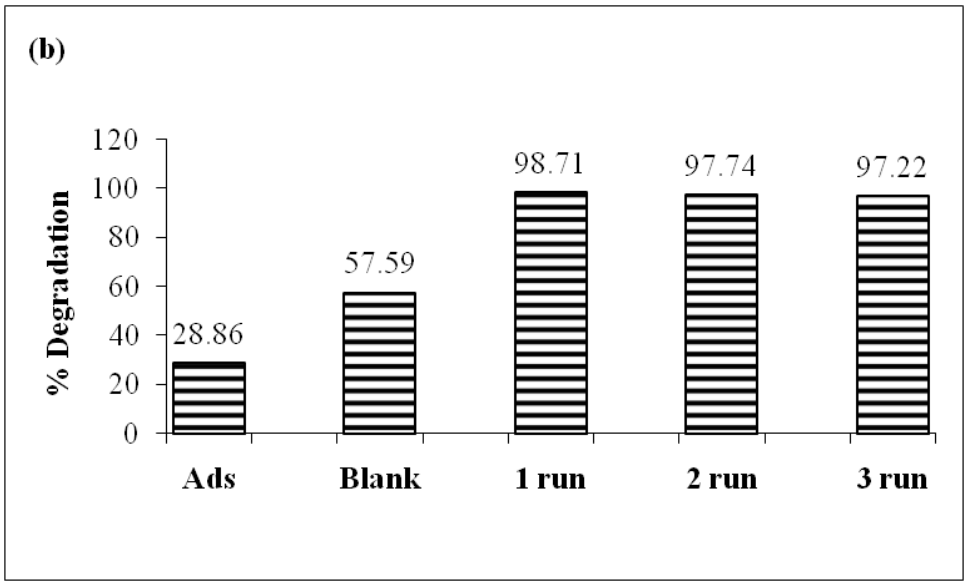

Figure-6.12. % **Degradation after the completion of reaction for (a) 10 ppm MB after 1.5 h and (b) 25 ppm MB after 3 h reaction time**

The results given in **Figures-6.11, 6.12 and 6.13** shows that the efficiency of the catalyst remains same even after the three cycles. The decrease in the COD value was 30 % for the blank experiment while it was observed almost 85 % in the presence of catalyst for all three runs for 25 ppm concentration after 3 h. The decrease in COD value for 10 ppm MB was observed only 12 % in blank experiment while almost 69 % decrease in COD value was observed in the presence of catalyst in all three runs after 1.5 h reaction time. The results demonstrate the catalytic efficiency for the degradation and mineralization.

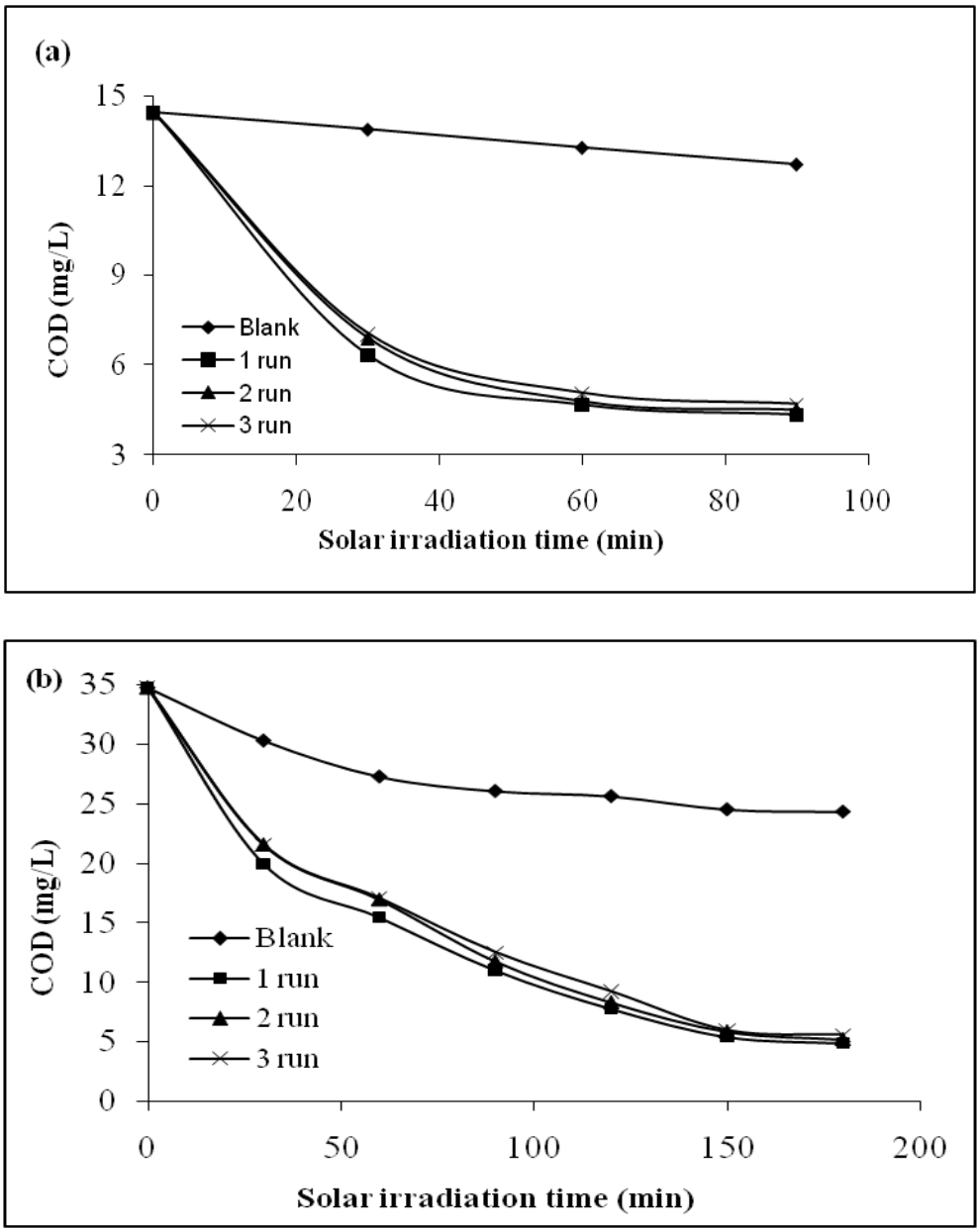

Figure-6.13. COD decrease with solar irradiation time for (a) 10 ppm MB and (b) 25 ppm MB

6.5.1.2. *Removal of p-nitroaniline (PNA)*

The **Figure-6.14 (a), 9 (b), Figure-6.15 (a), 10 (b)** and **Figure-6.16 (a), 11 (b)** shows the photocatalytic results for the PNA degradation after the 3 h reaction time.

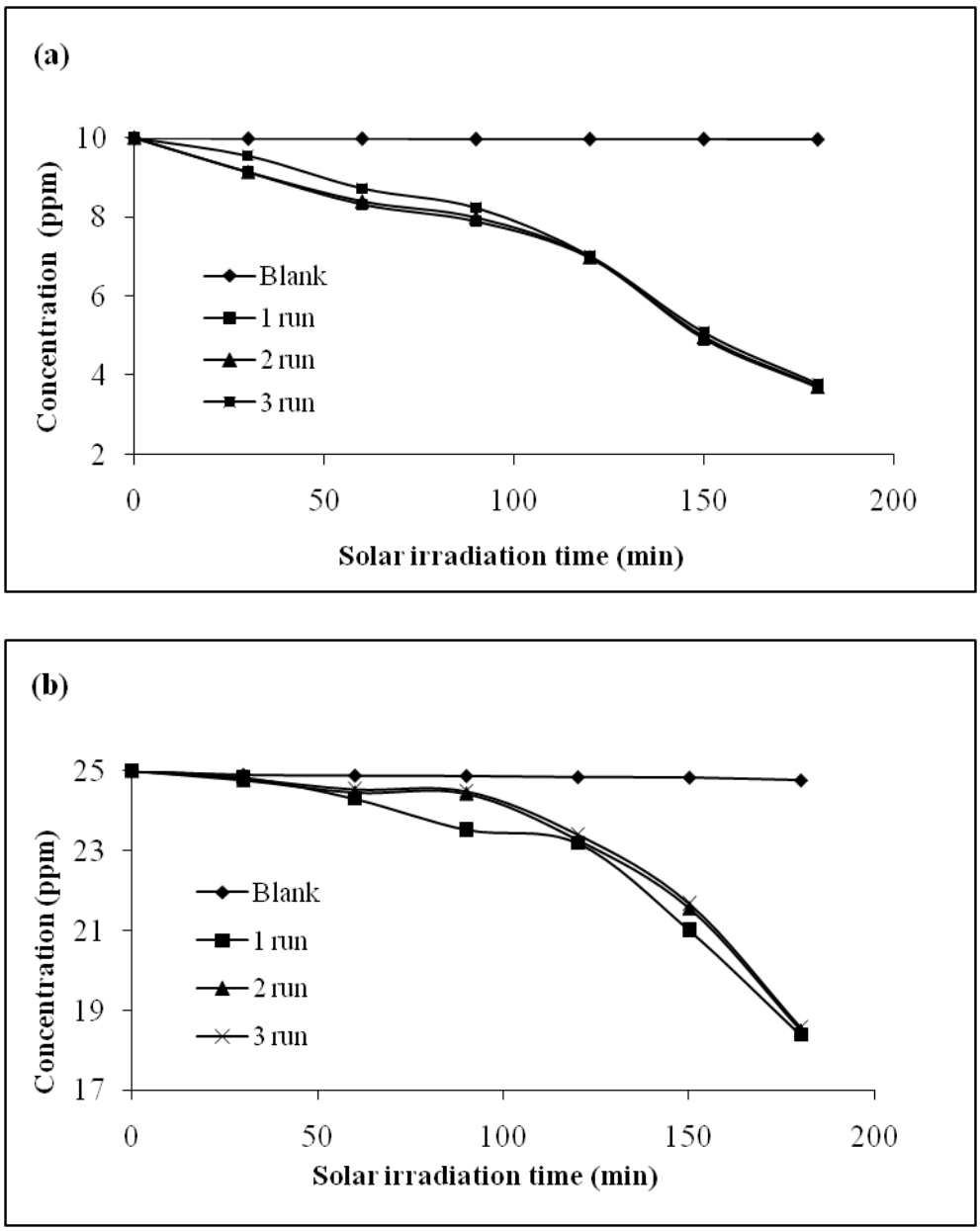

Figure-6.14. Concentration vs. Solar irradiation time for (a) 10 ppm PNA and (b) 25 ppm PNA

The PNA degradation was observed 26 and 63 % with 25 and 10 ppm initial concentration after 3 h reaction.

Blank controls showed that the PNA concentration remains constant for 25 ppm initial concentration and found decreased only 10 % with 10 ppm initial concentration when the irradiation is carried out under identical conditions but in the absence of any

photocatalyst. This shows the more resistant nature of PNA towards the photocatalytic degradation as compared to MB. The decrease in the PNA concentration due to adsorption was negligible in both the cases. The reusability results confirm the almost same efficiency of the catalyst even after the third cycle in the case of PNA degradation also as MB degradation.

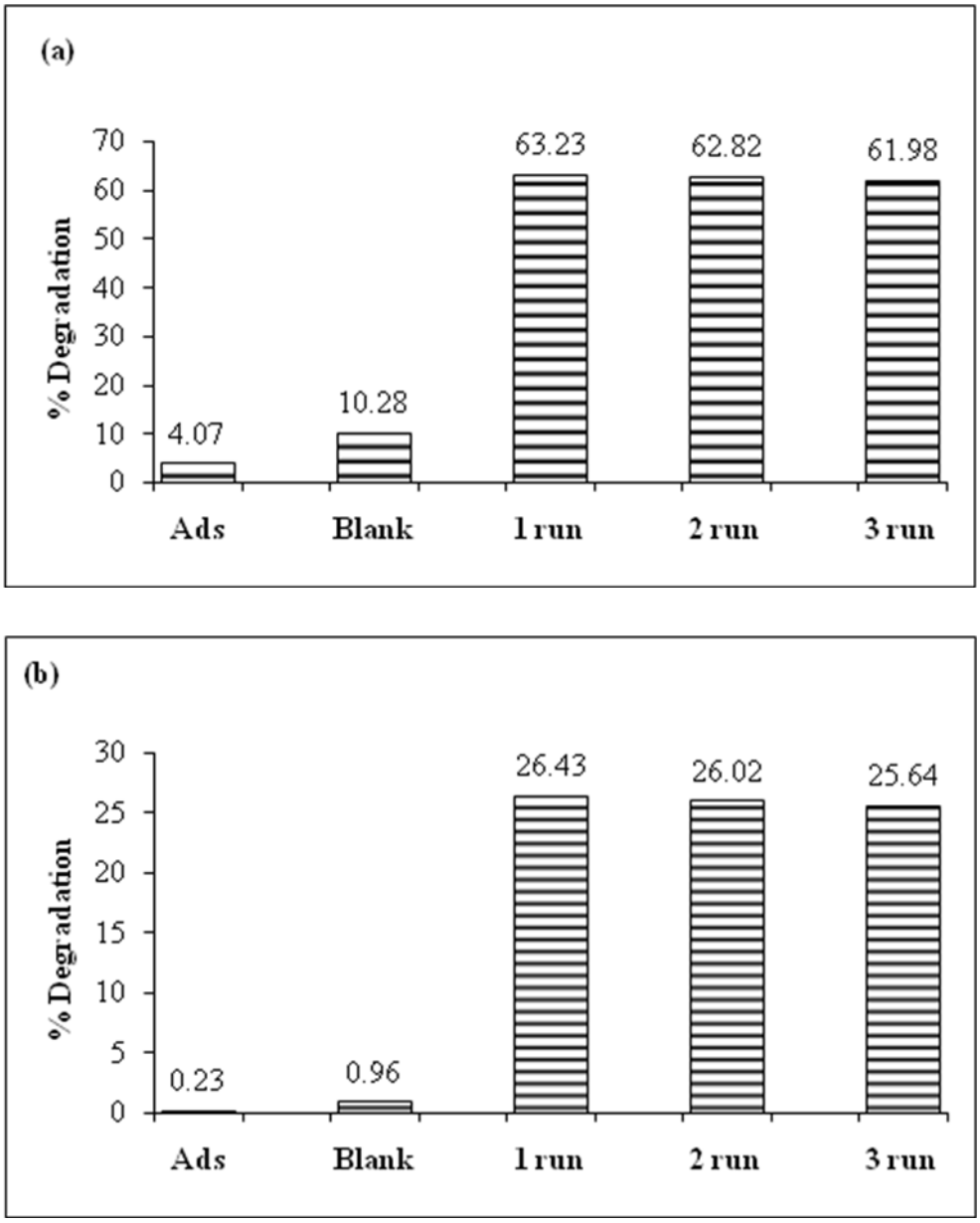

Figure-6.15. % Degradation after the completion of reaction for (a) 10 ppm PNA and (b) 25 ppm PNA after 3 h reaction time

The decrease in the COD value was 1 and 3 % only with the blank experiments for the 25 and 10 ppm concentration respectively. These values were observed almost 17 and 51 % in the presence of catalyst for all the three cycles for the 25 and 10 ppm PNA concentration respectively.

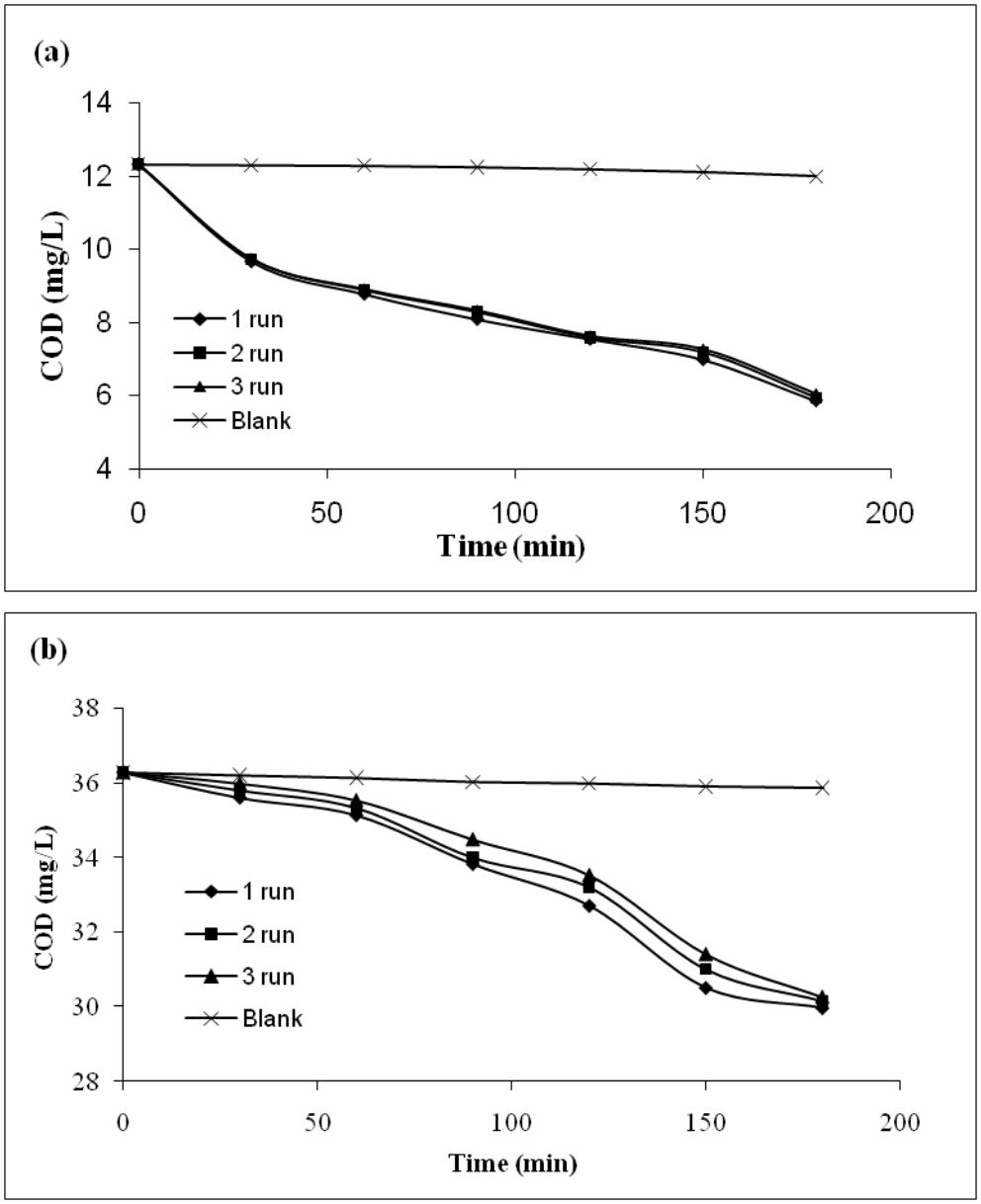

Figure-6.16. COD decrease with solar irradiation time for (a) 10 ppm PNA and (b) 25 ppm PNA

The results of the MB and PNA degradation demonstrate that MB is more pronounced for the degradation and mineralization as it acts as the sensitizer and can absorb the photons more promptly. This photon energy then can transfer to catalyst which helps to the e^-/h^+ generation in the catalyst and help to the degradation of the MB.

6.5.2. Photocatalytic degradation of *n*-decane and *n*-tridecane

The photocatalytic activity of the synthesized TiO_2 coated cenosphere catalyst was assessed for the photocatalytic oxidation of *n*-decane and *n*-tridecane for the initial amount of 3, 8 and 12 ml on the aqueous surface under the solar irradiation. The sample time, the day and reaction time performed and conditions of the reactions were noted as given in **Table-6.2**. The progress of the reaction was studied by considering the decrease in the initial amount of the hydrocarbon.

The decrease in the amount due to blank study (only under solar light and absence of catalyst) was also considered. The **Figure-6.17 and 6.18** shows the amount of hydrocarbon vs. solar light irradiation time curves for *n*-decane and *n*-tridecane respectively. Each data point in these plots corresponds to an independent experiment that was stopped at the required time and analyzed to determine the *n*-decane and *n*-tridecane content of the solution.

The decreases in the amount of the *n*-decane were observed 51, 47 and 29 % for 3, 8 and 12 ml initial amount after 6 h reaction under the solar light. The blank study showed the decrease in the amount of *n*-decane 16, 13 and 12 % for 3, 8 and 12 ml initial amount respectively for the same period of 6 h as given in **Table-6.3**.

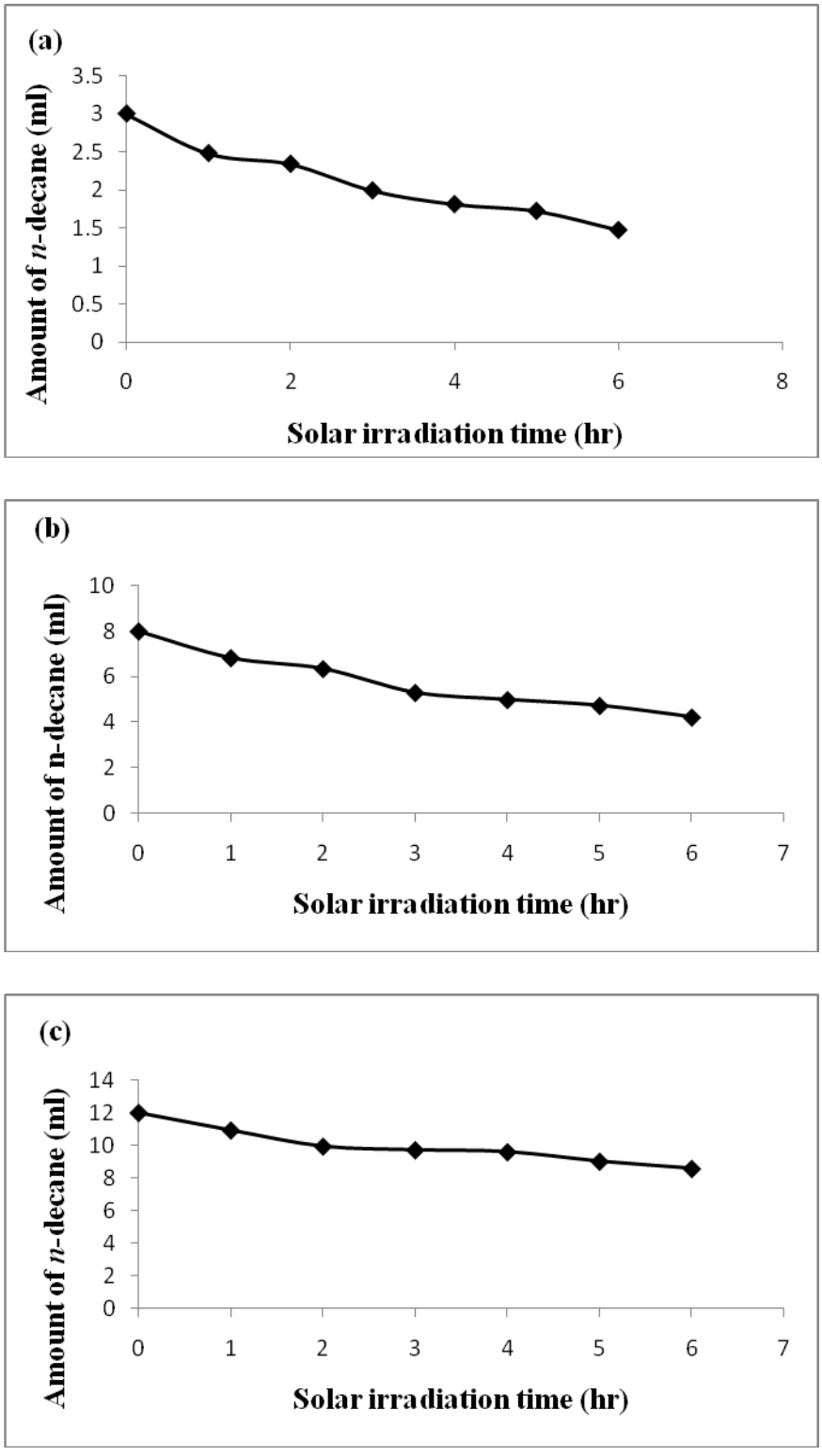

Figure-6.17. The Amount of *n*-decane with solar irradiation time for (a) 3 ml (b) 8 ml and (c) 12 ml

Table-6.3. The % decrease in the hydrocarbon amount after the 6 h reaction under the solar light

Amount of hydrocarbon	*n*-decane		*n*-tridecane	
	Solar light/catalyst	Only Solar light	Solar light/catalyst	Only Solar light
3 ml	51	16	36	5
8 ml	47	13	23	3
12 ml	29	12	19	2

The percentage decreases for the n-tridecane were observed 36, 23 and 19 % for 3, 8 and 12 ml initial amount of *n*-tridecane. The blank study showed the 5, 3 and 2 % decrease in the amount after the 6 h solar irradiation time. The decrease in the amount of hydrocarbon was found decreased with the increase in the initial amount taken.

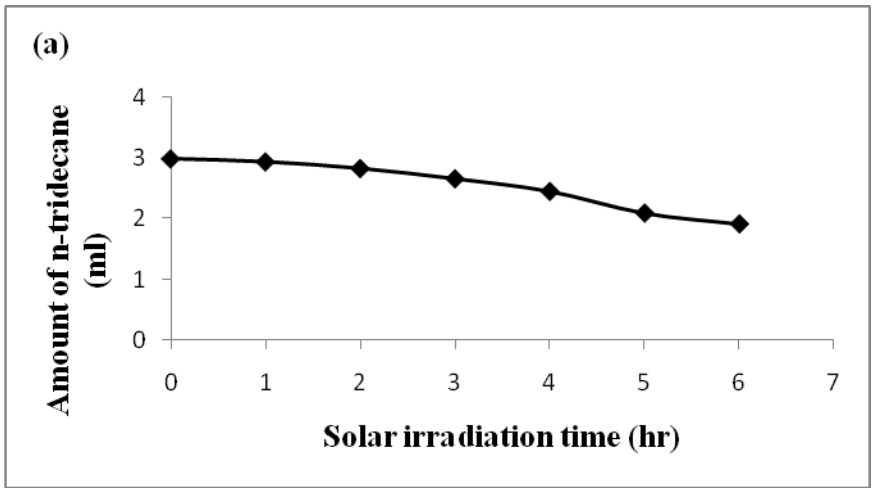

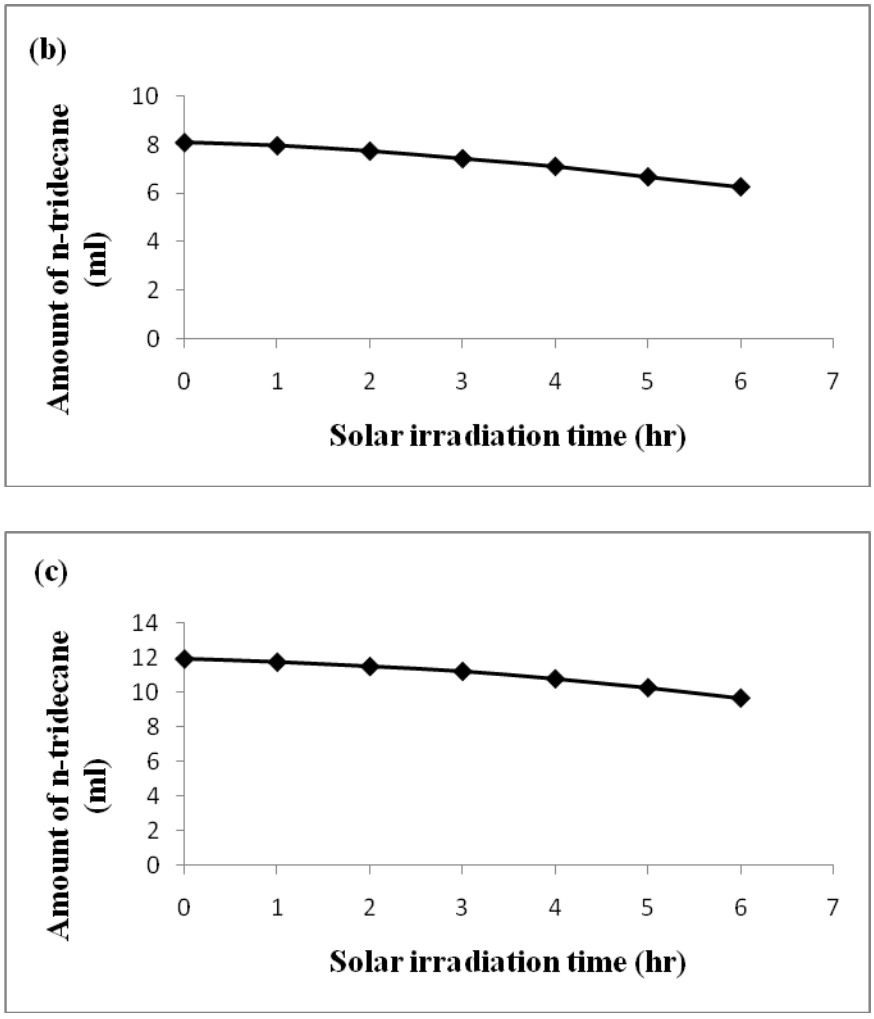

Figure-6.18. The Amount of *n*-tridecane with solar irradiation time for (a) 3 ml (b) 8 ml and (c) 12 ml

The e^-/h^+ pair generation process shown in **scheme-6.2** occurs in the TiO_2 particles attached at the cenospheres surface. These charge carriers migrates rapidly to the surface of catalyst particles where they are ultimately trapped and poised to undergo redox chemistry with suitable substrates. This process supposed to occur at the aqueous surface as the coated cenospheres particles float at the aqueous surface. The presence of water support to the oxidation process by creating the active hydroxyl radicals which are well known to take part in the photocatalytic oxidation process. The buoyant property of the prepared catalyst crafts it effective for the photocatalytic oxidation of the saturated hydrocarbon which makes a slick at the water surface.

6.6. REFERENCES

[1] Fox M. A.; Doan K. E.; Dulay M. T., *Res. Chem. Intermed.* **1994**, *20*, 711-721.

[2] Kim Y.; Yoon M., *J. Mol. Cat. A: Chemical.* **2001**, *168*, 257-263.

[3] Lee S.-K; Mills A., *J. Ind. Eng. Chem.* **2004**, *2*, 173-187.

[4] Mills A.; Lee S. –K., *J. Photochem. Photobiol., A: Chem.* **2002**, *152*, 233-247.

[5] Nair M.; Luo Z.; Heller A., *Ind. Eng. Chem. Res*. **1993**, *32*, 2318-2323.

[6] Fabiyi M. E.; Skelton R. L., *J. Photochem. Photobiol., A. Chem.* **2000**, *132*, 121-128.

[7] Matos J.; Laine J.; Hermann J. M., *Appl. Catal., B Environ*. **1998**, *18*, 281-291.

[8] Piperata G.; Meitchtry J. M.; Litter M. I., *Prog. Colloid & Polym. Sci*. **2004**, *128*, 303-308.

[9] Lohse S.; Rosentreter J. J., *Microchem. Journal.* **2006**, *82*, 66-72.

[10] Payne J. R.; Phillips C. R. *Environ. Sci. Technol*. **1985**, *19*, 569-579.

[11] Bongiovanni R.; Borgareello E.; Pe;izzetti E. *Chim. Ind. (Milan)* **1989**, *71(12*), 12-17.

[12] Hashimoto K.; Kawai T.; Sakata T. *J. Phys. Chem*. **1984**, *88*, 4083-4088.

[13] Pelizzetti E.; Minero C.; Maurino V.; Hidaka H.; Serpone N.; Terzian R. *Ann. Chim. (Rome)*, **1990**, *80*, 81.

[14] Li G., Ph.D. Thesis, *National University of Singapore, Singapore*, **2007**.

[15] Lee S. -W.; Drwiega J.; Wu C. –Y.; Mazyck D.; Sigmund W. M., *Chem. Mater*. **2004**, *16*, 1160-1164.

[16] Toyoda M.; Nanbu Y.; Kito T.; Hirano M.; Inagaki M., *Desalination*. **2003**, *159*, 273-282.

[17] Zhou J.: Chem M.; Qiao X G.; Wu L. M., *Langmuir*. **2006**, *22*, 10175-10179.

[18] Zhang H. Z.; Luo X. H.; Xu J.; Xiang B.; Yu D. P., *J. Phys. Chem. B*. **2004**, *108*, 14866-14869.

[19] Wang X. J.; Hu D. D.; Yang J. X., *Chem. Mater*. **2007**, *19*, 2610-2621.

[20] Cho W. –H.; kang D. –J.; Kim S. –G., *J. Mater. Sci*. **2003**, *38*, 2619-2625.

[21] Bhattacharyya A.; Kawi S.; Ray M. B., *Catal. Today*. **2004**, *98*, 431-439.

[22] Ding Z.; Hu X. J.; Yue P. L.; Lu G. Q.; Greenfield P. F., *Catal. Today*. **2001**, *68*, 173-182.

[23] Kuo D. –H.; Shueh C. –N., *Chem. Vapor depos*. **2003**, *9*, 265-271.

[24] Jung S. –C.; Kim B. –H.; Kim S. –J.; Imaishi N.; Cho Y. –I., *Chem. Vapor depos*. **2005**, *11*, 137-141.

[25] Zhang X. W.; Zhou W. H.; Lei L. C.; *Carbon*. **2006**, *44*, 325-333.

[26] Koumoto K.; Seo S.; Sugiyama T.; Seo W. S. Dressick W. J. *Chem. Mater*. **1999**, *11*, 2305-2309.

[27] Pizem H.; Sukenik C. N.; Sampathkumaran U.; McIlwain A. K.; De Guire M. R., *Chem. Mater*. **2002**, *14*, 2476-2485.

[28] Strohm H.; Löbmann P. *Chem. Mater*. **2005**, *17*, 6772-6780.

[29] Aixiang Z.; Weihao X.; Jian X., *Surf & Coating Technol*. **2005**, *197*, 142-147.

[30] Matsunaga T.; Kim J. K.; Hardcastle S.; Rohatgi P. K., *Minerals Sci. & Eng. A.* **2002**, *325*, 333-343.

[31] http://www.wikipedia.org

[32] Gillman, P. K., *Can J Anaesth.,* **2008**, *55*, 311–312.

[33] Gillman, P. K., *Anaesthesia,* **2006**, *61*, 1013–1014.

[34] http://www.msds.chem.ox.ac.uk

[35] http://www.chemeochemicals.gov.nz

Chapter 7

Summary, Conclusions and Future Prospects

Heterogeneous photocatalysis, one of the Advanced Oxidation Processes (AOPs), is emerging as an alternative process to conventional approaches for the destruction of hazardous chemical wastes such as high temperature incineration, amended activated sludge digestion, anaerobic digestion,. An efficient photocatalyst is a solid, that combines desirable adsoprtion and photoelectronic properties, which provides the catalyst ability (i) to absorb efficient photons; (ii) to generate electron-hole pairs and (iii) to separate them with a minimum of recombination. The solid materials mostly used as photocatalysts include chalcogenides like sulfides or oxides of the transition metals. It became apparent the novel redox reactions of organic and other inorganic substrates could be induced by band-gap irradiation of a variety of semiconductor particles (e.g. TiO_2, ZnO, CdS, and ZnS etc.), of sizes ranging from clusters and colloids to powders and large single crystals. These redox reactions are developed for the destruction of organic compounds to give CO_2, water and other associated inorganic components in water treatment process. Subsequently, heterogeneous photocatalysis has been utilized to remove a wide range of pollutants in liquid and gas phase over.

The recovery of photocatalyst after the reaction from the suspension is a very important aspect to make the catalyst reusable and the photocatalytic process cost effective. Another very important point that needs to be considered is fine TiO_2 particles of high surface area to achieve the maximum output in the practical application. These can be acquired by fixing or immobilization of TiO_2 particles on support material such as MCM-41, MCM-48, SBA-15, clay, silica gel, activated carbon and zeolites. Finding supports which improve adsorption without reducing photocatalytic activity may be most promising path to arrive at practical Photocatalytic systems. Recently, high surface area photocatalytic materials such as ETS-4 and ETS-10 are being synthesized that have in-built TiO_2 photoactive units. These are easy to recover and provide high surface area to adsorb the organic molecule. The present thesis is focused on doping with metal ions, impregnation in nonporous zeolites to enhance the photocatalytic activity of TiO_2 as described below:

The first chapter of the thesis deals with introduction of fundamentals of photocatalytic process and its application for environmental cleanup. This chapter includes overview of the materials used for the photocatalytic phenomena; especially for the degradation purpose. The classification, synthesis procedures and properties of semiconductor photocatalyst has been discussed. The different methods used to enhance the efficiency of the photocatalyst are also illustrated. A detailed literature survey for the current research trend and advantages of the photocatalytic process and limitations of the other process used for the environmental purification has been included.

The second chapter focuses on the photocatalytic activity of Fe (III) salts impregnated TiO_2 catalysts for studying the effect of counter anions on the photocatalytic activity of the salt impregnated catalysts. Acetophenone was selected as a model organic compound for the degradation purpose. The concentrations of the acetophenone at different time were analyzed using UV-Visible spectrophotometer. The photocatalytic activities of these prepared catalysts were studied in terms of initial rate and final percentage of degradation. Fe (III) ion impregnation of TiO_2 with different salts was observed to influence photocatalytic degradation of acetophenone. The observations have been discussed in terms of influence of the presence of Fe (III) ions on the recombination of the electron and holes generated during UV irradiation of TiO_2. Similarly, the effect of anion has been discussed in terms of radical scavenging ability of chloride and radical generating ability of sulfate anions. The impregnation of Fe (III) salts on Degussa P25 TiO_2 having different anions has been found to affect the activity of the photocatalyst for the degradation of acetophenone. The metal ion impregnation inhibits the recombination of the charge species electron and holes. It results in increase of the efficiency of catalyst which is observed in the form of increase in the final percentage degradation of acetophenone. The final percentage degradation increase continuously with increase in Fe (III) ion concentration and it was observed that anion effect is not significant in this case. On the contrary the initial rate of degradation is reduced in presence of the Fe (III) ion impregnated catalyst prepared with ferric nitrate and ferric chloride. This decrease in the rate is possibly due to partial blockage of the active sites of the catalyst by anions. Cl^- ion can also reduce the rate of degradation by scavenging oxidizing radical species. In the case of Fe (III) ion impregnated catalyst prepared with ferric sulfate, first the initial rate

was found to decrease as SO_4^{2-} ions are introduced in P25 by ferric sulfate. It is due to this reason that the SO_4^{2-} ions are present on the surface of catalyst P25 and deactivates a portion of the catalyst; however the rate was found to increase with the increasing amount of SO_4^{2-} ions, which could be due to the formation of reactive species such as $SO_4^{\bullet-}$ radicals.

The third chapter deals with the synthesis of the bare and transition metal ion impregnated Engelhard Titanosilicate-10 (ETS-10) and Engelhard titanosilicate-4 (ETS-4). Metal exchanged microporous titanium silicate M-ETS-10 and M-ETS-4 (M = Fe, Co, Ni, Cu and Ag) samples were prepared by ion exchange from their metal salt solutions. The photocatalytic activities of these synthesized samples were investigated for the photocatalytic decomposition and percentage degradation of nitrobenzene (NB). The kinetics of the reaction performed with these catalysts was studied by calculating the initial rates and rate constants. The mineralization of nitrobenzene in aqueous solution was confirmed by COD analysis. The results clearly show that the microporous zeolites ETS-10 and ETS-4 exhibit the photocatalytic activity under UV light. The noble transition metal ion exchanged ETS-10 and ETS-4 zeolites showed the better activity for the photocatalytic degradation as well as mineralization as compare to bare ETS-10 and ETS-4. This could be due to trapping of photogenerated e^- generated in $-O-Ti^{(IV)}-O-$ nanowires and working of transition metal as a sink for photogenerated electrons. Ag ion exchanged ETS-10 and ETS-4 catalyst shows maximum photocatalytic degradation and higher initial rate than bare and among all other transition metal exchanged ETS-10 and ETS-4 catalysts.

The fourth chapter describes the effect of preparation methods on the photocatalytic efficiency of the nanocrystalline titania catalysts. The nanocystalline TiO_2 photocatalyst were prepared by sol-gel, solution combustion and hydrothermal methods. The photocatalytic activity of synthesised catalysts was determined by the degradation of 3,3′-dimethylbiphenyl-4,4′-diamine (*o*-tolidine). The photocatalytic activities of the synthesized catalysts were compared with commercially available P-25 Degussa catalyst. The percentage degradation was determined using UV-visible spectrophotometer, while the mineralization was confirmed by total organic carbon analysis (TOC). A detailed

degradation pathway has been suggested based on electrospray ionization mass spectrometry (ESI-MS). The kinetics was studied by calculating rate constants of the performed reactions. The photocatalytic degradation of *o*-tolidine using P-25 and SG catalysts was higher as compared to SC and HT catalysts and mineralization was almost same using all catalysts. The initial rate of degradation was in the order of SG>P25>SC>HT. The result showed that percentage of degradation and mineralization are well pronounced in presence of catalyst. Mass spectra at different time interval of reaction demonstrate the formation of new molecules by the role of radicals formed during the degradation process. These molecules decompose ultimately to achieve complete mineralization, i.e., carbon dioxide, water and inorganic nitrogen which was confirmed by decreasing TOC values in all the reactions performed.

The fifth chapter consists preparation of zeolite based photocatalyst using TiO_2 coated $NaY_{5.5}$ zeolite. These catalysts were further modified with silver metal ion exchange. The photocatalytic activity of the catalysts was studied by degradation of aqueous *p*-nitrotoluene in presence of UV light. The initial rates and the rate constants were calculated for the kinetic study purpose for the performed reactions. The mineralization of *p*-nitrotoluene in aqueous solution was confirmed by COD analysis. This study demonstrated that the Ag metal ion exchange enhance the photocatalytic activity of the TiO_2 coated zeolite materials. The study on the photocatalytic activity of TiO_2 encapsulated $NaY_{5.5}$ zeolite with and without silver ion exchange towards degradation of *p*-nitrotoluene shows that the optimum loading of TiO_2 is required for the higher activity and the presence of silver ion enhance the photocatalytic activity. The catalyst $TiO_2/AgY_{5.5}$-2 with 2 w/w % loading of TiO_2 exhibited the highest photocatalytic activity for the degradation as well as mineralization of *p*-nitrotoluene among the studied catalysts. The higher loading of TiO_2 can block the pores of zeolite material which results in decrease in adsorption capacity of *p*-nitrotoluene in the catalyst. This could make the decomposition less effective. The presence of the silver ion improves the charge separation and thus enhances the photocatalytic activity of TiO_2. The intermediates suggested were confirmed by the HPLC and decreasing COD values confirmed the mineralization occurring in the process. The kinetics of the photocatalytic oxidation of the *p*-nitrotoluene was successfully modeled by an approximation of the Langmuir-

Hinshelwood (L-H) rate equation based on the hydroxyl radicals and direct hole attack. The reaction rate constants and adsorption constants were determined based on this L-H model.

The sixth chapter of the thesis deals with the TiO_2 coating of the fly-ash cenosphere. The sol-gel process was utilized to coat TiO_2 on the surface of fly-ash cenosphere particles. This is the novel approach to coat the cenosphere particles with TiO_2 photocatalyst using the simple sol-gel technique. Extensive characterization of coated particles was carried out by scanning electron microscopy (SEM), energy dispersive spectroscopy (EDX), X- ray diffraction (XRD), BET surface area, Inductively coupled plasma (ICP), and UV–VIS diffuse reflectance measurements (DRS). The photocatalytic application of these TiO_2 coated cenosphere photocatalysts was investigated by the degradation of dye Methylene blue (MB), nitro-aromatic compound *p*-nitroaniline (PNA) and saturated hydrocarbons *n*-decane and *n*-tridecane under the solar light irradiation. The degradation of the methylene blue and *p*-nitroaniline was investigated using UV-Visible spectrophotometer while degradation of hydrocarbons was investigated using gas chromatography (GC). The mineralization of the aqueous methylene blue and para-nitroaniline was confirmed by COD analysis. The fly-ash cenocsphere was successfully coated with TiO_2 nanoparticles to achieve the aim of a photocatalyst synthesis which shows activity at the aqueous surface to degrade the pollutants under the solar irradiation. The coating was found stable even after three time use of the catalyst in the photocatalytic reaction for MB and PNA. The TiO_2 nanoparticles were of the anatase phase by XRD and TEM analysis which is responsible for the photocatalytic activity. The catalyst was active under the solar light for the degradation. The efficiency of the used catalyst was similar to freshly prepared catalyst which confirms the reusability of the catalyst. The catalyst was efficient for the mineralization also which was confirmed by the COD analysis. *p*-nitroaniline showed more resistance for the degradation as compared to methylene blue. The blank and adsorption study showed that the presence of the catalyst and solar light was essential for the degradation as well as mineralization. The results demonstrated that the catalyst can be used effectively for the aquatic organic pollutants which float at the water surface such as *n*-decane and *n*-tridecane under the natural solar light.

FUTURE PROSPECTS

- **Visible-light-sensitive TiO_2**

  The modification of TiO_2 towards visible light sensitivity is thetopic of current interest in photocatalysis. One approach is to substitute metal ions such as Cr, Fe or Ni for a Ti site while another approach was to form Ti^{3+} sites by introducing an oxygen vacancy in TiO_2. However, these approaches have the lack of reproducibility and chemical stability and thus not widely accepted. Subsequently, the anion such as nitrogen, sulphur and carbon doped TiO_2 has attracted considerable attention. This kind of doping increases the absorbed photon number, but having the disadvantage of decreased photocatalytic activity. the simultaneous doping of nitrogen and sulfur into TiO_2 could narrow the band gap of TiO_2 by mixing N 2p and S 3p with the valence band composed of O 2p. It can be expected that the broad expanse of the electronic state, compared with the isolated one, will show the higher photocatalytic activities irradiated with visible light. However, the visible-light-induced photocatalytic activities of these anion-doped TiO_2 are insufficient and should be further enhanced. This investigation is now under way. These anion-doped TiO_2 are candidate photocatalysts in terms of reproducibility and chemical stability. Therefore, further research and practical applications are desirable.

- **Synthesis of new photocatalyst with high surface area and reusability**

  The research efforts have been directed to enhance the activity of the photocatalysts using various methods such as increasing catalyst surface-to-volume ratio, sensitization of the catalyst using dye molecules and doping the catalyst with non-metals such as nitrogen, carbon, and sulfur and catalyst impregnation of metal ions. The supporting titania catalyst on zeolites, clay and metal oxides were also tried to increase the photocatalytic activity. The titanosilicate zeolites ETS-4 and ETS-10 has in build photocatalytically active TiO_2 units and has been used in our study. This structural property make it more pronounced towards photocatalysis as it do not have the leaching problem of the photocatalytic active TiO_2 material from the support material. However, the

further research is required to prepare such type of new photocatalytic materials and enhance their photocatalytic activity.

- **Photocatalyst synthesis for hydrocarbon removal**

  The photocatalysts has been well studied for the degradation of organic compounds as well as dyes. However, this material can be used for the photocatalytic oxidation of the saturated hydrocarbon which makes a layer on the water surface. The different hydrocarbons from crude oil may get to the surface waters through transportation of crudes. Spill from oil pipes, tubes, reservoirs and tanks represent the serious problems, but in worst condition they may also flood and contaminant large amount soil and ground water. Moreover, all the photocatalysts are having high density and they cannot float on the aqueous surface. The saturated hydrocarbons which float on the aqueous surface cannot decompose by using these catalysts. The attempts must be done to overcome these problems and tried to prepare TiO_2 coated buoyant material. The TiO_2 coated cenosphere has been prepared and well tested in this study but still a lot of challenges are to be considered to improve their photocatalytic activity.

- **Design of nanostructure of TiO_2 surface for highly sensitive hydrophilicity**

  TiO_2 has been applied to indoor use for antibacterial purpose along with its decomposition property. However, the decomposition of pollutants and hydrophilic property in indoor use still require more effort. The TiO_2 surface does not undergo the highly hydrophilic conversion when the UV light has an intensity of 1 mW/cm^2, available in an ordinary living environment. Thus the design of highly sensitive TiO2 that undergoes highly hydrophilic conversion has been required. The hydrophilic conversion is controlled by the reconstruction of surface OH groups and different types of hydrophilic conversion behavior among the various single crystal faces are expected to be observed by comparing their surface atom alignments. As such, the high sensitization of TiO_2 under weak UV light is expected to increase the application areas to indoor conditions.

- **Synthesis of hydrophobic TiO_2 surface**

  The discovery of the photo-induced hydrophilicity has markedly widened the application field of TiO_2-coated materials. The highly hydrophobic TiO_2 surface could open a new application field. The UV irradiation of this hydrophobic TiO_2 can markedly change the surface wettability, i.e., the contact angle (CA) decreased to 0°. In addition, storing the samples in the dark for a long time has found the CA on the etched surface to further increase to approximately 140°, whereas the CA on the nonetched surface remained constant at around 80°. Thus the surface wettability from highly hydrophilic to hydrophobic can be controlled repeatedly by alternating between UV light and dark storage. At present, the hydrophobic conversion takes much time, and must be further enhanced. Another area of concern is super-hydrophobic surface (surface with a CA above 150°). The limited contact area between the solid surface and the water could change chemical reactions and/or bond formation through water, introducing novel properties on the surface. Therefore, the surface property of TiO_2 can be controlled by the preparation of the TiO_2 surface with CA more than 150°.

- **Photocatalytic decomposition of three dimensional pollutants**

  The photocatalysis phenomenon has been used for the pollution clean-up since few decades. However, the purification of the three-dimensional spaces by photocatalysis is much more difficult than that of the two-dimensional surface of building materials. The reason behind this is that the photocatalysis is a surface phenomenon and the reactants must be present at photocatalyst surface. Another reason is that the total concentrations of pollutants are higher in three dimensional spaces than the two dimensional spaces. The practical technologies are required in this field.

ANNEXURE - I

Publications

1. Effect of Anions on the Photocatalytic Activity of Fe(III) Salts Impregnated TiO_2. **Praveen K. Surolia,** Rajesh J. Tayade and Raksh V. Jasra, ***Industrial & Engineering Chemistry Research,*** 46 **(2007)**, 6196-6203.

2. Photocatalytic degradation of dyes and organic contaminants in water using nanocrystalline anatase and rutile TiO_2. Rajesh J. Tayade, **Praveen K. Surolia,** Ramchandra G. Kulkarni, Raksh V. Jasra, ***Science and Technology of Advanced Materials,*** 8 **(2007)** 455-462.

3. Photocatalytic degradation of 3,3'-dimethylbiphenyl-4,4'-diamine (*o*-tolidine) over nanocrystalline TiO_2 synthesized by sol-gel, solution combustion and hydrothermal methods. **Praveen K. Surolia**, Manoj A. Lazar, Rajesh J. Tayade and Raksh V. Jasra**.** ***Industrial & Engineering Chemistry Research,*** 47 **(2008)**, 5847-5855.

4. Enhanced Photocatalytic Activity by Silver Metal Ion Exchanged NaY Zeolite Photocatalysts for the Degradation of Organic Contaminants and Dyes in Aqueous Medium. Rajesh J. Tayade, **Praveen K. Surolia**, Manoj A. Lazar and Raksh V. Jasra**.** ***Industrial & Engineering Chemistry Research,*** 47 **(2008),** 7545-7551.

5. Photocatalytic degradation of nitrobenzene using transition metal exchanged ETS-10 zeolite. **(Manuscript Prepared)**.

6. Heterogeneous photocatalytic degradation of nitrobenzene in transition metals exchanged ETS-4 zeolite aqueous suspension. **(Manuscript Prepared)**.

7. Photocatalytic degradation of *p*-nitrotoluene using TiO_2 incorporated silver exchanged $NaY_{5.5}$ zeolite: Kinetic study and identification of degradation pathway. **(Manuscript Prepared)**.

8. Photodegradation of nitro-aromatic compounds catalyzed by nanosize TiO_2 prepared by sol-gel and solution combustion synthesis. **(Manuscript Prepared)**.

9. Photocatalytic oxidation of saturated hydrocarbon on water on buoyant cenosphere-attached titanium dioxide under solar light irradiation. **(Manuscript Prepared)**.

10. The design and characterization of TiO_2 attached buoyant cenosphere fly-ash with visible light photocatalytic activity. **(Manuscript Prepared)**.

ANNEXURE - II

Symposia / Conference / Awards

A. SYMPOSIA / CONFERENCE

1. "Sol-gel TiO_2 coating of cenospheres and their use for the photocatalytic degradation of Methylene Blue (MB) and *p*-nitroaniline (PNA) under the solar irradiation" *19th National Symposium on Catalysis*, organized by CSI at NCL, Pune, during 18 – 21 April 2009. **(Poster Presentation)**

2. "Photocatalytic Reactivity of Transition Metal Exchanged ETS-10 Zeolites" *22nd Gujarat Science Congress* at Bhavnagar University, Bhavnagar, Gujarat, on 9th March 2008 (**Oral Presentation**)

3. "Photocatalytic degradation of nitrobenzene using transition metal exchanged ETS-10 zeolites" *5th All Gujarat Research Scholars meet* at The M.S. University, Vadodra, Gujarat, on 17th February 2008. (**Oral Presentation**)

4. "Photocatalytic Behavior of Fe(III) Doped Titania Semiconductors Prepared from Different Fe(III) ion Sources" *18th National Symposium on Catalysis*, organized by CSI at IIP, Dehradun, during 16 – 18 April 2007. **(Poster Presentation)**

5. "Enhanced photocatalytic activity of TiO2 by Fe (III) ion impregnation" *4th All Gujarat Research Scholars meet* at The M.S. University, Vadodra, Gujarat, on 22nd January 2006. **(Poster Presentation, 3rd prize)**

6. "Photocatalytic Degradation of Organic Compounds in Water Using Pure and Metal Impregnated Mesoporous TiO_2" *National Symposium on photocatalysis for energy, environment & chemical industries* at M.L.S.University, Udaipur during 15-16 Dec.2005. **(Poster Presentation)**

7. Attended **"***17th National Symposium on Catalysis"* held at Central Salt & Marine Chemical Research Institute, Bhavnagar during 17 – 19th January 2005.

8. Attended "*National Workshop on Catalysis for Energy"* at Banaras Hindu University U.P. during 23 – 25th Feb. 2006.

B. AWARDS

1. **Senior Research Fellow-2007** (Council of Scientific and Industrial Research, India).
2. **Junior Research Fellow-2005** (Council of Scientific and Industrial Research, India).
3. **Best poster presentation award** during *4th All Gujarat Research Scholars meet* at The M.S. University, Vadodra, Gujarat, on 22nd January 2006.

Effect of Anions on the Photocatalytic Activity of Fe(III) Salts Impregnated TiO_2

Praveen K. Surolia, Rajesh J. Tayade, and Raksh V. Jasra*

Discipline of Inorganic Materials and Catalysis, Central Salt and Marine Chemicals Research Institute, Bhavnagar-364 002, India

This present work focuses on the photocatalytic activity of Fe(III) salt-impregnated TiO_2 catalysts for studying the effect of anion on the photocatalytic activity of the salt-impregnated catalysts. The salt-impregnated TiO_2 photocatalyst samples prepared using $FeCl_3$, $Fe(NO_3)_3$, and $Fe_2(SO_4)_3$ were characterized by X-ray diffraction (XRD), UV−vis diffuse reflectance spectrophotometry (DRS), Fourier transform infrared absorption spectrophotometry (FT-IR), and surface area measurement by N_2 adsorption. Fe(III) ion impregnation of TiO_2 with different salts is observed to influence photocatalytic degradation of acetophenone. Fe(III) salt anions were observed to influence the initial rate of degradation. For example, the initial rate of degradation of acetophenone decreases with an increase in percentage of Fe(III) ions in the case of the catalysts prepared using ferric nitrate and ferric chloride salts. However, the initial rate of degradation was observed to increase with ferric sulfate impregnated catalysts. The final percentage degradation of acetophenone was found to increase continuously with an increase in Fe(III) ion concentration, irrespective of the anion. These observations have been discussed in terms of influence of the presence of Fe(III) ions on the recombination of the electron and holes generated during UV irradiation of TiO_2. Similarly, the effect of anion has been discussed in terms of radical-scavenging ability of chloride and radical-generating ability of sulfate anions.

Introduction

In the last decade, research efforts have been directed to enhance the activity of the photocatalysts using various methods such as increasing catalyst surface-to-volume ratio, sensitization of the catalyst using dye molecules,[1,2] doping the catalyst with nonmetals such as nitrogen, carbon, and sulfur and catalyst impregnation of metal ions.[3−6] It has been demonstrated that the addition of a low percentage of a metal ion such as Pt, Ag, Au, Cu, Ni, Co, Fe, and Mg in TiO_2 improves[7−9] its photocatalytic activity. Fe metal ions impregnation has been studied for photocatalytic efficiency enhancement of the TiO_2 catalysts, and varied results are reported.[10−13] This could be due to the different synthesis methods, the percentage of ion impregnated, and the source used for the impregnation of Fe. For example, Choi et al.[10] suggested that the ability of a dopant to function as an effective electron-hole trap is related to the dopant concentration and reported the highest activity at 0.5 at. % of Fe(III). Li et al.[11] studied the photocatalytic oxidation of cyclohexane and found higher photocatalytic activity with Fe(III) ion impregnation. Vamathevan et al.[12] found lower activity of catalyst with 5 atomic % or higher loading of Fe(III) in TiO_2 particles for the degradation of sucrose. These studies concluded that an increasing amount of iron could cause its agglomeration at the surface of TiO_2 to form α-Fe_2O_3. This results in the reduction of catalytically active and electron relay sites and thereby negatively influences the photocatalytic activity. The present work was carried out to specifically study the effect of the anion of Fe(III) salts used for impregnation on the photocatalytic activity of P25 Degussa TiO_2 photocatalyst. To study the photocatalytic activity, degradation of acetophenone in aqueous medium was used as a model organic compound with ultraviolet irradiation.

Experimental Section

Materials. Titanium dioxide (P25) was purchased from Degussa Corporation (Degussa AG, Frankfurt, Germany). Ferric nitrate, ferric sulfate, and ferric chloride were procured from s. d. Fine Chem. Ltd., Mumbai, India. Acetophenone, analytical reagent (AR) grade, was purchased from E. Merck, India. Deionized distilled water was used to make up the reaction mixture.

Catalysts Preparation. Catalysts were prepared by wet impregnation method. P25 Degussa TiO_2 was suspended in aqueous solutions of the Fe(III) salt. The mixture was stirred for 36 h under normal room conditions to get the loading of Fe metal ion of 0.1, 0.5, 1.0, 5.0, and 10.0% (w/w) followed by drying of the slurry under vacuum using rotavapor and further drying in an oven at 353 K for 12 h. The thus-dried catalysts were thoroughly ground with an agate mortar pestle and calcined at 723 K temperature for 4 h in the presence of air. The impregnated TiO_2 catalysts with ferric nitrate were denoted as Ti−N1, Ti−N2, Ti−N3, Ti−N4, and Ti−N5, wherein the numeral denotes the percentage (w/w) of iron as 0.1, 0.5, 1.0, 5.0, and 10.0, respectively. Similarly for Fe, impregnated catalysts using ferric chloride and ferric sulfate were denoted as Ti−C1, Ti−C2, Ti−C3, Ti−C4, Ti−C5, Ti−S1, Ti−S2, Ti−S3, Ti−S4, and Ti−S5, respectively. The actual loading of Fe(III) ion was confirmed by inductively coupled plasma (ICP)−optical emission spectrophotometer analysis, and values are given in Table 3.

Catalyst Characterization. The catalysts were characterized by powder X-ray diffraction (XRD) recorded at 295 K using Phillips X'pert MPD system with Cu Kα_1 radiation (λ = 0.15405 nm). Diffraction patterns were measured in 2θ range from 10°−60° at a scan speed of 0.1° s^{-1}. The XRD peaks of crystal plane 101 for anatase appeared at 25.3 (2θ) and at 27.4 (2θ) for 110 plane of rutile. These peaks were selected to determine the percentage of anatase and rutile phases[14] in the TiO_2 sample. The percentage of anatase, A (%), was determined using the following equation,

$$A\ (\%) = 100/(1 + 1.265 I_R/I_A) \qquad (1)$$

where I_R is the intensity of the rutile peak at $2\theta = 27.4$ and I_A is the intensity of the anatase peak at $2\theta = 25.3$. The crystallite

* To whom correspondence should be addressed. E-mail: rvjasra@csmcri.org. Tel.: +91 278 2471793. Fax: +91 278 2567562.

10.1021/ie0702678 CCC: $37.00
Published on Web 08/16/2007

Photocatalytic Degradation of 3,3′-Dimethylbiphenyl-4,4′-diamine (*o*-Tolidine) over Nanocrystalline TiO_2 Synthesized by Sol−Gel, Solution Combustion, and Hydrothermal Methods

Praveen K. Surolia, Manoj A. Lazar, Rajesh J. Tayade, and Raksh V. Jasra*

Discipline of Inorganic Materials and Catalysis, Central Salt & Marine Chemicals Research Institute, Council of Scientific and Industrial Research, G. B. Marg, Bhavnagar-364002, India

The nanocrystalline titania catalysts were prepared by sol−gel, solution combustion, and hydrothermal methods. The catalysts were characterized by X-ray diffraction (XRD), Fourier-transform infrared spectrophotometry (FT-IR), scanning electron microscopy (SEM), and BET surface area analysis for their structural properties and by diffuse reflectance spectrophotometer (DRS) for band-gap studies. The photocatalytic activity of synthesized catalysts was determined by the degradation of 3,3′-dimethylbiphenyl-4,4′-diamine (*o*-tolidine). Commercially available P-25 Degussa catalyst was used as a reference catalyst to compare the photocatalytic activity. The percent degradation was determined using UV−visible spectrophotometer, while the mineralization was confirmed by total organic carbon analysis (TOC). A detailed degradation pathway has been suggested based on electrospray ionization mass spectrometry (ESI-MS). Comparison of different catalysts showed that degradation was favored with the sol−gel synthesized TiO_2 catalyst, while mineralization was nearly the same using a catalyst synthesized by sol−gel, solution combustion method, and commercial TiO_2 Degussa P25.

Introduction

The heterogeneous photocatalysis using a semiconductor has been reported to promote the degradation and total mineralization for a wide range of pollutants both from water and air.[1−5] Titanium dioxide has emerged as an excellent material for the photocatalytic degradation of toxic compounds which are hazardous to health. There are many studies dealing with photocatalytic degradation of organic pollutants from different class of compounds.[6−11] Most of these studies include a detailed examination of the primary processes of degradation, but provide little information on the reaction mechanism involved in the degradation and identification of major transient intermediates. Also, the literature on the photocatalytic degradation of nitrogen-containing aromatic compounds is sparse.[12−14]

In all the applications, the morphology, average particle size and size distribution, phase composition, and porosity of titania powders are important factors to be controlled. Nanoparticles show a great tendency to aggregate due to high surface energy combined with their high surface area to volume ratio. This aggregation tendency impedes their use in a variety of applications. For these reasons the synthesis of ultrafine particles with controlled size and surface chemistry is of technological interest. The different synthesis methods are responsible for different characteristics mentioned above. Thus the photocatalytic efficiency depends on the preparation method of the catalyst[15] that can influence significantly the composition and the size of the crystals and the surface distribution of hydroxyl groups.[16−18] The sol−gel method is a simple and versatile process for the synthesis of nanocrystalline materials. The solution combustion method is a single-step process, and it has been reported that this method gives fine particles/large surface area oxide materials such as alumina, ceria, titania, and zirconia. Micelles and inverse micelles are commonly employed to synthesize TiO_2 nanomaterials.[19−21]

The aromatics containing nitro and amino groups are toxic in nature [22−24] and act as an inhibitor for the biodegradation of other compounds of waste.[25−28] These pollutants enter into the environment during their manufacturing processes and in their use as chemical intermediates in chemical processes. The aromatic amines could cause cyanosis and increased respiratory rate from methamoglobinemia.[29] Regardless of exposure route or length, all aromatic amines affect the blood as the primary target organ and need to be stringently controlled.

In the present study, we have synthesized titania samples using different synthesis processes reported earlier[17,20,21] for the degradation of 3,3′-dimethylbiphenyl-4,4′-diamine (*o*-tolidine). The textural and electronic properties of catalysts were compared using different techniques. Their photocatalytic performance has been compared with a commercial Degussa P25 sample. An attempt was made to correlate structural properties of titanium dioxide to their photocatalytic activity. The mineralization achieved during the reaction was determined by total organic carbon (TOC) analysis. Electrospray ionization mass spectrometry (ESI-MS)[30,31] technique was used to identify possible major intermediates and photodegradation products, and a possible reaction pathway for mineralization has been suggested.

Experimental

Chemicals and Materials. Titanium dioxide (P25) was purchased from Degussa Corporation (Degussa AG, Frankfurt, Germany). Titanium(IV) tetraisopropoxide (97%) and glycine were procured from Sigma Aldrich, India. *o*-Tolidine (OT), *n*-hexanol and cyclohexane, AR grade, were purchased from E. Merk, India. Deionized distilled water was used to make up the reaction mixture.

Catalyst Preparation. The TiO_2 was synthesized by sol−gel,[17] solution combustion[20] and microemulsion mediated hydrothermal synthesis[21] methods as reported earlier. For sol−gel synthesis procedure, the titanium(IV) tetraisopropoxide was taken with the appropriate amount of dry ethanol in a 500

* To whom correspondence should be addressed. E-mail: rvjasra@gmail.com. Tel.: +91 278 2471793. Fax: +91 278 2567562.

10.1021/ie800073j CCC: $40.75
Published on Web 07/17/2008

Enhanced Photocatalytic Activity by Silver Metal Ion Exchanged NaY Zeolite Photocatalysts for the Degradation of Organic Contaminants and Dyes in Aqueous Medium

Rajesh J. Tayade, Praveen K. Surolia, Manoj A. Lazar, and Raksh V. Jasra*,†

Discipline of Inorganic Materials and Catalysis, Central Salt and Marine Chemicals Research Institute, (Council of Scientific and Industrial Research), G. B. Marg, Bhavnagar-364002, India

Zeolite-based photocatalyst have been prepared using TiO_2-coated NaY zeolite by post-synthesis modification with silver metal ion exchange. The characterization of the catalysts was carried out by X-ray diffraction (XRD), scanning electron microscopy (SEM), Inductively coupled plasma-optical emission spectrophotometry (ICP), Diffuse reflectance spectroscopy (DRS), Fourier transform infrared spectroscopy (FTIR), and N_2 adsorption techniques. The presence of metal ions and TiO_2 on zeolite surface was observed by UV-visible diffuse reflectance spectroscopy. It was found that the structure of the support materials is retained after the silver metal ion exchange. The photocatalytic activity of the catalysts was studied by degradation of aqueous nitrobenzene, acetophenone, methylene blue, and malachite green in the presence of UV light. The highest photocatalytic activity was obtained for silver metal ion exchanged photocatalysts coated with TiO_2 (2%, w/w) as compared to other silver exchanged NaY zeolite catalysts. This study demonstrated that the Ag metal ion exchanged TiO_2-coated NaY is a better catalyst as compared to the TiO_2-coated NaY photocatalysts.

1. Introduction

Zeolites[1−3] have demonstrated their potential as unique and versatile host materials for variety of chemical transformations.[4−8] Semiconductor-loaded zeolite and mesoporous materials such as MCM-41 have drawn attention as potential photocatalysts due to their unique pore structure and adsorption properties. Titanium dioxide has proved to be a potential photocatalytic semiconductor as it allows for the complete degradation of pollutants under ultraviolet irradiation. The advantages using zeolite or mesoporous support for titania photocatalysis include formation of ultrafine titania particles during sol-gel deposition; increased adsorption in the pores; surface acidity which enhances electron-abstraction; and decreased UV-light scattering as the main component of zeolite is silica.[9−13]

Zeolites are microporous materials with framework anions (AlO_2^-) and exchangeable cations in its structure, and the anion−cation pairs generate strong electrostatic fields[13,14] which strongly interact with polar adsorbates. Because of these attributes, zeolites are widely used as catalysts and adsorbents for organic synthesis and decomposition[15] as well as in waste-gas adsorption and wastewater treatment.[16,17] The fascinating properties of zeolites involving transition metal ions within the zeolite frameworks or cavities have opened new possibilities for many applications in catalysis[18] and photochemical processes.[19,20] The transition metal ion loaded or impregnated photocatalysts using various methods were shown to possess higher photocatalytic activity as compared to the bare photocatalyst due to charge separation.[21] These photocatalytic reactions were found to proceed with high efficiency and selectivity, displaying reaction mechanisms different from those observed on semiconducting photocatalysts, in which the photoelectrochemical reaction mechanism or charge separation plays an important role in determining the efficiency. Furthermore, the counter-cations in zeolites can easily be exchanged by other cations by an ion exchange method. The exchangeable sites are separated from each other within the zeolite cavities under well-controlled conditions. Zeolites can be modified through the incorporation of active species in the pores by various methods, for instance, ion exchange and impregnation.[22,23]

A method of supporting TiO_2 on zeolite, without losing the photosensitization of TiO_2 and the adsorption properties of zeolite, is an important aspect while preparing zeolite-based photocatalysts. Our earlier work has demonstrated the enhanced photocatalytic activity of the TiO_2-coated zeolites.[24] There is great interest in silver because of its importance in photocatalytic processes and because of its unique catalytic properties.[25,26] Therefore, to explore the possibility of further enhancement of the TiO_2-coated photocatalysts, we have synthesized silver-exchanged zeolite photocatalysts using the metal ion exchange method, and a photocatalytic study of the degradation of organic compounds like nitrobenzene and acetophenone and dyes like methylene blue and malachite was carried out in this work.

2. Experimental Section

2.1. Chemicals. Zeolite NaY with Si/Al ratio 5.5 was procured from Süd Chemie, Vadodara, India. Titanium tetraisopropoxide (97%), was procured from Aldrich. Silver nitrate, AR grade, was procured from Ranbaxy, India. Nitrobenzene (NB), AR grade (99.0%), Methylene blue (MB), and Malachite green (MG) were procured from s. d. Fine Chem. Limited, India. Acetophenone (AP) and COD standard chemical reagents from E. Merck India Ltd., India were used for the photocatalyst preparation.

2.2. Activation of Zeolite. Prior to the coating of TiO_2, it is required to remove the water present in the zeolite samples as the presence of water in the zeolite cavities and on an external surface could hydrolyze titanium tetraisopropoxide outside the zeolite cavity which may significantly affect the coating of TiO_2 inside the pores of the zeolite. Therefore, NaY zeolite was

* To whom correspondence should be addressed. Tel.: +91 265 6693935. Fax: +91 265 6693934. E-mail: rvjasra@gmail.com.

† Current address: R&D Centre, VMD, Reliance Industries Limited, Vadodara, 391 346, India.

10.1021/ie800441c CCC: $40.75
Published on Web 09/20/2008

Available online at www.sciencedirect.com
ScienceDirect
Science and Technology of Advanced Materials 8 (2007) 455–462
SCIENCE AND TECHNOLOGY OF ADVANCED MATERIALS
www.elsevier.com/locate/stam

Photocatalytic degradation of dyes and organic contaminants in water using nanocrystalline anatase and rutile TiO_2

Rajesh J. Tayade[a], Praveen K. Surolia[a], Ramchandra G. Kulkarni[b], Raksh V. Jasra[a,*]

[a]*Discipline of Inorganic Materials and Catalysis, Central Salt & Marine Chemicals Research Institute, G.B. Marg, Bhavnagar 364002, India*
[b]*Department of Physics, Saurashtra University, Rajkot 360005, India*

Received 13 April 2007; received in revised form 16 May 2007; accepted 28 May 2007
Available online 12 July 2007

Abstract

Nanocrystalline TiO_2 was synthesized by controlled hydrolysis of titanium tetraisopropoxide. The anatase phase was converted to rutile phase by thermal treatment at 1023 K for 11 h. The catalysts were characterized by X-ray diffraction (XRD), diffuse reflectance spectroscopy (DRS), Fourier-transform infrared absorption spectrophotometry (FT-IR) and N_2 adsorption (BET) at 77 K. This study compare the photocatalytic activity of the anatase and rutile phases of nanocrystalline TiO_2 for the degradation of acetophenone, nitrobenzene, methylene blue and malachite green present in aqueous solutions. The initial rate of degradation was calculated to compare the photocatalytic activity of anatase and rutile nanocrystalline TiO_2 for the degradation of different substances under ultraviolet light irradiation. The higher photocatalytic activity was obtained in anatase phase TiO_2 for the degradation of all substances as compared with rutile phase. It is concluded that the higher photocatalytic activity in anatase TiO_2 is due to parameters like band-gap, number of hydroxyl groups, surface area and porosity of the catalyst.

Keywords: Nanocrystalline TiO_2; Anatase; Rutile; Band-gap; Hydrothermal method; Photocatalysis; Dyes; Organic compounds

1. Introduction

Contaminants from industrial effluents often pose a major environmental problem. Semiconductor photocatalysis is one technique that has great potential to control aqueous organic contaminants or air pollutants. It holds several advantages over conventional oxidation processes, such as (1) complete mineralization of the pollutants, (2) use of near-UV or solar light, (3) no addition of other chemicals, and (4) operation at near room temperature [1–6]. Although photocatalytic degradations of trace toxic organic compounds in water or air have been investigated intensively in the past decade, there still remain some problems for practical applications [5]. Fundamental research regarding the preparation of photocatalysts with high photocatalytic activity, the immobilization of powder photocatalyst and the improvement of photocatalyst performance are priorities to be considered [5–8]. Among various oxide semiconductor photocatalysts, TiO_2 is an important photocatalyst due to its strong oxidizing power, non-toxicity and long-term photostability. Specific applications of TiO_2 crystalline particles are determined by their chemical, structural and physical properties. In particular, its surface state, the nature and concentration of surface-active centers and defects are considered to play important roles. TiO_2 exists in three different crystalline phases: rutile, anatase and brookite, among which rutile is a thermodynamic stable state, while the latter two phases are metastable states [9]. The photocatalytic activity of TiO_2 depends on its phase structure, crystallite size, specific surface areas and pore structure. For example, many studies have confirmed that the anatase phase of TiO_2 is a superior photocatalytic material for air purification, water disinfection, hazardous waste remediation and water purification [1,2]. However, it is not yet well understood which factors are responsible for the higher photocatalytic activity of anatase than rutile TiO_2.

In this work, we synthesized anatase and rutile nanocrystalline TiO_2 and tried to characterize both the

*Corresponding author. Tel.: +91 278 2471793; fax: +91 278 2567562.
E-mail address: rvjasra@csmcri.org (R.V. Jasra).

1468-6996/$ - see front matter © 2007 NIMS and Elsevier Ltd. All rights reserved.
doi:10.1016/j.stam.2007.05.006